Green Synthesis and Capacity Fade Mechanism of Lithium Titanate Nanosheet Anode for Lithium-Ion Batteries

Hsien-Chieh Chiu

Department of Mining and Material Engineering

McGill University
Montréal, Québec
Canada

A thesis submitted to McGill University in partial fulfillment of the requirements of the degree of Doctor of Philosophy

Upon topotactic transformation from lithium titatnate hydrates to lithium titanates, the residual strains causes lattice distortion around the Li ions environment that has profound influence on the Li ion storage properties of lithium titanates.

Abstract

In this thesis, nanostructured lithium titanate, $Li_4Ti_5O_{12}$ (nano-LTO), is synthesized and characterized in terms of phase transformations during different stages of synthesis and cycling, aiming towards the design of stable and high-power performing anodes for Li-ion batteries. In this context, the following aspects are considered: (i) development of a sustainable aqueous-based process for nano-LTO synthesis; (ii) determination of the crystallization kinetics of 2D lithium titanate hydrate crystals (LTH; $(Li_{2-x}H_x)Ti_2O_5 \cdot yH_2O$); (iii) probing the thermal transformation of LTH nanocrystals to nano-LTO; and (iv) understanding and controlling the capacity fade mechanism of nano-LTO upon cycling.

The devised process is a two-step chemical/annealing process. Step 1 involves aqueous solution reaction of LiOH with $TiCl_4$ at < 10 °C, Li/Ti = 1.3 and pH 11.5-12 to produce a hydrous precipitate, which is aged in LiOH solution at 80 °C to promote 2D LTH crystal formation. In step 2, the intermediate LTH crystals are converted to nanostructured LTO via thermal conversion (annealing over the temperature range 400 °C to 600 °C). It is demonstrated that the 2D shape of LTH crystals is preserved via proper annealing, yielding sheet-like morphology to nano-LTO during thermal conversion.

The 2D anisotropic growth of LTH nanocrystals, has been successfully studied via the employment of *in situ* Raman spectroscopy during isothermal solution aging. At the beginning of crystallization, mono-layered LTH nuclei are seen to form via oxygen diffusion; as the LTH nanosheet crystals grow anisotropically, they inter-block to limit their length to 50 nm. The LTH crystallization mechanism obeys the modified Johnson-Mehl-Avrami-Kolmogorov (JMAK) nucleation-growth kinetic model.

The mechanism of topotactic transformation of lepidocrocite LTH crystals into spinel LTO crystals was elucidated by synchrotron X-ray and other types of characterization. It was revealed that upon annealing, dehydration of LTH leads to topotactic transformation from a *C*-centered orthorhombic to a body-centered orthorhombic system. Dehydrated LTH then transforms into spinel LTO nanosheets. More importantly, it was shown that residual strain in the thermally formed LTO nanosheets is associated with structural relaxation, which is triggered by excess Li-ion storage upon cointercalation. These phenomena adversely affect the Li-ion intercalation properties of nano-LTO, leading to performance deterioration. Via carefully selecting the annealing protocol, it is demonstrated the residual strain elimination/manipulation opens the path for highly stable and high-power LTO nanosheet anodes.

Excessive Li storage in nano-LTO (over the stoichiometric $Li_7Ti_5O_{12}$ of 175 mAh/g) is a consequence of Li-ion occupation at vacancies in the near-surface region, which are thermodynamically unfavorable in bulk LTO. Those excessively intercalated Li ions trigger formation of the relaxed LTO structure, which interferes with Li-ion diffusion/storage and eventually causes capacity fade. A JMAK kinetic model was developed to describe the formation of relaxed LTO. Namely, the near-surface region of nano-LTO is completely converted into relaxed structure, via continuous nucleation at constant rate followed by isotropic growth. Once the near-surface zone of relaxed LTO is fully saturated, the capacity fade is then governed by electrolyte/LTO interfacial reaction instead. These findings would be very valuable as the Li-ion battery research community is working to understand and stabilize electrode materials from their synthesis to their long-term cycling performance.

Résume

Dans cette thèse, le titanate de lithium nano-structuré $Li_4Ti_5O_{12}$ (nano-LTO) est synthétisé et caractérisé en termes de transformations de phase atomique lors de différentes étapes de synthèse et cycle charge décharge. La récente recherche vise à la conception d'anodes stables et performantes pour une batteries Li-ion. Pour ce faire, les aspects suivants sont pris en considération :

(i) Développement d'un processus aqueux durable pour la synthèse de nano-LTO.

(ii) Détermination la cinétique de cristallisation du cristal d'hydrate de titanate de lithium en 2D (LTH; $(Li_{2-x}H_x)Ti_2O_5 \bullet yH_2O$).

(iii) Étude de la transformation thermique du nano-cristal LTH en nano-LTO.

(iv) Formulation mathématique sur la nature de dégradation de nano-LTO au cours de son cycle charge décharge.

La procédure de synthétisation contient deux étapes différentes :

(i) La réaction chimique en solution aqueuse de LiOH avec $TiCl_4$ à la température <10 °C, Li/Ti = 1.3 et pH = 11.5 - 12. Cette étape permet à produire un précipité hydraté dans une solution de LiOH à 80 °C. Celle-ci favorise la formation de cristaux de LTH en 2D.

(ii) La deuxième étape consiste à réchauffer le produit intermédiaire de LTH à une température entre 400-600 °C. Cette étape permet de convertir LTH en LTO nano-structuré par la conversion thermique tout en conservant sa morphologique 2D des cristaux de LTH.

La croissance anisotrope des nano-cristaux de LTH en 2D a été étudiée avec succès par l'entremise de la spectroscopie Raman in situ lors du vieillissement en solution isotherme. Au début de la cristallisation, les noyaux LTH monocouches se forment par diffusion des atomes d’oxygène. À mesure que les cristaux de LTH se développent de manière anisotrope, il est possible de former la structure atomique avec une longueur inférieure à 50 nm. En fait, le mécanisme de cristallisation LTH obéit au modèle cinétique de croissance nucléaire de Johnson-Mehl-Avrami-Kolmogorov (JMAK), avec modification pour en tenir compte de l'effet inter-blocage qui limite la croissance de cristaux LTH.

Le mécanisme de la transformation Topotactique des cristaux LTH Lepidocrocite dans des cristaux LTO spinelle a été expliqué par synchrotron et d'autres types de caractérisation. Il a été démontré que, la déshydratation de LTH provoque une transformation Topotactique d'un système orthorhombique centré en C vers un système orthorhombique centré sur le corps. La LTH déshydratée se transforme ensuite en nano-feuille de LTO spinelle. Cependant, il a été aussi montré que la contrainte résiduelle dans les nano-feuilles de LTO formées thermiquement est associée à la relaxation structurale déclenchée par l'excès de stockage de Li-ion lors de la co-calcination pendant le cycle initial. Ces phénomènes affectent négativement la performance électrochimique de nano-LTO. Notre recherche optimise la procédure dans le but d’obtenir des anodes à feuille de nano-LTO à haute puissance et hautement stables.

Le stockage excessif de Li dans le nano-LTO (sur le $Li_7Ti_5O_{12}$ stœchiométrique de 175 mAh/g) est une conséquence de l'occupation des Li-ion à des sites atomique vacants dans la région surfacique, qui sont thermodynamiquement défavorables pour le LTO massique. Ces ions Li excessivement intercalés déclenchent la formation de la structure LTO relâchée, ce qui interfère avec la diffusion et le stockage des ions de lithium et provoque éventuellement une diminution de sa capacité.

Un modèle cinétique JMAK a été développé pour décrire la formation de LTO relâché. Une réaction nucléaire continue à vitesse constante suivie d'une croissance isotrope pour convertir complètement la région proche de la surface du nano-LTO en une structure relâchée. Une fois que la zone proche de la surface du LTO relâché est complètement saturée, la perte de capacité est alors régie par une réaction d’interface électrolyte/LTO. Ces résultats seraient très importants car beaucoup de scientifiques travaillent à comprendre et à stabiliser les matériaux des électrodes durant leur synthèse dans le but d’obtenir une plus grande performance de cycle charge décharge.

Acknowledgements

At the beginning, my thanks go to my funding agency for financially supporting this research, which is of McGill Engineering Doctoral Award jointly funded by the McGill University Faculty of Engineering and the Natural Sciences and Engineering Research Council's strategic grant program. Among so many individuals who generously made contributions to the accomplishment of this thesis, my supervisor, Professor George P. Demopoulos, must be the foremost one with all my best gratitude. Without his advices, patience and offering this unique research opportunity, my life would be completely different from who I am now. Under his supervision, I always feel being completely supported and respected. This makes a great impact to me, both mentally and culturally, because how I used to be taught back to Taiwan is simply to follow the orders without doubts. Professor Demopoulos indeed trained me to become an independent researcher, instead of just a robot to act at someone's commands for my entire life.

Meanwhile, I greatly appreciate the experience of being able to work with Professor De-tong Jiang and his PhD student Zachary Arthur in University of Guelph. Although staying up for 60 hours in Canadian Light Source to cope with so many unexpectable troubles in order to get reliable experimental results is one of the most terrifying experience I have been so far, still I have learned much valuable knowledge on synchrotron X-ray techniques, battery design and virtue like perseverance. What didn't kill you makes you stronger, well at least mentally.

Hereby I want to thank all present/past members in Hydromet group. Six years are long enough to share unforgettable memories. Especially Dr. (or Professor from now on) Xia Lu, he is more like a mentor than simply a colleague even though we share the contradictory stand on my nationality. Also, the help from McGill staff like David Liu, Ranjan Roy, Barbara Hanley, Terry Zatylny and Monique Riendeau are of my deep gratitude.

In the meantime, I would like to acknowledge my family for their support throughout this process. I knew, Mom, I have never been a good kid on all possible definitions. And I have barely appreciated your sacrifices before. Until now, I finally realize how difficult it is to be a single mother carrying three children, and it is time for me to pay you back and take care of our family now. Finally, I must leave some words to my dad in here even though he is in a better place now. Hey, your son finally make it!

Foreword

As an alternative to the traditional thesis format, McGill University offers the option to Ph.D. candidates to use a manuscript-based thesis format. Chapter 3, 4, 5 and 6 of this thesis have been published already in refereed journals. Thus, whole chapters follow the format of journal papers beginning with the introduction and experimental details, which inevitably share some extent commons as the result of discussing similar topics.

Authorship contributions

Chiu, H. C.; Brodusch, N.; Gauvin, R.; Guerfi, A.; Zaghib, K.; Demopoulos, G. P. Aqueous Synthesized Nanostructured $Li_4Ti_5O_{12}$ for High-Performance Lithium Ion Battery Anodes. *J. Electrochem. Soc.* **2013,** *160* (5), A3041. DOI: 10.1149/2.008305jes

Chiu, H.-C.; Lu, X.; Elouatik, S.; Zaghib, K.; Demopoulos, G. P. Formation of Lithium Titanate Hydrate Nanosheets: Insight into a Two-Dimension Growth Mechanism by in Situ Raman. *Cryst. Growth. Des.* **2016,** *16* (7), 3898. DOI: 10.1021/acs.cgd.6b00470

Chiu, H.-C.; Lu, X.; Zhou, J.; Gu, L.; Reid, J.; Gauvin, R.; Zaghib, K.; Demopoulos, G. P. Capacity Fade Mechanism of $Li_4Ti_5O_{12}$ Nanosheet Anode. *Adv. Energy Mater.* **2016**, DOI:10.1002/aenm.201601825 10.1002/aenm.201601825, 1601825. DOI: 10.1002/aenm.201601825

Chiu, H.-C.; Lu, X.; Zhou, J.; Gu, L.; Reid, J.; Gauvin, R.; Zaghib, K.; Demopoulos, G. P. Annealing-regulated elimination of residual strain-induced structural relaxation for stable high-power $Li_4Ti_5O_{12}$ nanosheet anodes. *Nano Energy* **2017,** *32*, 533 DOI: 10.1016/j.nanoen.2016.12.063

All papers have been submitted for publication with the supervisor, Dr. George P. Demopoulos, as a coauthor. The author of this thesis has performed material synthesis, detailed material characterization and electrochemical tests. Some exceptions requiring more expertise in operation were conducted with the help from the coauthors, thus, *scanning electron microscopy* was performed by Mr. Nicolas Brodusch; Dr. Lin Gu conducted all data collection of *scanning transmission electron microscopy*. Synchrotron X-ray techniques of *X-ray diffraction* and *X-ray absorption near-edge structure* were performed by Dr. Joel Reid and Dr. Jigang Zhou, respectively, who also offered great help on data interpretation.

Dr. Samir Elouatik and Dr. Raynald Gauvin provided their guidance and schedule arrangement on *Raman spectroscopy* and *scanning electron microscopy,* respectively. Dr. Karim Zaghib and Dr. Abdelbast Guerfi from Hydro-Québec's research institute (IREQ) generously provided their resources and expertise on some *electrochemical tests*. Dr. Xia Lu made many contribution on conception, manuscript revision and data analysis.

I hereby give copyright clearance for the inclusion of the above papers, of which I am a co-author, into the Ph.D. dissertation of Hsien-chieh Chiu.

Signature: ______________________________________ Date: ______________________

Dr. George P. Demopoulos

Department of Mining and Material Engineering

McGill University

Montréal, Québec

Contents

Appendices

List of Figures

List of Tables

List of Symbols and Abbreviations

Symbols

η	Polarization losses
$\tilde{\mu}$	Mobility
μ_A	Electrochemical potential of electrons in the anode
μ_C	Electrochemical potential of electrons in the cathode
σ_i	Li-ion conductivity
σ_{spinel}	Electrical conductivity of $Li_4Ti_5O_{12}$ spinel
σ_{overLi}	Electrical conductivity of $Li_{7+x}Ti_5O_{12}$
τ	Nucleation time of that transformed grain
χ^2	Goodness of fit in Rietveld Refinement
ω	Raman shift
ΔE	Overpotential variation
ΔG	Gibbs free energy difference per atom of the phase
A	Pre-exponential factor in the Avrami equation
A_{ele}	Electrode surface area
A_{Geo}	The geometrical area of electrode
A_{true}	The total surface area of electrode material
C	Applied current rate representing the power capability; 1C = 175 mAh/g in LTO
D	Diffusivity
E_a	Activation energy

E_g	Activation energy for crystal growth
E_n	Activation energy for crystal nucleation
F	Faraday's constant
$I(t)$	Nucleation rate per unit of untransformed space at specified time t
I	Applied electrical current
I_{dis}	Discharge current of batteries
K	Arbitrary constant
L	Length
$\overline{L_\iota}$	Characteristic length of grain size
M_w	Molar mass
N_0	Initial nucleation rate
P_{out}	Delivered power of batteries
Q_{th}	Theoretical specific capacity; 175 mAh/g of LTO
Q	Total capacity of batteries
R	Electrical resistance
R_{Bragg}	Expected reliability factor in Rietveld Refinement
R_{wp}	Weighted reliability factor in Rietveld Refinement
T	Temperature
V(t)	Extended space of a single transformed grain at specified time t
V_{ch}	Charge voltage
V_{dis}	Discharge voltage
V_{oc}	Open circuit voltage
Z	Atomic number

a	Time exponent of nucleation process
d	Distance between atomic layers in a crystal
e	Magnitude of the electron charge
h	Cycle numbers
k_B	Boltzmann constant
m	Aggregation factor
n	Number of electrons
q	State of charge
t	Time
w	Width of crystals
v	Rate constant
x	Fraction of transformed space during crystallization
d_g	Dimensionality of crystal growth
$r(h)$	Growth rate at a specified cycle number
x_{extended}	Extended fraction of transformed space during crystallization
$x(t)_{\text{overLi}}$	Fraction transformed from $Li_4Ti_5O_{12}$ into $Li_{7+x}Ti_5O_{12}$
z	Valence number of charge carriers

Abbreviations

BET	Brunauer–Emmett–Teller surface area
CV	Cyclic voltammetry
DEC	Diethyl carbonate
DMC	Dimethyl carbonate
DOD	Depth of discharge
EC	Ethylene carbonate
EIS	Electrochemical impedance spectroscopy
EV	Electric vehicles
FY	Fluorescence yield
HAADF	High-angle annular-dark-field
HEV	Hybrid electric vehicles
HOMO	Highest occupied molecular orbital
ICP-AES	Inductively coupled plasma - atomic emission spectroscopy
JMAK	Johnson-Mehl-Avrami-Kolmogorov equation
NMP	N-methyl pyrrolidinone
PE	Polyethylene
PHEV	Plug-in hybrid electric vehicles
PP	Polypropylene
PVDF	polyvinylidene fluoride
LIB	Lithium ion batteries
LTH	Lithium titanate hydrates, $(Li_{2-x}H_x)Ti_2O_5 \cdot yH_2O$
LTO	Lithium titanates, $Li_4Ti_5O_{12}$
LUMO	Lowest unoccupied molecular orbital

SAE-NMR	Spin-alignment echo nuclear magnetic resonance
SAED	Selected area electron diffraction
SEM	Scanning electron microscopy
SEI	Solid electrolyte interphase
SOC	State of charge
STEM	Scanning transmission electron microscope
TEM	Transmission electron microscopy
TEY	Total electron yield
TG-DTA	Thermo gravimetric - differential thermal analysis
XANES	X-ray absorption near-edge structure
XRD	X-ray diffraction

Chapter 1

Introduction

1.1. Energy Transition of Modern Society

By 2025, the continuously growing 8 billion global population would consume 130,000 TWh energy annually.[1.1] Presently, fossil fuels like coal, natural gas and oil, still dominate accounting for over 90% of energy supply, as given in Table 1.[1.2] The consequence of such huge consumption of fossil fuels is the serious threat of global climate change and severe environmental issues such as smog that is happening in China and India that adversely affect the health of the people living in those areas.[1.3]

Table 1.1. Worldwide energy consumption by fuel.[1.2]

Energy supply (%)	1973	1998	2010	2020
Combustible fuels	97.3	96.4	90.8	92.2
Nuclear	0.9	1.3	5.8	4.4
Hydroelectricity	1.8	2.1	2.6	2.6
Geothermal, wind, solar and heat	0.1	0.2	0.7	0.8

Driven by the raised public concern about climate change and gradually tightened regulations on fuel/energy and greenhouse-gas emission, energy usage is experiencing a shift toward sustainable energy supply. Thus, the wide deployment of renewable energy technologies that can deliver energy without pollutants such as carbon dioxide becomes imperative.[1.4]

1.2. Batteries - Key Technology for Using Renewable Energy

The reason for the popularity of fossil fuels is mostly because of their overwhelming advantage as *energy storage media* that are *readily transportable*.[1.5] They can be stored until they are needed and transported by rail, road, or pipeline to where they are going to be utilized. Nonetheless, most of green energy sources such as solar and wind generate electricity in an intermittent way that necessitates the storage of surplus electricity. An ideal and convenient method for renewable energy storage/transportation is through the electrochemical devices, for example, rechargeable lithium-ion batteries (LIBs).

LIBs over the past twenty years have seen remarkable market growth driven by the ubiquitous proliferation of portable electronic devices. Now, they find new applications in transportation, i.e., electromobility, and electric-grid stationary storage.[1.6] The electromobility market is experiencing significant growth as a result of the introduction of strict regulations on fuel efficiency and emissions by various governments. For example, at least 20 percent of all global road transport vehicles must be electrically driven by 2030 according to the **The Paris Declaration on Electro-Mobility and Climate Change & Call to Action** of Lima – Paris Action Agenda of *2015 United Nations Climate Change Conference* (COP21, Paris).[1.7]

As a result of these developments, the market of *electromobility* for LIBs is rapidly expanding, thus, reaching 20,000 MWh in 2015 in comparison to worldwide LIB sales of 60,000 MWh.[1.8] This growth in global LIB market for only transportation application is estimated to climb up to $221 billion by 2024.[1.8,9]

1.3.Criteria for Near-Term LIB Development

Apparently, not only the electrification of transportation benefits the LIB market, but the commercial success of electromobility also heavily depends on the development of appropriate LIB technologies. While the state-of-the-art LIB chemistry of lithium cobalt oxide ($LiCoO_2$)/graphite can meet the criteria on specific energy (i.e., how much energy the battery can store), it is generally considered unsuitable for automotive applications because of its inherent safety risks and the long-term expected shortage of cobalt. Therefore, many alternative chemistries have been proposed to fulfill mass market demand. In general, advanced batteries need to exhibit the characteristics of *Durability* in more than 1,000 cycles of their deep-cycle life, 10-year calendar life or longer, and wide survival temperature range from -40 to 85 ^{o}C. *Cost* must be further reduced as well, for example, down to as low as US$150/kWh for electric vehicles (Figure 1.1b)[1.10]; in addition to the *Energy/Power Requirement* presented in the Ragone plot of Figure 1.1a. The last, but most

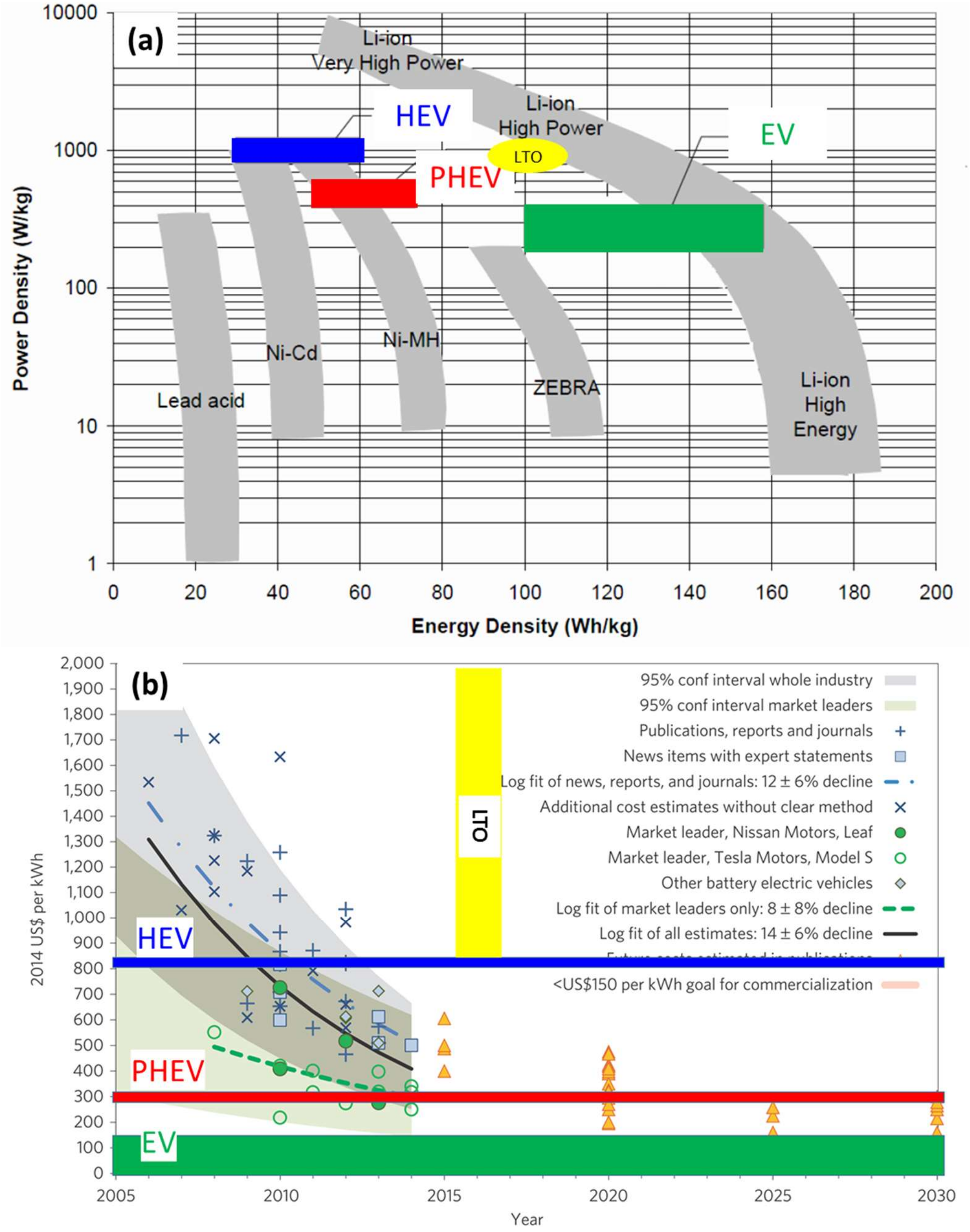

Figure 1.1. (a) Ragone plot including energy/power criteria modified from Ref. **1.**11; (b) cost of LIBs modified from Ref. **1.**12 for various electromobility applications. Battery targets for hybrid electric vehicle (HEV), plug-in hybrid electric vehicle (PHEV) and electric vehicle (EV) are marked in blue, red and green, respectively.[1.10] Yellow represents the performance of LTO.[1.13]

critical criterion in electromobility is *Safety*. This is so because a single accident can rapidly turn public opinion against electromobility and create serious market setback.

1.4. A Solution to Durability and Safety Challenge: LTO

Currently, no single battery chemistry can satisfy all criteria. As a result, all manufacturers have to manage the trade-offs to meet their product requirements. Lithium titanate ($Li_4Ti_5O_{12}$, LTO) is promoted by several companies, including Altair Nano,[1.14] EnerDel,[1.15] and Toshiba,[1.16] as a promising anode material because of the advantages of: (i) long lifetime due to "zero-strain" feature (0.2 vol.% change) during cycling;[1.17] (ii) rate capability that enables rapid charge within 6 min to 80% SOC;[1.16] (iii) excellent safety thanks to the stable crystal structure; and (iv) outstanding low-temperature performance even at -30 ºC.[1.16] There have been many commercialisation examples of LTO for specific applications. For example, Toshiba supplied LTO batteries to University of Sheffield, UK, for a 2MW energy storage system.[1.18] In the meantime, Toshiba also partnered with Johnson Controls to use LTO batteries on the start-stop system for hybrid electric vehicles (HEVs) and plug-in hybrid electric vehicles (PHEVs).[1.19]

Nanostructured LTO

One of the reasons for the superior performance of LTO is due to its amenability to nanostructuring. Intrinsically, the relatively low Li-ion diffusivity[1.20] (ca. 10^{-9}-10^{-16} $cm^2\ s^{-1}$ that is lower compared to 10^{-10} $cm^2\ s^{-1}$ of graphite that is the most common anode material[1.21]) and poor electronic conductivity[1.22] (10^{-8}-10^{-13} S cm^{-1}) lead to sluggish electrode kinetics, thus, poor capacity retention at high rate. Preparation of structurally stable nano-LTO particles can profoundly improve rate capability because it shortens the transport distance of both Li ions and electrons within the grains, and simultaneously increase the exposed active surface area to electrolyte.

1.5.Challenges in Penetration of nano-LTO

High battery cost

However, the cost of LTO battery is still expensive that ranges from 800 to 2000/kWh,[1.13] as marked by the yellow region in Figure 1.1b; this is so because of their relatively low energy density and non-competitive material production cost.

Energy-intensive material production

Cost-efficient production of nanostructured LTO requires not only savings in energy consumption,[1.1] but also minimizing the carbon footprint of the battery manufacturing process. In other words, there is a need for nano-LTO production via "green synthesis methods" that only use environmentally benign and nontoxic chemicals.

Nanosize effect on LTO

In addition to the benefits on kinetics improvement, nanosizing LTO has impact on the storage mechanism as well that leads to size-dependent electrochemical properties. Kavan et al. found that the Li-ion diffusivity decreases by orders of magnitude when the particle size declines from µm-scale to nm-scale.[1.20] Also, Borghols et al. reported that the near-surface environment of LTO particles allows excess Li-ion storage, leading to a larger storage capacity and irreversible capacity loss, most likely due to surface reconstruction.[1.23] All those outcomes reveal that, in order to optimize the performance of nano-LTO batteries, our knowledge about their Li storage mechanism must be extended from the well-established two-phase dynamics during intercalation/deintercalation at microscale, to understand the mechanism behind the size-effect at nanoscale. 2D nanostructures are of particular interest because of their acknowledged importance in renewable energy application.[1.24]

1.6.Objectives of this Research

Therefore, this work has a dual goal, namely, (i) the development of a sustainable synthesis process for nano-LTO that exhibits scale-up potential, and (ii) the studying/elucidation of the dynamics of Li-ion intercalation/deintercalation in LTO nanosheet anodes during cycling.

Towards this goal, the present study focuses on the aqueous preparation of a nanosheet-structured intermediate phase using only inorganic raw materials at temperature below the boiling point of water. The intermediate phase then serves as template to produce LTO with tailored nanostructure via thermal conversion at different annealing temperature.

The LTO nanocrystals prepared under different conditions were deployed to study the impact of subtle structure change taking place during synthesis on their electrochemical performance. Based on the discovered linkage between LTO structure evolution and electrochemical performance degradation during cycling, a general description of the capacity fade mechanism of nano-LTO was established. More specifically the overall objectives include:

1. Aqueous preparation of nanosheet intermediate phase from inorganic precursors at a temperature below the boiling point of water.
2. Elucidation of the mechanism of thermal conversion from intermediate phase into spinel LTO.
3. Determination of the electrochemistry of prepared spinel LTO nanocrystals.
4. Correlation of preparation conditions to nano-LTO's performance as electrode materials.
5. Elucidation of the capacity fade mechanism of nano-LTO.

1.7.Organization of The Thesis

The thesis is divided into seven chapters, followed by appendices providing supporting information and important external data. This introduction of Chapter 1 states why a new synthesis method for the preparation of 2D LTO nanocrystals is critical to support the expansion of car battery market. Literature review (Chapter 2) provides selected information of LIBs, material properties and synthesis methods of nanostructured spinel LTO. A proof of concept for the proposed synthesis strategy is described in Chapter 3. Step-by-step exploration of the preparation of nanosheet intermediate phase, and the subsequent thermal conversion from intermediate phase into spinel LTO and the electrochemistry of obtained 2D LTO nanocrystals are discussed in Chapters 4 & 5, respectively. A kinetic model to describe LTO degradation is given in Chapter 6. This thesis is completed with a final chapter (Chapter 7) that summarizes the important conclusions, claims of originality, and provides some ideas for further research as future work.

1.8. References

(**1.**1) Larcher, D.; Tarascon, J. M. Towards greener and more sustainable batteries for electrical energy storage. *Nat Chem* **2015,** *7* (1), 19.

(**1.**2) Julien, C.; Mauger, A.; Vijh, A.; Zaghib, K. *Lithium Batteries: Science and Technology*; Springer, 2015.

(**1.**3) Hallquist, M.; Munthe, J.; Hu, M.; Wang, T.; Chan, C. K.; Gao, J.; Boman, J.; Guo, S.; Hallquist, Å. M.; Mellqvist, J.et al. Photochemical smog in China: scientific challenges and implications for air-quality policies. *National Science Review* **2016**, DOI:10.1093/nsr/nww080 10.1093/nsr/nww080.

(**1.**4) Goodenough, J. B. Batteries and a Sustainable Modern Society. *The Electrochemical Society Interface* **2016,** *25* (3), 67.

(**1.**5) Dell, R. M.; Rand, D. A. J. Energy storage — a key technology for global energy sustainability. *J. Power Sources* **2001,** *100* (1–2), 2.

(**1.**6) Dunn, B.; Kamath, H.; Tarascon, J.-M. Electrical Energy Storage for the Grid: A Battery of Choices. *Science* **2011,** *334* (6058), 928.

(**1.**7) Change, U. N. F. C. o. C., 2015; Vol. 2016.

(**1.**8) Pillot, C. In *33rd International Battery Seminar & Exhibit*; Avicenne Energy: Fort Lauderdale, Florida 2016.

(**1.**9) Research, N., 2016; Vol. 2016.

(**1.**10) USCAR; USCAR, 2017; Vol. 2017.

(**1.**11) Celine Cluzel, C. D. “Cost and performance of EV batteries,” The Committee on Climate Change, 2012.

(**1.**12) Nykvist, B.; Nilsson, M. Rapidly falling costs of battery packs for electric vehicles. *Nature Clim. Change* **2015,** *5* (4), 329.

(**1.**13) Board, C. A. R. “Advanced Clean Transit Battery Cost for Heavy-Duty Electric Vehicles ” California Environmental Protection Agency, 2016.

(**1.**14) Altairnano; Altairnano, 2017; Vol. 2017.

(**1.**15) EnerDel, I.; EnerDel, Inc., 2015; Vol. 2017.

(**1.**16) Corporation, T.; Toshiba Corporation 2016; Vol. 2017.

(**1.**17) Scharner, S.; Weppner, W.; Schmid-Beurmann, P. Evidence of Two-Phase Formation upon Lithium Insertion into the $Li_{1.33}Ti_{1.67}O_4$ Spinel. *J. Electrochem. Soc.* **1999,** *146* (3), 857.

(**1.**18) Bush, S.; Electronics Weekly, 2014; Vol. 2017.

(**1.**19) Miller, G.; PRNewswire, 2015; Vol. 2017.

(**1.**20) Kavan, L.; Prochazka, J.; Spitler, T. M.; Kalbac, M.; Zukalova, M. T.; Drezen, T.; Gratzel, M. Li insertion into $Li_4Ti_5O_{12}$ p(Spinel) - Charge capability vs. particle size in thin-film electrodes. *J. Electrochem. Soc.* **2003,** *150* (7), A1000.

(**1.**21) Yu, P.; Popov, B. N.; Ritter, J. A.; White, R. E. Determination of the Lithium Ion Diffusion Coefficient in Graphite. *J. Electrochem. Soc.* **1999,** *146* (1), 8.

(**1.**22) Chen, C. H.; Vaughey, J. T.; Jansen, A. N.; Dees, D. W.; Kahaian, A. J.; Goacher, T.; Thackeray, M. M. Studies of Mg-Substituted Li4−xMg x Ti5O12 Spinel Electrodes (0≤x≤1) for Lithium Batteries. *J. Electrochem. Soc.* **2001,** *148* (1), A102.

(**1.**23) Borghols, W. J. H.; Wagemaker, M.; Lafont, U.; Kelder, E. M.; Mulder, F. M. Size Effects in the $Li_{4+x}Ti_5O_{12}$ Spinel. *J. Am. Chem. Soc.* **2009,** *131* (49), 17786.

(**1.**24) Peng, L.; Zhu, Y.; Chen, D.; Ruoff, R. S.; Yu, G. Two-Dimensional Materials for Beyond-Lithium-Ion Batteries. *Adv. Energy Mater.* **2016,** *6* (11), 1600025.

Chapter 2

Literature Review

In this chapter, an introduction to Li-ion batteries (LIB) is first provided, followed by details about lithium titanate ($Li_4Ti_5O_{12}$, LTO) as an advanced anode material. In particular, after introducing the essential fundamentals of LIBs, the material properties and nanostructurization of LTO are reviewed. The last part of the chapter provides a review of the different preparation methods of 2D LTO nanocrystals and their electrochemical performance, as this type of LTO nanomaterial is in the core of this thesis.

2.1. Lithium ion battery fundamentals

2.1.1. Working principle and key parameters of LIBs

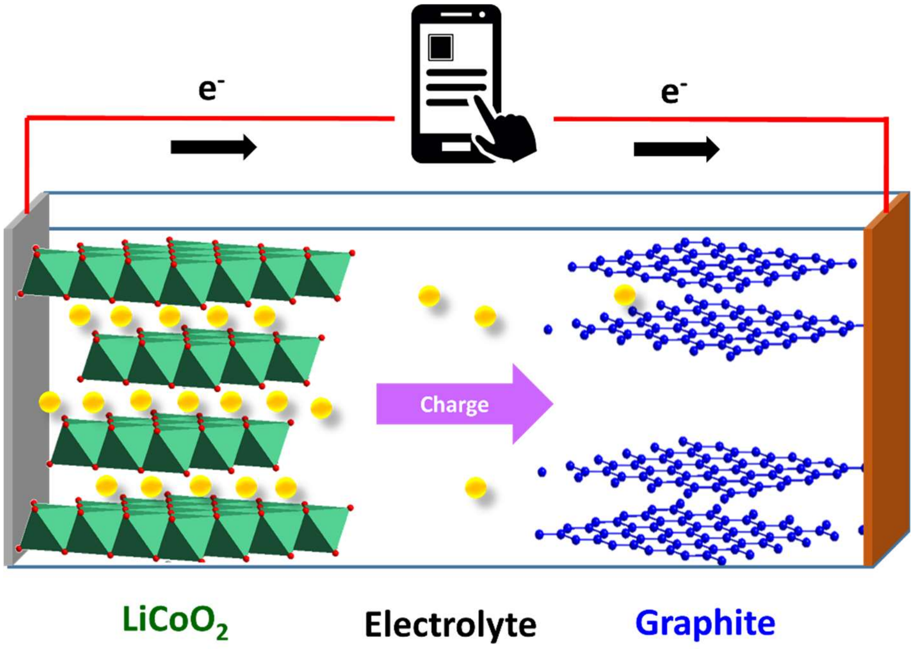

Figure 2.1. Schematic of a lithium ion battery with graphite as the anode, $LiCoO_2$ as the cathode in an organic liquid electrolyte ($LiPF_6$ in EC/DEC). During charge, lithium ions (yellow spheres) move towards the graphite through the electrolyte and, electrons move through the external circuit (black arrows).

A typical LIB consists of two porous electrodes, one anode made of graphite coated on Cu foil; and one cathode made of the Li-host compound such as $LiCoO_2$ coated on Al foil, plus a Li-ion conducting organic electrolyte. 1M lithium hexafluorophosphate ($LiPF_6$) salt dissolved in organic solvents of ethylene carbonate/diethyl carbonate (EC/DEC) is the most popularly used electrolyte recipe. This sandwich structure of $LiCoO_{2(s)}|LiPF_6\text{-EC-DEC}_{(l)}|Graphite_{(s)}$ cell is presented in Figure 2.1, where each electrode, in addition to the active material (i.e., graphite or $LiCoO_2$), comprises conductive additive and binder components. The former is usually carbon black and the latter is polyvinylidene fluoride (PVDF), respectively.

A pristine assembled LIB is initially at the fully discharged state (corresponding to 0 % of battery state of charge, SOC), with $LiCoO_2$ being fully lithiated and graphite fully delithiated. To "activate" batteries, the "formation protocol" must be applied for charging. Upon charge, Li ions are released from $LiCoO_2$, migrate across the electrolyte, and eventually intercalate into graphite; while electrons circulate through the external circuit to maintain global electrical neutrality as illustrated in Figure 2.1. The electrochemical potential differences of Li ions and electrons between the electrodes provide the driving force for Li-ion intercalation/deintercaltion:

$$xLi^{+}+xe^{-}+6C\leftrightarrow LiC_6 \text{ (anode)}$$

$$LiCoO_2\leftrightarrow Li_{1-x}CoO_2+ xLi^{+}+xe^{-} \text{ (cathode)} \quad (2\text{-}1)$$

where the forward direction represents the charge process and the reverse direction represents the discharge process. Overall, the full reaction can be written as:

$$LiCoO_2+6C\leftrightarrow Li_{1-x}CoO_2+ LiC_6 \quad (2\text{-}2)$$

Regarding LIB operations, some critical parameters are often used as metrics for performance evaluation: (i) durability, (ii) energy density, and (iii) power density. The *energy density* (specific energy) is usually expressed as the product of theoretical specific capacity Q_{th} (as per Faraday's law) and open circuit voltage (V_{oc}):

$$Q_{th}V_{oc} = \frac{-nF}{M_w}V_{oc} = \frac{\Delta G}{M_w} \quad (2\text{-}3)$$

where M_w is the molar mass of the designated material, n is the number of electrons, F is Faraday's constant, and ΔG is the Gibbs free energy. When using LTO as an example, the specific theoretical capacity Q_{th} is calculated as:

$$Q_{th} = \frac{-nF}{M_w} = \frac{3(mol)\times 96500(\frac{Coulomb}{mol})}{459.1(\frac{g}{mol})} \times \frac{1000}{3600} = 175 mAh/g$$

The *rate (power) capability* is typically expressed in terms of C-rate, to normalize the applied current with respect to the theoretical specific capacity of electrode material. For example, a 2C rate means to discharge/charge an LTO electrode in 1/2 hour by applying current of 2 × 175 mA/g = 350 mA/g. And the power that a battery can deliver is the product of the discharge current and the voltage:

$$\mathrm{P}_{out} = I_{dis} V_{dis} \tag{2-4}$$

where P_{out} is the delivered power, I_{dis} is the discharge current, and V_{dis} is the discharge voltage. More specifically, V_{dis} is reduced from its open-circuit value V_{oc} by the polarization losses η(I) also known as overpotential:

$$V_{dis=} V_{oc} - \eta(I) \tag{2-5}$$

And vice versa, the voltage during charging assumes a value higher than V_{oc} by the polarization amount η(I) (or overpotential):

$$V_{ch=} V_{oc} + \eta(I) \tag{2-6}$$

Polarization losses can be of different origin, namely (I) activation polarization, (II) concerntration polarization, and (III) ohmic polarization, at a given current,[2.1,2]:

I. The activation polarization is the overpotential due to charge transfer kinetic of the electrochemical reaction,[2.3,4] which is a logarithmic function of the current density. As such the activation overpotential is roughly propotional to the ratio of geometrical and true area as:[2.5]

$$\eta(I)_{active} \sim \frac{A_{Geo}}{A_{true}} \tag{2-7}$$

where A_{true} is the total surface area of electrode material particles, and A_{Geo} is the geometrical area of electrode. This relationship clearly points out to the benefit of nanosizing to reduce activation polarization.

II. The concerntration polarization arises when the mass transport (diffusion) is not rapid enough in comparison to charge transfer reaction. It usually occurs at the solid electrolyte interphase (SEI) and in the Li-ion host crystals at high current. Just like activation polarization η(I)$_{\text{active}}$, the magnitude of concentration polarization η(I)$_{\text{con}}$ also depends nolinearly on the charge/discharge current.

III. The ohmic polarization of a battery is the sum of the resistance of each component of a battery, and is linearly propotional to the applied current (Ohm's law).

The *durability* of batteries is usually considered in terms of: (1) the cycle life and (2) calendar life. The latter is the fading time before a batterry is completely inoperable. Meanwhile, the energy storage efficiency can be expressed in terms of Coulombic efficiency as:

$$\frac{\int_0^{Q_{dis}} V_{dis}(q)}{\int_0^{Q_{ch}} V_{ch}(q)} \times 100\% \qquad (2\text{-}8)$$

$$Q = \int_0^{\Delta t} I dt = \int_0^{q} dq \qquad (2\text{-}9)$$

where q is state of charge; Q the total capacity (mAh/g) that is gained/lost upon operation.[2.6]

2.1.2. Design considerations

The functioning of a LIB can be better understood by referring to the schematic energy diagram[2.6,7] in Figure 2.2. Ideally, during discharge process, the redox reactions occurring at the electrodes enable electrons to flow through the external circuit, in the direction from anodes with higher Fermi energy (left-hand side), to cathode with a lower Fermi energy (right-hand side). Fermi energy level is the energy where the electron occupation probability equals 0.5, and represents the electrochemical potential of electrons. Therefore, the open-circuit voltage V_{OC} of the cell system satisfies:

$$eF_{\ oc} = -\Delta E_F = \mu_A^e - \mu_C^e \qquad (2.10)$$

where e is the magnitude of the electron charge, F is Faraday's constant, μ_A and μ_C refer to electrochemical potential of electrons in the anode and the cathode, respectively.

For intercalation compounds like LTO, the charge compensation during intercalation/deintercalation is fulfilled by oxidation/reduction of transition metals (i.e., Ti^{3+}/Ti^{4+} couple in LTO). And the electrochemical potential variation of electrons during intercalation/deintercalation is roughly “fixed” by the hybridization between titanium and oxygen ions, which is the result of mixing of atomic orbitals. Therefore, only insignificant change in open-circuit voltage is exhibited upon Li-ion intercalation/deintercalation in LTO.

In the meantime, there is an “operational window” of the organic electrolyte, which is in the range from the lowest unoccupied molecular orbital (LUMO) to the highest occupied molecular orbital (HOMO) of the electrolyte.[2.8] For a thermodynamically stable LIB, both μ_A and μ_C must lie in this range, as the black dash lines shown in Figure 2.2. Nonetheless, in practice, the μ_A of graphite and metallic lithium locate above the LUMO of electrolyte (as the red ellipse in Figure 2.2). This results in electrolyte reduction unless a passivation SEI layer is formed at the anode surface, as a kinetic barrier to prevent further reduction. While SEI formation is critical to make the operation of the LIB possible, this comes at a cost as it leads to a decline of the Coulombic efficiency. On the contrary, LTO lies perfectly below the LUMO of electrolyte, which dictates LTO is an ideal anode material with stable chemistry.

2.1.3. *Safety issues of classical LIBs*

Recently, LIBs have been promoted into application fields that require both high energy and high-power density.[2.9] However, these two demands bring up substantial safety concerns.[2.10,11] For example, the UN aviation agency has officially forbidden the shipment of LIBs as cargo on passenger aircrafts because of their fire risk.[2.12] Even though the probability of catching fire and/or explosion is rare (*ca.* one in 1 million to one in 10 million)[13], the safety of LIBs remains a concern.

From the perspective of battery chemistry, the fire risk is raised because commercial LIBs contain both combustible materials (*i.e.*, organic solvent in the electrolyte) and highly reactive oxidizing agents (metallic Li or lithiated graphite). Such dangerous combination can lead to battery thermal runaway.[2.13-15]

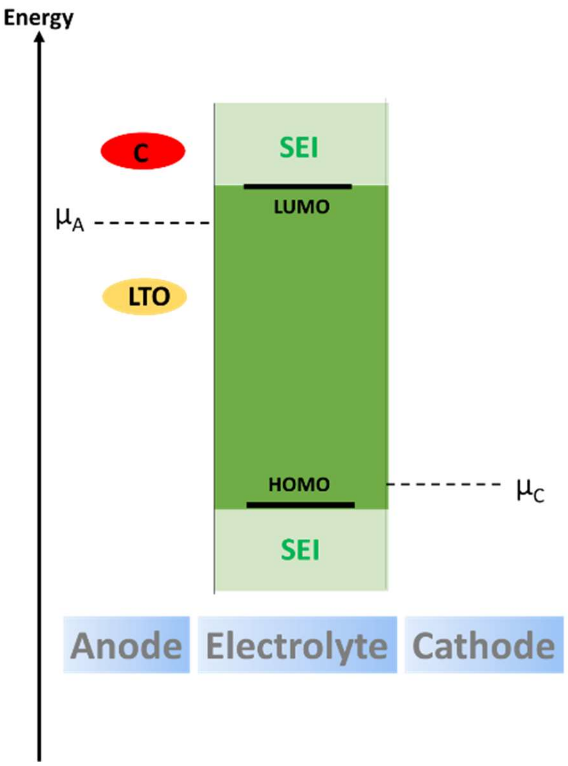

Figure 2.2. Schematic representation of the relative energy diagram of the electrolyte, the anode and the cathode, where the LUMO and HOMO represent the lowest unoccupied and highest occupied molecular orbitals, respectively; μ_A, μ_C are the electrochemical potentials of anode and cathode. Meanwhile, the electrochemical potentials of graphite (red) and LTO (orange) are designated as well.

In a nutshell, the mechanism of thermal runaway in a classical graphite/Li metal oxide LIB can be divided into a series of chemical reaction steps:[2.10,16]

a. Low-rate reaction of electrolyte/lithiated graphite anode at 90 °C.

b. Breakdown of SEI layer occuring at 120 °C, causing violent electrolyte reduction at the surface of lithiated graphite anodes.

c. Onset of exothermic reaction as a result of cathode decomposition happening at 140 °C.

d. Oxygen release at 180 °C because of cathode material decomposition.

e. Finally, above 250 °C, the lithiated graphite reacts with the PVDF binder used in fabricating the electrodes.

The thermal runaway process is illustrated with the help of the data summarized in Figure 2.3.[2.17] If the critical temperature is reached, which lies in the range of 100-150 ºC as the fist peak in Figure 2.3, a chain reaction including aforementioned process *a*-c is at the onset of the subsequent catastrophic exothermic reaction. Therefore, the safety of LIBs can be greatly improved, by replacing graphite with an alternative anode material like LTO that has no such readily chemical ignition behavior.

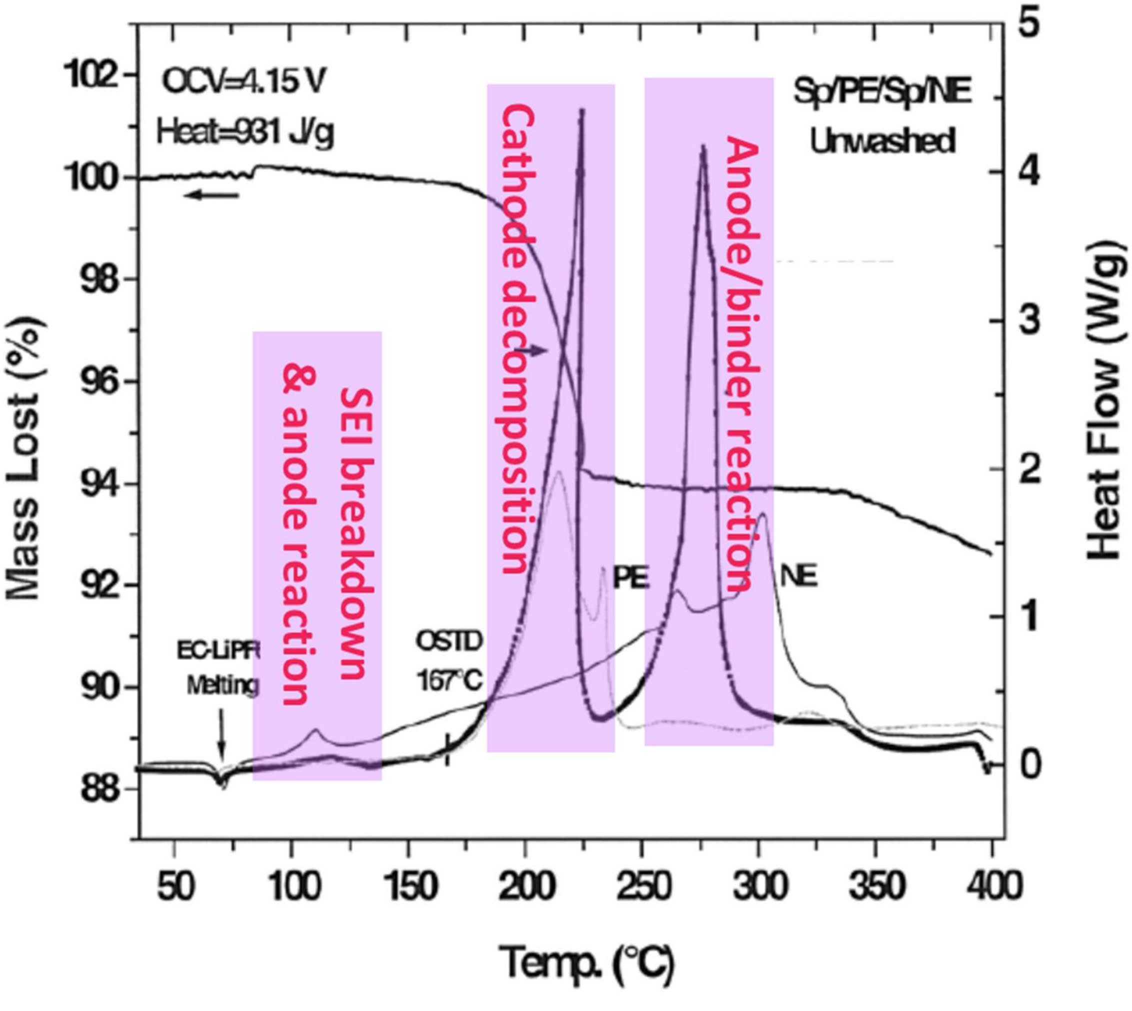

Figure 2.3. Differential scanning calorimetric (DSC) and thermogravimetric (TG) analyses of LiCoO$_2$/graphite LIBs; original data from Figure 4 in Reference **2.**17. The peaks in the red blocks correspond to the different stages of the thermal runaway process.

2.2. Fundamental properties of LTO

With the view of replacing graphite to improve safety, different anode candidates have been considered. Among these, LTO is the most successful one because it does not only guarantee significantly improved safety, but also provide the advantage of prolonged lifespans and high power capability.[2.18-20]

2.2.1. *Crystal structure of LTO*

The basic crystal structure of LTO is a cubic spinel with symmetry of $Fd\bar{3}m$ space group, whose lattice parameter is 8.3595 Å.[2.19] Oxygen anions occupy $32e$ sites to establish a cubic-close packed framework. At room temperature, the tetrahedral $8a$ sites of LTO are occupied by Li ions alone; and octahedral $16d$ sites are occupied by 1/6 Li ions and 5/6 Ti ions, respectively. As a result, LTO has compositional formula $(Li_3)^{8a}[Li_1Ti_5]^{16d}(O_{12})^{32e}$.

The octahedral empty sites for cations of $16c$ and tetrahedral sites of $8b$ and $48f$ can theoretically accommodate intercalated Li ions, nonetheless, the tetrahedral ones are less energetically favorable.[2.21] Namely, the stable product of Li-ion intercalation has formula of $(Li_6)^{16c}[Li_1Ti_5]^{16d}(O_{12})^{32e}$, which has the rock-salt structure of space group $Fm\bar{3}m$ with lattice parameter of 8.3538 Å.[2.22] Figure 2.4 shows the crystal structure of each phase.

2.2.2. *Li storage properties of LTO*

Li storage in LTO is fulfilled via Li-ion intercalation, which can be expressed as:[2.23]

$$Li_4Ti_5O_{12}+3e^-+3Li^+ \leftrightarrow Li_7Ti_5O_{12} \tag{2-11}$$

The forward direction represents Li-ion intercalation, and the reverse direction of the deintercalation process. The theoretical capacity is 175 mAh/g, calculated by using the mass of $Li_4Ti_5O_{12}$ and above reaction equation. Upon intercalation, the Li ions originally residing at $8a$ sites eventually move to empty $16c$ sites and so do the externally intercalated Li ions; this is done in order to balance the electrostatic repulsion among them.[2.24] This process is accompanied by a phase transformation from spinel to rock-salt structure, but surprisingly with negligible change in volume at macroscale, i.e., 0.2 %. This is so probably because of the

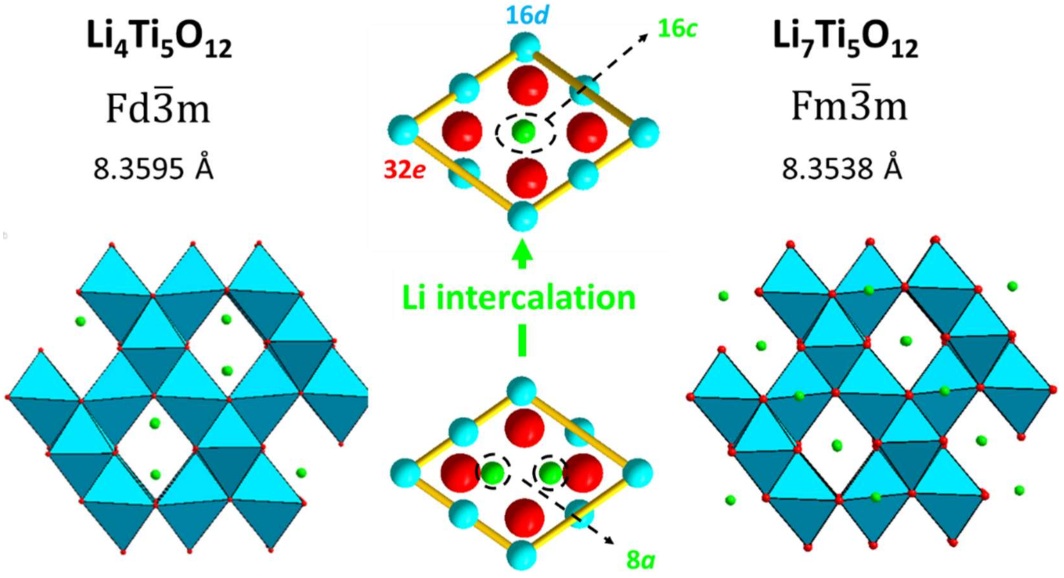

Figure 2.4. Perspective view of LTO structure. The polyhedron indicates the repeating unit of $[Li_{1/6}Ti_{5/6}]O_6$, where the cyan sphere at central positions is $[Li_{1/6}Ti_{5/6}]$, red sphere is oxygen, green sphere is lithium. During lithiation, the symmetry changes from $Fd\bar{3}m$ into $Fm\bar{3}m$ accompanied with lattice constant reduction from 8.3595 to 8.3538 Å.

strong covalency in the Ti-O bonding properties, which helps to establish a robust host framework to accommodate intercalated Li ions.

The charge balance upon intercalation is accomplished by Ti^{4+}/Ti^{3+} reduction in LTO, which causes the elongation of the Ti-O bond length. Recent collaborative research of our group with the Institute of Physics in China, it has revealed that LTO undergoes considerable reversible lattice deformation that helps modulate the Ti-O bond stretching/shrinking during charging/discharging. As a result, this local deformation phenomenon facilitates the attainment of the macroscopic "zero-strain" feature.[2.25]

Figure 2.5(a) shows the typical galvanostatic charge-discharge profile for a LTO anode, which is characterized by the rapid potential drop at the beginning and at the end, and a voltage plateau at approximately 1.55 V vs. Li/Li^+. This plateau is generally attributed to spinel/rock-salt coexistence over a wide stoichiometric range of $Li_{4+x}Ti_5O_{12}$, $0.1<x<2.9$.[2.22,26,27] However, the “zero-strain” feature of LTO imposes a profound influence on the spinel/rock-salt equilibrium as well. Namely, instead of the two-phase separation, spinel and rock-salt phases are intimately mixed as nanodomains at above 80 K in µm-sized LTO particles because of low interface and strain energy on the two-phase boundaries.[2.28-30] This causes a quasi-solid solution behavior of $Li_{4+x}Ti_5O_{12}$ on their open-circuit voltage relaxation.[2.29]

2.2.3. *Carrier transport in LTO*

The net transport of the charge carriers that comprises the cooperative motion of electrons and Li ions, determines the electrical properties and electrochemical response of LTO batteries.[2.31] However, because of its intrinsic complexity and coupling effect with the spinel/rock-salt interface propagation, the dynamics of Li-ion intercalation/deintercalation in LTO remains ambiguous.[2.32] For instance, recent results of neutron diffraction and Rietveld refinement studies showed that Li-ion diffusion in spinel structure occurs along diffusion path in <110> directions, while jumping occurs among the 8*a*-32*e*-32*e*-8*a* low-energy positions.[2.33] These findings contradict the long-standing image of 16*c*-8*a*-16*c* diffusion pathway in spinel $Li_4Ti_5O_{12}$.[2.34,35]

Li-ion diffusivity in LTO is a function of the Li content and coordination environment of mobile Li ions[2.30,32,34,36]; e.g., partially lithiated LTO (i.e., $Li_{4+x}Ti_5O_{12}$, $0<x<3$) exhibits outstanding diffusivity (*ca.* 10^{-6} cm^2/s).[37] This is so because of the strong Coulomb repulsion between the Li ions occupying neighboring 8*a* and 16*c* sites across the boundaries of spinel/rock-salt nanodomains.[2.32]

Nevertheless, pristine spinel $Li_4Ti_5O_{12}$ is a poor ionic conductor that possesses a 3.80 eV band gap with ultraslow Li diffusion.[2.38-40] The latter is impeded by a high-energy barrier (*ca.* 0.86 eV) in $Li_4Ti_5O_{12}$ as experimentally determined using spin-alignment echo nuclear magnetic resonance (SAE-NMR).[2.34] The same conclusion was also made by Ziebarth *et al.* who theoretically predicted high energy barriers for Li-ion diffusion as a result of trapping of mobile Li vacancies at 16*d* sites.[2.35]

Spinel/rock-salt transformation is accompanied with a transition in LTO's electronic structure from an insulator to a metallic conductor.[2.38,39] As a result, the electronic conductivity of lithiated phase $Li_7Ti_5O_{12}$ improves to 2.46 S/cm at 300 K accompanied with a color change from white into black.[2.41] The color evolution during discharge is evident in Figure 2.5(b).[2.41] Also the diffusion energy barrier in the rock-salt $Li_7Ti_5O_{12}$ is about 0.20 eV that is lower than in spinel $Li_4Ti_5O_{12}$.[2.40,42,43] In other words, lithiated $Li_7Ti_5O_{12}$ exhibits much better electrode kinetics than pristine $Li_4Ti_5O_{12}$. This gives a hint to another material improvement strategy that any electronic conductivity restriction caused by spinel $Li_4Ti_5O_{12}$ can be compensated via tailoring the irreversible capacity loss of LTO batteries.[2.44]

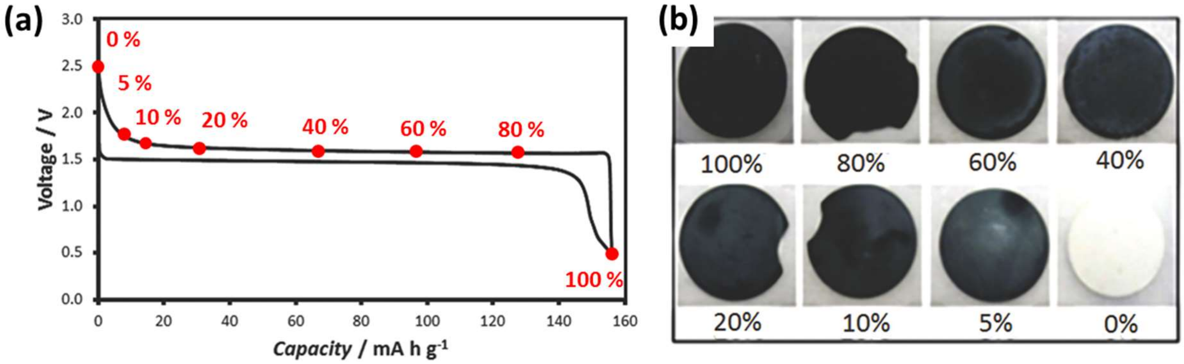

Figure 2.5. (a) Charge/discharge voltage profile of LTO electrode operated in the voltage range of 0.5-2.5 V, where the red dots correspond to the different state of charge (SOC, %). (b) LTO electrodes collected at different SOC: the white specimen (0%) is $Li_4Ti_5O_{12}$ and the black one (100 %) is $Li_7Ti_5O_{12}$, respectively. The figures are modified from Figures 1 & 3 in Reference **2.**41.

2.2.4. Pros and cons of LTO as anode materials

It is of special interest to see how the material properties of LTO influence the battery performance when replacing graphite with LTO, which can be evaluated based on their *cyclability, safety and rate capability,* respectively.

Cyclability. Because of its "zero-strain" feature,[2.45] manifested with negligible (0.2%) volume change during electrochemical Li intercalation/deintercalation,[2.46] LTO batteries exhibit outstanding lifetime of about 50 times better compared to graphite-based batteries. Zaghib *et al.* is the first group to demonstrate that LTO has excellent cyclability even when operated in a harsh environment.[2.20] In their report, nanocrystalline LTO prepared by high energy ball

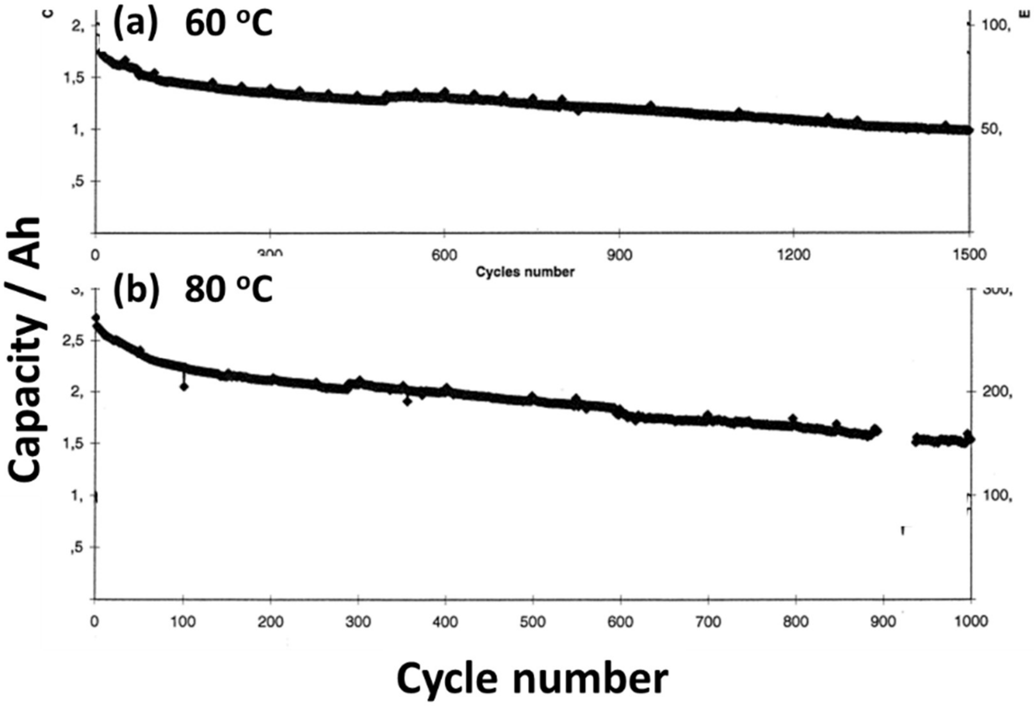

Figure 2.6. Cycle life of half cell Li/solid-polymer electrolyte/LTO operated at elevated temperature: (a) 60 and (b) 80 °C for 1500 and 1000 cycles, respectively. The figures are modified from Figure 5 and 6 in Reference **2.**20.

milling was used as the electrode material in solid-polymer electrolyte batteries, and were tested at 60 and 80 °C. As presented in Figure 2.6, the capacity retention reached 60 % and 70 % after cycling for 1500 cycles at 60 °C and 1000 cycles at 80 °C, respectively.

Safety. The electrochemical Li-ion intercalation process in LTO causes a flat voltage plateau at 1.55 V *vs.* Li/Li$^+$, which means SEI formation due to electrolyte reduction is theoretically impossible. Meanwhile, it also eliminates the threat of lithium plating that is a major concern in graphite anodes.[2.47] As a result, using LTO as anode material can greatly reduce the risk of thermal runaway.

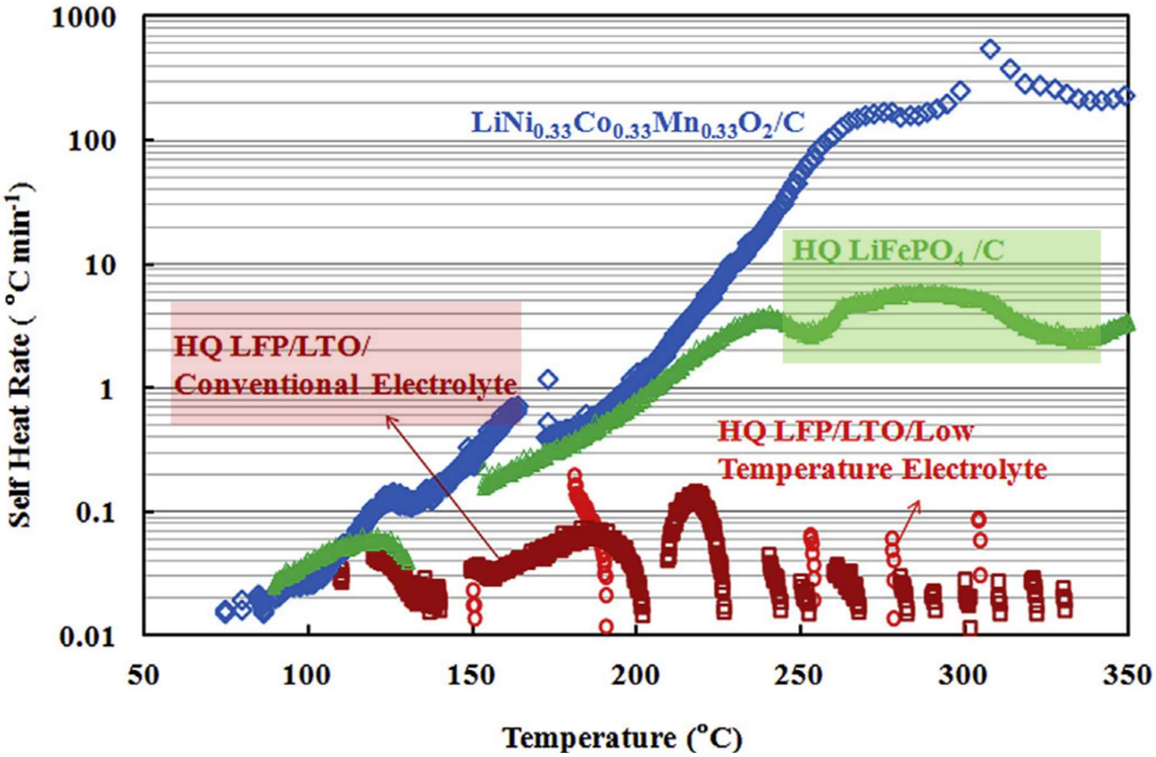

Figure 2.7. Semenov plots of 18650 cells using various chemistries: batteries using $LiPF_6$ electrolyte and $LiFePO_4$(LFP)//C (green), LFP//LTO (scarlet), $LiNi_{1/3}Co_{1/3}Mn_{1/3}O_2$//C (blue); or $LiPF_6$/LiFSI = 1/0.2 as electrolyte and LFP//LTO cell (red). The figures are modified from Figure 13 in Reference **2.**48.

LTO's superior safety was demonstrated by Zaghib *et al.*[2.47-49] Upon comparison of the Semenov plots (Figure 2.7) of LFP//C (green) and LFP//LTO (scarlet) cells - where $LiPF_6$ electrolyte was employed in both cases, a significant temperature increase can be seen in the temperature range of 120-230 ºC in the case of LFP//C (or more severe in $LiNi_{1/3}Co_{1/3}Mn_{1/3}O_2$/C, blue). This is so because of the decomposition reaction of SEI forming on graphite, which is absent in LFP//LTO.

Rate capability. However, LTO would exhibit some kinetic problems as an alternative for graphite, because of its intrinsically low Li-ion diffusivity and electronic conductivity. Namely, LTO possesses Li-ion diffusivity in the range from 10^{-9} to 10^{-16} cm^2/s, compared to graphite (10^{-9}-10^{-11} cm^2/s) when being partially lithiated.[2.37] And $Li_4Ti_5O_{12}$ is known as a wide bandgap insulator (3.8 eV). In other words, it requires modification from a kinetics standpoint to improve its performance.

2.3.Size effect of nano-LTO

Among so many modification methods trying to enhance the electrode kinetics of LTO, nanostructurization becomes dominant as it effectively reduces the length of rate-limiting diffusion pathway in LTO crystals. Interestingly, crystallite size has substantial influence on electrochemical performance of intercalation compounds, including $LiFePO_4$,[2.50] TiO_2[2.51,52] and LTO, etc. Those altered Li storage properties of nanosized intercalation compounds such as the excess capacity and broaden solubility limit correspond to the variations in thermodynamic conditions, which are widely considered as the consequence of energy penalty from strain, interface and surface energy contribution. [2.51-54] Nonetheless, the “zero-strain” property makes LTO a unique material whose nanosize effect is governed by crystallographic properties instead of aforementioned thermodynamic conditions.

Size-dependent electrochemistry of LTO was systematically explored Kavan *et al.,* [2.55] where Li diffusivity of LTO drastically decreases by 1000 times when particle size reduces from 1 um to 9 nm (Figure 2.8). Pang *et al.* made similar conclusion using *in situ* neutron diffraction characterization that the Li-ion filling rate into empty 16*c* sites of larger-size LTO (500 nm) was almost 1.3 times higher than smaller-size LTO (200 nm). [2.56] This size-dependent Li diffusivity could be understood as the result of nanostructure-induced lattice distortion. [2.57] Song *et al.* showed that 1% volume contraction of the rock-salt structure would significantly enhance the activation energy (from 0.43 eV to 0.61 eV) and results in Li diffusivity dropping from 4.9×10^{-11} to 5.5×10^{-14} cm^2 s^{-1}. [2.58]

Nanosize effect also leads to the curved voltage profile and excess Li capacity of nano-LTO. [2.54,60-65] According to calculations conducted by Swapna *et al.*, [2.60] energetically favorable (111) facets of LTO can accommodate Li intercalation to exceed 175 mAh/g (*i.e.*, more than 3 Li ions) by simultaneously occupying tetrahedral 8*a* and octahedral 16*c* sites. This cointercalation triggers surface reconstruction/relaxation that alleviates strong Coulomb repulsion among neighboring Li ions. In addition to excessive Li intercalation in the near-surface region, nano-LTO exhibits a curved voltage profile as a result of the orientation-dependent coordination environment of Li ions

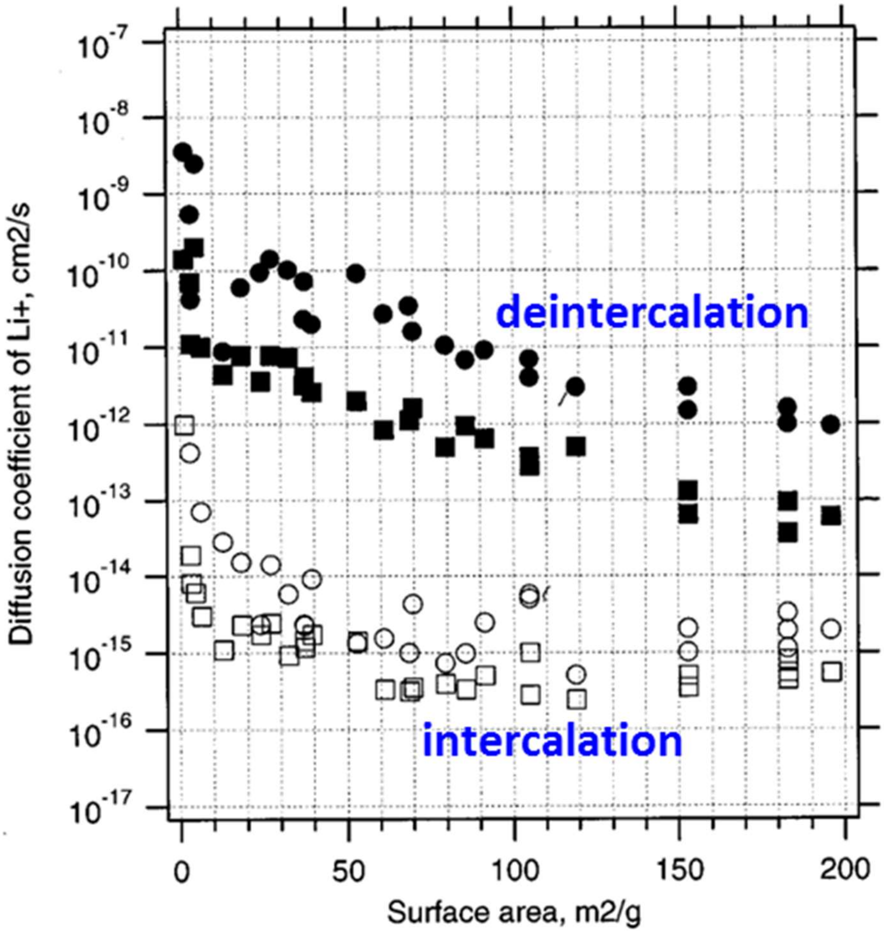

Figure 2.8. Li diffusivity variation with respect to the surface area. The solid squares/circles are of Li deintercalation from $Li_7Ti_5O_{12}$, and open symbols are of Li intercalation into $Li_4Ti_5O_{12}$. The figures are modified from Figure 1 & 3 in Reference **2.**59.

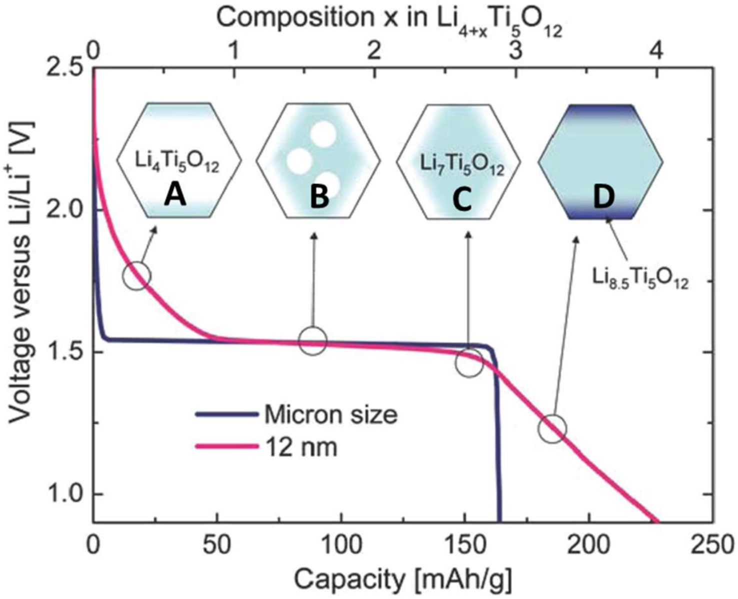

Figure 2.9. Comparison of the voltage profile of micron-size and nano-size LTO crystals. The inserted schematic suggests the mechanism of curved voltage profile and excess capacity of nano-LTO. Step A: Li insertion first occurs on low chemical potential (high voltage) crystallographic facets on the surface; Step B: Subsequent Li insertion into high chemical potential facets in the bulk; Step C: Full lithiation in the bulk and in the end, Step D: Ansitropic intercalation of excess Li ions. The figures are modified from Figure 1 & 3 in Reference **2.**54.

in the near-surface region. Therefore, those influences are because Li intercalation occurs at more favorable and less favorable active sites, respectively, in the near-surface region. The whole mechanism is schematically summarized in Figure 2.9. Thus, the crystallographic facets with high electrochemical voltage are intercalated first right above the plateau (A); intercalation into bulk region subsequently occurs leading to the voltage plateau (B); in the end of the intercalation process, those facets with lower electrochemical voltage are intercalated (C&D). However, the large surface area of nano-LTO also enhances battery performance deterioration manifested by high irreversible capacity loss and the notorious gas generation. [**2.**66-71] The former of capacity fade seems to stem from the surface reconstruction/relaxation induced by 8*a*-16*c* cointercalation. [**2.**61,62] What more interesting is that such structural reconstruction/relaxation leads to the changes in re-dox voltage of nano-LTO as the coordination environment of Li ions in reconstructed/relaxed LTO is altered. [**2.**72]

Besides, the latter of the notorious swelling issue in LTO-based LIBs become unignorable at elevated temperature because of severe gas generation reaction, **2.**67,68,70,71,73 as shown in Figure 2.10. The mechanism of LTO gassing can be broken down into: i) hydrolytic decomposition of electrolyte because of trace amounts of water that yields HF; **2.**66 ii) intrinsic catalysis by Ti^{4+} species; **2.**67 and iii) electrolyte reduction from lithiated LTO. **2.**69 Hydrogen, CO, CO_2 and C_2H_4 are the main gaseous products of the electrolyte/LTO reaction, with the simultaneous formation of SEI layers majorly consisting of Li_2CO_3 and lithium alkyl carbonate (ROCOOLi). **2.**67-69

Figure 2.10. Images of LTO batteries after 1000 cycles, operated at (a) 25 °C and (b) 55 °C, respectively. The figures are modified from Figure 1 & 3 in Reference **2.**74.

2.4. Nano-LTO preparation

2.4.1. Promising of 2D nanostructure

As is the famous case of graphene, the peculiar properties of 2D nanocrystals ignite research interest in both fundamental aspects and applications over the past decade. **2.**75-78 The signature feature of 2D nanomaterials is that they have strong in-plane bonds to form atomic lattices, and those atomic lattices are weakly bonded to each other in out-of-plane orientation. This unique 2D structure leads to unexpected electronic and optical properties due to the quantum confinement of electrons in two dimensions. For example, their extraordinarily large specific surface area (over 1000 m^2/g) draws attention in scientific areas such as catalysis[2.79] and electrochemistry[2.80] because of the ensuing high surface activity.

In the meantime, 2D morphology can effectively take advantage of the aforementioned anisotropic Li storage properties of nano-LTO to tailor their electrochemistry such as the voltage profile and capacity,

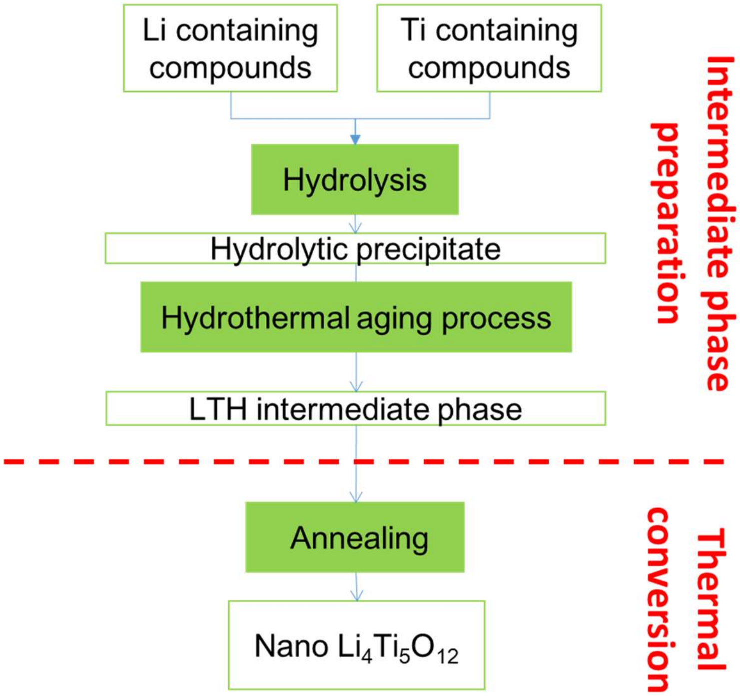

Figure 2.11. Flowchart of 2D LTO nanocrystal preparation via 2-step synthesis strategies

2.4.2. Synthesis of 2D LTO nanocrystals

To prepare 2D LTO nanocrystals, a prominent two-step strategy has been proposed. [2.64,81-85] As schematically expressed in Figure 2.11, those two steps are: (i) preparation of intermediate phase with 2D morphology- layered lithium tiatanate hydrates (LTH); and then (ii) thermal conversion to prepare final products, from the prepared LTH phase into spinel $Li_4Ti_5O_{12}$. The advantage of applying this strategy can be readily understood from the morphology evolution during LTH/LTO phase transformation. As the presented example in Figure 2.12, the metastable 2D morphology of LTO are preserved from the intermediate LTH phase. This feature opens up a unique opportunity for easily scale-up production of 2D nanocrystals, without the requirements in costly surfactants and expensive synthesis equipment. From the summary of all published synthesis methods that took this strategy (Table 1), the possibility of cost reduction and being environmentally friendly becomes much clearer. Namely, the always used organic Ti compounds can be replaced by inexpensive inorganic chemical compounds in aqueous processes; and a cost-effective alternative for the hydrothermal aging process would be greatly helpful as well.

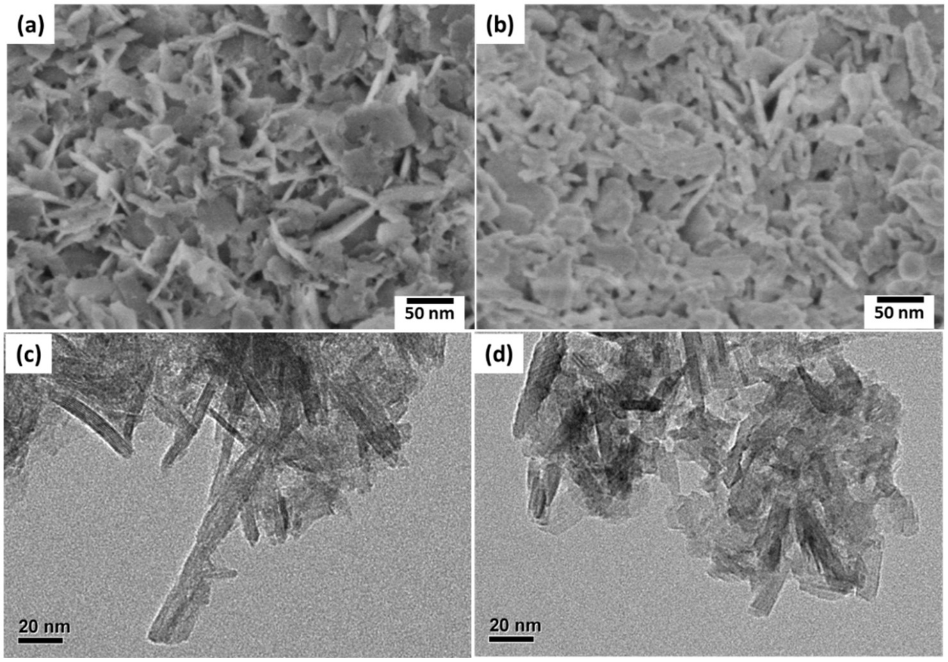

Figure 2.12. the morphology of 2D nanocrystals of (a,c) LTH and (b,d) LTO phases.

The intrinsically 2D morphology of LTH can be attributed to its *C*-centered orthorhombic crystal structure of space group *Cmcm*, whose unit-cell dimensions are a = 3.80102(7) Å, b = 16.70231(6) Å, and c=3.00765(3) Å. It can be further described by lepidocrocite (γ-FeOOH) layered structure consisting of stacked 2D $Ti_\delta O_2$ atomic periodicities ($\delta = 0.91$ [2.86] and 0.87 [2.87]) via edge-sharing and corner-sharing (Figure 2.13). Li ions and hydroxyl groups occupy trigonal prismatic 4*c* sites in the interlayer space as other lepidococite alkaline titanates such as $Cs_xTi_{2-x/4}\square_{x/4}O_4$ [2.88] and $K_{0.8}Ti_{1.73}Li_{0.27}O_4$ [2.89]. Neighboring 2D lattices are held together by either the hydrogen bands between the hydroxyl groups and 2-coordinated oxygen ions on the 2D lattices, or the Coulombic interaction of interlayer Li ions/negatively charged 2D lattices. The negative charge of 2D lattices comes from the vacancies or Li substitution at Ti sites. [2.90,91]

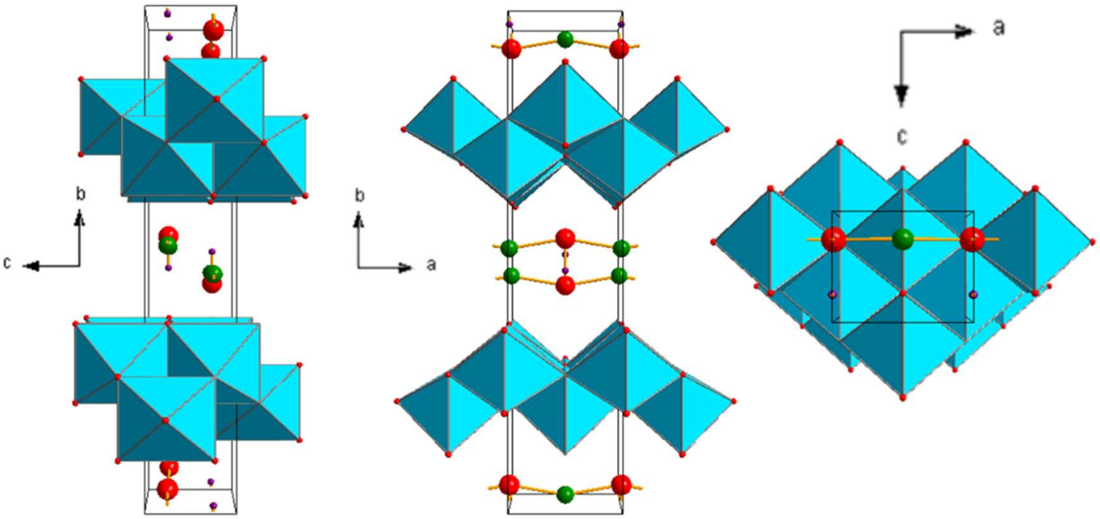

Figure 2.13. The schematic of the proposed orthorhombic lepidocrocite LTH (space group *Cmcm*) model. Red balls are oxygen atoms, green represents lithium atoms and the small purple balls are hydrogen.

Such structural architecture provides an ideal platform of possibly fast electron/ion exchange in the interlayer space, with different inorganic and organic species including H^+, Li^+, OH^-, and others. [2.88,90-94] This superior ion-exchange feature can also be exploited in advanced electrode materials for energy storage/conversion systems or nanoelectronic devices. For the energy application field, the recent work of Shirpour *et al.* reported lepidocrocite $K_{0.8}Ti_{1.73}Li_{0.27}O_4$ as intercalation host for sodium and lithium-ion storage that delivered 300 and 600 mAh/g initial discharge capacity, respectively. [2.89] In the meantime, many successful applications in the filed of photocatalysis can be found as well. [2.95]

2.4.3. *Optimization of the synthesis process*

Many successful examples of preparation of 2D LTO nanocrystals from LTH intermediate phase are made: Liu *et al.* prepared nanostructured LTO by a combination of microwave-assisted hydrothermal process to synthesize LTH precursors, and the thermal conversion was subsequently conducted at elevated temperature. [2.83] Wang *et al.* synthesized rutile-TiO_2 nanocoated LTO nanosheets via similar hydrothermal process but without the assistances of microwaves. [2.82]

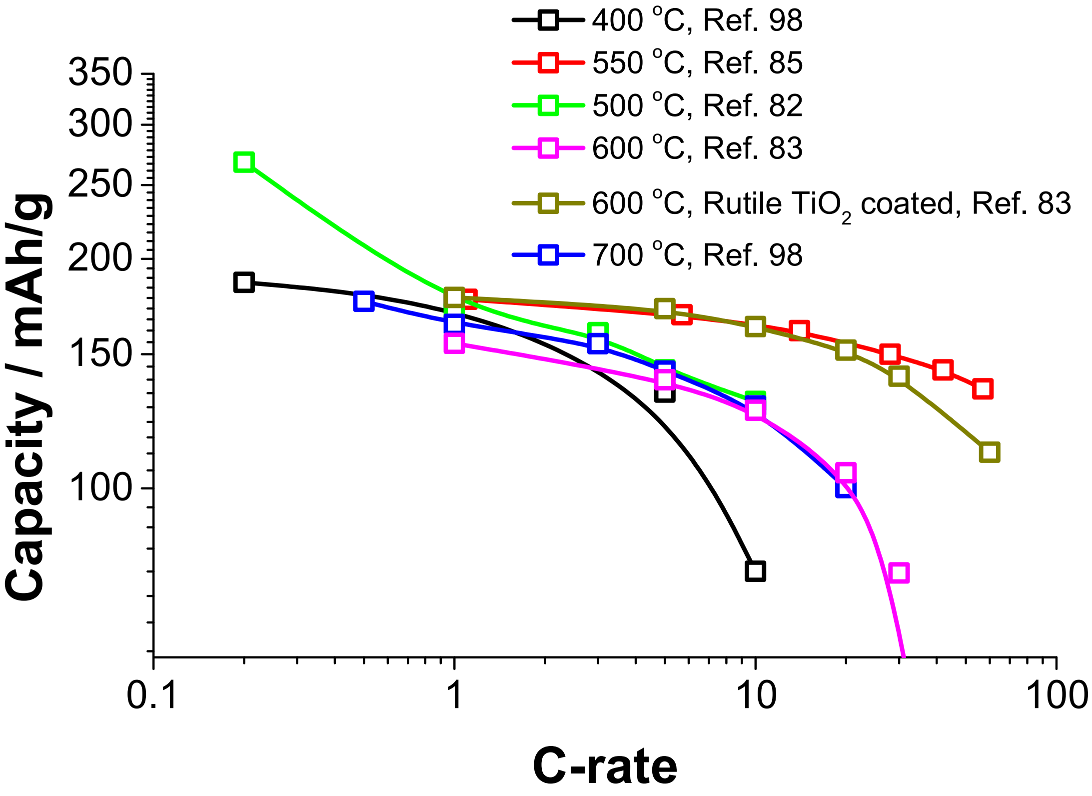

Figure 2.14. Comparison of rate capability of 2D LTO nanocrystals prepared from different methods. The preparation conditions of each curve are labeled as: black curve was annealed at 400 °C; [2.96] red at 550 °C; [2.84] green at 500 °C; [2.81]; magenta and dark yellow were annealed at 600 °C and the later corresponds to rutile TiO_2 coated LTO nanosheets; [2.82] blue at 700 °C. [2.97]

Although their great success, LTH/LTO transformation and the mechanism responsible for the preservation of 2D morphology still remain unknown. In the meantime, few understandings are made on the formation kinetics of each phase. Lack of knowledge limits our capability of material design and property manipulation in 2D LTO nanocrystal electrodes. Figure 2.14 makes a good example of this difficulty. By comparing among the reported rate capability of 2D LTO nanocrystals, the purity and annealing temperature seem to play important roles to determine the electrochemical response. Nonetheless, there are always contradictions to each conclusion. For example, the rutile-nanocoated LTO nanosheets obtained after 600 ºC annealing exhibit superior rate capability (dark yellow). According to the report of Wang et al., the rutile nanocoating helped to improve the rate capability of LTO nanosheets as the significant improvement from the magenta curve. [2.82] But a phase-pure LTO nanosheet crystal has even better performance, which was prepared at merely 550 ºC (red). [2.84] Furthermore, Li *et al.* synthesized LTO nanosheets at only 400 ºC (black), [2.96] which provided a relatively poor performance comparing to those annealed at around 500 and 550 ºC (green and magenta). [2.81,84] However, the data provided by Xiao *et al.* of 700 ºC annealed LTO nanosheets (blue) have similar performance with those annealed at 500-550 ºC. Those contradictions imply a more systematic study of 2D LTO nanocrystals is required.

Table 2.1. Summary of reported 2D LTO nanocrystal preparation applying two-step synthesis strategy

synthesis method	Ti source	Li source	solvent	aging process	annealing process	Reference
hydrothermal thermal	Titanium tetrachlodire / Titanium isopropoxide	mixed LiCl + LiOH / LiOH	water / water + alcohol	Hydrothermal at 190 °C	400 °C	**2.**92
hydrothermal thermal	titanium tetraisopropoxide	LiOH	water + H_2O_2	Hydrothermal at 130 °C, 12h	550 °C, 6h	**2.**84
sol-gel + hydrothermal	Titanium butoxide + cetyltrimethylammonium bromide (CTAB) in ethonal	LiOH	water	Hydrothermal at 180 °C, 24h	400 °C, 2h	**2.**96
hydrothermal	Titanium butoxide	LiOH	water	Hydrothermal at 180 °C, 20h	500 °C	**2.**81
microwave hydrothermal	titanium tetraisopropoxide	LiOH	water + H_2O_2	Microwave Hydrothermal at 130 and 170 °C, respectively, 20 min	550 °C, 6h	**2.**83
hydrothermal	Titanium butoxide	LiOH	ethanol	Hydrothermal at 180 °C, 36h	500 - 700 °C, 6h	**2.**82
hydrothermal	Titanium butoxide	LiOH	ethanol + water	Hydrothermal at 140 °C, 12h	700 °C	**2.**97
hydrothermal	titanium foil	LiOH	water	Hydrothermal at 200 °C, 24h	550 °C, 3h	**2.**85
sol-gel + hydrothermal	Titanium butoxide mixed in ethylene glycol at 160 °C	LiOH	water	hydrothermal at 130 °C, 7 days	400 °C, 2h	**2.**98
hydrothermal	titanium tetraisopropoxide + ammonia	LiOH	water + ethylene glycol	Hydrothermal at 170 °C	500 °C, 2h	**2.**99

2.5.References

(**2.**1) Winter, M.; Brodd, R. J. What Are Batteries, Fuel Cells, and Supercapacitors? *Chemical Reviews* **2004,** *104* (10), 4245.

(**2.**2) Park, M.; Zhang, X.; Chung, M.; Less, G. B.; Sastry, A. M. A review of conduction phenomena in Li-ion batteries. *J. Power Sources* **2010,** *195* (24), 7904.

(**2.**3) Bai, P.; Cogswell, D. A.; Bazant, M. Z. Suppression of Phase Separation in $LiFePO_4$ Nanoparticles During Battery Discharge. *Nano Lett.* **2011,** *11* (11), 4890.

(**2.**4) Bai, P.; Bazant, M. Z. Charge transfer kinetics at the solid-solid interface in porous electrodes. *Nat. Commun.* **2014,** *5*, 3585.

(**2.**5) Julien, C.; Mauger, A.; Vijh, A.; Zaghib, K. *Lithium Batteries: Science and Technology*; Springer, 2015.

(**2.**6) Goodenough, J. B.; Park, K.-S. The Li-Ion Rechargeable Battery: A Perspective. *J. Am. Chem. Soc.* **2013,** *135* (4), 1167.

(**2.**7) Goodenough, J. B.; Kim, Y. Challenges for Rechargeable Li Batteries. *Chem. Mater.* **2010,** *22* (3), 587.

(**2.**8) Goodenough, J. B. Batteries and a Sustainable Modern Society. *The Electrochemical Society Interface* **2016,** *25* (3), 67.

(**2.**9) Kang, K.; Meng, Y. S.; Bréger, J.; Grey, C. P.; Ceder, G. Electrodes with High Power and High Capacity for Rechargeable Lithium Batteries. *Science* **2006,** *311* (5763), 977.

(**2.**10) Ribiere, P.; Grugeon, S.; Morcrette, M.; Boyanov, S.; Laruelle, S.; Marlair, G. Investigation on the fire-induced hazards of Li-ion battery cells by fire calorimetry. *Energy. Environ. Sci.* **2012,** *5* (1), 5271.

(**2.**11) Armand, M.; Tarascon, J. M. Building better batteries. *Nature* **2008,** *451* (7179), 652.

(**2.**12) Reuters; Vol. 2016.

(**2.**13) Wang, Q.; Ping, P.; Zhao, X.; Chu, G.; Sun, J.; Chen, C. Thermal runaway caused fire and explosion of lithium ion battery. *J. Power Sources* **2012,** *208*, 210.

(**2.**14) MacNeil, D. D.; Lu, Z.; Chen, Z.; Dahn, J. R. A comparison of the electrode/electrolyte reaction at elevated temperatures for various Li-ion battery cathodes. *J. Power Sources* **2002,** *108* (1–2), 8.

(**2.**15) Hatchard, T. D.; MacNeil, D. D.; Basu, A.; Dahn, J. R. Thermal Model of Cylindrical and Prismatic Lithium-Ion Cells. *J. Electrochem. Soc.* **2001,** *148* (7), A755.

(**2.**16) Wen, J.; Yu, Y.; Chen, C. A Review on Lithium-Ion Batteries Safety Issues: Existing Problems and Possible Solutions. *Materials Express* **2012,** *2* (3), 197.

(**2.**17) Maleki, H.; Deng, G.; Anani, A.; Howard, J. Thermal Stability Studies of Li-Ion Cells and Components. *J. Electrochem. Soc.* **1999,** *146* (9), 3224.

(**2.**18) Ferg, E.; Gummow, R. J.; de Kock, A.; Thackeray, M. M. Spinel Anodes for Lithium-Ion Batteries. *J. Electrochem. Soc.* **1994,** *141* (11), L147.

(**2.**19) Deschanvres, A.; Raveau, B.; Sekkal, Z. Mise en evidence et etude cristallographique d'une nouvelle solution solide de type spinelle $Li_{1+x}Ti_{2-x}O_4$ $0 \leqslant x \leqslant 0, 333$. *Mater. Res. Bull.* **1971,** *6* (8), 699.

(**2.**20) Zaghib, K.; Simoneau, M.; Armand, M.; Gauthier, M. Electrochemical study of $Li_4Ti_5O_{12}$ as negative electrode for Li-ion polymer rechargeable batteries. *J. Power Sources* **1999,** *81* (0), 300.

(**2.**21) Aldon, L.; Kubiak, P.; Womes, M.; Jumas, J. C.; Olivier-Fourcade, J.; Tirado, J. L.; Corredor, J. I.; Pérez Vicente, C. Chemical and Electrochemical Li-Insertion into the $Li_4Ti_5O_{12}$ Spinel. *Chem. Mater.* **2004,** *16* (26), 5721.

(**2.**22) Scharner, S.; Weppner, W.; Schmid-Beurmann, P. Evidence of Two-Phase Formation upon Lithium Insertion into the $Li_{1.33}Ti_{1.67}O_4$ Spinel. *J. Electrochem. Soc.* **1999,** *146* (3), 857.

(**2.**23) Colbow, K. M.; Dahn, J. R.; Haering, R. R. Structure and electrochemistry of the spinel oxides $LiTi_2O_4$ and $Li_{4/3}Ti_{5/3}O_4$. *J. Power Sources* **1989,** *26* (3–4), 397.

(**2.**24) Kataoka, K.; Takahashi, Y.; Kijima, N.; Hayakawa, H.; Akimoto, J.; Ohshima, K.-i. A single-crystal study of the electrochemically Li-ion intercalated spinel-type $Li_4Ti_5O_{12}$. *Solid State Ionics* **2009,** *180* (6-8), 631.

(**2.**25) Lu, X.; Gu, L.; Hu, Y.-S.; Chiu, H.-C.; Li, H.; Demopoulos, G. P.; Chen, L. New Insight into the Atomic-Scale Bulk and Surface Structure Evolution of $Li_4Ti_5O_{12}$ Anode. *J. Am. Chem. Soc.* **2015,** *137* (4), 1581.

(**2.**26) Murphy, D. W.; Cava, R. J.; Zahurak, S. M.; Santoro, A. Ternary LixTiO2 phases from insertion reactions. *Solid State Ionics* **1983,** *9-10, Part 1* (0), 413.

(**2.**27) Colbow, K. M.; Dahn, J. R.; Haering, R. R. Structure and electrochemistry of the spinel oxides $LiTi_2O4$ and $Li_{4/3}Ti_{5/3}O_4$. *J. Power Sources* **1989,** *26* (3-4), 397.

(**2.**28) Lu, X.; Zhao, L.; He, X.; Xiao, R.; Gu, L.; Hu, Y.-S.; Li, H.; Wang, Z.; Duan, X.; Chen, L.et al. Lithium Storage in $Li_4Ti_5O_{12}$ Spinel: The Full Static Picture from Electron Microscopy. *Adv. Mater.* **2012,** *24* (24), 3233.

(**2.**29) Wagemaker, M.; Simon, D. R.; Kelder, E. M.; Schoonman, J.; Ringpfeil, C.; Haake, U.; Lutzenkirchen-Hecht, D.; Frahm, R.; Mulder, F. M. A kinetic two-phase and equilibrium solid solution in spinel $Li_{4+x}Ti_5O_{12}$. *Adv. Mater.* **2006,** *18* (23), 3169.

(**2.**30) Wagemaker, M.; van Eck, E. R.; Kentgens, A. P.; Mulder, F. M. Li-ion diffusion in the equilibrium nanomorphology of spinel $Li_{4+x}Ti_5O_{12}$. *J. Phys. Chem. B* **2009,** *113* (1), 224.

(**2.**31) Julien, C. M.; Mauger, A.; Zaghib, K.; Groult, H. Comparative Issues of Cathode Materials for Li-Ion Batteries. *Inorganics* **2014,** *2* (1), 132.

(**2.**32) Schmidt, W.; Bottke, P.; Sternad, M.; Gollob, P.; Hennige, V.; Wilkening, M. Small Change-Great Effect: Steep Increase of Li Ion Dynamics in $Li_4Ti_5O_{12}$ at the Early Stages of Chemical Li Insertion. *Chem. Mater.* **2015,** *27* (5), 1740.

(**2.**33) Laumann, A.; Boysen, H.; Bremholm, M.; Fehr, K. T.; Hoelzel, M.; Holzapfel, M. Lithium Migration at High Temperatures in $Li_4Ti_5O_{12}$ Studied by Neutron Diffraction. *Chem. Mater.* **2011,** *23* (11), 2753.

(**2.**34) Wilkening, M.; Amade, R.; Iwaniak, W.; Heitjans, P. Ultraslow Li diffusion in spinel-type structured $Li_4Ti_5O_{12}$-A comparison of results from solid state NMR and impedance spectroscopy. *Phys. Chem. Chem. Phys.* **2007,** *9* (10), 1239.

(**2.**35) Ziebarth, B.; Klinsmann, M.; Eckl, T.; Elsässer, C. Lithium diffusion in the spinel phaseL$Li_4Ti_5O_{12}$ and in the rocksalt phase $Li_7Ti_5O_{12}$ of lithium titanate from first principles. *Phys. Rev. B: Condens. Matter Mater. Phys.* **2014,** *89* (17), 174301.

(**2.**36) Wilkening, M.; Iwaniak, W.; Heine, J.; Epp, V.; Kleinert, A.; Behrens, M.; Nuspl, G.; Bensch, W.; Heitjans, P. Microscopic Li self-diffusion parameters in the lithiated anode material $Li_{4+x}Ti_5O_{12}$ ($0 < x < 3$) measured by ^{7}Li solid state NMR. *Phys. Chem. Chem. Phys.* **2007,** *9* (47), 6199.

(**2.**37) Yu, P.; Popov, B. N.; Ritter, J. A.; White, R. E. Determination of the Lithium Ion Diffusion Coefficient in Graphite. *J. Electrochem. Soc.* **1999,** *146* (1), 8.

(**2.**38) Ouyang, C. Y.; Zhong, Z. Y.; Lei, M. S. Ab initio studies of structural and electronic properties of $Li_4Ti_5O_{12}$ spinel. *Electrochem. Commun.* **2007,** *9* (5), 1107.

(**2.**39) Zhong, Z.; Ouyang, C.; Shi, S.; Lei, M. Ab initio Studies on $Li_{4+x}Ti_5O_{12}$ Compounds as Anode Materials for Lithium-Ion Batteries. *ChemPhysChem* **2008,** *9* (14), 2104.

(**2.**40) Chen, Y. C.; Ouyang, C. Y.; Song, L. J.; Sun, Z. L. Lithium ion diffusion in $Li_{4+x}Ti_5O_{12}$: From ab initio studies. *Electrochim. Acta* **2011,** *56* (17), 6084.

(**2.**41) Young, D.; Ransil, A.; Amin, R.; Li, Z.; Chiang, Y.-M. Electronic Conductivity in the $Li_{4/3}Ti_{5/3}O_4$-$Li_{7/3}Ti_{5/3}O_4$System and Variation with State-of-Charge as a Li Battery Anode. *Adv. Energy Mater.* **2013,** *3* (9), 1125.

(**2.**42) Morgan, D.; Van der Ven, A.; Ceder, G. Li Conductivity in Li_xMPO_4 (M=Mn, Fe, Co, Ni) Olivine Materials. *Electrochem. Solid. St.* **2004,** *7* (2), A30.

(**2.**43) Bhattacharya, J.; Van der Ven, A. Phase stability and nondilute Li diffusion in spinel $Li_{1+x}Ti_2O_4$. *Phys. Rev. B: Condens. Matter Mater. Phys.* **2010,** *81* (10), 104304.

(**2.**44) Kim, C.; Norberg, N. S.; Alexander, C. T.; Kostecki, R.; Cabana, J. Mechanism of Phase Propagation During Lithiation in Carbon-Free $Li_4Ti_5O_{12}$ Battery Electrodes. *Adv. Funct. Mater.* **2012**, DOI:10.1002/adfm.201201684 10.1002/adfm.201201684, n/a.

(**2.**45) Wagemaker, M.; Mulder, F. M.; Van der Ven, A. The Role of Surface and Interface Energy on Phase Stability of Nanosized Insertion Compounds. *Adv. Mater.* **2009,** *21* (25-26), 2703.

(**2.**46) Sun, Y.; Zhao, L.; Pan, H.; Lu, X.; Gu, L.; Hu, Y. S.; Li, H.; Armand, M.; Ikuhara, Y.; Chen, L.et al. Direct atomic-scale confirmation of three-phase storage mechanism in $Li_4Ti_5O_{12}$ anodes for room-temperature sodium-ion batteries. *Nat. Commun.* **2013,** *4*, 1870.

(**2.**47) Zaghib, K.; Dontigny, M.; Guerfi, A.; Trottier, J.; Hamel-Paquet, J.; Gariepy, V.; Galoutov, K.; Hovington, P.; Mauger, A.; Groult, H.et al. An improved high-power battery with increased thermal operating range: C–$LiFePO_4$//C–$Li_4Ti_5O_{12}$. *J. Power Sources* **2012,** *216*, 192.

(**2.**48) Zaghib, K.; Dontigny, M.; Perret, P.; Guerfi, A.; Ramanathan, M.; Prakash, J.; Mauger, A.; Julien, C. M. Electrochemical and thermal characterization of lithium titanate spinel anode in C–$LiFePO_4$//C–$Li_4Ti_5O_{12}$ cells at sub-zero temperatures. *J. Power Sources* **2014,** *248*, 1050.

(**2.**49) Zaghib, K.; Dontigny, M.; Guerfi, A.; Charest, P.; Rodrigues, I.; Mauger, A.; Julien, C. M. Safe and fast-charging Li-ion battery with long shelf life for power applications. *J. Power Sources* **2011,** *196* (8), 3949.

(**2.**50) Meethong, N.; Huang, H.-Y. S.; Carter, W. C.; Chiang, Y.-M. Size-Dependent Lithium Miscibility Gap in Nanoscale $Li_{1-x}FePO_4$. *Electrochem. Solid. St.* **2007,** *10* (5), A134.

(**2.**51) Wagemaker, M.; Borghols, W. J. H.; Mulder, F. M. Large Impact of Particle Size on Insertion Reactions. A Case for Anatase Li_xTiO_2. *J. Am. Chem. Soc.* **2007,** *129* (14), 4323.

(**2.**52) Borghols, W. J. H.; Wagemaker, M.; Lafont, U.; Kelder, E. M.; Mulder, F. M. Impact of Nanosizing on Lithiated Rutile TiO_2. *Chem. Mater.* **2008,** *20* (9), 2949.

(**2.**53) Meethong, N.; Huang, H. Y. S.; Speakman, S. A.; Carter, W. C.; Chiang, Y. M. Strain Accommodation during Phase Transformations in Olivine-Based Cathodes as a Materials Selection Criterion for High-Power Rechargeable Batteries. *Adv. Funct. Mater.* **2007,** *17* (7), 1115.

(**2.**54) Wagemaker, M.; Mulder, F. M. Properties and promises of nanosized insertion materials for Li-ion batteries. *Acc. Chem. Res.* **2013,** *46* (5), 1206.

(**2.**55) Kavan, L.; Prochazka, J.; Spitler, T. M.; Kalbac, M.; Zukalova, M. T.; Drezen, T.; Gratzel, M. Li insertion into $Li_4Ti_5O_{12}$ p(Spinel) - Charge capability vs. particle size in thin-film electrodes. *J. Electrochem. Soc.* **2003,** *150* (7), A1000.

(**2.**56) Pang, W. K.; Peterson, V. K.; Sharma, N.; Shiu, J. J.; Wu, S. H. Lithium Migration in $Li_4Ti_5O_{12}$ Studied Using in Situ Neutron Powder Diffraction. *Chem. Mater.* **2014,** *26* (7), 2318.

(**2.**57) Kang, K.; Ceder, G. Factors that affect Li mobility in layered lithium transition metal oxides. *Phys. Rev. B: Condens. Matter Mater. Phys.* **2006,** *74* (9), 094105.

(**2.**58) Song, K.; Seo, D. H.; Jo, M. R.; Kim, Y. I.; Kang, K.; Kang, Y. M. Tailored Oxygen Framework of $Li_4Ti_5O_{12}$ Nanorods for High-Power Li Ion Battery. *J. Phys. Chem. Lett.* **2014,** *5* (8), 1368.

(**2.**59) Kavan, L.; Procházka, J.; Spitler, T. M.; Kalbáč, M.; Zukalová, M.; Drezen, T.; Grätzel, M. Li Insertion into $Li_4Ti_5O_{12}$ (Spinel) : Charge Capability vs. Particle Size in Thin-Film Electrodes. *J. Electrochem. Soc.* **2003,** *150* (7), A1000.

(**2**.60) Ganapathy, S.; Wagemaker, M. Nanosize Storage Properties in Spinel $Li_4Ti_5O_{12}$ Explained by Anisotropic Surface Lithium Insertion. *Acs Nano* **2012,** *6* (10), 8702.

(**2**.61) Borghols, W. J. H.; Wagemaker, M.; Lafont, U.; Kelder, E. M.; Mulder, F. M. Size Effects in the $Li_{4+x}Ti_5O_{12}$ Spinel. *J. Am. Chem. Soc.* **2009,** *131* (49), 17786.

(**2**.62) Feng, W.; Lijun, W.; Chao, M.; Dong, S.; Yimei, Z.; Jason, G. Excess lithium storage and charge compensation in nanoscale $Li_{4+x}Ti_5O_{12}$. *Nanotechnology* **2013,** *24* (42), 424006.

(**2**.63) Shu, J. Electrochemical behavior and stability of $Li_4Ti_5O_{12}$ in a broad voltage window. *J Solid State Electr* **2009,** *13* (10), 1535.

(**2**.64) Chiu, H. C.; Brodusch, N.; Gauvin, R.; Guerfi, A.; Zaghib, K.; Demopoulos, G. P. Aqueous Synthesized Nanostructured $Li_4Ti_5O_{12}$ for High-Performance Lithium Ion Battery Anodes. *J. Electrochem. Soc.* **2013,** *160* (5), A3041.

(**2**.65) Ge, H.; Li, N.; Li, D.; Dai, C.; Wang, D. Electrochemical characteristics of spinel $Li_4Ti_5O_{12}$ discharged to 0.01&0 V. *Electrochem. Commun.* **2008,** *10* (5), 719.

(**2**.66) Belharouak, I.; Koenig, G. M.; Tan, T.; Yumoto, H.; Ota, N.; Amine, K. Performance Degradation and Gassing of $Li_4Ti_5O_{12}/LiMn_2O_4$ Lithium-Ion Cells. *J. Electrochem. Soc.* **2012,** *159* (8), A1165.

(**2**.67) He, Y.-B.; Li, B.; Liu, M.; Zhang, C.; Lv, W.; Yang, C.; Li, J.; Du, H.; Zhang, B.; Yang, Q.-H.et al. Gassing in $Li_4Ti_5O_{12}$-based batteries and its remedy. *Sci. Rep.* **2012,** *2*.

(**2**.68) He, Y.-B.; Liu, M.; Huang, Z.-D.; Zhang, B.; Yu, Y.; Li, B.; Kang, F.; Kim, J.-K. Effect of solid electrolyte interface (SEI) film on cyclic performance of $Li_4Ti_5O_{12}$ anodes for Li ion batteries. *J. Power Sources* **2013,** *239*, 269.

(**2**.69) Wu, K.; Yang, J.; Liu, Y.; Zhang, Y.; Wang, C.; Xu, J.; Ning, F.; Wang, D. Investigation on gas generation of $Li_4Ti_5O_{12}/LiNi_{1/3}Co_{1/3}Mn_{1/3}O_2$ cells at elevated temperature. *J. Power Sources* **2013,** *237*, 285.

(**2**.70) Bernhard, R.; Meini, S.; Gasteiger, H. A. On-Line Electrochemical Mass Spectrometry Investigations on the Gassing Behavior of $Li_4Ti_5O_{12}$ Electrodes and Its Origins. *J. Electrochem. Soc.* **2014,** *161* (4), A497.

(**2**.71) He, M.; Castel, E.; Laumann, A.; Nuspl, G.; Novák, P.; Berg, E. J. In Situ Gas Analysis of $Li_4Ti_5O_{12}$ Based Electrodes at Elevated Temperatures. *J. Electrochem. Soc.* **2015,** *162* (6), A870.

(**2.**72) Hirayama, M.; Kim, K.; Toujigamori, T.; Cho, W.; Kanno, R. Epitaxial growth and electrochemical properties of $Li_4Ti_5O_{12}$ thin-film lithium battery anodes. *Dalton Trans.* **2011,** *40* (12), 2882.

(**2.**73) Devie, A.; Dubarry, M.; Liaw, B. Y. Overcharge Study in $Li_4Ti_5O_{12}$ Based Lithium-Ion Pouch Cell: I. Quantitative Diagnosis of Degradation Modes. *J. Electrochem. Soc.* **2015,** *162* (6), A1033.

(**2.**74) Gao, J.; Gong, B.; Zhang, Q.; Wang, G.; Dai, Y.; Fan, W. Study of the surface reaction mechanism of $Li_4Ti_5O_{12}$ anode for lithium-ion cells. *Ionics* **2015**, DOI:10.1007/s11581-015-1435-x 10.1007/s11581-015-1435-x, 1.

(**2.**75) Wang, Q. H.; Kalantar-Zadeh, K.; Kis, A.; Coleman, J. N.; Strano, M. S. Electronics and optoelectronics of two-dimensional transition metal dichalcogenides. *Nat Nanotechnol* **2012,** *7* (11), 699.

(**2.**76) Novoselov, K. S.; Jiang, D.; Schedin, F.; Booth, T. J.; Khotkevich, V. V.; Morozov, S. V.; Geim, A. K. Two-dimensional atomic crystals. *Proc Natl Acad Sci U S A* **2005,** *102* (30), 10451.

(**2.**77) Coleman, J. N.; Lotya, M.; O'Neill, A.; Bergin, S. D.; King, P. J.; Khan, U.; Young, K.; Gaucher, A.; De, S.; Smith, R. J.et al. Two-dimensional nanosheets produced by liquid exfoliation of layered materials. *Science* **2011,** *331* (6017), 568.

(**2.**78) Nicolosi, V.; Chhowalla, M.; Kanatzidis, M. G.; Strano, M. S.; Coleman, J. N. Liquid Exfoliation of Layered Materials. *Science* **2013,** *340* (6139), 1224619.

(**2.**79) Pyun, J. Graphene oxide as catalyst: application of carbon materials beyond nanotechnology. *Angew Chem Int Ed Engl* **2011,** *50* (1), 46.

(**2.**80) Brownson, D. A.; Banks, C. E. Graphene electrochemistry: an overview of potential applications. *Analyst* **2010,** *135* (11), 2768.

(**2.**81) Li, N.; Mei, T.; Zhu, Y.; Wang, L.; Liang, J.; Zhang, X.; Qian, Y.; Tang, K. Hydrothermal synthesis of layered $Li_{1.81}H_{0.19}Ti_2O_5.xH_2O$ nanosheets and their transformation to single-crystalline $Li_4Ti_5O_{12}$ nanosheets as the anode materials for Li-ion batteries. *CrystEngComm* **2012,** *14* (20), 6435.

(**2.**82) Wang, Y.-Q.; Gu, L.; Guo, Y.-G.; Li, H.; He, X.-Q.; Tsukimoto, S.; Ikuhara, Y.; Wan, L.-J. Rutile-TiO_2 Nanocoating for a High-Rate $Li_4Ti_5O_{12}$ Anode of a Lithium-Ion Battery. *J. Am. Chem. Soc.* **2012,** *134* (18), 7874.

(**2.**83) Liu, J.; Li, X.; Yang, J.; Geng, D.; Li, Y.; Wang, D.; Li, R.; Sun, X.; Cai, M.; Verbrugge, M. W. Microwave-assisted hydrothermal synthesis of nanostructured spinel $Li_4Ti_5O_{12}$ as anode materials for lithium ion batteries. *Electrochim. Acta* **2012,** *63* (0), 100.

(**2.**84) Chen, J.; Yang, L.; Fang, S.; Tang, Y. Synthesis of sawtooth-like $Li_4Ti_5O_{12}$ nanosheets as anode materials for Li-ion batteries. *Electrochim. Acta* **2010,** *55* (22), 6596.

(**2.**85) Chen, S.; Xin, Y.; Zhou, Y.; Ma, Y.; Zhou, H.; Qi, L. Self-supported $Li_4Ti_5O_{12}$ nanosheet arrays for lithium ion batteries with excellent rate capability and ultralong cycle life. *Energy. Environ. Sci.* **2014**, DOI:10.1039/c3ee42646g 10.1039/c3ee42646g.

(**2.**86) Manga, K. K.; Zhou, Y.; Yan, Y. L.; Loh, K. P. Multilayer Hybrid Films Consisting of Alternating Graphene and Titania Nanosheets with Ultrafast Electron Transfer and Photoconversion Properties. *Adv. Funct. Mater.* **2009,** *19* (22), 3638.

(**2.**87) Tanaka, T.; Ebina, Y.; Takada, K.; Kurashima, K.; Sasaki, T. Oversized titania nanosheet crystallites derived from flux-grown layered titanate single crystals. *Chem. Mater.* **2003,** *15* (18), 3564.

(**2.**88) Gao, T.; Fjellvåg, H.; Norby, P. Defect Chemistry of a Zinc-Doped Lepidocrocite Titanate $Cs_xTi_{2-x/2}Zn_{x/2}O_4$ (x = 0.7) and its Protonic Form. *Chem. Mater.* **2009,** *21* (15), 3503.

(**2.**89) Shirpour, M.; Cabana, J.; Doeff, M. Lepidocrocite-type Layered Titanate Structures: New Lithium and Sodium Ion Intercalation Anode Materials. *Chem. Mater.* **2014,** *26* (8), 2502.

(**2.**90) Sasaki, T.; Watanabe, M.; Michiue, Y.; Komatsu, Y.; Izumi, F.; Takenouchi, S. Preparation and Acid-Base Properties of a Protonated Titanate with the Lepidocrocite-Like Layer Structure. *Chem. Mater.* **1995,** *7* (5), 1001.

(**2.**91) Sasaki, T.; Kooli, F.; Iida, M.; Michiue, Y.; Takenouchi, S.; Yajima, Y.; Izumi, F.; Chakoumakos, B. C.; Watanabe, M. A Mixed Alkali Metal Titanate with the Lepidocrocite-like Layered Structure. Preparation, Crystal Structure, Protonic Form, and Acid−Base Intercalation Properties. *Chem. Mater.* **1998,** *10* (12), 4123.

(**2.**92) Sugita, M.; Tsuji, M.; Abe, M. Synthetic Inorganic Ion-Exchange Materials. LVIII. Hydrothermal Synthesis of a New Layered Lithium Titanate and Its Alkali Ion Exchange. *Bull. Chem. Soc. Jpn.* **1990,** *63* (7), 1978.

(**2.**93) Gao, T.; Fjellvåg, H.; Norby, P. Raman Scattering Properties of a Protonic Titanate $H_xTi_{2-x/4}\square_{x/4}O_4{\cdot}H_2O$ ($\square$, vacancy; x = 0.7) with Lepidocrocite-Type Layered Structure. *J. Phys. Chem. B* **2008,** *112* (31), 9400.

(**2.**94) Bavykin, D. V.; Walsh, F. C. Kinetics of alkali metal ion exchange into nanotubular and nanofibrous titanates. *J. Phys. Chem. C* **2007,** *111* (40), 14644.

(**2.**95) Yu, Y. L.; Zhang, P.; Guo, L. M.; Chen, Z. D.; Wu, Q.; Ding, Y. H.; Zheng, W. J.; Cao, Y. The Design of TiO_2 Nanostructures (Nanoparticle, Nanotube, and Nanosheet) and Their Photocatalytic Activity. *J. Phys. Chem. C* **2014,** *118* (24), 12727.

(**2.**96) Li, G.; Xia, J.; Jiao, J.; Chen, L.; Shen, P. Low-temperature Synthesis of Peony-like Spinel $Li_4Ti_5O_{12}$ as a High-performance Anode Material for Lithium Ion Batteries. *Chinese Journal of Chemistry* **2011,** *29* (9), 1824.

(**2.**97) Xiao, L.; Chen, G.; Sun, J.; Chen, D.; Xu, H.; Zheng, Y. Facile synthesis of $Li_4Ti_5O_{12}$ nanosheets stacked by ultrthin nanoflakes for high performance lithium ion batteries. *Journal of Materials Chemistry A* **2013**, DOI:10.1039/c3ta12569f 10.1039/c3ta12569f.

(**2.**98) Jiang, Y.-M.; Wang, K.-X.; Wu, X.-Y.; Zhang, H.-J.; Bartlett, B. M.; Chen, J.-S. $Li_4Ti_5O_{12}/TiO_2$ Hollow Spheres Composed Nanoflakes with Preferentially Exposed $Li_4Ti_5O_{12}$ (011) Facets for High-Rate Lithium Ion Batteries. *Acs Applied Materials & Interfaces* **2014**, DOI:10.1021/am504931r 10.1021/am504931r.

(**2.**99) Tang, Y. F.; Yang, L.; Qiu, Z.; Huang, J. S. Preparation and electrochemical lithium storage of flower-like spinel $Li_4Ti_5O_{12}$ consisting of nanosheets. *Electrochem. Commun.* **2008,** *10* (10), 1513.

Chapter 3

Aqueous Synthesized Nanostructured $Li_4Ti_5O_{12}$ for High-Performance Lithium Ion Battery Anodes

One of the principal objectives of this research is to develop a sustainable process that is flexible enough to prepare various types of nano-LTO. This was pursued from the standpoint of the new process being environmentally benign and energy – effective.

Unlike the majority of methods employed to nanomaterial preparation, which rely on the use of organic (often toxic) chemicals and solvents to control nucleation & growth, crystal morphology and phase stabilization, the present work makes use of only inorganic precursors and water. This was achieved via aqueous preparation (at a temperature below the boiling point of water) of sheet-like nanocrystals of lithium titanate hydrate (LTH, $(Li_{2-x}H_x)Ti_2O_5 \cdot yH_2O$), which is subsequently thermally transformed to LTO.

To the best of our knowledge, this is the first work that describes the synthesis of alkali metal titanates without resorting to hydrothermal/sovothermal treatment in an autoclave at temperatures >> 100°C. Avoiding this energy-intensive treatment, which is the result of the high specific heat of water, helps to reduce the energy consumption. Meanwhile, LTH provides an intimate mixture of cations at atomic scale that enhances the yield of the thermal conversion to spinel LTO avoiding application of excessive high annealing temperatures.

This Chapter was previously published in: **Chiu HC**, Brodusch N, Gauvin R, Guerfi A, Zaghib K, Demopoulos GP. Aqueous Synthesized Nanostructured $Li_4Ti_5O_{12}$ for High-Performance Lithium Ion Battery Anodes. *J Electrochem Soc*. 2013;160(5):A3041-A7. DOI: 10.1149/2.008305jes.

3.1.Abstract

Nanostructured $Li_4Ti_5O_{12}$ (LTO) was prepared via a novel process comprising low-temperature (<100 °C) aqueous synthesis and annealing of the hydrous intermediate phase

$Li_{1.81}H_{0.19}Ti_2O_5 \cdot 2H_2O$ (LTH) using only LiOH and $TiCl_4$ as precursors. Nanosheet-structured LTH converted to either LTO nanosheets (102 $m^2 \cdot g^{-1}$) or LTO nanoparticles (28 $m^2 \cdot g^{-1}$) upon annealing at 400 and 600 ºC respectively, each exhibiting unique electrochemical performance properties. The nanosheet-structured LTO exhibited higher initial charge capacity (228.3 vs. 187.3 $mAh \cdot g^{-1}$ at 1.0 V cut-off and C/24 rate) than the nanoparticle-structured LTO. Furthermore, the LTO nanosheets taking advantage of their short diffusion path exhibited better rate capability than the LTO nanoparticles; for example, their discharge capacity at 15 C was 115 $mAh \cdot g^{-1}$ vs. 68.4 $mAh \cdot g^{-1}$ at 1.2 V cut-off for the LTO nanoparticles. Meanwhile, the LTO nanoparticles exhibited better cyclability than the LTO nanosheets because of their higher crystallinity. Thus after 130 1C cycles with cut off at 1.2 V (vs. Li/Li^+), the discharge capacity of the nanosheets was 132.9 $mAh \cdot g^{-1}$ while that of nanoparticles was 150.7 $mAh \cdot g^{-1}$, corresponding to 85 and 97 % discharge capacity retention respectively. The newly synthesized nanostructured LTO material can offer a low cost scalable solution for high-performance LIB anodes.

3.2.Introduction

Lithium ion batteries (LIB) have become the power source of choice for portable devices and advantageously positioned for application to electric vehicles (EVs), hybrid electric vehicles (HEVs) and plug-in electric vehicles (PHEV),[3.1] because of their high energy density[3.2,3] and long cycling life.[3.4,5] Graphite is currently the most common anode material used in commercial LIB, but it suffers from safety issues and poor abuse tolerance for land transportation applications.[3.6] Among the various alternatives to graphite, spinel lithium titanate ($Li_4Ti_5O_{12}$; LTO) has been identified as having great application potential due to its favorable physicochemical characteristics. Firstly, LTO is known as a zero-strain intercalation compound with only 0.2 % volume change as it takes three lithium ions to reversibly form the rock-salt $Li_7Ti_5O_{12}$ with theoretical capacity 175 mAh/g.[3.7-9] Secondly, the operational voltage of LTO is at 1.55 V vs. Li/Li^+, hence avoiding the formation of solid electrolyte interphase (SEI)[3.10] from which lithiated graphite (below 0.2 V vs. Li/Li^+) suffers.[3.11] Consequently, LTO is characterized by high coulombic efficiency,[3.7] excellent cycle life[3.8] and in particular superb safety.[3.10]

However, there is a kinetic problem of low electronic conductivity of LTO (ca. 10^{-13} S·cm^{-1})[3.12] which hinders its usage in automotive LIB. Much effort has been focused on synthesizing nanoscale LTO,[3.12-17] which can overcome the kinetic problem by shortening the diffusion path for electrons and lithium ions. An additional advantage of LTO nanosizing is that its capacity can increase above the theoretical value of 175 mAh/g[3.18] as a result of near-surface lithium ion accommodation.[3.12,17,19,20] When the latter happens, a curved open-circuit voltage profile is obtained as result of near-surface region distribution of redox potentials.[3.17,19] Furthermore, the voltage profile can be tailored via controlling the shape and morphology of nanostrucutred LTO.[3.17] In this context, nanostruutred LTO with different morphologies, such as nanotubes[3.14] and nanowires,[3.21] nanosheets[3.22-26] and nanoparticles[3.27-30] have been synthesized and tested.

Up to now, various routes have been advanced to prepare nanostructured LTO that include solid-state reaction,[3.28,29,31,32] sol-gel,[3.33-36] and hydrothermal processes.[3.16,22-24,26,30,37,38] Typically, these methods employ a two-step approach requiring high temperatures for synthesis of an intermediate (at T> 100 °C) and post-annealing the latter (at T>600 °C). For example, Matsui et al. prepared β-Li_2TiO_3 and TiO_2 by solid state method as intermediate phases from which 70 nm LTO with narrow size distribution was obtained after high-energy ball-milling that was followed by annealing at 700 °C.[3.29] Laumann et al. synthesized as intermediate phase α-Li_2TiO_3 via a hydrothermal process at 180 °C from which after annealing at 800 °C LTO was produced; however, LTO was not pure as it contained in the range of 3-5 wt% β-Li_2TiO_3 as second phase.[3.39,40] According to the study of Khomane et al.,[3.35] hexadecyl-trimethyl ammonium bromide (CTAB) was used to assist the sol-gel synthesis at 100 °C of an intermediate to LTO precipitate along lithium acetate and titanium isopropoxide (TTIP) as precursors in ethanol. The said intermediate material was subsequently annealed at 800 °C.[3.35] The two-step strategy wherein LTO is synthesized via post-annealing of intermediate phase is widely used because the region of spinel LTO in the phase diagram of Li-Ti-O is extremely narrow[3.41,42] making it very difficult to obtain phase-pure LTO. Recently, C base-centered orthorhombic $Li_{1.81}H_{0.19}Ti_2O_5·2H_2O$ (LTH) with layered structure was used as a new intermediate phase for synthesis of LTO.[3.26] Conversion of LTH to LTO can conveniently take place at as low temperature as 350 °C[3.43] hence it can provide an advantageous route to synthesis of nanostructured LTO. To the best of our knowledge, LTH has been only prepared successfully previously by hydrothermal reaction using amorphous hydrous TiO_2 pre-prepared by hydrolyzing organic titanium precursors such as TTIP and tetrabutyl titanate (TBT). [3.23-26,30,37,38,44] According to the previous studies,[3.23,26,30] the electrochemical performance of the final nanostructured LTO product is highly dependent on the purity and crystallinity of LTH hence its annealing is very important.

The present study reports for the first time a low temperature (< 100 ºC) aqueous process employing inorganic precursors ($TiCl_4$ and LiOH) for the synthesis of nanosheet-structured LTH as intermediate phase that is transformed by annealing at 400 or 600 ºC into nanosheet or nanoparticle –structured LTO. The newly synthesized LTO material is extensively characterized in terms of structure and electrochemical response showing great promise as low cost scalable solution to high-performance LIB anode fabrication.

3.3.Experimental

Synthesis

A preliminary report on the synthesis method is published elsewhere.[3.45] Basically the synthesis of LTO involved first the preparation of the intermediate LTH phase followed after by the transformation of the latter to LTO via annealing. For the preparation of LTH a hydrous precipitate was caused to form first by reaction of 180 mL of 1.33 M lithium hydroxide aqueous solution (98.0% $LiOH{\cdot}H_2O$, Sigma-Aldrich, USA) with 20 mL of 2 M aqueous titanium tetrachloride (99.0% $TiCl_4$, Sigma-Aldrich, USA) solution. The $TiCl_4$ solution was added drop-wise at a rate of 1 $mL{\cdot}min^{-1}$ into ice-cold LiOH solution under vigorous stirring. The solution temperature was controlled below 10 ºC to avoid premature hydrolysis of $TiCl_4$ during the precipitation reaction. The terminal pH was in the range of 11.5-12 at which stirring continued for 2 hours. The as-prepared white precipitate was collected through a centrifuge and washed for 3 times with deionized water before it was transferred into a closed vessel for aging at 80 ºC (without stirring) for 36 hours. Aging was necessary to induce crystallization of the intermediate LTH phase. After that, the crystalline LTH precursor material was oven dried at 80 ºC before subjected to annealing for 2 hours in ambient atmosphere at 400 and 600 ºC.

Characterization

The LTH and LTO materials were examined using the Hitachi S-4700 field-emission scanning electron microscope (FE-SEM) at an accelerating voltage of 10 kV and the Hitachi SU-8000 at 30 kV. The transmission electron microscopic images, the selected area electron diffraction (SAED) patterns, and high-resolution transmission electron microscopy (HR-TEM) images were taken using the Philips CM200 TEM microscope at an accelerating voltage of 200 kV. The phase composition of the samples was determined by X-ray diffraction (XRD) employing the Rigaku Rotaflex D-Max diffractometer equipped with a rotating anode, a copper target ($\lambda(\mathrm{CuK}\alpha_1) = 0.15406$ nm), a monochromator composed of a graphite crystal, and a scintillator detector. The diffractometer used 40 kV and 20 mA. The Brunauer–Emmett–Teller (BET) surface area was determined using the Micromeritics TriStar 3000 apparatus under nitrogen-controlled atmosphere. Each sample weighed approximately 200 mg and had been degassed for 4 hrs at 80 °C prior to nitrogen physisorption.

Electrochemistry

The electrochemical performance, including rate capability and charge/discharge capacity, of nanostructured LTO was evaluated at room temperature with coin cells in which a metallic lithium foil was used as the counter electrode. The employed organic electrolyte was a mixture of 1 M $LiPF_6$ with ethylene carbonate (EC), diethyl carbonate (DEC) in a ratio 3 : 7 (volume ratio) with 2 wt% by total weight of vinylene carbonate (VC) as additive. The composite electrodes were made of the active material, synthesized nanostructured LTO, (89 wt%), conductive carbon black (6 wt%) and polyvinylidene fluoride (PVDF) binder (5 wt%) homogeneously dispersed in N-methyl pyrrolidinone (NMP), coated on Al-foil. The loading of prepared electrodes was 4.73 ± 0.04 mg·cm^{-2} for the 400 ºC annealed LTO and 4.12 ± 0.02 mg·cm^{-2} for the 600 ºC annealed LTO. Then, these electrodes were dried at 110 ºC in vacuum for 12 hours. The coin cells were assembled in an argon-filled glove box (M. Braun Co., $[O_2] < 1$ ppm, $[H_2O] < 1$ ppm). In the present work, charge represents the lithiation and discharge the delithiation of the electrode since LTO is used as anode material in LIBs. A constant-current protocol (C/24) was used for formation cycles in the potential range from 2.5 V to the cut-off voltage of 1.0 V and 1.2 V vs. Li/Li$^+$, respectively.

3.4.Results and Discussion

3.4.1. Synthesis and Characterization

Preparation of intermediate LTH phase: The intermediate LTH phase was produced via a two-step chemical process sequence comprising in step 1 reaction of LiOH solution with $TiCl_4$ solution at T< 10 °C and pH 11.5-12 to produce a hydrous precipitate; and subsequent aging at 80 °C in step 2 of the hydrous precipitate to produce crystalline LTH (white powder), Figure 3.1 shows the XRD patterns of the dried precipitate before and after aging at 80 ºC. As it can be deduced the as-prepared precipitate right after reaction of LiOH and $TiCl_4$ was an amorphous compound. Crystalline orthorhombic layered-structured LTH (JCPDS card No. 47-0123), was obtained after aging treatment at 80 ºC for 36 hours, as shown in Figure 3.1 (b). The lattice parameters of the 80 ºC synthesized LTH, given in Table 1, are smaller than the theoretical values which are 1.666, 0.3797 and 0.3007 nm in *a*, *b* and *c* axis, respectively. The smaller lattice parameters apparently reflect the nanocrystalline character of LTH as confirmed with SEM and TEM data (Figure 3.2). In Figure 3.2 (a), the SEM image indicates that the intermediate phase LTH had a nanoflower structure consisting of 2D nanosheets. Figure 3.2 (b) is the TEM image of aggregated LTH nanosheets, whose individual sheet size was in the range of 60 to 200 nm and approximately 10 nm in thickness. As deduced from the continuous SAED circle patterns (Figure 3.2 (c)), the aggregated LTH nanosheets consisted of randomly oriented crystallites whose crystallinity was not fully developed (nanocrystalline), as also shown from the XRD analysis (Figure 3.1). Finally, the HR-TEM image of an individual nanosheet shown in Figure 3.2 (d) revealed that the lattice spacing was about 0.85 nm, corresponding to the lattice spacing of the (200) plane for layered-structured orthorhombic LTH.[3.46]

Preparation of LTO by annealing: Figure 3.3 shows the XRD diffraction patterns of LTO (JCPDS Card No. 49-0207) after annealing at 400 and 600 ºC for 2 hours. It is clear that the LTO degree of crystallinity improved with the elevation of annealing temperature from 400 to 600 ºC. The increased crystallinity can be deduced not only from the clear resolution of (533) and (622) peaks around 75º after annealing at 600 ºC, but also from the lattice parameters of LTO that increased

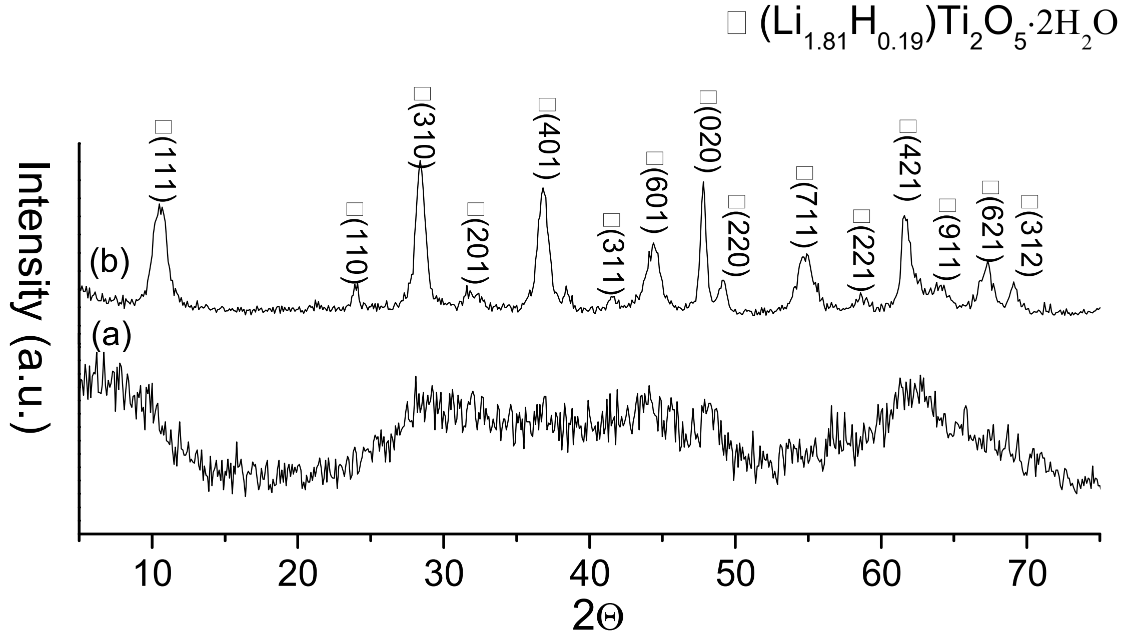

Figure 3.1. XRD diffraction patterns of as-prepared precipitate (a) and 80 ºC aged intermediate LTH (b).

from 0.8354 nm to 0.8355 nm, when the annealing temperature was raised from 400 ºC to 600 ºC (Table 1), getting closer to the theoretical value of 0.3557 nm.

The annealing treatment had influence not only on the crystal structure, but also the morphology of the products. Figure 3.4 (a) is the SEM image of 400 ºC annealed LTO; it can be seen the nanoflower morphology was retained with some growth of LTO nanosheets to have occurred yielding about 10 nm thick pedals (see TEM image in Figure 3.4 (b)). Figure 3.4 (c) is the SAED pattern, which shows clear polycrystalline features despite the relatively low annealing temperature (400 ºC) employed to obtain spinel LTO. An HR-TEM image in Figure 3.4 (d) indicates the lattice distance was approximately 0.48 nm, which is in accordance with the (111) spacing of spinel LTO.

Annealing was also attempted at 600 ºC and the resultant LTO microstructures are presented in Figure 3.5. As seen in Figure 3.5 (a), the morphology of LTO changed from nanoflower at 400 ºC (Figure 3.4 (a)) to nanoparticle at 600 ºC (Figure 3.5 (a)). This change in morphology may reflect a shift from nanodomain crystal order to microdomain longer-range order as a result of diffusion and rearrangement of atoms with temperature elevation. Thus, upon raising the annealing temperature from 400 to 600 °C the individual LTO crystallite size was seen to increase to around 60-100 nm, as shown in Figure 3.5 (b), while its specific surface area decreased from 102 $m^2 \cdot g^{-1}$ to 28 $m^2 \cdot g^{-1}$. The SAED pattern of an individual 600 ºC annealed LTO nanoparticle, Figure 3.5 (c), corresponded to a single crystal dot pattern of [001] zone axis, which qualitatively shows the difference in crystallinity between the 400 ºC and the 600 ºC annealed LTO nanomaterials. The HR-TEM image of an individual LTO particle given in Figure 3.5 (d) corresponds to (111) plane, which has lattice spacing 0.48 nm.

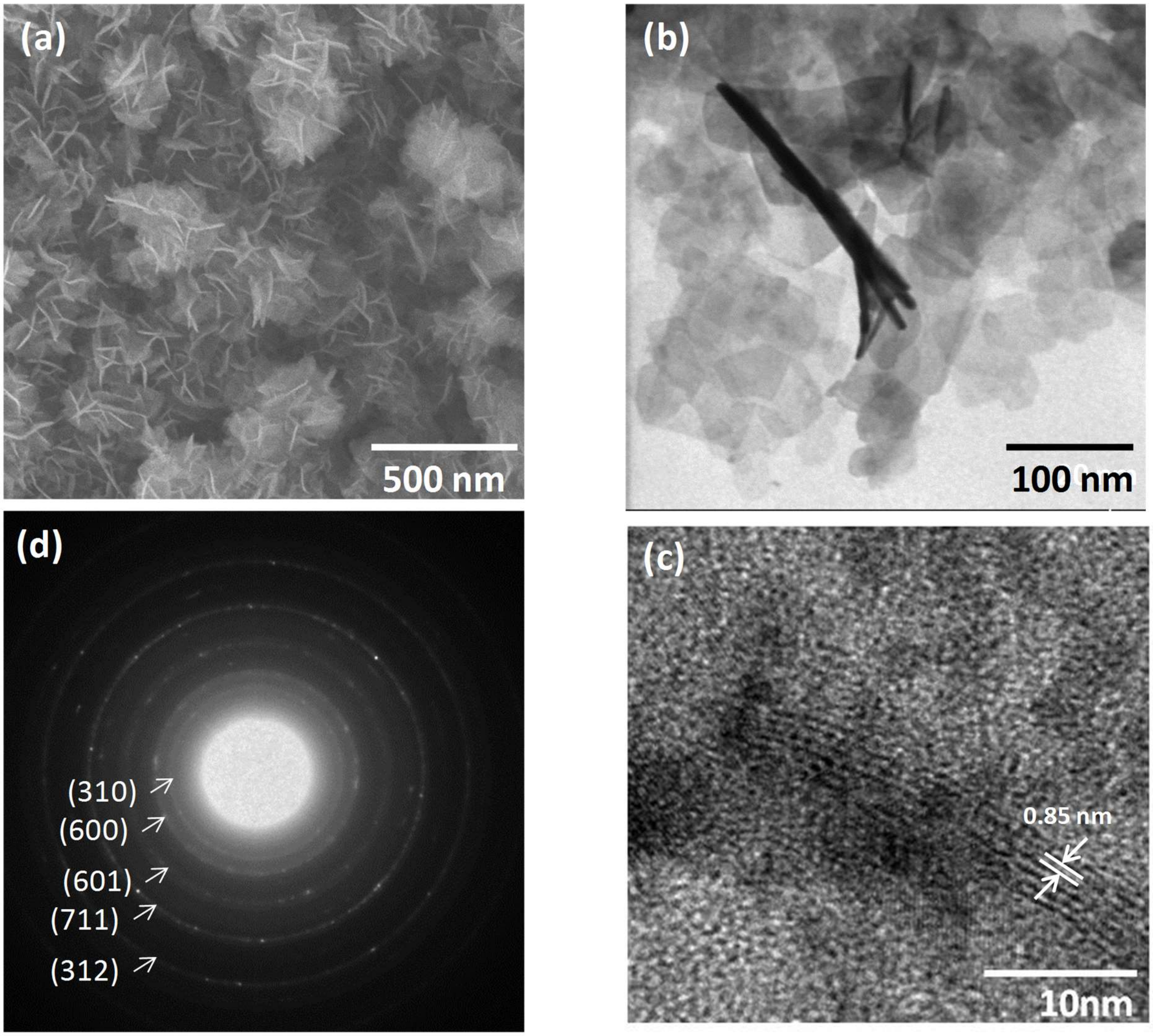

Figure 3.2. Nanostructure images/patterns of LTH (80 ºC aged) intermediate phase: (a) SEM, (b) TEM, (c) SAED and (d) HR-TEM.

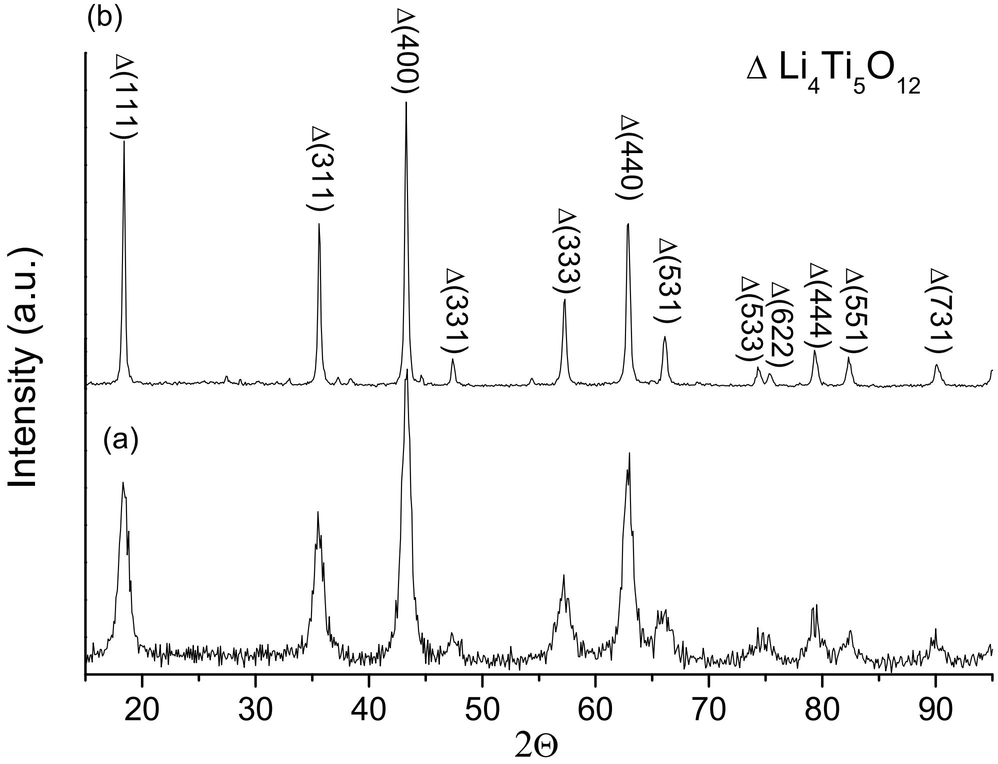

Figure 3.3. XRD patterns of LTO produced after annealing for two hours at: (a) 400 and (b) 600 °C.

Table 3.1. Crystal lattice parameters of LTH intermediate phase and LTO obtained after annealing at 400 and 600 °C

Phase	Annealing temperature (°C)	Crystal system	Lattice parameter *a* (nm)	*b* (nm)	*c* (nm)
$(Li_{1.81}H_{0.19})Ti_2O_5 \cdot 2H_2O$	--	Orthorhombic	1.6330(7)	0.3701(7)	0.2922(4)
$Li_4Ti_5O_{12}$	400	Cubic	0.8354(4)		
	600		0.8355(6)		

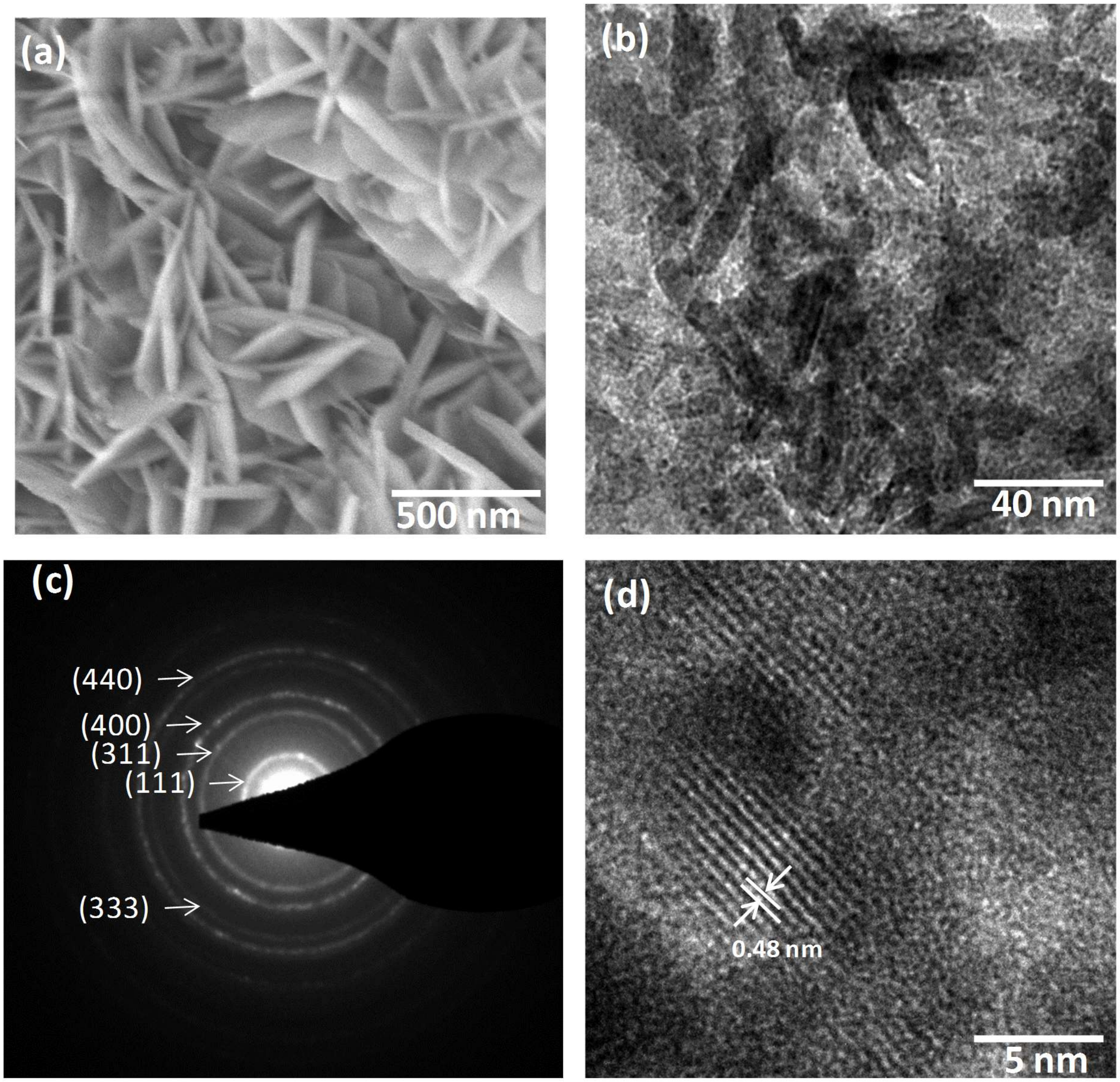

Figure 3.4. Nanostructure images/patterns of LTO (400 °C annealed) phase: (a) SEM, (b) TEM, (c) SAED and (d) HR-TEM.

3.4.2. Electrochemical response

It has been demonstrated previously that crystallinity has direct influence on the electrochemical performance of LTO.[3.27] This was investigated further in the present work by evaluating the impact of crystallinity but also nanostructure on electrochemical anode properties of the LTO obtained after 400 and 600 °C annealing of aqueous-synthesized LTH. To this end coin cells with Li foil as counter electrode were assembled and tested with the two nanostructured LTO materials. Figure 3.6 (a) shows the galvanostatic charge/discharge voltage profiles at C/24 with cut-off at 1.0 V or 1.2 V vs. Li/Li$^+$ and Table 2 summarizes the initial charge/discharge capacity data for the two LTO materials.

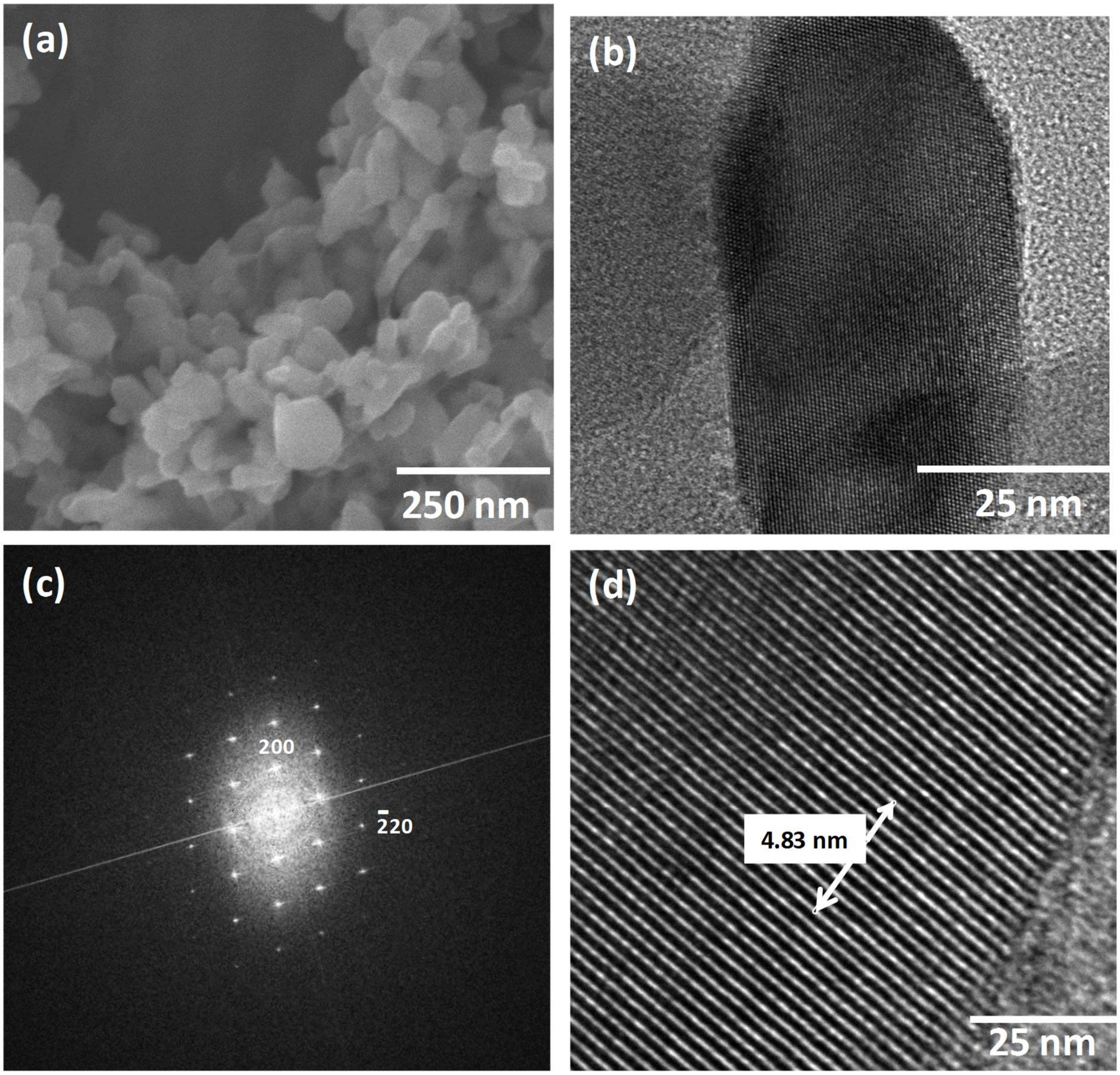

Figure 3.5. Nanostructure images/patterns of LTO (600 °C annealed) phase: (a) SEM, (b) TEM, (c) SAED of [001] zone axis and (d) HR-TEM.

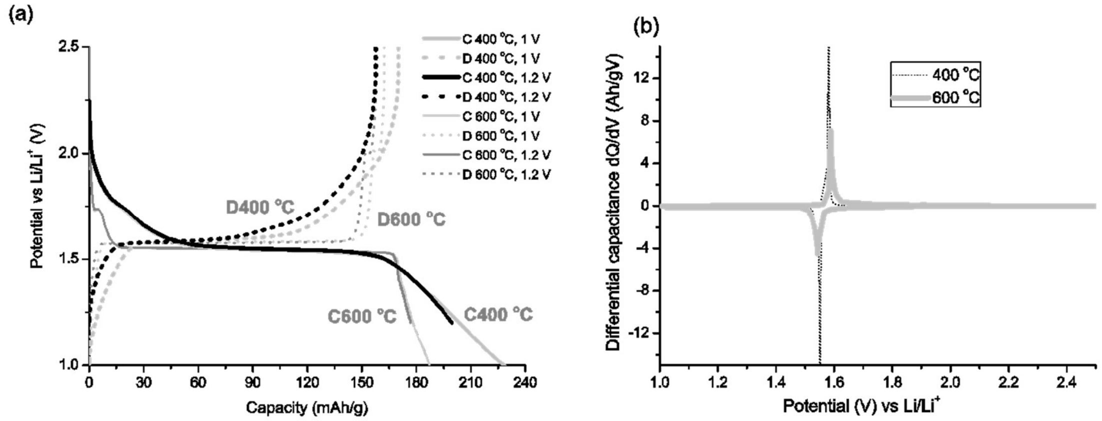

Figure 3.6. (a) Galvanostatic discharge/charge voltage profiles and (b) the corresponding differential capacitance of the 400 and 600 °C annealed LTO at C/24 in the potential range from 2.5 V to 1.0 or 1.2 V vs. Li/Li$^+$, respectively.

Table 3.2. Initial charge/discharge capacity of the two annealed LTO materials in C/24 formation cycle

Annealing T (°C)	Cut-off Voltage vs. Li/Li$^+$ (V)	Capacity (mAh/g)		Efficiency (%)
		Charge	Discharge	
400	1	228.3	170.3	74.6
	1.2	199.6	187.2	93.8
600	1	187.3	162.4	86.7
	1.2	176.9	158.0	89.3

For the 600 °C annealed LTO, a typical constant voltage profile for first-order phase transition (co-existence of spinel LTO and rock-salt $Li_7Ti_5O_{12}$)[3.47] with a plateau at 1.55 V vs. Li/Li$^+$ was exhibited. The charge capacity was 176.9 mAh·g^{-1} with cut-off at 1.2 V vs. Li/Li$^+$. This is in line with the theoretical capacity of 175 mAh·g^{-1}. However, when the operational voltage was extended to 1.0 V vs. Li/Li$^+$, the charge capacity increased to 187.3 mAh·g^{-1}. According to Figure 3.6 (b) there was only one pair of redox couple peaks, precisely corresponding to intercalation of

LTO at 1.55 V, meaning that the excess lithium ions were intercalated into LTO and no SEI film formed during first charge which is usually formed in the range 0.2-0.8 V vs. Li/Li$^+$.[3.11,48] It has been reported that in nanosized LTO, the intercalation of lithium ions into empty tetrahedral *8a* sites is possible,[3.13,20] especially in the near surface region of LTO particles that can explain the observed excess here as well. The degree of excess intercalation would increase with increasing particle surface area. On the contrary, the discharge capacity (delithiation of LTO) was only about 160 mAh·g^{-1} for both cut-off voltages of 1.0 and 1.2 V vs. Li/Li$^+$, i.e. an irreversible capacity loss was observed. This loss may be attributed to the lithium ions occupying *8a* sites near the surface that as reported lead to short *8a-16c* Li distances that are energetically unfavorable.[3.13] In addition the occupation of *8a* sites implies fewer empty vacancies available leading to a reduction of the diffusion coefficient as observed by Kavan et al.[3.49]

As for the 400 °C annealed LTO nanosheets, curved rather than flat voltage profiles were obtained with first charge capacity of 228 mAh·g^{-1} for cut-off at 1 V vs. Li/Li$^+$ (this corresponds to $Li_{7.9}Ti_5O_{12}$) and 199.6 mAh·g^{-1} for 1.2 V cut-off (corresponding to $Li_{7.4}Ti_5O_{12}$). Such curved voltage profile and high capacity have been reported for nanoparticles of 30 nm or less in size tested over a broader operational voltage window.[3.13,18,50] Firstly, the curved voltage profile may be attributed to near the surface chemical potential variation, a feature of nanosized intercalation compounds that has attracted recently a lot of attention.[3.17,19,51,52] During intercalation, low chemical potential surface sites would be occupied first leading to a higher voltage above the voltage plateau. After that lithium ions diffuse into the bulk, which is characterized with the chemical potential corresponding to the voltage plateau. Eventually the surface sites with high chemical potential would be occupied at a lower voltage than the plateau. Secondly, the higher initial charging capacity exhibited by the LTO nanosheets can be explained on the basis of increasing *8a* occupancy (in addition to fully occupied *16c* sites) with increasing surface area (102 m^2·g^{-1} vs. 28 m^2·g^{-1}).[3.13] However, this excess charge capacity was associated with significant irreversible capacity loss as seen in Table 2. In the previous paragraph reference was made to other works that have attributed such loss to a reduction of the diffusion coefficient[3.49] as a result of fewer empty vacancies available due to the simultaneous occupation of *16c and 8a* sites near nanoscale surfaces.[3.13] Furthermore this type of near the surface *8a* site excess lithium occupancy (beyond the stoichiometric rock-salt $Li_7Ti_5O_{12}$ composition) has been proposed to induce localized structural reconstruction at the surface leading to the observed partial irreversible trapping of lithium.[3.17,20]

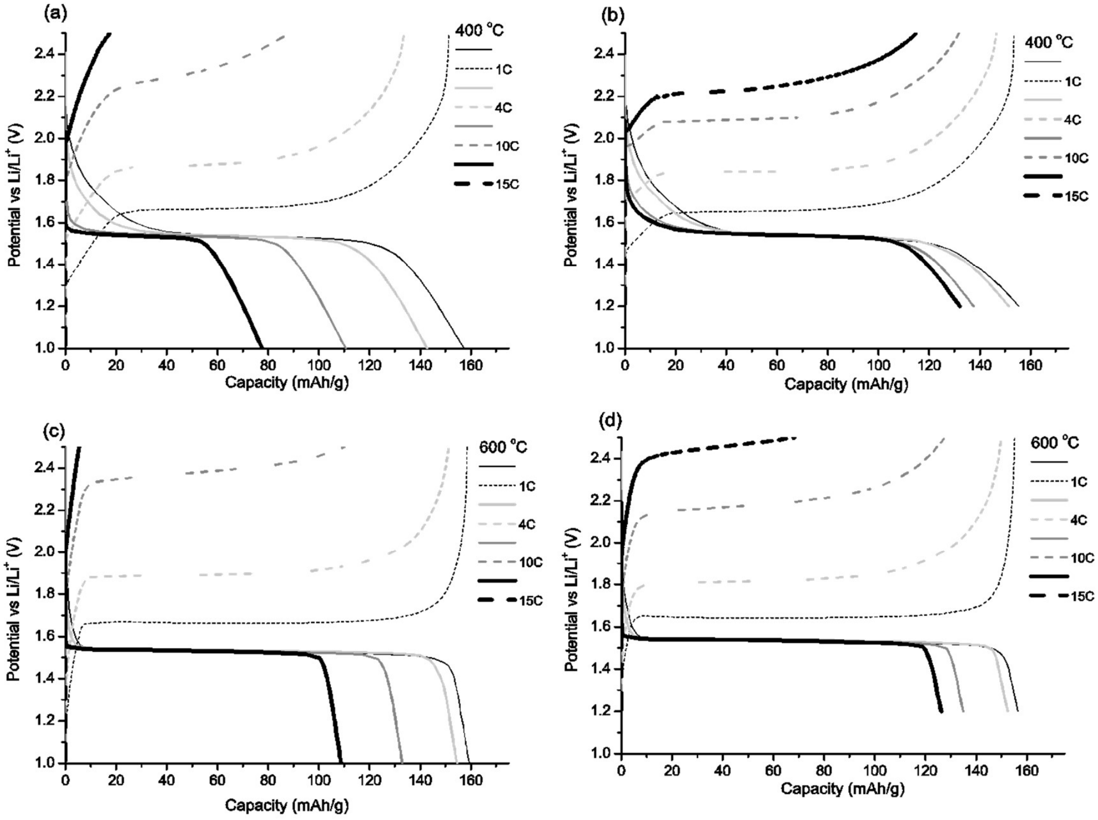

Figure 3.7. Capacity vs. potential profiles of (a,b) 400 °C annealed LTO nanosheets and (c,d) 600 °C annealed LTO nanoparticles under discharge at various rates and constant charge at 0.25C. The operational voltage was in the range of (a,c) 2.5- 1.0 V and (b,d) 2.5-1.2 V vs. Li/Li$^+$.

Figure 3.7 shows the discharge rate performance of 400 and 600 °C annealed LTO, in which the charge rate was kept constant at 0.25C. The discharge rate was varied from 1C (0.74 mA/cm^2) to 15C over the operating voltage range from 2.5 to 1.0 or 1.2 V vs. Li/Li$^+$. Table 3 summarizes the initial capacity data at different discharge rates. First it can be noted that both materials exhibited higher rate capability when the cut-off voltage was 1.2 V rather than 1.0 V. In other words, the extra capacity afforded by the lower cut-off voltage (1.0 V) was lost upon increasing the discharge rate. This loss in capacity was more pronounced with the LTO nanosheet material (400 °C). At cut-off voltage 1.2 V both LTO nanomaterials exhibited essentially the same rate capability up to 10C rate. Thus, at 1C rate the discharge capacity was 153.5 vs. 155.2 mAh·g$^-$

^{1}, while at 10C rate the corresponding values for the LTO nanosheets and nanoparticles were 131.9 vs. 127.7 mAh·g^{-1} respectively.

Table 3.3. Rate performance of 400 and 600 °C annealed LTO materials

Annealing	Cut-off Voltage	Charge/discharge capacity (mAh/g)			
T (°C)	vs. Li/Li^{+} (V)	0.25Ch/1D	0.25Ch/4D	0.25Ch/10D	0.25Ch/15D
400	1	157.5/151.3	143.0/133.7	110.7/88.1	77.8/17.6
	1.2	155.4/153.5	151.4/146.6	137.5/131.9	132.2/115.0
600	1	159.6/158.5	154.6/151.3	133.0/110.1	108.9/5.4
	1.2	156.6/155.2	152.5/150.0	134.9/127.7	126.3/68.4

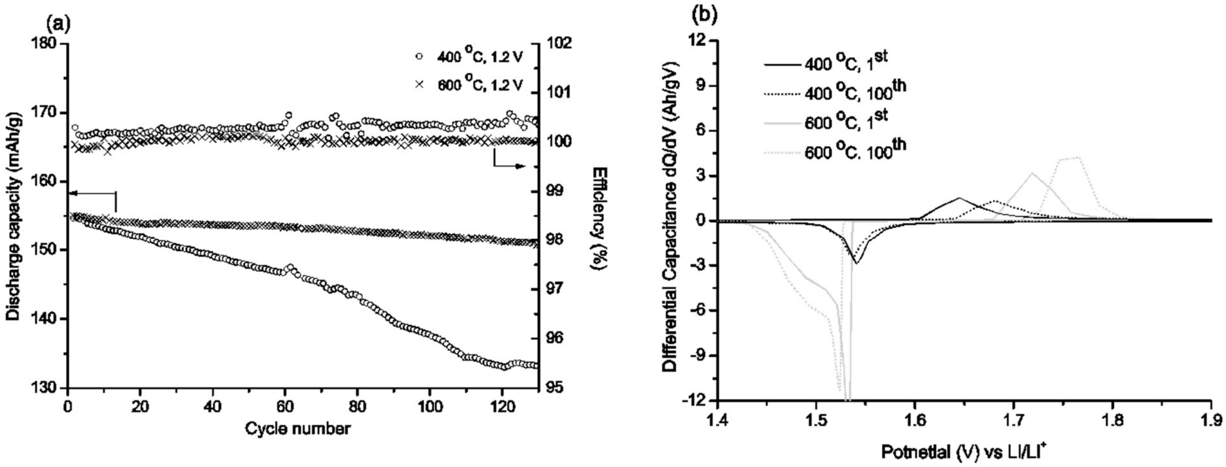

Figure 3.8. (a) Cycling galvanostatic 0.25C charge / 1C discharge performance of 400 °C annealed LTO nanosheets and 600 °C annealed LTO nanoparticles over the voltage range from 2.5 to1.2 V vs. Li/Li^{+}. Also shown (b) is the differential capacitance corresponding to the first and 100th cycle of the nanosheet LTO operating in the voltage range 2.5-1.2 V vs. Li/Li^{+}.

These values compare favorably with other hydrothermally prepared nanostructured LTO materials.$^{3.23-26,38}$ For example, according to Liu et al., the 1C discharge capacity of nanoflower-like and nanoparticle LTO prepared by microwave-assisted hydrothermal synthesis and annealed at 550 ºC for 6 hours exhibited initial discharge capacities of 176.7 and 109.8 mAh g^{-1} respectively (26) vs. 153.5 (nanosheets) and 155.2 (nanoparticles) mAh·g^{-1} of the present work. At the same time hydrothermally prepared LTO annealed at 600 ºC, as reported by Shen et al., delivered 150 mAh·g^{-1} at 1C but only 81.2 mAh·g^{-1} at 10C, the latter improving to 140 mAh·g^{-1} after the same LTO was tested as graphene nanocomposite.[3.53]

By comparison at 10C both nanostructured LTO materials synthesized in the present work delivered ~ 130 mAh·g^{-1} without making use of graphene, a truly remarkable result. However, at higher rate (15C) the nanosheet LTO material performed better than the nanoparticle LTO material (115.0 vs. 68.4 mAh·g^{-1}) reflecting the shorter diffusion path characterizing the nanosheets. The cyclability of the two nanostructured LTO materials was evaluated by 0.25C charge and 1C discharge over 130 cycles, and the results are given in Figure 3.8. As it can be seen the 600 ºC annealed LTO material (nanoparticles) yielded better cycle performance (only 3% capacity loss after 130 1C cycles) than the 400 ºC annealed LTO nanosheets (15% capacity loss after 130 1C cycles), apparently reflecting their higher degree of crystallinity in agreement with previous reports.[3.27] In the meantime, both materials exhibited nearly 100% coulombic efficiencies after the first few cycles. Furthermore, for the nanosheet LTO material, the reversible capacity seems to stabilize after 120 or so cycles at ~135 mAh g^{-1}. Based on analysis of the differential capacitance between first and 100th cycle (see for example Figure 3.8(b)) the potential difference between cathodic peaks was seen to increase by about 30 mV suggesting the observed capacity loss may be associated with either the electrode polarization-induced structural changes, or the side reaction on the surface of Li counter electrode. Future detailed *in-situ* material characterization studies are hoped to shed light in the underlying mechanism behind the capacity loss exhibited by the nanosheet-structured LTO.

3.5.Conclusions

In conclusion, a facile low-temperature process to synthesize nanostructured and pure LTO ($Li_4Ti_5O_{12}$) material as candidate for high-performing LIB anodes was successfully developed and tested. The nanostructure of LTO was controlled via the aqueous preparation of the intermediate LTH ($Li_{1.81}H_{0.19}Ti_2O_5·2H_2O$) phase and the subsequent transformation of the latter to LTO via annealing at 400 and 600 ºC for 2 hours, respectively. The intermediate LTH phase was prepared via a two-step chemical process sequence comprising in step 1 reaction of LiOH solution with $TiCl_4$ at T< 10 °C and pH 11.5-12 to produce a hydrous precipitate that was aged in step 2 at 80 °C to promote LTH crystallization. The resultant nano-LTO material was in the form of 10 nm thick nanosheets with 102 $m^2 \cdot g^{-1}$ surface area after annealing at 400 ºC; annealing at 600 ºC resulted in nanoparticle LTO material with surface area reduced to 28 $m^2 \cdot g^{-1}$; each of the two nanostructured LTO materials exhibiting unique electrochemical performance properties. Thus, the LTO nanosheets (obtained after annealing at 400 ºC) yielded a curved voltage profile typical of nanosized intercalation compounds with first discharge capacity equal to 228 $mAh \cdot g^{-1}$ for 1.0 V cut-off at C/24 rate; on the contrary, the LTO nanoparticles (obtained after annealing at 600 ºC) exhibited a voltage plateau at 1.55 V with first discharge capacity equal to 187.3 $mAh \cdot g^{-1}$, well above the theoretical value of 175 $mAh \cdot g^{-1}$. Both LTO nanomaterials exhibited high rate capability. At cut-off voltage 1.2 V the two LTO materials exhibited essentially the same rate capability up to 10 C rate. Thus, at 1 C rate the discharge capacity was 153.5 vs. 155.2 $mAh \cdot g^{-1}$, while at 10 C rate the corresponding values for the LTO nanosheets and nanoparticles were 131.9 vs. 127.7 $mAh \cdot g^{-1}$ respectively. But nanosheets exhibited better rate capability at 15C because of their shorter diffusion path than nanoparticles. Finally, the 600 ºC annealed LTO nanoparticles yielded excellent cyclability retaining 97 % capacity after 130 cycles at 1C (~150 $mAh \cdot g^{-1}$), while the reversible capacity of the nanosheet LTO material stabilized after 120 cycles at ~135 $mAh \cdot g^{-1}$. Given the simpler method of synthesis and electrode fabrication employed in the present work the produced nanostructured LTO materials may offer a low cost and scalable solution as high-performance anodes in LIB automotive applications.

3.6.Acknowledgements

This work is supported by Natural Sciences and Engineering Research Council of Canada (NSERC). The authors would like to thank Mr. David Liu of the McGill Facility for Electron Microscopy Research and Ms. Julie Trottier of Institut de recherche d'Hydro-Québec (IREQ) for their help with the TEM and electrochemical characterization work respectively.

3.7.References

(**3.**1) Wagner, F. T.; Lakshmanan, B.; Mathias, M. F. Electrochemistry and the Future of the Automobile. *J. Phys. Chem. Lett.* **2010,** *1* (14), 2204.

(**3.**2) Winter, M.; Besenhard, J. O.; Spahr, M. E.; Novák, P. Insertion Electrode Materials for Rechargeable Lithium Batteries. *Adv. Mater.* **1998,** *10* (10), 725.

(**3.**3) Tarascon, J. M.; Armand, M. Issues and challenges facing rechargeable lithium batteries. *Nature* **2001,** *414* (6861), 359.

(**3.**4) Armand, M.; Tarascon, J. M. Building better batteries. *Nature* **2008,** *451* (7179), 652.

(**3.**5) Etacheri, V.; Marom, R.; Elazari, R.; Salitra, G.; Aurbach, D. Challenges in the development of advanced Li-ion batteries: a review. *Energy. Environ. Sci.* **2011,** *4* (9), 3243.

(**3.**6) Yao, X. L.; Xie, S.; Chen, C. H.; Wang, Q. S.; Sun, J. H.; Li, Y. L.; Lu, S. X. Comparisons of graphite and spinel $Li_{1.33}Ti_{1.67}O_4$ as anode materials for rechargeable lithium-ion batteries. *Electrochim. Acta* **2005,** *50* (20), 4076.

(**3.**7) Zaghib, K.; Armand, M.; Gauthier, M. Electrochemistry of Anodes in Solid-State Li-Ion Polymer Batteries. *J. Electrochem. Soc.* **1998,** *145* (9), 3135.

(**3.**8) Ohzuku, T.; Ueda, A.; Yamamoto, N. Zero-Strain Insertion Material of $LiLi_{1/3}Ti_{5/3}O_4$ for Rechargeable Lithium Cells. *J. Electrochem. Soc.* **1995,** *142* (5), 1431.

(**3.**9) Colbow, K. M.; Dahn, J. R.; Haering, R. R. Structure and electrochemistry of the spinel oxides $LiTi_2O_4$ and $Li_{4/3}Ti_{5/3}O_4$. *J. Power Sources* **1989,** *26* (3–4), 397.

(**3.**10) Scharner, S.; Weppner, W.; Schmid-Beurmann, P. Evidence of Two-Phase Formation upon Lithium Insertion into the $Li_{1.33}Ti_{1.67}O_4$ Spinel. *J. Electrochem. Soc.* **1999,** *146* (3), 857.

(**3.**11) Andersson, A. M.; Edström, K. Chemical Composition and Morphology of the Elevated Temperature SEI on Graphite. *J. Electrochem. Soc.* **2001,** *148* (10), A1100.

(**3.**12) Wagemaker, M.; van Eck, E. R.; Kentgens, A. P.; Mulder, F. M. Li-ion diffusion in the equilibrium nanomorphology of spinel $Li_{4+x}Ti_5O_{12}$. *J. Phys. Chem. B* **2009,** *113* (1), 224.

(**3.**13) Borghols, W. J. H.; Wagemaker, M.; Lafont, U.; Kelder, E. M.; Mulder, F. M. Size Effects in the $Li_{4+x}Ti_5O_{12}$ Spinel. *J. Am. Chem. Soc.* **2009,** *131* (49), 17786.

(**3.**14) Lee, S. C.; Lee, S. M.; Lee, J. W.; Lee, J. B.; Lee, S. M.; Han, S. S.; Lee, H. C.; Kim, H. J. Spinel $Li_4Ti_5O_{12}$ Nanotubes for Energy Storage Materials. *J. Phys. Chem. C* **2009,** *113* (42), 18420.

(**3.**15) Wang, Y.; Liu, H.; Wang, K.; Eiji, H.; Wang, Y.; Zhou, H. Synthesis and electrochemical performance of nano-sized $Li_4Ti_5O_{12}$ with double surface modification of Ti(III) and carbon. *J. Mater. Chem.* **2009,** *19* (37), 6789.

(**3.**16) Nugroho, A.; Kim, S. J.; Chung, K. Y.; Cho, B.-W.; Lee, Y.-W.; Kim, J. Facile synthesis of nanosized $Li_4Ti_5O_{12}$ in supercritical water. *Electrochem. Commun.* **2011,** *13* (6), 650.

(**3.**17) Ganapathy, S.; Wagemaker, M. Nanosize Storage Properties in Spinel $Li_4Ti_5O_{12}$ Explained by Anisotropic Surface Lithium Insertion. *Acs Nano* **2012,** *6* (10), 8702.

(**3.**18) Shu, J. Electrochemical behavior and stability of $Li_4Ti_5O_{12}$ in a broad voltage window. *J Solid State Electr* **2009,** *13* (10), 1535.

(**3.**19) Wagemaker, M.; Mulder, F. M. Properties and Promises of Nanosized Insertion Materials for Li-Ion Batteries. *Acc Chem Res* **2012**, DOI:10.1021/ar2001793 10.1021/ar2001793.

(**3.**20) Hirayama, M.; Kim, K.; Toujigamori, T.; Cho, W.; Kanno, R. Epitaxial growth and electrochemical properties of $Li_4Ti_5O_{12}$ thin-film lithium battery anodes. *Dalton Trans.* **2011,** *40* (12), 2882.

(**3.**21) Kim, J.; Cho, J. Spinel $Li_4Ti_5O_{12}$ Nanowires for High-Rate Li-Ion Intercalation Electrode. *Electrochem. Solid. St.* **2007,** *10* (3), A81.

(**3.**22) Tang, Y.; Yang, L.; Fang, S.; Qiu, Z. $Li_4Ti_5O_{12}$ hollow microspheres assembled by nanosheets as an anode material for high-rate lithium ion batteries. *Electrochim. Acta* **2009,** *54* (26), 6244.

(**3.**23) Li, N.; Mei, T.; Zhu, Y.; Wang, L.; Liang, J.; Zhang, X.; Qian, Y.; Tang, K. Hydrothermal synthesis of layered $Li_{1.81}H_{0.19}Ti_2O_5.xH_2O$ nanosheets and their transformation to single-crystalline $Li_4Ti_5O_{12}$ nanosheets as the anode materials for Li-ion batteries. *CrystEngComm* **2012,** *14* (20), 6435.

(**3.**24) Chen, J.; Yang, L.; Fang, S.; Tang, Y. Synthesis of sawtooth-like $Li_4Ti_5O_{12}$ nanosheets as anode materials for Li-ion batteries. *Electrochim. Acta* **2010,** *55* (22), 6596.

(**3.**25) Li, G.; Xia, J.; Jiao, J.; Chen, L.; Shen, P. Low-temperature Synthesis of Peony-like Spinel $Li_4Ti_5O_{12}$ as a High-performance Anode Material for Lithium Ion Batteries. *Chinese Journal of Chemistry* **2011,** *29* (9), 1824.

(**3.**26) Liu, J.; Li, X.; Yang, J.; Geng, D.; Li, Y.; Wang, D.; Li, R.; Sun, X.; Cai, M.; Verbrugge, M. W. Microwave-assisted hydrothermal synthesis of nanostructured spinel $Li_4Ti_5O_{12}$ as anode materials for lithium ion batteries. *Electrochim. Acta* **2012,** *63* (0), 100.

(**3.**27) Kim, D. H.; Ahn, Y. S.; Kim, J. Polyol-mediated synthesis of $Li_4Ti_5O_{12}$ nanoparticle and its electrochemical properties. *Electrochem. Commun.* **2005,** *7* (12), 1340.

(**3.**28) Guerfi, A.; Sévigny, S.; Lagacé, M.; Hovington, P.; Kinoshita, K.; Zaghib, K. Nano-particle $Li_4Ti_5O_{12}$ spinel as electrode for electrochemical generators. *J. Power Sources* **2003,** *119-121* (0), 88.

(**3.**29) Matsui, E.; Abe, Y.; Senna, M.; Guerfi, A.; Zaghib, K. Solid-State Synthesis of 70 nm $Li_4Ti_5O_{12}$ Particles by Mechanically Activating Intermediates with Amino Acids. *Journal of the American Ceramic Society* **2008,** *91* (5), 1522.

(**3.**30) Laumann, A.; Bremholm, M.; Hald, P.; Holzapfel, M.; Fehr, K. T.; Iversen, B. B. Rapid Green Continuous Flow Supercritical Synthesis of High Performance $Li_4Ti_5O_{12}$ Nanocrystals for Li Ion Battery Applications. *J. Electrochem. Soc.* **2012,** *159* (2), A166.

(**3.**31) Lin, C.-Y.; Duh, J.-G. Porous $Li_4Ti_5O_{12}$ anode material synthesized by one-step solid state method for electrochemical properties enhancement. *J. Alloy. Compd.* **2011,** *509* (8), 3682.

(**3.**32) Guerfi, A.; Charest, P.; Kinoshita, K.; Perrier, M.; Zaghib, K. Nano electronically conductive titanium-spinel as lithium ion storage negative electrode. *J. Power Sources* **2004,** *126* (1-2), 163.

(**3.**33) Hao, Y.-J.; Lai, Q.-Y.; Lu, J.-Z.; Wang, H.-L.; Chen, Y.-D.; Ji, X.-Y. Synthesis and characterization of spinel $Li_4Ti_5O_{12}$ anode material by oxalic acid-assisted sol–gel method. *J. Power Sources* **2006,** *158* (2), 1358.

(**3.**34) Hao, Y.-j.; Lai, Q.-y.; Liu, D.-q.; Xu, Z.-u.; Ji, X.-y. Synthesis by citric acid sol–gel method and electrochemical properties of $Li_4Ti_5O_{12}$ anode material for lithium-ion battery. *Materials Chemistry and Physics* **2005,** *94* (2–3), 382.

(**3.**35) Khomane, R. B.; Prakash, A. S.; Ramesha, K.; Sathiya, M. CTAB-assisted sol–gel synthesis of $Li_4Ti_5O_{12}$ and its performance as anode material for Li-ion batteries. *Mater. Res. Bull.* **2011,** *46* (7), 1139.

(**3.**36) Hao, Y.; Lai, Q.; Xu, Z.; Liu, X.; Ji, X. Synthesis by TEA sol–gel method and electrochemical properties of $Li_4Ti_5O_{12}$ anode material for lithium-ion battery. *Solid State Ionics* **2005,** *176* (13-14), 1201.

(**3.**37) Lin, Y.-S.; Tsai, M.-C.; Duh, J.-G. Self-assembled synthesis of nanoflower-like $Li_4Ti_5O_{12}$ for ultrahigh rate lithium-ion batteries. *J. Power Sources* **2012,** *214* (0), 314.

(**3.**38) Wang, Y.-Q.; Gu, L.; Guo, Y.-G.; Li, H.; He, X.-Q.; Tsukimoto, S.; Ikuhara, Y.; Wan, L.-J. Rutile-TiO_2 Nanocoating for a High-Rate $Li_4Ti_5O_{12}$ Anode of a Lithium-Ion Battery. *J. Am. Chem. Soc.* **2012,** *134* (18), 7874.

(**3.**39) Laumann, A.; Boysen, H.; Bremholm, M.; Fehr, K. T.; Hoelzel, M.; Holzapfel, M. Lithium Migration at High Temperatures in $Li_4Ti_5O_{12}$ Studied by Neutron Diffraction. *Chem. Mater.* **2011,** *23* (11), 2753.

(**3.**40) Laumann, A.; Fehr, K. T.; Wachsmann, M.; Holzapfel, M.; Iversen, B. B. Metastable formation of low temperature cubic Li_2TiO_3 under hydrothermal conditions — Its stability and structural properties. *Solid State Ionics* **2010,** *181* (33-34), 1525.

(**3.**41) Mohammadi, M.; Fray, D. Low temperature nanostructured lithium titanates: controlling the phase composition, crystal structure and surface area. *Journal of Sol-Gel Science and Technology* **2010,** *55* (1), 19.

(**3.**42) Mergos, J. A.; Dervos, C. T. Structural and dielectric properties of Li_2O-doped TiO_2. *Materials Characterization* **2009,** *60* (8), 848.

(**3.**43) Sugita, M.; Tsuji, M.; Abe, M. Synthetic Inorganic Ion-Exchange Materials. LVIII. Hydrothermal Synthesis of a New Layered Lithium Titanate and Its Alkali Ion Exchange. *Bull. Chem. Soc. Jpn.* **1990,** *63* (7), 1978.

(**3.**44) Tang, Y. F.; Yang, L.; Qiu, Z.; Huang, J. S. Preparation and electrochemical lithium storage of flower-like spinel $Li_4Ti_5O_{12}$ consisting of nanosheets. *Electrochem. Commun.* **2008,** *10* (10), 1513.

(**3.**45) Chiu, H.-c.; Demopoulos, G. P. A Novel Green Approach to Synthesis of $Li_4Ti_5O_{12}$ Nanopartculate Anode material. *Meeting Abstracts* **2012,** *MA2012-02* (10), 993.

(**3.**46) Sugita, M. Synthetic inorganic ion-exchange materials. LVIII, Hydrothermal synthesis of a new layered lithium titanate and its alkali ion exchange. *Bull. Chem. Soc. Jpn.* **1990,** *63* (7), 1978.

(**3.**47) Aldon, L.; Kubiak, P.; Womes, M.; Jumas, J. C.; Olivier-Fourcade, J.; Tirado, J. L.; Corredor, J. I.; Pérez Vicente, C. Chemical and Electrochemical Li-Insertion into the $Li_4Ti_5O_{12}$ Spinel. *Chem. Mater.* **2004,** *16* (26), 5721.

(**3.**48) Zhang, S. S.; Jow, T. R.; Amine, K.; Henriksen, G. L. $LiPF_6$–EC–EMC electrolyte for Li-ion battery. *J. Power Sources* **2002,** *107* (1), 18.

(**3.**49) Kavan, L.; Procházka, J.; Spitler, T. M.; Kalbáč, M.; Zukalová, M.; Drezen, T.; Grätzel, M. Li Insertion into $Li_4Ti_5O_{12}$ (Spinel) : Charge Capability vs. Particle Size in Thin-Film Electrodes. *J. Electrochem. Soc.* **2003,** *150* (7), A1000.

(**3.**50) Ge, H.; Li, N.; Li, D.; Dai, C.; Wang, D. Electrochemical characteristics of spinel $Li_4Ti_5O_{12}$ discharged to 0.01&0 V. *Electrochem. Commun.* **2008,** *10* (5), 719.

(**3.**51) Van der Ven, A.; Wagemaker, M. Effect of surface energies and nano-particle size distribution on open circuit voltage of Li-electrodes. *Electrochem. Commun.* **2009,** *11* (4), 881.

(**3.**52) Wagemaker, M.; Mulder, F. M.; Van der Ven, A. The Role of Surface and Interface Energy on Phase Stability of Nanosized Insertion Compounds. *Adv. Mater.* **2009,** *21* (25-26), 2703.

(**3.**53) Shen, L.; Yuan, C.; Luo, H.; Zhang, X.; Yang, S.; Lu, X. In situ synthesis of high-loading $Li_4Ti_5O_{12}$-graphene hybrid nanostructures for high rate lithium ion batteries. *Nanoscale* **2011,** *3* (2), 572.

Chapter 4

Formation of Lithium Titanate Hydrate Nanosheets: Insight into a Two-Dimension Growth Mechanism by in Situ-Raman

As it was described in the previous chapter, LTO is prepared via the thermal conversion of the intermediate sheet-like crystals of LTH. The crystallinity of prepared LTH nanocrystals profoundly influences the characteristics, such as purity, particle size, morphology and even the electrochemical performance of nano-LTO. In this context, to allow for optimization of the LTO nanocrystal properties, it is highly desirable first to understand the LTH formation mechanism.

To this end, in situ-Raman was employed to elucidate the crystallization process of two-dimensional LTH nanocrystals. Crystallization proceeds via nucleation and subsequent two-dimensional anisotropic growth that is impeded by the growth of neighboring crystals. The crystallization mechanism was found to obey a modified version of the Johnson−Mehl−Avrami−Kolmogorov (JMAK) kinetic model. The Chapter has been previously published in: **Chiu HC**, Lu X, Elouatik S, Zaghib K, Demopoulos GP. *Formation of Lithium Titanate Hydrate Nanosheets: Insight into a Two-Dimension Growth Mechanism by in Situ Raman*. *Cryst Growth Des.* 2016;16(7):3898-904. DOI: 10.1021/acs.cgd.6b00470.

4.1.Abstract

Orthorhombic lepidocrocite-type lithium titanate hydrates (LTH), as one important member among 2D materials, have drawn much attention due to their potential applications in nanoelectronics, energy conversion and energy storage devices. However, only few efforts have focused on anisotropic growth mechanism that determines the formation kinetics of LTH and/or even their derivatives. In this context, *in-situ* Raman observation was employed to the isothermal crystallization of LTH nanosheet crystals from amorphous precursor precipitate. During isothermal crystallization, the formation of mono-layered LTH nuclei is controlled by oxygen diffusion with activation energy of 0.72 eV; anisotropic growth along (010) planes induces inter-blocking effect among LTH nanosheet crystals, which limits their size up to 50 nm. The

nucleation-growth crystallization kinetics of LTH nanosheets were accurately interpreted by the modified Johnson-Mehl-Avrami-Kolmogorov (JMAK) model, which considered their anisotropic 2D growth. Beyond LTH, the present study that combines *in-situ* spectroscopic monitoring with kinetic modeling paves the way towards deeper comprehension and ultimate control of the growth kinetics of 2D titanate materials.

4.2.Introduction

Over the past decade, many efforts have been devoted into the promising research field of two-dimensional (2D) materials.[4.1-3] 2D materials are defined as those materials with strong in-plane bonds to form atomic lattices, which are weakly bonded to each other in out-of-plane orientation. This unique 2D structure leads to unexpected electronic and optical properties due to the quantum confinement of electrons in two dimensions. As is the famous case of graphene, their peculiar properties ignite research interest in both fundamental aspects and applications.[4.3,4] For example, their extraordinarily large specific surface area (over 1000 m^2/g) draws attention in scientific areas such as catalysis[4.5] and electrochemistry[4.6] because of the ensuing high surface activity.

One important member in 2D material family, layered titanates,[4.7-11] are considered of great potential in wide range of applications such as ion exchange[4.12], electrochemical (de)intercalation[4.13] and photocatalysis.[4.14] Among various layered titanates, orthorhombic lepidocrocite-type (γ-FeOOH) layered titanates are made up of stacked 2D atomic periodicities (e.g., $Ti_\delta O_2$, $\delta = 0.91$[4.15] and 0.87)[4.16] as simple as the interlayer arrangement of graphite. Such structural architecture facilitates fast electron/ion exchange behavior with different inorganic and organic species, including H^+, Li^+, OH^-, and others.[4.17-21] This superior ion-exchange feature can be exploited in advanced electrode materials for energy storage/conversion systems or nanoelectronic devices. For the energy application field, the recent work of Shirpour *et al.* reported lepidocrocite-type $K_{0.8}Ti_{1.73}Li_{0.27}O_4$ as intercalation host for sodium and lithium-ion storage that delivered 300 and 600 mAh/g initial discharge capacity, respectively.[4.13] Also other reports about their proton conductivity makes layered titanates promising candidates as electrolytes in fuel cells [4.22,23]. As for the field of nanoelectronics, Osada *et al.* proposed a prototype of titanate-based field-emission transistors (FET), which comprise layer-by-layer architecture of lepidocrocite titanate / poly(diallyldimethylammonium chloride) (PDDA).[4.9] Despite its rather low mobility around 5×

10^{-2} cm^2 V^{-1} S^{-1}, atomic-scale multilayered design could open a rewarding avenue for fabricating flexible and transparent optoelectronic devices based on layered titanates.

To fully exploit their potential, special attention to the synthesis process can be the key element to meet the rising demand for high-quality layered titanates.[4.24,25] As example, the top-down strategy via exfoliation of large crystals of layered titanates may be mentioned. In this regard, Gao *et al.*[4.18,19] prepared $H_xTi_{2-x/4}\square_{x/4}O_4\cdot H_2O$ nanosheets by exfoliation from a proton-exchanged $Cs_xTi_{2-x/4}\square_{x/4}O_4$ single crystal *via* intercalation of tetra-butyl ammonium organic cation in alkaline aqueous solution at 60 °C; alternatively the bottom-up strategy was reported by Takezawa *et al.,* by which nanocrystals of layered titanates are prepared from TiF_4 precursor in alkaline environment.[4.26] Recently, ever since firstly proposed by Kasuga *et al.,*[4.27] the most widely employed method is alkaline hydrothermal synthesis making use of raw TiO_2 materials.[4.28-30]

The different synthesis strategies are controlled by the respective 2D crystal formation mechanism. Bottom-up synthesis can be understood as the result of a nucleation-growth reaction. For example, the $\boldsymbol{A}_2Ti_3O_7$ ($\boldsymbol{A}$ = Li, Na, *etc.*) 2D nuclei are constituted by vertex and edge-shared TiO_6 octahedral units in highly alkaline environment with $\boldsymbol{A}$ ions inserted between the two $Ti_3O_7^{2-}$ slabs.[4.31,32] As for the top-down synthesis, the sheet-type atomic lattices are generally believed being stripped from layered monoclinic tri-titanate crystals via the creation of a concentration imbalance between H^+ and OH^-.[4.33] In contrast Yang *et al.* hypothesized that formation of orthorhombic lepidocrocite-type titanate nanotubes was accomplished *via* chemical bond destruction in alkaline environment.[4.34] The short Ti-O bonds in TiO_6 octahedra that constitute TiO_2 crystals were cut off by the action of OH^- to form linear fragments as the nanotube building units. However, Yoshida *et al.'s* direct observation of TiO_6 octahedron-forming titanate nanotubes [4.35] makes Yang's assumed bond-breaking mechanism unlikely.

It becomes apparent therefore that clarifying the formation mechanism of layered titanates is of both scientific and engineering importance.[4.36,37] However, this is not trivial because not only most ambiguity is from lack of information about transition states during synthesis, but also because the anisotropic morphology of layered titanates complicates the kinetic behavior. In this regard, *in-situ* characterization can play a crucial role due to its capability to capture short-lived transition states. A robust kinetic model considering the influence of 2D anisotropic growth in layered titanates is as well required for making possible on-demand crystal design for different applications.

Herein, time-resolved *in-situ* Raman characterization was employed to characterize the isothermal crystallization process of a lepidocrocite-type lithium titanate hydrate (LTH). Raman scattering spectroscopy has been proven successful in determining the formation of 2D materials, *e.g.* graphene [4.38] because of its high sensitivity to short-range ordered or amorphous materials. Also, Raman spectroscopy is capable to readily distinguish different polymorphs of nanostructured titania (anatase, brookite and rutile) and layered titanates [4.39-42]. Some complementary techniques were also employed, including X-ray diffraction (XRD) and transmission electron microscopy (TEM). Further, a kinetic model that considers the influence of anisotropic growth in 2D materials was introduced to quantitatively interpret the pattern variation in Raman spectra and the crystallization kinetics of LTH crystals.

4.3.Experimental procedures

4.3.1. Synthesis of LTH phase

The synthesis method for LTH phase is adopted from our previous work[4.43] and can be roughly divided into two steps. In the first step, an LTH precursor was prepared by a "cold-neutralization" process. The hydrolytic precipitate formed during this process was the result of the neutralization of 2 **M** titanium tetrachloride (99.0% $TiCl_4$, Sigma-Aldrich, USA) aqueous solution and 1.33 **M** lithium hydroxide (LiOH) aqueous solution (98.0% $LiOH \cdot H_2O$, Sigma-Aldrich, USA) under vigorous stirring. Thus, 20 mL of $TiCl_4$ aqueous solution was drop-wise added at 1 mL/min rate into 180 mL LiOH aqueous solution. The temperature of the mixed solution was controlled at about 2 ^{o}C to avoid premature nucleation of titania during the precipitation reaction, and the final pH was in the range of 11.5 - 12 at which the solution was continuously stirred for 2 hours. The as-neutralized white precipitates were collected, rinsed with DI water and then adjusted to Li/Ti ratio 1.3 and pH of 10.5 by using 0.25 **M** LiOH aqueous solution. In the second step, the cold-neutralized precipitate/LiOH solution colloidal suspension was subjected to "isothermal aging" with vigorous agitation at the selected aging temperature (90, 75 and 50 ^{o}C) for different times to induce LTH nanocrystal formation. Layered LTH crystals were recovered by washing with DI water and dried at the corresponding aging temperature. In the meantime, the same suspension was used to prepare well-crystalline samples *via* hydrothermal treatment at 240 ºC for 48 hours for comparison.

4.3.2. Material characterization

A Hitachi SU–8000 cold-field emission scanning electron microscope (CFE-SEM) (Hitachi High Technologies, Rexdale, Canada) and a Philips CM200 Transmission Electron Microscope (TEM) at 200 kV were employed for LTH morphology characterization. Spectroscopic techniques were employed to reveal the information about composition and crystal structure. For example, PXRD patterns were collected using a Bruker D8 Discover GADDS XRD^2-microdiffractometer with Bragg–Brentano geometry, at 40 kV, 20 mA for Cu Kα (λ = 1.5406 Å). Raman spectroscopy was performed with a Renishaw RM 3000 & InVia spectrophotometer by using 513.5 nm Ar ion laser. Raman spectra were collected every 6 min, including spectrum harvesting for 1 min. A home-made sample holder for *in-situ* Raman measurement was used and described hereinafter. The aforementioned suspension of the as-neutralized precursor in LiOH aqueous solution was confined between two discs of borosilicate glass, which was used as the contact window for *in-situ* Raman measurements, with the assistance of a Teflon O-ring. Then epoxy was applied to seal the reactor as to supress water evaporation while leaving a small pinhole to balance the pressure. The illustration of the custom-made reactor set-up is given in Appendix B (Figure B8). Then the sealed home-made sample holder was placed on a temperature controlled hot plate to collect the *in-situ* Raman spectra at the crystallization temperature.

4.3.3. Kinetic modelling

For extracting quantitative kinetic information, all collected *in-situ* Raman spectra were normalized and calibrated with respect to the sharp band around 400 cm^{-1}. This feature is the contribution from the solvent water in the suspension that plays the role of internal standard. By setting the crystallinity of the LTH sample synthesized hydrothermally at 240 ºC as 100%, the relative crystallinity $x(t)$ could be determined from the fraction of the integrated intensity of each band in the spectrum, with reference to the corresponding one of the 240 ºC hydrothermal sample. The bands of 401 and 433 cm^{-1} were chosen because these features were of little significance in the as-neutralized precipitate. Finally, eq. (B7b) was applied to derive the crystallinity kinetics, with the aid of Avrami plots of $ln[-ln(1-x(t))]\ vs\ ln(t)$.

4.4. Results and discussion

4.4.1. 2D nanostructure of LTH

The sheet-like morphology and the crystal structure of LTH is provided in Figure 4.1. Figure 4.1a and 1b are the macroscopic morphology of as-prepared LTH obtained *via* 90 ºC isothermal aging for 24 hours, where the two-dimensionally sheet-like primary particles have width of around 50 nm and thickness of *ca.* 5 nm as deduced from the dark strips shown in Figure 4.1b. The high length / thickness ratio clearly indicates that LTH crystals prefers to grow anisotropically along certain crystallographic orientation. The corresponding selected area electron diffraction (SAED) pattern as the insertion in Figure 4.1b exhibits typical polycrystalline ring features, which can be perfectly indexed as the orthorhombic lepidocrocite structure with *Cmcm* space group (No.63).

The high-resolution TEM (HR-TEM) image in Figure 4.1c reveals that LTH primary particles are single-crystal laminations separated by 0.85 nm interspace. According to the crystal structure presented in Figure 4.1d, the host lamination layers that exhibit *Cmcm* symmetry comprise TiO_6 octahedral units connected two-dimensionally via edge-sharing and corner-sharing in parallel with (010) planes. The multilayered structure of LTH is stabilized by the interaction between negatively charged TiO_6 host layers and the species in the interlayer space. The interlayer includes hydrogen bonds from water molecules as well as intercalated Li ions.

The plausible structural model of *Cmcm* lepidocrocite LTH was established by XRD analysis, whose results are given in Figure 4.2 and Figure B2 in Appendix B, and schematically provided in Figure B1 in Appendix B. According to the proposed crystal model, the unit cell dimensions are a = 3.8020 Å; b = 16.6729 Å; and c = 3.0093 Å. Distorted TiO_6 octahedra with C_{2v} symmetry are composed of polar Ti-O with bond length 1.89 Å and equatorial Ti-O of 2.08 and 1.94 Å. In the interspace between TiO_6 slabs, severely distorted LiO_4 tetrahedra reside to create a considerable inter-spacing $d_{(020)}$ = 8.3364 Å demonstrating the tendency of Li^+ mobility and location uncertainty.

4.4.2. Long-range order evolution of LTH

The formation of LTH crystal structure and the morphology development during isothermal aging was monitored by *ex-situ* XRD and TEM, respectively. The diffused XRD pattern in Figure 4.2e indicates the nanocrystallinity (short-range order)

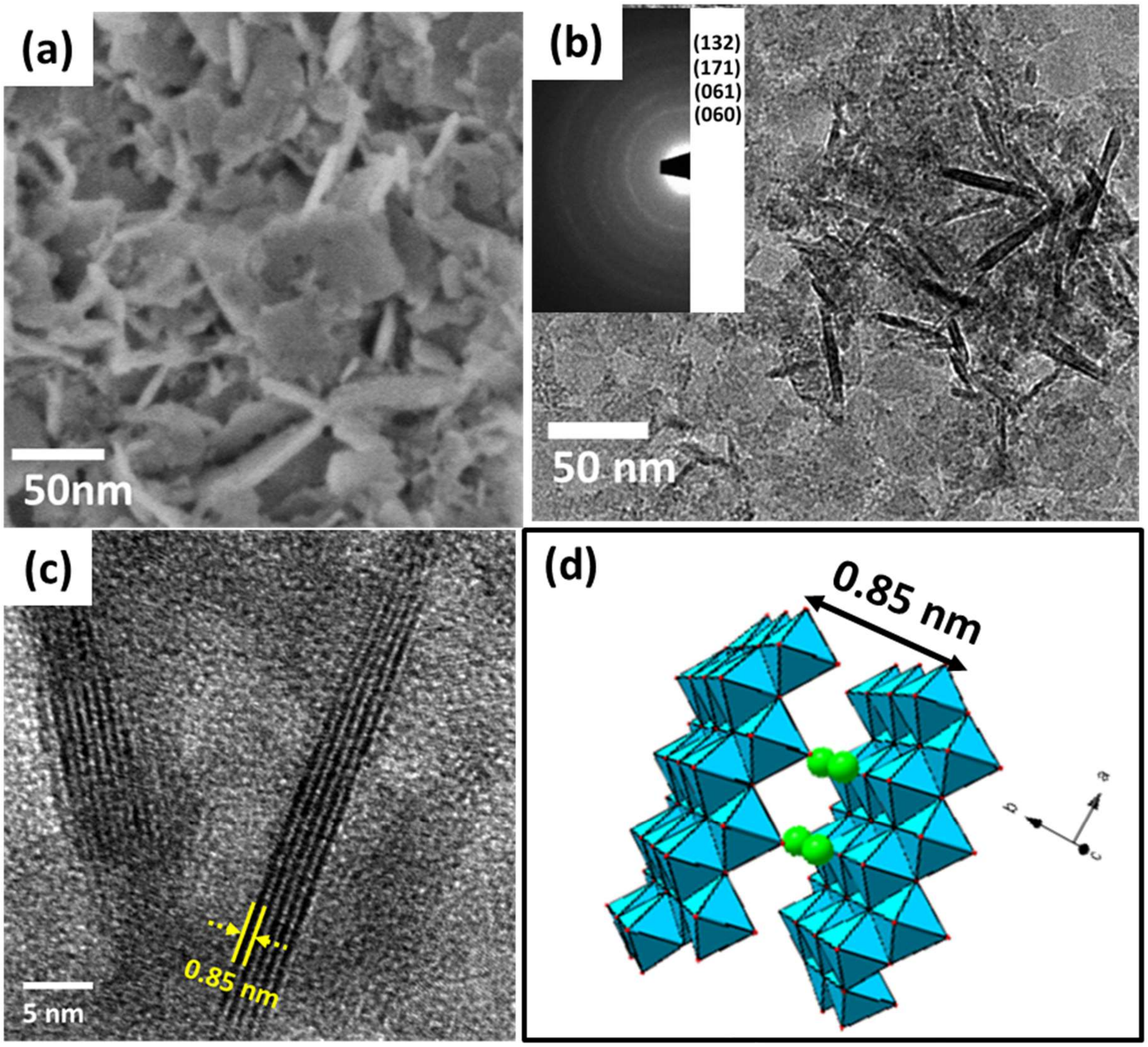

Figure 4.1. Morphology of LTH crystals obtained by isothermal aging at 90 °C for 24 hours: (a) SEM (b) TEM images with accompanying selected area electronic diffraction (SAED) pattern, (c) HR-TEM of LTH sheets, and (d) the schematic diagram of LTH crystal structure, in which the green balls represent the hydrated lithium ions and/or water molecules, and the cyan-blue octahedra are TiO_6 units.

of the as-neutralized precipitate. The broadened but remarkable shoulders indexed to (0k0) (k = 4, 6, 8) are the result of the anisotropic morphology of LTH nuclei. After isothermal aging at 90 ºC for 3 hours, crystallization of the short-range ordered precipitate into long-range order LTH

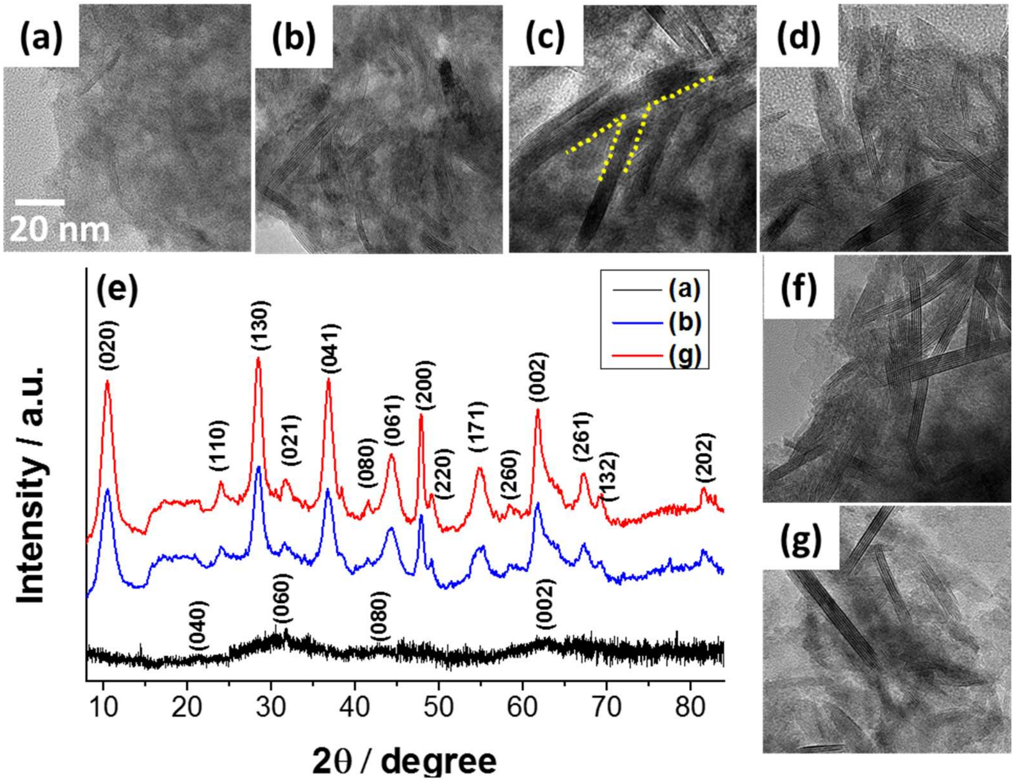

Figure 4.2. LTH crystallization: Evolution of crystal morphology from (a) as-neutralized precursor and after aging at 90 ºC isothermally for (b) 3, (c) 6, (d) 10.5, (f) 16 and (g) 23.5 hours; and (e) the corresponding XRD patterns of samples at (a), (b) and (g) conditions.

framework has been established as evidence by the crystalline XRD pattern of Figure 4.2e. No significant difference in the peak-width of XRD patterns obtained at 3 hours and 23.5 hours is observed signalling that the LTH crystal structure if fully developed; however peak sharpening is evident as the result of LTH grain size growth, which shows a quasi-linear relationship with time increasing from 9.4 nm at 3 hours to 10.5 nm at 23.5 hours as given in Figure B2c in Appendix B.

Direct observation on time-evolution of LTH particle size during isothermal crystallization was studied in depth by TEM imaging of crystal samples collected at different aging times. According to collected images in Figure 4.2, the size of LTH nanosheets anisotropically grows into 5 by 50 nm nanoplates along their (010) planes in the end of isothermal aging process. Before initiation of the isothermally aging process, some small (2-10 nm in length) LTH quasi-crystals as nuclei are embedded in the amorphous precipitate as the nuclei, which consisted of single-layer or few-layer TiO_6 sheets as shown in Figure 4.2a and Figure B3a in Appendix B. As the isothermal aging process proceeds to 3 hours, the size of LTH nanosheets grows to length of 10-20 nm as shown in Figure 4.2b and S3b, yet the thickness is limited to approximately 5 nm. Subsequently, anisotropic growth leads to crystal extension along *ac*-plane of LTH further reaching 50 nm in length after aging for 6 hours. However, in correspondence with the deduced crystal size evolution obtained from XRD, further isothermal aging after 6 hours does not benefit LTH growth as the crystal size barely changes. Such arrest in further LTH nanosheet crystal growth was determined to be the result of impingement occurring, thus the new growing LTH nanosheet meets another one as marked in Figure 4.2c. As the isothermal aging process further proceeds, the probability for crystal to crystal inter-blocking increases, hence the length of LTH nanosheets to be confined at around 50 nm.

Time-evolution of the morphology of LTH crystals is also probed by TEM characterization. Figure B3 in Appendix B reveals the curved features of both quasi-crystals (in the form of single-layer / few-layer nuclei) embedded in the as-neutralized precipitate, as well the initially formed (after 3 hours aging) LTH nanosheets. But the curved LTH crystals are gradually straightened with the crystallinity increase. Like the DNA folding,[4.44] the dimensionality / geometrical shape of layered titanates can be tailored *via* the manipulation of the surrounding chemical environment.[4.45-47] The mechanism resulting in the curved morphology will be discussed later in next section.

Based on the characterization results of long-range order evolution of LTH, the following picture of LTH isothermal crystallization dynamics can be drawn as: Initially, the curved LTH nuclei are established from the amorphous precipitate. Before inter-blocking effects occurring, both nucleation and anisotropic growth via coarsening process, contribute to enhance the crystallinity of LTH crystals. As isothermal crystallization proceeds, the anisotropic growth of

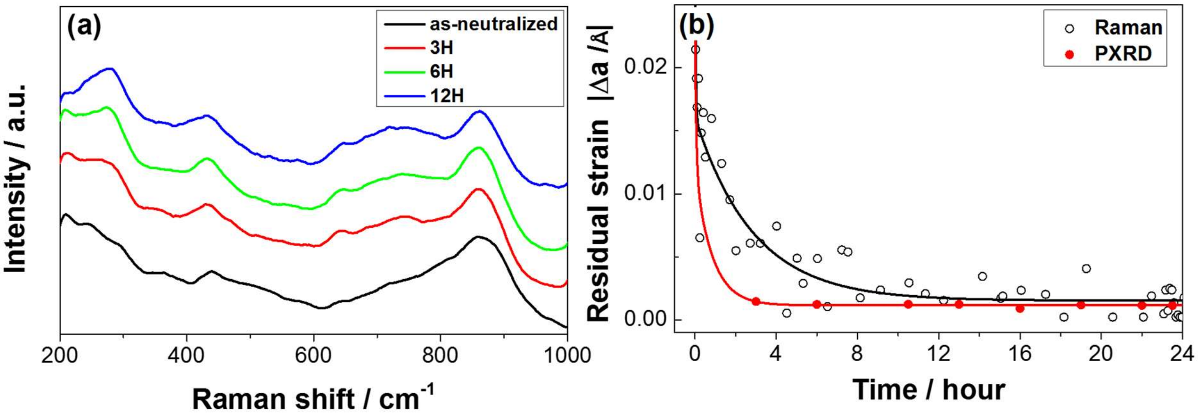

Figure 4.3. (a) Selected *in-situ* Raman spectra of the as-neutralized precursor precipitate (black) and LTH crystal samples obtained after isothermal crystallization for 3 (red), 6 (green) and 12 (blue) hours at 90 °C. (b) Relative residual LTH crystal strain based on lattice parameter differences estimated *via* Raman (black circles) and PXRD (red points) as a function of crystallization time at 90 °C.

LTH nanosheet crystals is obstructed due to crystal-to-crystal inter-blocking among the straightened sheets. Eventually, nucleation gradually fades away as the result of amorphous precursor consumption and the whole crystallization process reaches the equilibrium state.

4.4.3. Short-range order evolution of LTH

By applying *in-situ* Raman measurements the transitional states of LTH with short-range order was able to be probed. This real-time information would be highly valuable in developing strategies for controlled synthesis of 2D crystal materials. The spectrum of well-crystalline LTH crystals serving as reference material is given in Figure B4 in Appendix B to determine the characteristic vibration modes. The said reference LTH crystals were prepared *via* hydrothermal processing[4.13,17,48] at 240 °C for 48 hours. Like many orthorhombic layered titanates,[4.18,19,39,41] the LTH Raman spectrum comprises three main contributions at 279, 433 and 855 cm^{-1} as fingerprints of layered titanate structure;[4.49,50] with some subtle bands also at 401, 575, 642, 685, and 747 cm^{-1}. All features can be assigned to the signature vibrational modes of *Cmcm* lepidocrocite structure and are analogous to other titanates that also possess lepidocrocite structure, *e.g.* $H_xTi_{2-x/4}\square_{x/4}O_4\cdot H_2O$[4.19] and $K_{0.8}Ti_{1.73}Li_{0.27}O_4$.[4.13]

Examining first the Raman spectrum of the as-neutralized precipitate as provided in Figure 4.3a, we note the presence of the 855 cm^{-1} band as the most significant feature. This peak is also presented in the crystallized LTH phase albeit with some change as it becomes sharper with a minor blue shift. This 855 cm^{-1} band is usually referred to the stretching mode of short Ti-O bond with length of 1.89Å, sticking out towards the interspace among TiO_6 host layers.[4.51,52] Such distortion of TiO_6 octahedra is believed to be induced by hydroxyl group in the interlayer space. For example, the water adsorption on TiO_2 rutile (101) planes leads to lattice distortion in the near-surface region.[4.53] Wang *et al.* also provided direct evidence of lattice distortion of $Ti_{0.87}O_2$ nanosheets as the result of columbic repulsion during stacking.[4.54] Besides the dominant band at 855 cm^{-1}, the surrounding broad shoulder in the range from 600 to 1000 cm^{-1} in the as-neutralized precipitate, corresponds to the vibrations of Ti-O and O-H bonds.[4.55,56] Such a broaden dispersion of vibration modes is a clear indication of the short-range order of the precursor precipitate. Their detailed assignment follows the report of Łuczyn´ska-Szymczak *et al.*: the band near 670 cm^{-1} is assigned to stretching Ti–O modes mixed with the O-H bending vibrations.[4.56] As for the band at 640 cm^{-1}, it relates to the out-of-plane deformation of the Ti–O–Ti bonds, accompanied by the O–H group twisting.[4.56] In other words, LTH nuclei established during the cold-neutralization process are highly hydrated.

The Raman spectra of the evolving LTH crystals start to exhibit the significant features of long-range ordered *Cmcm* symmetry (Figure 4.3a) as the isothermal crystallization proceeds. Three A_g mode bands 297, 433 and 685 cm^{-1} corresponding to the vibrational modes of Ti-O bonds in Figure 4.3a gradually become prominent, with observable blue shift. The intensity enhancement of A_g bands indicates anisotropic growth of LTH crystals to build the long-range ordered structure. The anisotropic growth of LTH crystals can be understood as the result of the Li-ion / OH^- specific adsorption on (010) planes.[4.12,13,49] This orientation-dependent adsorption confines the degree of freedom of the lattice extension, hence only the condensation of TiO_6 octahedra occurring on the edge of (010) planes of LTH structure is allowed.

On the other hand, the observed blue shift reflects the shrinkage of Ti-O bonds as a consequence of lattice distortion evolution during the LTH crystallization, thus the morphology changes from curved into parallel. In general, residual strain is supposed to be insignificant when nucleation occurs in a fluid phase[4.57] hence giving rise the highest O_h symmetry to TiO_6 octahedra. But in the early stage of crystallization (up to 4 to 8 hours, as the transition point in Figure 3b), the mono-layered nuclei of LTH exhibit imbalanced concentration of specifically adsorbed Li^+ / OH^- due to the short-range order. This chemical imbalance causes the increase of surface tension to favour LTH nuclei bending, which raises strain energy as energy compensation to avoid further bending.[4.33,58] This chemically induced bending mechanism are also responsible for the hydrothermal exfoliation process of layered titanates such as monoclinic $H_2Ti_3O_7$.[4.33,59-61] As isothermal crystallization proceeds, the morphology of LTH crystals evolves from the initially curved structure being rectified to a symmetrical one (*i.e.*, parallel lattice fringes). This morphological transition is driven by the disorder reduction of Li^+ / OH^- arrangement in the interlayer space. Finally, the long-range order of *Cmcm* symmetry confines the bond lengths and angles making the symmetry of well-crystalline LTH crystals break down to C_{2v}. The aforementioned morphological transition was further quantitatively monitored (Figure 4.3b) by determining the residual crystal strain on the basis of the band shift of the dominant A_g band 433 cm^{-1} of the *in-situ* Raman spectra (refer to Appendix B). In addition, the lattice parameters estimated by Le Bail refinement of *ex-situ* PXRD is used for comparison, to guarantee the reliability of the derived estimates from *in-situ* Raman measurements. As can be seen in Figure 4.3b, both *in-situ* and *ex-situ* results show the dilative strain, arising from the relaxed Ti-O bonds in LTH nuclei, being released after isothermally aging at 90 °C for minimum 4 hours. This result is also consistent with the O_h-C_{2v} symmetry breakdown, as the result of crystallization dynamics by clusting of hydrated Ti complexes, into long-range ordered LTH crystals. Also the difference between *ex-situ* and *in-situ* observation implies the advantage of *in-situ* measurement that provides complete information of LTH crystallization.

4.4.4. Temperature influence on LTH crystallization

The temperature dependency of LTH crystallization kinetics is also revealed via *in-situ* observation. *In-situ* Raman spectra of LTH crystals aged at different temperatures, namely 90, 75 and 50 °C (refer to Figure B5 in Appendix B) are concentrated and expressed as contour plots in Figure 4.4. It is clarified that the bands before 300 cm^{-1} are removed because the optic grid of

Raman aperture was cut off at 200 cm^{-1} having as consequence partial loss of information of the strong band at 273 cm^{-1}.

In the case of 90 ºC isothermal crystallization (Figure 4.4a), the broad shoulder ranging from 600 to around 1000 cm^{-1} where a strong peak stands out around 855 cm^{-1}, represents the existence of short-range ordered LTH nuclei in in the as-prepared precipitate (refer to Figure 4.3a.) The large shoulder was gradually separated into two regions: one ranging from 640 to 800 cm^{-1} corresponding to Ti-O-Ti stretching mode in *Cmcm* symmetry; and the band at 855 cm^{-1} (circa 3 hours in Figure 4.3a.) Also the band at 433 cm^{-1} of Ti-O vibration becomes more prominent with the progress of crystallization. Moving now to the crystallization data obtained at 75 ºC (Figure 4.4b) the zone-splitting around 855 cm^{-1} is delayed till 8 hours of aging compared to 3 hours at 90 ºC, reflecting the slower crystallization kinetics at low temperature. The crystallization kinetics slow down even more at 50 ºC (Figure 4.4c) in terms of no distinguishable zone-separation. This implies abundant short-range ordered LTH crystals to dominate until the considerable development of 433 cm^{-1} band after 12 hours.

According to the observed spectral evolution of nanosheet crystal nucleation and growth the formation of LTH crystals can be sequentially divided into the following basic steps: (i) The highly hydrated 6-fold coordinated TiO_6 octahedra start to assemble into larger molecules as building units. Both Raman spectroscopy and XRD provided direct evidence of the short-rage ordered titanate compound; also, the HR-TEM observation confirmed the dominantly short-ranged ordered features of as-neutralized precursor precipitate. (ii) The specifically adsorbed lithium ions at the surface-surrounding electrical double layer shield (010) planes from direct collision of building units, hence allowing only edge-shared / corner-shared arrangement. As a result, LTH crystals assume 2D morphology by anisotropic extension along (010) planes. This was deduced from the XRD and HR-TEM characterization. The anisotropic growth along ac-plane leads to the relatively strong (0k0) diffraction, and their 2D morphology. The extension of Ti-O framework is energetically favored, in other words, Li-O-Ti connection impedes the growth along b-axis. In-situ Raman characterization, on the other side, reveals how the Cmcm long-range order was established. (iii) The short-range order of LTH nuclei leads to considerable chemical imbalance of specifically adsorbed ions causing a curvature in the morphology. But with the progressive development of crystallinity the disorder in the interlayer space is reduced giving rise to the final parallel nanosheet morphology. The curved features can be readily observed in the TEM images at the beginning of crystallization (e.g., Figure 4.2a), but the curved features are gradually straightened as the reaction proceeded (Figure 4.2g); also from the c-axis lattice constant variation (interspace distance, calculated from the peak shift in XRD patterns) in Figure 4.3b, the interlayer space shrinks as the isothermal crystallization proceeded. This compression in LTH means their crystals become more organized, more crystalline. Highly disordered structure triggers structure relaxation, which therefore results in the high interspace distance. In other words, the interlayer distance is an indication of the order in the interspace of LTH. Gajovic et al. also observed such relationship between Na/H ratio and the interlayer space.

4.4.5. Kinetic modelling of LTH crystallization

Finally, the isothermal crystallization kinetics of LTH was quantitatively modeled, by analysing the transformation fraction (*i.e.* degree of crystallinity) from the amorphous precipitate into LTH nanosheet crystals. To develop a kinetic model for the case of isothermal crystallization of LTH, several assumptions are employed: (i) crystallization proceeds *via* the nucleation-growth mode; (ii) nucleation occurs in a uniform, random inside the mother matrix at constant rate; (iii) an interface-controlled growth is assumed because the crystallization reaction began in an infinite, short-range ordered mother matrix and (iv) the growth rate of LTH nanosheets is constant, at least along its (010) planes. On the basis of these assumptions the universal Johnson-Mehl-Avrami-Kolmogorov (JMAK) kinetic model was selected to describe the crystallization of LTH. However, some modifications on the JMAK kinetic model are deemed necessary to allow the anisotropic growth of LTH crystals. In this context, an analytical mathematical model proposed by Kooi[4.62,63] was applied. A detailed derivation of this modified JMAK kinetic model (Equation B7b) for anisotropic growth of LTH phase nanosheets is included in the Appendix B.

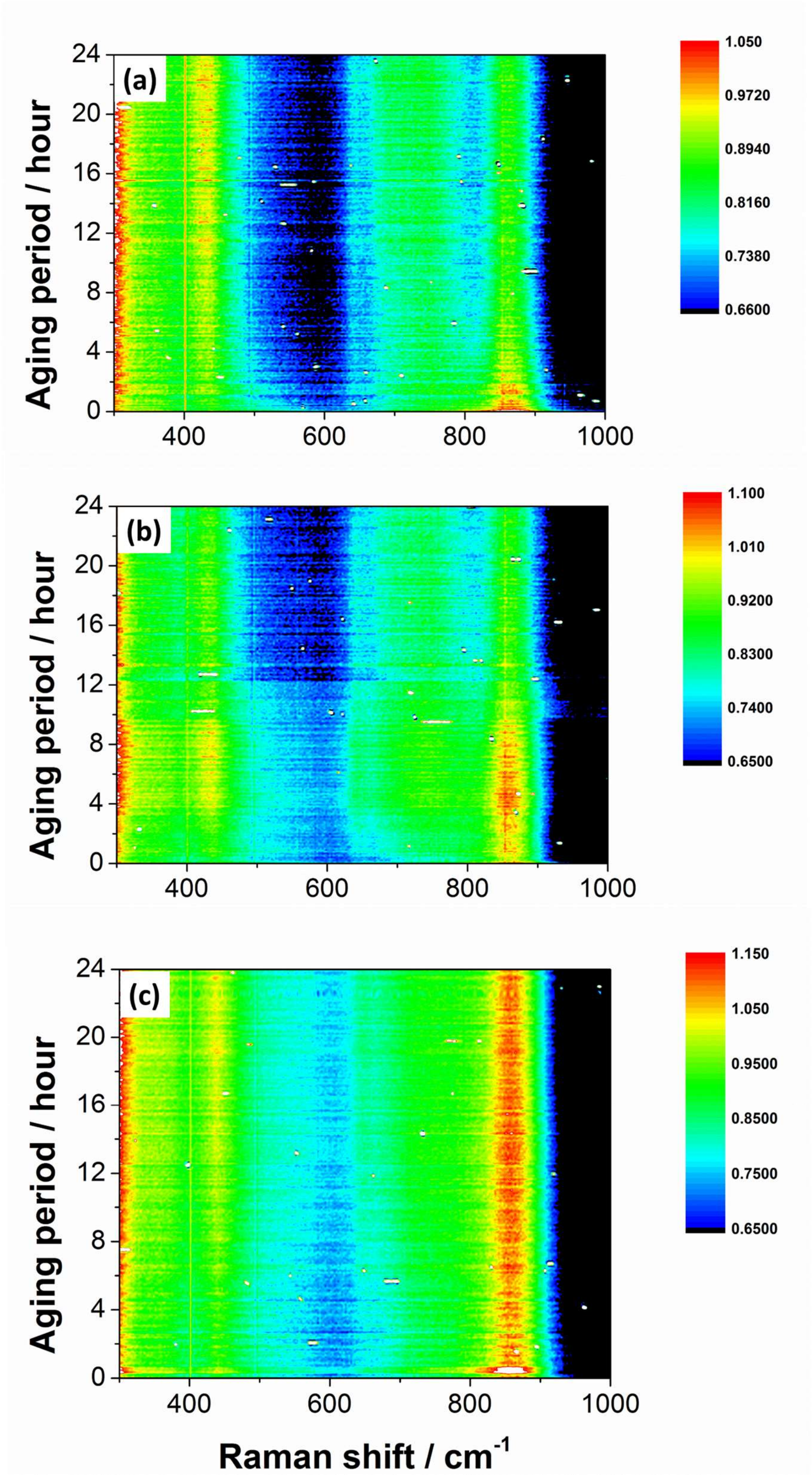

Figure 4.4. *In-situ* Raman measurements for 24 hours at (a) 90, (b) 75, and (c) 50 °C. Note that the intensity scales in the different figures vary from each other to emphasize the feature evolution.

According to the derivation found in the Appendix B, the Avrami exponent for 2D growth drops from the “textbook” value of 3, to 1/3. This drop in Avrami exponent can be understood as the consequence of decrease in crystallization rate due to inter-particle blocking effect. According to Figure B6 in Appendix B, the Avrami exponent 1/3 provides a satisfactory representation of the inter-blocking effect that limits crystal growth. This is even better illustrated by considering the data in Figure 4.5. Here a comparison between the experimental LTH crystallization data derived from the *in-situ* Raman measurements (open dots)-refer to “Kinetic modelling” information given in the **Experimental procedures** section- and the corresponding kinetic plots (solid curves) of the anisotropic-growth JMAK model is presented. The good match between the simulation and experimental data in Figure 4.5 means that the employed assumptions are largely accurate. Namely, the isothermal crystallization of LTH from amorphous precipitate is a nucleation-growth process. And the anisotropic growth is interface-controlled by the condensation on the edge of (010) planes.

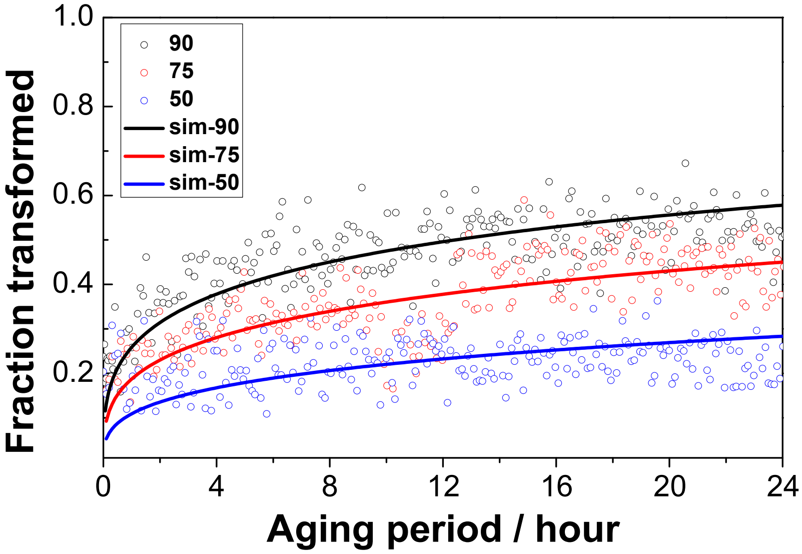

Figure 4.5. The crystallization fraction of LTH as a function of isothermal aging time at (a) 90 (black), (b) 75 (red), and (c) 50 (blue) °C, in which the discrete data points are experimental data converted from the *in-situ* Raman measurements; and the solid lines are the theoretical JMAK kinetic model plots representing the anisotropic growth process.

According to Eq. (S7a), because of the influence of inter-blocking effect that limits the nanosheet length to 50 nm (Figure 4.1b), crystallization in the growth blocking regime only depends on nucleation process. In this regime by using the intercepts of the linear Avrami plots for the three temperatures shown in Figure B6 in Appendix B, the Arrhenius plot of Figure B7 is generated allowing the estimation of the activation energy of nucleation process. The activation energy was caculated to be 0.72 eV (69.13 kJ $\cdot$ mol^{-1} $\cdot$ K^{-1}). This value is quite close to many reported oxygen diffusion-controlled processes being responsible for TiO_2 polymorph formation.[4,64-66] In other words, the nucleation of LTH appears to be determined by oxygen diffusion.

4.5.Conclusion

The developed theoretical model combined with the *in-situ* Raman observation provides a comprehensive picture of the underlying formation mechanism of LTH nanosheets. In the early stage of LTH crystallization, both nucleation and anisotropic growth have considerable contribution to the transformation from amorphous precursor precipitate. Nucleation is characterized by oxygen diffusion to constitute the 2D framework consisted of edge-shared and cornered-shared TiO_6 octahedra. The obtained LTH nuclei possess mono-layer and curved 2D morphology. 2D growth of LTH nanosheet crystals is initialized *via* condensation occurring on the edges of (010) facets, and parallel stacking to establish long-range ordered structure with *Cmcm* symmetry. But the prominent inter-blocking effect due to anisotropic growth slows down the crystallization kinetics. The theoretical JMAK model was successfully modified to take into account the influence of anisotropic growth resulting in excellent description of the isothermal crystallization kinetics of LTH.

The crystallization knowledge of LTH cannot only be valuable for implementation to other layered titanates and their derivatives, but also could be useful in manipulating the properties of 2D materials more generally. As such the present work makes an invaluable contribution to further development and ultimately application of 2D layered titanates in nanoelectronics, catalysis and Li/Na rechargeable batteries.

4.6.Acknowledgments

Professor Gauvin's group is thanked for the use of their SEM. Financial support received by NSERC and Hydro-Quebec is gratefully acknowledged. H-C Chiu also acknowledges reception of a McGill Engineering Doctoral Award (MEDA).

4.7.References

(**4.**1) Coleman, J. N.; Lotya, M.; O'Neill, A.; Bergin, S. D.; King, P. J.; Khan, U.; Young, K.; Gaucher, A.; De, S.; Smith, R. J.et al. Two-dimensional nanosheets produced by liquid exfoliation of layered materials. *Science* **2011,** *331* (6017), 568.

(**4.**2) Nicolosi, V.; Chhowalla, M.; Kanatzidis, M. G.; Strano, M. S.; Coleman, J. N. Liquid Exfoliation of Layered Materials. *Science* **2013,** *340* (6139), 1224619.

(**4.**3) Novoselov, K. S.; Jiang, D.; Schedin, F.; Booth, T. J.; Khotkevich, V. V.; Morozov, S. V.; Geim, A. K. Two-dimensional atomic crystals. *Proc Natl Acad Sci U S A* **2005,** *102* (30), 10451.

(**4.**4) Wang, Q. H.; Kalantar-Zadeh, K.; Kis, A.; Coleman, J. N.; Strano, M. S. Electronics and optoelectronics of two-dimensional transition metal dichalcogenides. *Nat Nanotechnol* **2012,** *7* (11), 699.

(**4.**5) Pyun, J. Graphene oxide as catalyst: application of carbon materials beyond nanotechnology. *Angew Chem Int Ed Engl* **2011,** *50* (1), 46.

(**4.**6) Brownson, D. A.; Banks, C. E. Graphene electrochemistry: an overview of potential applications. *Analyst* **2010,** *135* (11), 2768.

(**4.**7) Bavykin, D. V.; Friedrich, J. M.; Walsh, F. C. Protonated titanates and TiO2 nanostructured materials: Synthesis, properties, and applications. *Adv. Mater.* **2006,** *18* (21), 2807.

(**4.**8) Hong, Z. S.; Wei, M. D. Layered titanate nanostructures and their derivatives as negative electrode materials for lithium-ion batteries. *Journal of Materials Chemistry A* **2013,** *1* (14), 4403.

(**4.**9) Osada, M.; Sasaki, T. Exfoliated oxide nanosheets: new solution to nanoelectronics. *J. Mater. Chem.* **2009,** *19* (17), 2503.

(**4.**10) Bavykin, D. V.; Walsh, F. C. *Titanate and titania nanotubes: synthesis, properties and applications*; Royal Society of Chemistry, 2010.

(**4.**11) Bavykin, D. V.; Walsh, F. C. Elongated Titanate Nanostructures and Their Applications. *Eur J Inorg Chem* **2009,** *2009* (8), 977.

(**4.**12) Bavykin, D. V.; Walsh, F. C. Kinetics of alkali metal ion exchange into nanotubular and nanofibrous titanates. *J. Phys. Chem. C* **2007,** *111* (40), 14644.

(**4.**13) Shirpour, M.; Cabana, J.; Doeff, M. Lepidocrocite-type Layered Titanate Structures: New Lithium and Sodium Ion Intercalation Anode Materials. *Chem. Mater.* **2014,** *26* (8), 2502.

(**4.**14) Yu, Y. L.; Zhang, P.; Guo, L. M.; Chen, Z. D.; Wu, Q.; Ding, Y. H.; Zheng, W. J.; Cao, Y. The Design of TiO_2 Nanostructures (Nanoparticle, Nanotube, and Nanosheet) and Their Photocatalytic Activity. *J. Phys. Chem. C* **2014,** *118* (24), 12727.

(**4.**15) Manga, K. K.; Zhou, Y.; Yan, Y. L.; Loh, K. P. Multilayer Hybrid Films Consisting of Alternating Graphene and Titania Nanosheets with Ultrafast Electron Transfer and Photoconversion Properties. *Adv. Funct. Mater.* **2009,** *19* (22), 3638.

(**4.**16) Tanaka, T.; Ebina, Y.; Takada, K.; Kurashima, K.; Sasaki, T. Oversized titania nanosheet crystallites derived from flux-grown layered titanate single crystals. *Chem. Mater.* **2003,** *15* (18), 3564.

(**4.**17) Sugita, M.; Tsuji, M.; Abe, M. Synthetic Inorganic Ion-Exchange Materials. LVIII. Hydrothermal Synthesis of a New Layered Lithium Titanate and Its Alkali Ion Exchange. *Bull. Chem. Soc. Jpn.* **1990,** *63* (7), 1978.

(**4.**18) Gao, T.; Fjellvåg, H.; Norby, P. Defect Chemistry of a Zinc-Doped Lepidocrocite Titanate $Cs_xTi_{2-x/2}Zn_{x/2}O_4$ ($x = 0.7$) and its Protonic Form. *Chem. Mater.* **2009,** *21* (15), 3503.

(**4.**19) Gao, T.; Fjellvåg, H.; Norby, P. Raman Scattering Properties of a Protonic Titanate $H_xTi_{2-x/4}\square_{x/4}O_4 \cdot H_2O$ ($\square$, vacancy; $x = 0.7$) with Lepidocrocite-Type Layered Structure. *J. Phys. Chem. B* **2008,** *112* (31), 9400.

(**4.**20) Sasaki, T.; Watanabe, M.; Michiue, Y.; Komatsu, Y.; Izumi, F.; Takenouchi, S. Preparation and Acid-Base Properties of a Protonated Titanate with the Lepidocrocite-Like Layer Structure. *Chem. Mater.* **1995,** *7* (5), 1001.

(**4.**21) Sasaki, T.; Kooli, F.; Iida, M.; Michiue, Y.; Takenouchi, S.; Yajima, Y.; Izumi, F.; Chakoumakos, B. C.; Watanabe, M. A Mixed Alkali Metal Titanate with the Lepidocrocite-like Layered Structure. Preparation, Crystal Structure, Protonic Form, and Acid−Base Intercalation Properties. *Chem. Mater.* **1998,** *10* (12), 4123.

(**4.**22) Thorne, A.; Kruth, A.; Tunstall, D.; Irvine, J. T.; Zhou, W. Formation, structure, and stability of titanate nanotubes and their proton conductivity. *J Phys Chem B* **2005,** *109* (12), 5439.

(**4.**23) Yamada, M.; Wei, M. D.; Honma, I.; Zhou, H. S. One-dimensional proton conductor under high vapor pressure condition employing titanate nanotube. *Electrochem. Commun.* **2006,** *8* (9), 1549.

(**4.**24) Ou, H. H.; Lo, S. L. Review of titania nanotubes synthesized via the hydrothermal treatment: Fabrication, modification, and application. *Separation and Purification Technology* **2007,** *58* (1), 179.

(**4.**25) Wang, L.; Sasaki, T. Titanium oxide nanosheets: graphene analogues with versatile functionalities. *Chem Rev* **2014,** *114* (19), 9455.

(**4.**26) Takezawa, Y.; Imai, H. Bottom-up synthesis of titanate nanosheets with hierarchical structures and a high specific surface area. *Small* **2006,** *2* (3), 390.

(**4.**27) Kasuga, T.; Hiramatsu, M.; Hoson, A.; Sekino, T.; Niihara, K. Formation of titanium oxide nanotube. *Langmuir* **1998,** *14* (12), 3160.

(**4.**28) Bavykin, D. V.; Kulak, A. N.; Walsh, F. C. Metastable Nature of Titanate Nanotubes in an Alkaline Environment. *Cryst. Growth. Des.* **2010,** *10* (10), 4421.

(**4.**29) Kiatkittipong, K.; Ye, C. H.; Scott, J.; Amal, R. Understanding Hydrothermal Titanate Nanoribbon Formation. *Cryst. Growth. Des.* **2010,** *10* (8), 3618.

(**4.**30) Huang, J. Q.; Huang, Z.; Guo, W.; Wang, M. L.; Cao, Y. G.; Hong, M. C. Facile synthesis of titanate nanoflowers by a hydrothermal route. *Cryst. Growth. Des.* **2008,** *8* (7), 2444.

(**4.**31) Chen, Q.; Zhou, W. Z.; Du, G. H.; Peng, L. M. Trititanate nanotubes made via a single alkali treatment. *Adv. Mater.* **2002,** *14* (17), 1208.

(**4.**32) Pan, H.; Lu, X.; Yu, X.; Hu, Y.-S.; Li, H.; Yang, X.-Q.; Chen, L. Sodium Storage and Transport Properties in Layered $Na_2Ti_3O_7$ for Room-Temperature Sodium-Ion Batteries. *Adv. Energy Mater.* **2013,** *3* (9), 1186.

(**4.**33) Zhang, S.; Peng, L. M.; Chen, Q.; Du, G. H.; Dawson, G.; Zhou, W. Z. Formation mechanism of H2Ti3O7 nanotubes. *Phys Rev Lett* **2003,** *91* (25), 256103.

(**4.**34) Yang, J. J.; Jin, Z. S.; Wang, X. D.; Li, W.; Zhang, J. W.; Zhang, S. L.; Guo, X. Y.; Zhang, Z. J. Study on composition, structure and formation process of nanotube $Na_2Ti_2O_4(OH)_2$. *Dalton Trans.* **2003**, DOI:10.1039/b305585j 10.1039/b305585j(20), 3898.

(**4.**35) Yoshida, K.; Miao, L.; Tanaka, N.; Tanemura, S. Direct observation of TiO_6 octahedron forming titanate nanotube by advanced transmission electron microscopy. *Nanotechnology* **2009,** *20* (40), 405709.

(**4.**36) Shannon, R. D.; Pask, J. A. Kinetics of the Anatase-Rutile Transformation. *Journal of the American Ceramic Society* **1965,** *48* (8), 391.

(**4.**37) Kumar, K.-N. P.; Keizer, K.; Burggraaf, A. J. Textural evolution and phase transformation in titania membranes: Part 1.—Unsupported membranes. *J. Mater. Chem.* **1993,** *3* (11), 1141.

(**4.**38) Sun, Z.; Yan, Z.; Yao, J.; Beitler, E.; Zhu, Y.; Tour, J. M. Growth of graphene from solid carbon sources. *Nature* **2010,** *468* (7323), 549.

(**4.**39) Gao, T.; Fjellvag, H.; Norby, P. Crystal structures of titanate nanotubes: a Raman scattering study. *Inorg Chem* **2009,** *48* (4), 1423.

(**4.**40) Gajovic, A.; Friscic, I.; Plodinec, M.; Ivekovic, D. High temperature Raman spectroscopy of titanate nanotubes. *Journal of Molecular Structure* **2009,** *924* (0), 183.

(**4.**41) Gao, T.; Wu, Q. L.; Fjellvag, H.; Norby, P. Topological properties of titanate nanotubes. *J. Phys. Chem. C* **2008,** *112* (23), 8548.

(**4.**42) Gao, T.; Fjeld, H.; Fjellvag, H.; Norby, T.; Norby, P. In situ studies of structural stability and proton conductivity of titanate nanotubes. *Energy. Environ. Sci.* **2009,** *2* (5), 517.

(**4.**43) Chiu, H. C.; Brodusch, N.; Gauvin, R.; Guerfi, A.; Zaghib, K.; Demopoulos, G. P. Aqueous Synthesized Nanostructured $Li_4Ti_5O_{12}$ for High-Performance Lithium Ion Battery Anodes. *J. Electrochem. Soc.* **2013,** *160* (5), A3041.

(**4.**44) Travers, A.; Muskhelishvili, G. DNA supercoiling - a global transcriptional regulator for enterobacterial growth? *Nat Rev Microbiol* **2005,** *3* (2), 157.

(**4.**45) Ma, R. Z.; Bando, Y.; Sasaki, T. Nanotubes of lepidocrocite titanates. *Chem. Phy. Lett.* **2003,** *380* (5-6), 577.

(**4.**46) Ma, R. Z.; Bando, Y.; Sasaki, T. Directly rolling nanosheets into nanotubes. *J. Phys. Chem. B* **2004,** *108* (7), 2115.

(**4.**47) Ma, R.; Sasaki, T. Nanosheets of oxides and hydroxides: Ultimate 2D charge-bearing functional crystallites. *Adv Mater* **2010,** *22* (45), 5082.

(**4.**48) Li, N.; Mei, T.; Zhu, Y.; Wang, L.; Liang, J.; Zhang, X.; Qian, Y.; Tang, K. Hydrothermal synthesis of layered $Li_{1.81}H_{0.19}Ti_2O_5.xH_2O$ nanosheets and their transformation to single-crystalline $Li_4Ti_5O_{12}$ nanosheets as the anode materials for Li-ion batteries. *CrystEngComm* **2012,** *14* (20), 6435.

(**4.**49) Ma, R.; Sasaki, T.; Bando, Y. Alkali metal cation intercalation properties of titanate nanotubes. *Chem Commun (Camb)* **2005**, DOI:10.1039/b415983g 10.1039/b415983g(7), 948.

(**4.**50) Ma, R.; Fukuda, K.; Sasaki, T.; Osada, M.; Bando, Y. Structural features of titanate nanotubes/nanobelts revealed by Raman, X-ray absorption fine structure and electron diffraction characterizations. *J. Phys. Chem. B* **2005,** *109* (13), 6210.

(**4.**51) Kudo, A.; Kondo, T. Photoluminescent and photocatalytic properties of layered caesium titanates, $Cs_2Ti_nO_{2n+1}$ (n=2, 5, 6). *J. Mater. Chem.* **1997,** *7* (5), 777.

(**4.**52) Ocana, M.; Garciaramos, J. V.; Serna, C. J. Low-Temperature Nucleation of Rutile Observed by Raman-Spectroscopy during Crystallization of Tio2. *Journal of the American Ceramic Society* **1992,** *75* (7), 2010.

(**4.**53) Schaub, R.; Wahlstrom, E.; Ronnau, A.; Lagsgaard, E.; Stensgaard, I.; Besenbacher, F. Oxygen-mediated diffusion of oxygen vacancies on the TiO2(110) surface. *Science* **2003,** *299* (5605), 377.

(**4.**54) Wang, Y.; Sun, C.; Yan, X.; Xiu, F.; Wang, L.; Smith, S. C.; Wang, K. L.; Lu, G. Q.; Zou, J. Lattice distortion oriented angular self-assembly of monolayer titania sheets. *J Am Chem Soc* **2011,** *133* (4), 695.

(**4.**55) Su, Y.; Balmer, M. L.; Bunker, B. C. Raman spectroscopic studies of silicotitanates. *J. Phys. Chem. B* **2000,** *104* (34), 8160.

(**4.**56) Luczynska-Szymczak, K.; Starosta, W.; Druzbicki, K. Solid-state DFT-assisted Raman study of titaniate nanostructures. *Spectrochim Acta A Mol Biomol Spectrosc* **2013,** *116*, 646.

(**4.**57) Leite, E. R.; Ribeiro, C. *Crystallization and growth of colloidal nanocrystals*; Springer Science & Business Media, 2011.

(**4.**58) Zhang, S.; Chen, Q.; Peng, L. M. Structure and formation of $H_2Ti_3O_7$ nanotubes in an alkali environment. *Phys. Rev. B: Condens. Matter Mater. Phys.* **2005,** *71* (1), 014104.

(**4.**59) Tsai, C. C.; Teng, H. Nanotube formation from a sodium titanate powder via low-temperature acid treatment. *Langmuir* **2008,** *24* (7), 3434.

(**4.**60) Tsai, C.-C.; Teng, H. Structural Features of Nanotubes Synthesized from NaOH Treatment on TiO2with Different Post-Treatments. *Chem. Mater.* **2006,** *18* (2), 367.

(**4.**61) Tsai, C. C.; Teng, H. S. Regulation of the physical characteristics of Titania nanotube aggregates synthesized from hydrothermal treatment. *Chem. Mater.* **2004,** *16* (22), 4352.

(**4.**62) Kooi, B. J. Monte Carlo simulations of phase transformations caused by nucleation and subsequent anisotropic growth: Extension of the Johnson-Mehl-Avrami-Kolmogorov theory. *Phys. Rev. B: Condens. Matter Mater. Phys.* **2004,** *70* (22), 224108.

(**4.**63) Kooi, B. J. Extension of the Johnson-Mehl-Avrami-Kolmogorov theory incorporating anisotropic growth studied by Monte Carlo simulations. *Phys. Rev. B: Condens. Matter Mater. Phys.* **2006,** *73* (5), 054103.

(**4.**64) Thorwarth, G.; Mandl, S.; Rauschenbach, B. Rutile formation and oxygen diffusion in oxygen PIII-treated titanium. *Surf Coat Tech* **2001,** *136* (1-3), 236.

(**4.**65) Zhang, H. Z.; Banfield, J. F. Kinetics of crystallization and crystal growth of nanocrystalline anatase in nanometer-sized amorphous titania. *Chem. Mater.* **2002,** *14* (10), 4145.

(**4.**66) Wahlstrom, E.; Vestergaard, E. K.; Schaub, R.; Ronnau, A.; Vestergaard, M.; Laegsgaard, E.; Stensgaard, I.; Besenbacher, F. Electron transfer-induced dynamics of oxygen molecules on the TiO2(110) surface. *Science* **2004,** *303* (5657), 511.

Chapter 5

Annealing-Regulated Elimination of Residual Strain-Induced Structural Relaxation for Stable High-Power $Li_4Ti_5O_{12}$ Nanosheet Anodes

As described in the previous chapters, spinel LTO nanosheets are prepared via thermal phase transformation of 2D lepidocrocite LTH crystals. In this chapter, the LTH-LTO phase transformation is studied in detail and the properties of the annealed LTO are related to its electrochemical performance. In particular, it is shown the thermal conversion process to induce lattice strain in the resultant nano-LTO crystals, which causes structural relaxation that leads to performance deterioration during cycling.

The Chapter was previously published in: **Chiu H-C**, Lu X, Zhou J, Gu L, Reid J, Gauvin R, et al. *Annealing-regulated elimination of residual strain-induced structural relaxation for stable high-power* $Li_4Ti_5O_{12}$ *nanosheet anodes. Nano Energy*. 2017; 32:533-41. DOI: 10.1016/j.nanoen.2016.12.063.

5.1.Abstract

Nanoscale $Li_4Ti_5O_{12}$ (LTO) is considered a promising anode material for Li-ion batteries because of its outstanding safety. However, cointercalation-induced structural relaxation adversely affects its Li-ion storage properties. Therefore, there is a need to elucidate the connection between electrochemistry and LTO structural relaxation of nano-LTO. Herein, various LTO nanosheet crystals with designated degrees of residual strain were prepared by varying the annealing temperature. The cyclability and rate capability of the prepared 2D LTO nanocrystals were evaluated. During annealing, dehydration of layered lithium titanate hydrate precursors (LTH, $(Li_{2-x}H_x)Ti_2O_5 \bullet yH_2O$), leads to topotactic transformation from a *C*-centered orthorhombic to a body-centered orthorhombic system. Dehydrated LTH is then converted into spinel LTO nanosheets. Residual strain induced during transformation causes LTO structure distortion rendering Li-O bonding more covalent. Strongly covalent Li-O bonds screen the Li-Li Coulomb repulsion when 8*a*-16*c* cointercalation occurs, leading to large irreversible capacity loss and deteriorated

cyclability. Meanwhile, rich irreversible Li intercalation degrade the power capability of LTO nanocrystals despite their high surface area. In addition to mechanism elucidation, conditions are identified to eliminate residual strain-induced structural relaxation giving rise to nanosheet anodes with superior power and highly reversible cycling performance.

5.2.Introduction

To meet the growing demand for Li-ion battery (LIB)-powered electromobility,[5.1] it is essential to improve current LIB performance including long life span and high power capability. Applying two-dimensionally nanostructured spinel lithium titanates $Li_4Ti_5O_{12}$ (LTO) as anodes provides a unique opportunity to accomplish both targets considering LTO's well known "zero-strain" property of merely 0.2% volume change during charge/discharge operation[5.2] This "zero-strain" property arises because the lattice parameters of the end members of the two-phase intercalation reaction, $Li_4Ti_5O_{12}$ (8.3595Å) and the lithiated phase of $Li_7Ti_5O_{12}$ (8.3538Å), are quite close.[5.3] Introducing 2D nanostructure can effectively solve the issue of the intrinsically poor electronic conductivity of spinel $Li_4Ti_5O_{12}$ (energy gap 3.8 eV),[5.4-7] therefore opening the path for improved power capability by shortening the diffusion length and enhancing the surface area.[5.8-11]

Li storage in LTO is accomplished via intercalation of Li ions. During lithiation (intercalation), the external Li ions intercalate into the 16*c* vacancies in $Li_4Ti_5O_{12}$, or more specifically $(Li_3)^{8a}[\ ]^{16c}[Li_1Ti_5]^{16d}(O_{12})^{32e}$ (where empty brackets represent the vacancies) to deliver a specific capacity of 175 mAh/g. Such Li intercalation results in the formation of the discharged LTO product $Li_7Ti_5O_{12}$, which can be described more precisely as $(Li_6)^{16c}[Li_1Ti_5]^{16d}(O_{12})^{32e}$.[5.12,13] The phase separation between spinel $Li_4Ti_5O_{12}$ and rock-salt $Li_7Ti_5O_{12}$ leads to a voltage plateau at 1.55 V *vs.* Li/Li^+.[5.5,14-17]

Nonetheless, those Li ion storage properties would be altered when the LTO material is nanostructured.[5.18-20] For example, because Li-ion diffusion depends on the coordination environment along the diffusion pathways,[5.12,13] the relaxed LTO nanocrystal structure (*i.e.*, distorted lattice) due to high surface-to-volume ratio will have an impact on power capability. The size-dependent Li diffusivity of nano-LTO was studied by Kavan *et al.*,[5.21] who found a dramatic decrease by orders of magnitude as the particle size shrinks from 1 μm to 9 nm. Pang *et al.* arrived to the same conclusion from *in situ* observations using neutron powder diffraction.[5.15]

Nano-LTO also allows excess Li intercalation beyond $Li_7Ti_5O_{12}$ stoichiometry, which leads to larger initial storage capacity manifested with curved voltage profile.[5.18] The excess Li capacity is the consequence of simultaneous occupation of Li ions at 8*a* and 16*c* sites in the near-surface region, causing structural reconstruction/relaxation. Ganapathy *et al.* proposed that structural relaxation increases the nearest Li-Li distance thereby the higher intercalation voltage, which varies with different crystallographic orientations.[5.22] Such reconstruction/relaxation in the near-surface region results in a large irreversible capacity loss, the mechanism of which is discussed elsewhere.[5.23]

The orientation-dependent Li storage mechanism of LTO is responsible for the curved voltage profile in nanosized LTO as well. Hirayama *et al.* found that epitaxial-grown LTO thin film along the [111] and [110] directions exhibited distinct curved voltage profiles instead of the typical flat two-phase curves.[5.24] The challenge therefore remains for controlling/eliminating structural relaxation in LTO nanocrystals, in particular of 2D morphology, to optimize their potential in high-power applications without sacrificing extended lifespan.[5.25]

To prepare 2D nanocrystals of LTO, one common strategy is through the thermal conversion of precursor layered 2D lithium titanate hydrates (LTH).[5.26-34] For example, Liu *et al.* prepared nanostructured LTO by a combination of microwave-assisted hydrothermal process to synthesize LTH precursors, and their subsequent thermal conversion at elevated temperature.[5.29] Wang *et al.* synthesized rutile-TiO_2 nanocoated LTO nanosheets via similar hydrothermal process but without the assistances of microwaves.[5.28] In our earlier research, we have described a green process with 100 % inorganic precursors operating in ambient atmosphere below the boiling point of water,[5.27] hence offering an energy-competitive alternative to the hydrothermal process.

Even though the same synthesis strategy has been applied by various groups, there are significant differences between the various LTO nanosheet materials, a critical matter that has not been adequately considered. For example, Chen *et al.* prepared LTO nanosheets at 550°C annealed for 6 hours with power capabilities of 177 mAh/g at 1.1 C, 169 mAh/g at 5.7 C and 150 mAh/g at 20C, respectively.[5.30] But similar LTO nanosheet materials prepared after annealing at 700°C for 6 hours by Xiao *et al.* could only deliver 164.1 mAh/g at 1 C, 142.5 mAh/g at 5 C and 100.2 mAh/g at 20 C.[5.35] In contrast to the previous examples, Wang *et al.* prepared LTH nanosheets annealed at different temperatures[5.28] and found that higher annealing temperature leads to better electrochemical performance in both cyclability and rate capability. The root cause behind those performance contradictions is still unclear, most likely because the transformation mechanism from LTH to LTO that occurs during thermal conversion (annealing) has not been understood, hence limiting our ability to reach the optimized 2D LTO nanocrystal-based anode design.

In this context, the present research study is divided into two parts: the first part reveals the phase transformation mechanism from a 2D LTH lepidocrocite crystal structure into LTO spinel nanosheets. Based on the newly obtained knowledge about this transformation, the degree of lattice distortion in LTO nanosheet crystals can be readily controlled by regulating the annealing process. By characterizing the corresponding changes in cyclability and rate capability with respect to lattice distortion for the different annealed LTO nanosheet crystals, the dependency of electrochemistry on residual strain-induced structural relaxation upon cycling is understood, leading to the design of high power LTO nanosheet anodes.

5.3.Experimental Section

5.3.1. Synthesis

The synthesis of LTO nanosheet crystals is a modification of our earlier described process.[5.27] It involves low-temperature (<100°C) aqueous synthesis of LTH layered nanocrystals, followed by their thermal conversion (annealing) in ambient atmosphere. The details of LTH synthesis can be found in another publication.[5.32] In the first step, amorphous precipitate is formed as the result of the hydrolysis of 20 mL of 2 M $TiCl_4$ (99.0%, Sigma-Aldrich, USA) aqueous solution by reaction with 180 mL of 1.33 M LiOH aqueous solution (98.0% $LiOH\cdot H_2O$, Sigma-Aldrich, USA) under vigorous stirring. The $TiCl_4$ solution is added drop-wise at 1 mL/min rate into the LiOH solution; the temperature must be maintained at about 2-4°C and the final pH kept in the range of 11.5 – 12. The amorphous precipitate is afterwards collected and re-dispersed in a new 0.25 M LiOH aqueous solution (50 mL) with the Li/Ti ratio at 1.3. The re-dispersed suspension is subjected to isothermal aging at 85°C for 24 hours in a mechanically-agitated glass reactor. Note that in our earlier work,[5.27] aging process did not involve Li/Ti ratio regulation or agitation. Those two new modifications were very effective in improving the quality of LTO nanosheet crystals. After aging, the LTH nanocrystals are recovered, washed and subjected to annealing in ambient atmosphere, with the temperature varied from 200 to 800ºC for different retention times using a ramp rate of 3ºC/min.

5.3.2. Material Characterization

Microstructure analysis was performed with a Hitachi SU–8000 cold-field emission scanning electron microscope (SEM, Hitachi High Technologies, Rexdale, Canada), a Philips CM200 transmission electron microscope (TEM) at 200 kV, and a JEM-ARM Model 200F TEM microscope operated at 200 kV to acquire aberration-corrected scanning TEM (STEM) images, respectively. The attainable spatial resolution of the microscope was 80 pm at an incident semi-angle of 25 mrad for aberration-corrected STEM. A Micromeritics TriStar 3000 apparatus was used for N_2 absorption/desorption, in order to determine the Brunaer-Emmett-Teller (BET) surface area.

Chemical composition was determined with the assistance of an inductively coupled plasma optical emission spectrometer (ICP-OES, Thermo Jarell Ash Trace Scan) and a thermogravimetric analyzer/differential scanning calorimeter (Thermal Analyzer (TGA/DSC 1, Mettler Toledo) that monitored weight loss and heat flow when heating from room temperature to 800°C at a heating rate of 15°C/min in ambient atmosphere.

Laboratory powder X-ray diffraction (PXRD) data was obtained with a Bruker D8 Discover GADDS XRD2-microdiffractometer using Bragg–Brentano geometry, at 40 kV, 20 mA for Cu Kα (λ = 1.5418 Å). The collected PXRD patterns were analyzed using TOPAS (Version 4.2, Bruker AXS, Karlsruhe, Germany).

Raman spectroscopy was performed for the short-range order variation with a Renishaw RM 3000 & InVia spectrophotometer by applying 513.5 nm Ar-ion laser. The samples for Raman characterization were all mixed with silicon powder (325 mesh, 99%, Sigma-Aldrich) that was used as internal standard for calibration.

Advanced synchrotron X-ray characterization was conducted at the Canadian Light Source (CLS). The samples for PXRD analysis were loaded in 0.5 mm inner diameter Kapton capillaries which were sealed at both ends with a Loctite adhesive. Diffraction signals were collected using the Canadian Macromolecular Crystallography Facility beamline (CMCF-BM or 08B1-1) at CLS. 08B1-1 is a bending magnet beamline with a Si (111) double crystal monochromator. 2-dimensional (2D) data was obtained using a Rayonix MX300HE detector with an active area of 300 mm × 300 mm. The patterns were collected at an energy of 18 keV ($\lambda = 0.68880$ Å) and capillary-detector distance of 250 mm. The sample-detector distance, detector centering and tilt were calibrated using a lanthanum hexaboride (LaB_6) standard reference material from the National Institute for Standards and Technology (NIST SRM 660a LaB_6) and the calibration parameters were applied to all patterns. After calibration, the 2D patterns were integrated to obtain standard 1D powder diffraction patterns. A pattern from an empty Kapton capillary was subtracted from the sample data during integration. Again, TOPAS (Version 4.2, Bruker AXS, Karlsruhe, Germany) were employed for Rietveld refinement.

X-ray absorption near-edge structure (XANES) spectroscopy was carried out at the Canadian Light Source (CLS). The Ti L-edge and the O K-edge spectra were collected on the spherical grating monochromator (SGM) beamline ($\Delta E/E$:~10^{-4}); Li K-edge spectra were obtained on the plane grating monochromator (PGM) beamline ($\Delta E/E$:~10^{-4}). The total electron yield (TEY) mode using specimen current was employed to record the XANES spectra. Background subtraction and normalization of the X-ray absorption near-edge structure (XANES) spectra were conducted using Athena.[5.36]

5.3.3. Electrochemistry

For electrochemical measurements, CR2032 coin cells were used. LTO nanosheet electrodes were prepared for half-cell tests by mixing the prepared LTO nanosheet crystals, carbon black and poly(vinylidene fluoride) in a mass ratio of 8:1:1. Cell assembly was conducted in an argon-filled glove box (M. Braun Co., [O_2] < 0.5 ppm, [H_2O] < 0.5 ppm), with a 25 μm polypropylene (PP)/polyethylene (PE) separator (PP/PE/PP, Celgard 2325) and 1 M $LiPF_6$ in ethylene carbonate (EC) and dimethyl carbonate (DMC) (1:1, v/v) as an electrolyte.

Galvanostatic experiments were performed in a standard battery cycler (BT2043-10V-100mA-40, Arbin) and cyclic voltammetry (CV) was performed in a BioLogic VSP potentiostat/galvanostat/EIS system. The polarization variation was plotted based on differential capacity (dQ/dV) evolution during the galvanostatic cycle test at 1 C rate (1 C = 175 mA/g). More details and theoretical background can be found in our earlier published research.[5.23] Differential capacitance, defined as the relative change in capacity (dQ) over the corresponding voltage range (dV), was determined via a simple two-point numerical differentiation from the collected charge/discharge voltage profiles of 1 C cycles whose characteristic examples are given in Figure C1a. All collected dQ/dV plots were then presented as a contour plot with respect to the cycle numbers, as given in Figure C1b. The color temperature in the polarization variation figures represents the intensity of the peaks of the differential capacitance curves, which correspond to the phase equilibrium voltage of the spinel/rock-salt phase transformation.

5.4.Results and Discussion

To answer how LTO nanosheets are obtained from the phase transformation of lepidocrocite LTH, two important requirements are the crystal structure of the layered LTH and the reaction pathway of the LTH/ LTO phase transformation.

5.4.1. Phase determination of lepidocrocite LTH

The results of synchrotron PXRD characterization and the respective Rietveld refinement can be found in Figure 5.1a and Table C1 of the Appendix C. The initial guess of positional parameters for the atoms in LTH was deduced from the reported lepidocrocite-type titanates such as $Cs_xTi_{2-x/4}\square_{x/4}O_4$, where $\square$ represents the vacancies[5.37] and $K_{0.8}Ti_{1.73}Li_{0.27}O_4$.[5.38] Among all possible candidates, the *C*-centered orthorhombic system with space group *Cmcm* of highest symmetry was assumed, which led to residual factors of χ^2 : 5.05; R_{Bragg}: 4.77; R_{wp}: 4.46. The refined crystal structure of LTH develops the unit-cell dimensions of *a* = 3.80102(7) Å, b = 16.70231(6) Å, and c=3.00765(3) Å, whose polyhedral representation is given in Figure C2 of the Appendix C. The crystal structure of LTH consists of two-dimensionally corrugated lattices of edge- and corner-sharing TiO_6 octahedra, with interlayer groups of Li ions and hydroxyl groups occupying trigonal prismatic 4*c* sites in the interlayer space. Neighboring 2D lattices are held together by either the hydrogen bonds between the hydroxyl groups and 2-coordinated oxygen ions on the 2D lattices, or by the Coulomb interaction of interlayer Li ions/negatively charged 2D lattices. The negative charge of 2D lattices comes from the Li substitution or vacancies at Ti sites.[5.39,40]

The size and morphology of the as-prepared LTH crystals can be deduced from TEM images shown in Figure 5.1b and Figure C3 of the Appendix C. Typical LTH crystals have a sheet-like morphology with a width of about 100 nm. The single-crystalline features of

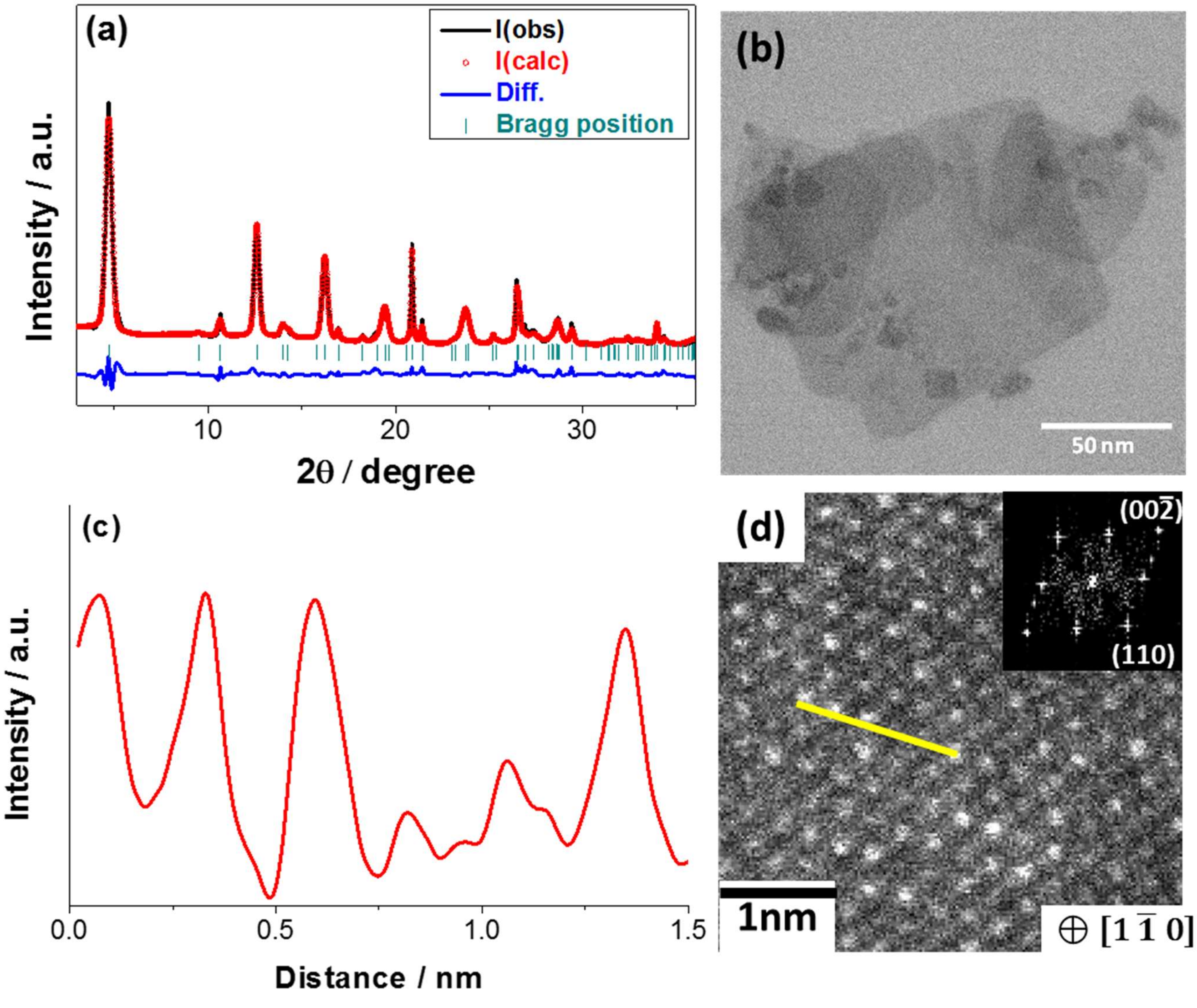

Figure 5.1. (a) Rietveld refinement results of syn-XRD with reliability factors of: χ^2 : 5.05 R_{Bragg}: 4.77; R_{wp}: 4.46; (b) the STEM image of the synthesized LTH nanosheets; (c) the corresponding line-scan profile of the yellow line in (d) HAADF image projecting along $[1\bar{1}0]$.

LTH nanocrystals in Figure C3b of the Appendix C reveals their thickness to be 5 nm, and to consist of 5-7 layers of 2D lattices with interlayer distance of $d_{(020)} = 8.35$ Å.

The composition of LTH is non-stoichiometric, which is a typical feature of lepidocrocite-type titanates;[5.32,37-44] the formula can be written as $(Li_{2-x}H_x)Ti_2O_5{\bullet}yH_2O$. With the assistance of ICP and TGA analyses (Figure C4 of the Appendix C), the values of the compositional parameters x and y were determined to be 0.5 ± 0.018 and 1 ± 0.076, respectively.

In addition to the chemical analysis, the non-stoichiometry of the produced LTH nanocrystals could be directly deduced from high-angle annular-dark-field (HAADF) STEM images. Figure 5.1d gives a LTH nanosheet crystal along the pole of $[1\bar{1}0]$ direction. The signal intensity collected by HAADF detector is proportional to $Z^{1.7}$,[5.45,46] where Z is the atomic number. The presence of vacancies or doped Li ions (Z=3) at Ti sites in LTH crystals can be readily distinguished from Ti ions (Z=22). But it is impossible to distinguish directly the Li vacancies or (doped) substitution sites because of the low atomic number of Li. As a result, the line scan (Figure 5.1c) along the yellow line in Figure 5.1d, whose contrast in the image is adjusted to the intensity of the scan profile, can help to reveal the defects at Ti sites. Namely, the disappearance of peaks at 0.8 and 1.1 nm indicates either Li substitution or vacancies.

5.4.2. Phase transformation from lepidocrocite LTH into spinel LTO

During annealing in air, the as-prepared LTH nanosheet crystals undergo two transitions: (i) dehydration to remove the crystal water/hydroxyl groups, corresponding to an endothermal reaction happening at about 170ºC and 10.7 wt% weight loss as given in Figure C4a in the Appendix C. The crystallinity of the as-prepared LTH degrades, as illustrated in Figure 5.2a (red), because disorder in the inter-layer space increases as a result of crystal water removal. This results in contraction of the interlayer distance $d_{(020)}$ in lepidocrocite LTH structure, which corresponds to the peak shift from 10.6 º toward higher angles. (ii) The formation of LTO coincides with the diffused exothermic peak at around 360ºC. Such a small feature implies a facile phase transformation from lepidocrocite LTH into spinel LTO. As the annealing temperature was raised to 300ºC, the Bragg reflections of spinel LTO began to appear but they were still mixed with LTH features. The intensities of the (004) and (044) Bragg reflections of spinel LTO (green pattern in

Figure 5.2a) suggest possible preferred orientation of the annealed LTO crystals. As the annealing temperature was increased to 350°C, phase-pure and well-crystallized LTO started emerging.

Figure 5.2b summarizes the crystal structure evolution during annealing. The interlayer distance of LTH remarkably decreases because of dehydration, while the LTO nuclei have a compressed unit cell which gradually expands as the temperature increases.

By taking advantage of the high sensitivity to short-range order of Raman spectroscopy, the crystal structure evolution during annealing was monitored. As-prepared *Cmcm* lepidocrocite LTH exhibits three main characteristic bands at 279, 433 and 855 cm^{-1},[5.37,38,47-49] illustrated at 200°C in Figure 5.2g. They can be assigned to the vibrational modes of bending of Ti-O-Ti bond, stretching of O-Ti-O, and short Ti-O bond sticking out towards the interlayer space.[5.50,51] After dehydration at 250°C, a new band develops at 695 cm^{-1}, with a decline in the band at 279 cm^{-1}. At the same time, nanocrystallization due to dehydration makes the band less sharp. Those changes are the results of a topotactic transformation from *C*-centered orthorhombic,[5.38] to body-centered orthorhombic system.[5.37,44] The transformation is accomplished by horizontally gliding of 2D lattices along the *c*-axis by *c*/2. Such topotactic transformation has been also reported for other derivatives of lepidocrocite titanates, when undergoing ion exchanging,[5.40] dehydration,[5.47] or cation doping.[5.38] The fading band at 279 cm^{-1} becomes even broader and more diffuse after annealing at 300 °C, while a new shoulder appears at 233 cm^{-1}. A blue shift is observed in the bands originally located at 443 and 695 cm^{-1} (250 °C, red pattern), towards 438 and 685 cm^{-1} (300 °C, green pattern), respectively. Those changes imply the symmetry of TiO_6 octahedra changes during LTH→LTO transformation. In LTH lepidocrocite, TiO_6 octahedra have point symmetry of C_{2v} with six different Ti-O poles, yielding a band at 276 cm^{-1}. However, the equatorial oxygens are co-planar with polar O-Ti-O bond angles of 180 ° in D_{3d} symmetry of LTO spinel, yielding a vibrational mode at 233 cm^{-1}. These two different TiO_6 octahedra are illustrated in Figure C5 of the Appendix C. As a result, their relative intensity changes in correspondence to the consumption of LTH and the establishment of LTO spinel structure. Similarly, the blue shift of O-Ti-O stretching mode (443 cm^{-1} in red pattern of Figure 5.2g) means Ti-O bond length converges from a wide distribution in the range of 1.89-2.08 Å in C_{2v} of LTH, to a single value of 1.99 Å in D_{3d} of LTO. Based on these findings, the short-ranged order of dehydrated LTH can be approximately considered as a layer-by-layer nanocomposite of Li_2O and TiO_2. Such intimate packing of

Li_2O/TiO_2 in atomic scale helps to reduce the activation energy for LTO spinel formation, as the small exothermal peak at 363.2°C in Figure C4 of the Appendix C suggests.

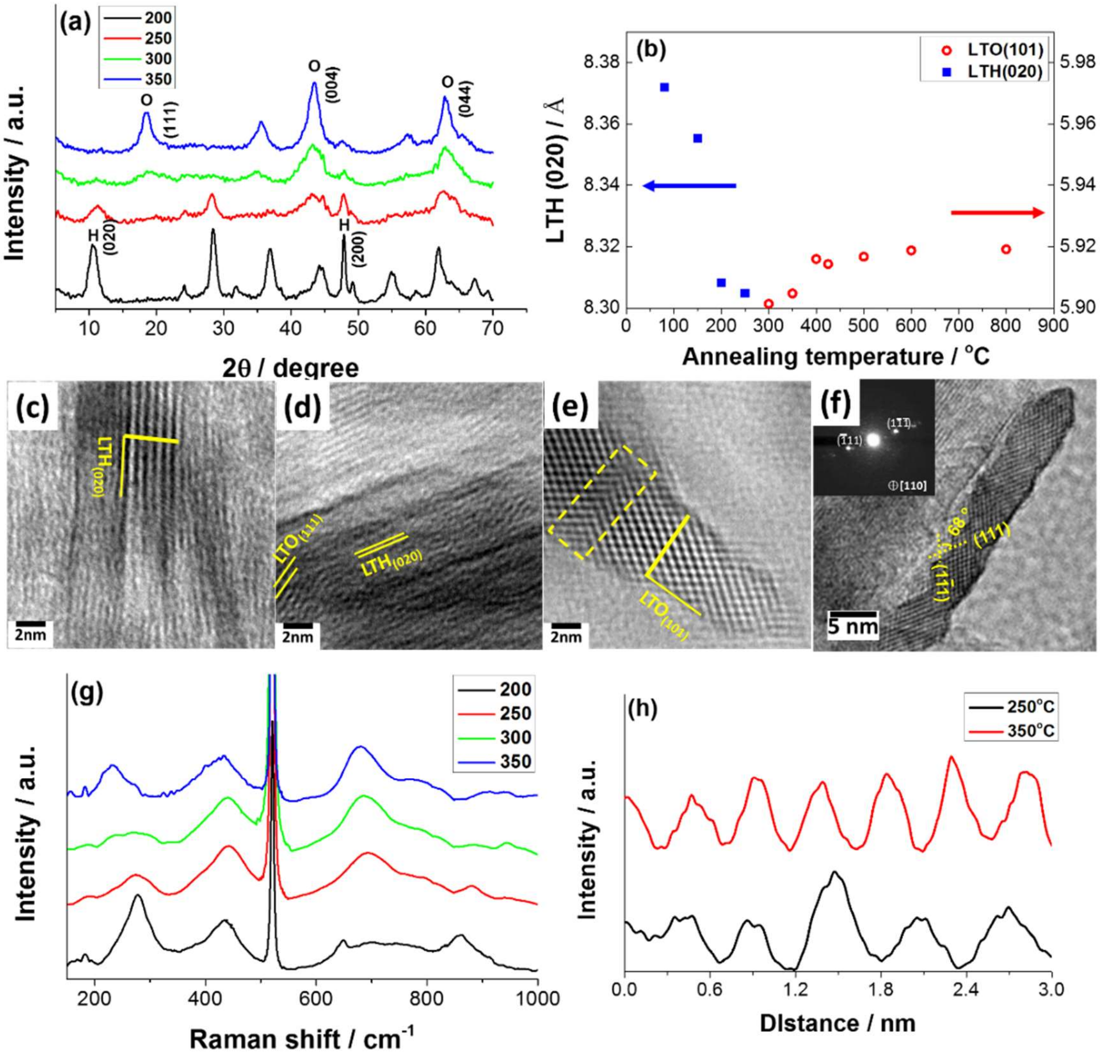

Figure 5.2. (a) XRD of LTO samples prepared at different annealing temperature in the range of 200-350 °C and (b) the average change of plane distance of LTH (020) and LTO (101) during annealing, which was estimated from XRD patterns (a); the corresponding TEM microstructure of (c) 250 (d) 300 (e) 350 (f) 500°C annealed samples. The intersection between (111) planes in (f) results in 68° zig-zag surface features; the selected area electronic diffraction (SAED) pattern (insert) exhibits the single-crystal characteristics of the spinel structure. (g) Raman spectra of each LTO annealed at different temperature. (h) The line scans along the yellow line in (c) & (e), respectively.

The structure evolution from 2D lepidocrocite to 3D spinel during LTH→LTO transformation is clearly observed in Figure 5.2c-f. As the result of dehydration, the contraction of LTH nanosheet crystals can be clearly seen in Figure 5.2c (collected after 250°C annealing for 6 hours). The interlayer spacing $d_{(020)}$ (thin yellow line in Figure 5.2c) decreases from the original value of 0.835 nm to around 0.6 nm (black profile in Figure 5.2h). The dehydration-induced volume contraction is inhomogeneous as illustrated by the variability in the periodic intervals among peaks in Figure 5.2h. This is because of residual water/hydroxyl groups that were not yet removed during dehydration, and increase disorder causing crystallinity to deteriorate.

As the annealing temperature increases to 300°C, the nucleation of LTO spinel begins. As a result, coexistence of LTO and LTH phases can be directly seen in Figure 5.2d, consistent with the PXRD and Raman characterization. The (020) planes of LTH can be observed, which are parallel to the long axis of nanosheet crystals. Small nuclei of LTO exhibit (111) planes with inter-angle of about 40 degrees with respect to the long axis of LTH.

Complete transformation of mother matrix LTH into LTO occurs after annealing at higher annealing temperature (>300°C). Figure 5.2e gives a single-crystalline LTO nanosheet crystal after 350°C annealing. Some defects can still be observed in the LTO nanocrystals obtained at this temperature; for instance, there is a clear twin boundary circled in Figure 5.2e. Those defects are eliminated by annealing at 500°C, as illustrated in Figure 5.2f. The atom rearrangement for defect elimination results in zig-zag features that are intersections of (111) and $(1\bar{1}1)$ planes with 68° inter-angles. This signature feature, as a consequence of employing layered structured LTH as precursor, has also been reported by Wang *et al.*[5.28] and typically appears in LTO nanocrystals as seen in Figure C6 of the Appendix C.

The whole phase transformation mechanism from LTH lepidocrocite to LTO spinel is summarized in the schematic of Figure C8 in the Appendix C. Dehydration at 250°C of LTH nanosheets results in a contraction of the interlayer distance $d_{(020)}$ into about 0.6 nm, as per the black profile (250°C) in Figure 5.2h. The accompanying gliding of 2D lattices triggers a topotactic transformation from a *C*-centered orthorhombic into a body-centered orthorhombic lepodicrocite structure. Nanocrystalline LTO nuclei are established via local diffusion, and then grow along the preferred orientation [101] of LTO spinel, which has $d_{(010)}$ spacing of 5.91 Å (red profile in Figure

5.2h) and is parallel to the long-axis of the sheet-like morphology. The consistency in their d-spacing values and morphology-orientation relationship of $d_{(020)}^{LTH}$ and $d_{(101)}^{LTO}$, implies there is little rearrangement of oxygen ions when establishing LTO from LTH mother matrix. Furthermore, the LTH→LTO transformation leaves zig-zag surface features as a vestige.

5.4.3. Growth of LTO Nanosheet Crystals

The intimate packing of Li_2O and TiO_2 in the dehydrated LTH structure described previously provides a favorable crystallization template for LTO formation. According to the Raman spectra of Figure 5.3a collected at different times during annealing at 500°C, the LTO formation reaction occurs rather quickly with the product having developed decent crystallinity within merely 7 min. As isothermal annealing further proceeds, crystal growth contributes to further crystallinity improvement as evident by the peaks of each vibrational mode that become sharper. Similar conclusions can be drawn from the observed changes in the corresponding PXRD patterns (Figure 5.3b), where the information on grain size growth can be extracted from the peak width broadening. Figure 5.3c gives the grain size evolution as a function of time during annealing at 350 (blue), 425 (red) and 500 (black) °C, respectively. During annealing at 500°C, the grain size of LTO nanosheet crystals increases sharply at the beginning (*ca.* within 1 hour) thereafter remaining constant at around 9 nm. Lower annealing temperature provides less driving force for growth, so smaller grain sizes and relatively sluggish kinetics are obtained when annealing at 350 and 425°C, as evident by the corresponding depressed curves in Figure 5.3c.

According to Figure 5.2, LTO nanosheet crystals preferentially grow along the [101] direction, which is attributed to oriented attachment (OA) growth of LTO nuclei.[5.52-54] In the TEM image of Figure 5.2d (or enlarged view in Figure C9 of the Appendix C), some small LTO nuclei, which are parallel to each other along [111] of spinel structure, are seen to have been established in the mother matrix of dehydrated LTH undergoing annealing at 300°C. After increasing the annealing temperature to 500°C (Figure 5.3d), all dehydrated LTH matrix appears to have converted into LTO nanodomains with size of about 10 nm. Most of LTO nanodomains align to each other along the [111] direction indicated by yellow arrows. In other words, the sheet morphology of the mother matrix and the cubic symmetry of LTO provide ideal conditions for OA growth. The former factor confines the degrees of freedom of growth of LTO nuclei, and forces these nuclei to be close to each other; the latter factor in turn increases the probability of effective alignment for OA growth.

Quantitative analysis of OA growth of LTO nanosheet crystals is accomplished by employing the kinetic model proposed by Zhan *et al.*,[5.55] whose results are given as the dash lines in Figure 5.3c. Model parameters are tabulated in Table C2 in the Appendix C. The activation energy for LTO nanocrystal growth is estimated at 119.3 kJ/mol. This value is consistent with the reported activation energy of oxygen ion diffusion in rutile TiO_2.[5.56] Thus, the anisotropic growth of LTO nanocrystals is a diffusion-controlled process, which is determined by solid-state oxygen diffusion to eliminate the boundaries and defects among grains.

5.4.4. Influence of Residual strain on electronic structure of LTO nanosheets

According to the LTH→LTO transformation data presented above, it becomes evident that annealing at different temperature would induce atomic positions into metastable equilibrium states. Their distinction can be quantitatively estimated from the evolution of the coordinate change of oxygen with respect to annealing temperature, which is obtained by Rietveld refinement of PXRD data of each LTO annealed product (Figure C10a and Table C3 of the Appendix C). When annealing temperature is raised, oxygen ions would move toward Ti ions to change angles and length of Ti-O bonds, and elongate Li-O bonds. Such elimination of structural distortion, which is illustrated in Figure C10b of the Appendix C, would modulate their orbital hybridization. As a result, XANES spectroscopy was applied to elucidate the change in their electronic structure.

In LTH lepidocrocite, TiO_6 octahedra have symmetry of point group C_{2v}, which is different from point group D_{3d} in LTO spinel. This difference leads to deviation in their Ti L-edge XANES spectra that are shown in Figure 5.4b. The most significant one is the splitting of e_g bands at around 462 eV, which are marked as e_g' and e_g" in Figure 5.4b. The difference in the e_g features is attributed to the high degree of tetrahedral distortion of TiO_6 octahedra in LTO spinel. By carefully comparing the intensity ratio of t_{2g}/e_g, the 600°C annealed LTO gives the highest t_{2g}/e_g ratio. This is because of large crystal field splitting (10Dq)[5.57] or otherwise fewer completely coordinated Ti ions (*i.e.*, lower-coordination environment than 6-fold)[5.58,59] reflecting its better crystallinity. This observation is consistent with the general expectation that the crystallinity of LTO improves as annealing temperature increases.

O K-edge XANES was used to characterize the covalency of Ti-O bonds, and the results are given in Figure 5.4c. The spectrum of as-prepared LTH exhibits similarity to Li_2CO_3, particularly the strong peak at about 532 eV, meaning the surface of the LTH nanocrystals is covered by a lithium carbonate-like compound. This can probably be ascribed to the lithium ions and hydroxyl groups in the interlayer space, which behave like LiOH absorbing CO_2 from air during storage. For the different prepared LTO nanocrystal samples, the ratio between the contribution from Ti_{3d}- O_{2p} hybridization (pre-edge region in the range of 532-536 eV) and that from the Ti_{4sp}-O_{2p} hybridization (after the threshold value of 536 eV), is used to determine their Ti-O hybridization

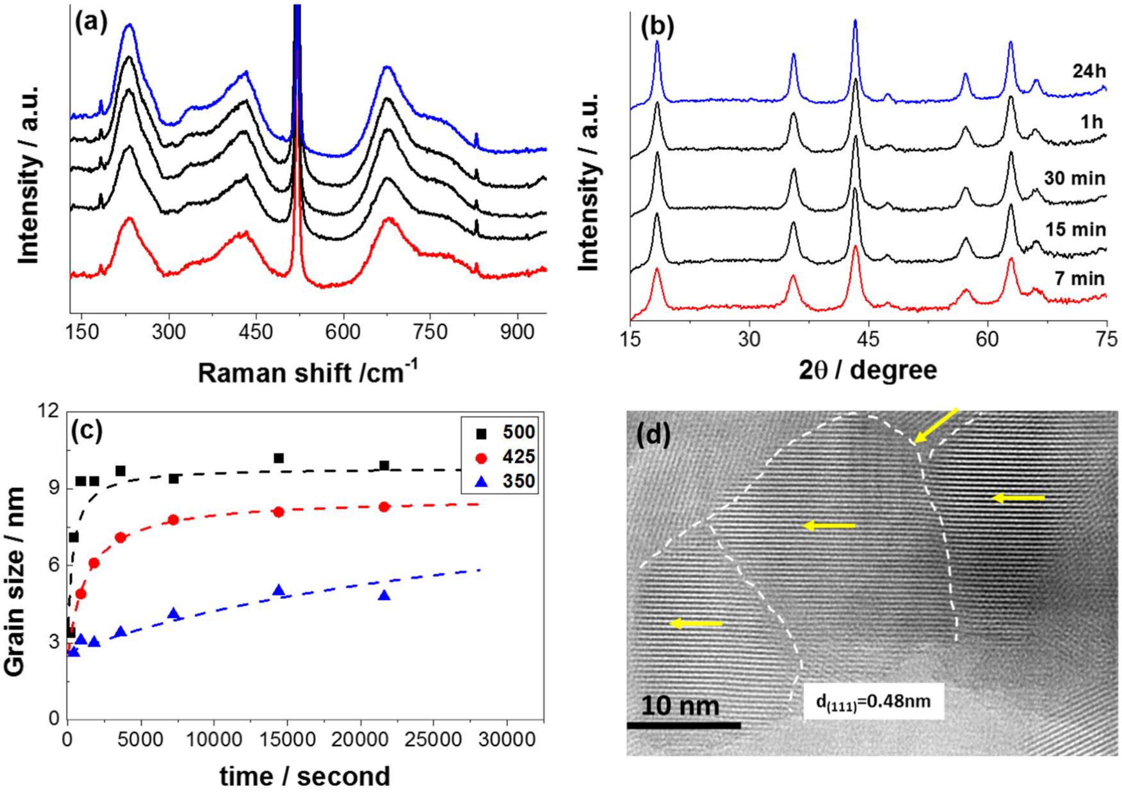

Figure 5.3. (a) Raman spectra and (b) XRD patterns of the LTO samples annealed at 500^{o}C for different periods ranging from 7 min to 24 hours. (c) The grain growth kinetics of LTO nanosheets via OA growth mode. The dash lines represent theoretical kinetic model predictions described in detail in the Appendix C. (d) TEM microstructure of LTO nanosheets annealed at 500^{o}C for 30 mins, where yellow arrows point along [111] direction.

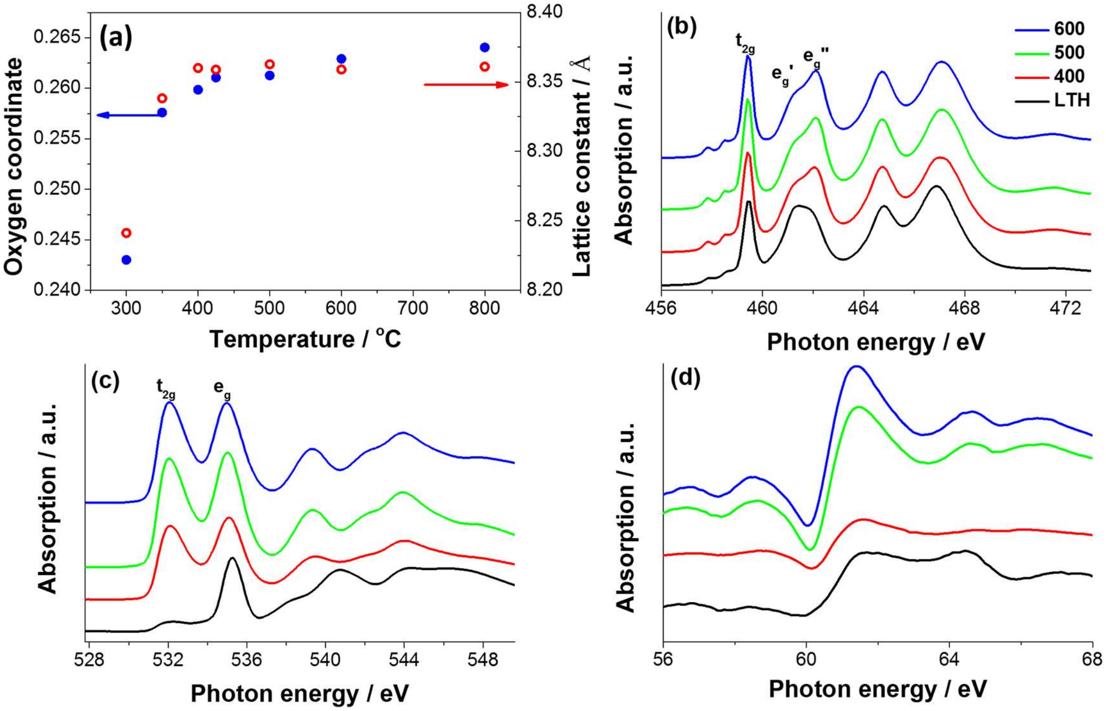

Figure 5.4. (a) Oxygen coordinated for different annealed LTO crystals derived from Rietveld refinement. Normalized TEY mode of XANES of (b) Ti L-edge, (c) O K-edge and (d) Li K-edge collected from LTH (black), and LTO nanosheets annealed at 400 (red), 500 (green) and 600°C (blue) for 6 hours.

characteristics. This ratio is proportional to the hole numbers in the unoccupied 3*d* orbitals, and hence higher ratio means higher Ti-O covalency. As a result, the 600°C annealed LTO exhibits the strongest covalent Ti-O bonds according to the ratio magnitude; while the 400°C annealed one behaves the opposite.

In the low-temperature (*e.g.*, 400°C) annealed LTO crystal, the charge density variation due to more ionic (i.e., less covalent) Ti-O bonds, is balanced by more covalent Li-O bonds. In Li K-edge XANES (Figure 5.4d), as-prepared LTH (black) exhibits features similar to Li_2CO_3 and $LiOH \cdot H_2O$. This implies again that the surface chemistry is determined by lithium hydroxide-like compounds in the interlayer space. A significant peak is presented at 62 eV in Li K-edge XANES spectra (Figure 5.4d), whose intensity highly depends on the ionic properties of Li-O bonds. This feature is prominent in the spectra of LTO annealed at 500 and 600°C but not in the spectra of

LTO annealed at 400°C. Usually the electrons in Li 1*s* orbitals are excited to the excited level of Li 2*p* orbitals, and the created holes would interact with the excited electrons and hence form excitons. But the deeply hybridized Li-O bonds make Li 2*s* or 2*p* orbitals occupied and thus causing weak excitons. As a result, the exciton peak at 62 eV becomes less prominent. In other words, the LTO nanocrystals annealed at lower temperature, would bear severe residual thermal strain as oxygen ions sit closer to Li ions. Such strain-induced distortion in turn would cause higher covalency in Li-O bonds.

5.4.5. Dependence of electrochemistry on residual strain

By performing annealing at different temperatures, the electronic structure of LTO spinel can be effectively modified. As a consequence, the electrochemical performance of LTO nanosheet crystals, including their cyclability and rate capability, is altered in response to the modified electronic structure.

Figure 5.5a, c and e shows the polarization evolution during galvanostatic testing at 1C rate of the 400, 500 and 600°C annealed samples, respectively; as it can be seen the voltage plateau is shifting during cycling as represented by the contour plots. The corresponding capacity results of 1C cycle tests are given in Figure 5.5b and Figure C11a of the Appendix C. According to our earlier research,[5.23], the polarization evolution corresponds to formation kinetics of relaxed LTO that is induced by 8*a*-16*c* cointercalation in the near-surface region. And relaxed LTO formation would lead to considerable irreversible capacity loss. In the formation cycle at 1C rate, the 400°C annealed LTO has the highest initial irreversible loss and lowest Coulombic efficiency of only 80.5%. This indicates that LTO nanosheet crystals annealed at lower temperature tolerate more 8*a*-16*c* cointercalation. Possible explanations for this could be either the higher surface area that provides more available active sites for cointercalation, or more flexible structure which allows deeper degree of cointercalation. However, this trend in the irreversible loss cannot be satisfactorily explained by merely the factor of surface area. According to BET specific surface area characterization, there is only small difference among the different LTO nanocrystal samples (Table C3 of the Appendix C). In other words, the influence of the crystal structure and bonding characteristics must be considered.

As mentioned above, the strong covalency of Li-O bonds in the LTO nanocrystals annealed at 400°C would screen Coulomb repulsion between the cointercalated Li ions in the neighboring 8*a* and 16*c* sites. As a result, LTO nanocrystals annealed at lower temperature are capable of accommodating excess intercalated Li ions in the near-surface region, because of their relaxed LTO structure induced by residual strain. A deeper degree of cointercalation would require longer periods (*i.e.*, more cycles) to accomplish the transformation, whose rate is expected to depend on the applied current, operational voltage range, etc. For example, in the case of 400°C annealed LTO nanocrystals, it took 7 cycles to finish the first transition of polarization increase; it took another 5 cycles to complete the formation of irreversibly lithiated LTO, as evident by the second transition of polarization decrease at ca. 12 cycles in Figure 5.5a. In contrast, it only took 2 cycles and 3 cycles, respectively, for each transition with 600°C annealed LTO nanocrystals.

But annealing at elevated temperature does not only improve cyclablity by suppressing capacity fade caused by cointercalation-induced structural relaxation, but also improves the rate capability of LTO nanosheet anodes (see Ragone plot in Figure 5.5d) by reducing the irreversibly intercalated sites that impede Li ion transport. As illustrated in Figure C11c of the Appendix C, the 400°C annealed LTO exhibits the lowest Coulombic efficiency of merely 77 % in the C/20 formation cycle. High population of irreversibly intercalated Li ions retards Li diffusion due to lower Li-ion diffusivity / conductivity as shown in Figure C12d.

As a result, the 400°C annealed LTO delivers relatively low capacity in the subsequent cycles especially at faster rate (see Ragone plot in Figure 5.5d). On the contrary, 600°C annealed LTO shows better Coulombic efficiency of 93% in the formation cycle and therefore can deliver more capacity at high rate. In terms of attained capacity at high rate, the LTO nanosheet crystals annealed at 600°C (NS@600) yielded an impressive ~140 mAh/g at 20C versus only ~80 mAh/g and ~60 mAh/g for LTO NS@500 and LTO NS@400 respectively. The whole picture of structural stability-dependent rate capability becomes clearer when comparing their exhibited overpotential at various rates. According to the Tafel plot of Figure 5.5f, there is no difference in overpotential behavior among the three LTO samples. From the above it is concluded that the rate capability of LTO nanosheet electrodes is determined by structural stability instead of polarization factors. The structural stability (*i.e.* suppression of cointercalation-induced structural relaxation) is achieved via elimination of residual thermal strain by regulating the annealing temperature.

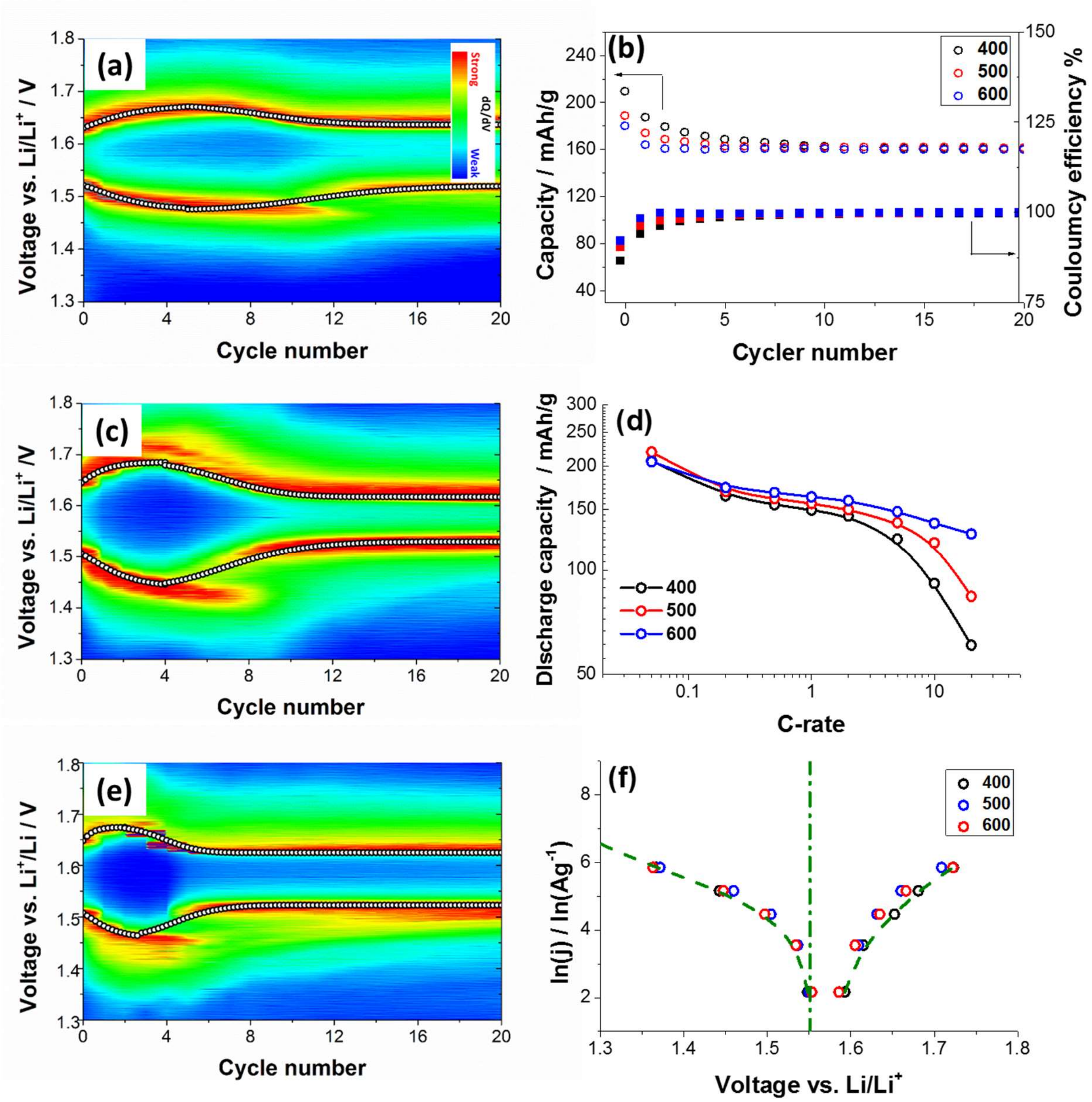

Figure 5.5. Polarization evolution during galvanostatic charge/discharge at 1C rate of (a) 400, (c) 500, (e) 600°C annealed LTO nanosheet electrodes, and (b) the corresponding cycling performance of each sample. (d) Ragone plot in the current range of 0.05-20 C, of which the voltage plateau variation with respect to the applied constant current is presented as Tafel plot in (f). The green dash line in (f) represents the equilibrium potential of LTO 1.55 V *vs.* Li/Li$^+$.

5.5.Conclusion

The formation mechanism of LTO spinel nanosheet crystals via topotactic transformation of 2D LTH lepidocrocite is determined. This understanding could guide the design and production of advanced two-dimensionally functional nanomaterials using similar strategies. For example, preparation of $LiFePO_4$ using γ-FeOOH as precursor may be explored. Properly manipulating the chemical bonding (degree of covalency) properties is essential to design structurally stable intercalation nano-compounds for long-term cyclability at high rate. Nanocrystals with distorted lattice originated from the residual strain of phase transformations are vulnerable to the cointercalation-induced structural relaxation, hence to shorter lifespan due to increased capacity fade. Eliminating residual strain by controlled annealing was shown to enhance both the rate capability and cyclability, and this opens a path for high-performance LTO electrode materials based on stabilized nanocrystal structure. The findings of this work can also rationalize the size-effects of nano-LTO, for instance, the reported size-dependent diffusivity of nano-LTO. According the CV results presented in Figure C12 in the Appendix C, despite having LTO nanocrystals prepared with approximately similar surface area, it is the stabilized LTO nanocrystals annealed at 600ºC that exhibit the best Li diffusivity; this is so because there are less irreversibly trapped Li ions impeding the diffusion process.

5.6.Acknowledgments

This work is supported through a Hydro-Québec/Natural Sciences & Engineering Research Council of Canada (NSERC) Collaborative R&D research grant. Synchrotron radiation measurements were performed at the CLS, which is supported by CFI, NSERC, University of Saskatchewan, Province of Saskatchewan, Western Economic Diversification Canada, NRC Canada, and CIHR. Expert assistance by Dr. Lucia Zuin in CLS for data collection and processing of Li K-edge XANES spectra is especially acknowledged.

5.7.References

(**5.**1) Gröger, O.; Gasteiger, H. A.; Suchsland, J.-P. Review—Electromobility: Batteries or Fuel Cells? *J. Electrochem. Soc.* **2015,** *162* (14), A2605.

(**5.**2) Ohzuku, T.; Ueda, A.; Yamamoto, N. Zero-Strain Insertion Material of $LiLi_{1/3}Ti_{5/3}O_4$ for Rechargeable Lithium Cells. *J. Electrochem. Soc.* **1995,** *142* (5), 1431.

(**5.**3) Scharner, S.; Weppner, W.; Schmid-Beurmann, P. Evidence of Two-Phase Formation upon Lithium Insertion into the $Li_{1.33}Ti_{1.67}O_4$ Spinel. *J. Electrochem. Soc.* **1999,** *146* (3), 857.

(**5.**4) Pan, H.; Lu, X.; Yu, X.; Hu, Y.-S.; Li, H.; Yang, X.-Q.; Chen, L. Sodium Storage and Transport Properties in Layered $Na_2Ti_3O_7$ for Room-Temperature Sodium-Ion Batteries. *Adv. Energy Mater.* **2013,** *3* (9), 1186.

(**5.**5) Lu, X.; Zhao, L.; He, X.; Xiao, R.; Gu, L.; Hu, Y.-S.; Li, H.; Wang, Z.; Duan, X.; Chen, L.et al. Lithium Storage in $Li_4Ti_5O_{12}$ Spinel: The Full Static Picture from Electron Microscopy. *Adv. Mater.* **2012,** *24* (24), 3233.

(**5.**6) Lu, X.; Gu, L.; Hu, Y.-S.; Chiu, H.-C.; Li, H.; Demopoulos, G. P.; Chen, L. New Insight into the Atomic-Scale Bulk and Surface Structure Evolution of $Li_4Ti_5O_{12}$ Anode. *J. Am. Chem. Soc.* **2015,** *137* (4), 1581.

(**5.**7) Su, D.; Wang, F.; Ma, C.; Jiang, N. Engineering nano-composite Li4Ti5O12 anodes via scanning electron-probe fabrication. *Nano Energy* **2013,** *2* (3), 343.

(**5.**8) Coleman, J. N.; Lotya, M.; O'Neill, A.; Bergin, S. D.; King, P. J.; Khan, U.; Young, K.; Gaucher, A.; De, S.; Smith, R. J.et al. Two-dimensional nanosheets produced by liquid exfoliation of layered materials. *Science* **2011,** *331* (6017), 568.

(**5.**9) Nicolosi, V.; Chhowalla, M.; Kanatzidis, M. G.; Strano, M. S.; Coleman, J. N. Liquid Exfoliation of Layered Materials. *Science* **2013,** *340* (6139), 1224619.

(**5.**10) Novoselov, K. S.; Jiang, D.; Schedin, F.; Booth, T. J.; Khotkevich, V. V.; Morozov, S. V.; Geim, A. K. Two-dimensional atomic crystals. *Proc Natl Acad Sci U S A* **2005,** *102* (30), 10451.

(**5.**11) Wang, C.; Wang, S.; Tang, L.; He, Y.-B.; Gan, L.; Li, J.; Du, H.; Li, B.; Lin, Z.; Kang, F. A robust strategy for crafting monodisperse Li4Ti5O12 nanospheres as superior rate anode for lithium ion batteries. *Nano Energy* **2016,** *21*, 133.

(**5.**12) Ziebarth, B.; Klinsmann, M.; Eckl, T.; Elsässer, C. Lithium diffusion in the spinel phaseL$Li_4Ti_5O_{12}$ and in the rocksalt phase $Li_7Ti_5O_{12}$ of lithium titanate from first principles. *Phys. Rev. B: Condens. Matter Mater. Phys.* **2014,** *89* (17), 174301.

(**5.**13) Schmidt, W.; Bottke, P.; Sternad, M.; Gollob, P.; Hennige, V.; Wilkening, M. Small Change-Great Effect: Steep Increase of Li Ion Dynamics in $Li_4Ti_5O_{12}$ at the Early Stages of Chemical Li Insertion. *Chem. Mater.* **2015,** *27* (5), 1740.

(**5.**14) Wagemaker, M.; van Eck, E. R.; Kentgens, A. P.; Mulder, F. M. Li-ion diffusion in the equilibrium nanomorphology of spinel $Li_{4+x}Ti_5O_{12}$. *J. Phys. Chem. B* **2009,** *113* (1), 224.

(**5.**15) Pang, W. K.; Peterson, V. K.; Sharma, N.; Shiu, J. J.; Wu, S. H. Lithium Migration in $Li_4Ti_5O_{12}$ Studied Using in Situ Neutron Powder Diffraction. *Chem. Mater.* **2014,** *26* (7), 2318.

(**5.**16) Wagemaker, M.; Simon, D. R.; Kelder, E. M.; Schoonman, J.; Ringpfeil, C.; Haake, U.; Lutzenkirchen-Hecht, D.; Frahm, R.; Mulder, F. M. A kinetic two-phase and equilibrium solid solution in spinel $Li_{4+x}Ti_5O_{12}$. *Adv. Mater.* **2006,** *18* (23), 3169.

(**5.**17) Laumann, A.; Boysen, H.; Bremholm, M.; Fehr, K. T.; Hoelzel, M.; Holzapfel, M. Lithium Migration at High Temperatures in $Li_4Ti_5O_{12}$ Studied by Neutron Diffraction. *Chem. Mater.* **2011,** *23* (11), 2753.

(**5.**18) Borghols, W. J. H.; Wagemaker, M.; Lafont, U.; Kelder, E. M.; Mulder, F. M. Size Effects in the $Li_{4+x}Ti_5O_{12}$ Spinel. *J. Am. Chem. Soc.* **2009,** *131* (49), 17786.

(**5.**19) Feng, W.; Lijun, W.; Chao, M.; Dong, S.; Yimei, Z.; Jason, G. Excess lithium storage and charge compensation in nanoscale $Li_{4+x}Ti_5O_{12}$. *Nanotechnology* **2013,** *24* (42), 424006.

(**5.**20) Wagemaker, M.; Mulder, F. M. Properties and promises of nanosized insertion materials for Li-ion batteries. *Acc. Chem. Res.* **2013,** *46* (5), 1206.

(**5.**21) Kavan, L.; Procházka, J.; Spitler, T. M.; Kalbáč, M.; Zukalová, M.; Drezen, T.; Grätzel, M. Li Insertion into $Li_4Ti_5O_{12}$ (Spinel) : Charge Capability vs. Particle Size in Thin-Film Electrodes. *J. Electrochem. Soc.* **2003,** *150* (7), A1000.

(**5.**22) Ganapathy, S.; Wagemaker, M. Nanosize Storage Properties in Spinel $Li_4Ti_5O_{12}$ Explained by Anisotropic Surface Lithium Insertion. *Acs Nano* **2012,** *6* (10), 8702.

(**5.**23) Chiu, H.-C.; Lu, X.; Zhou, J.; Gu, L.; Reid, J.; Gauvin, R.; Zaghib, K.; Demopoulos, G. P. Capacity Fade Mechanism of $Li_4Ti_5O_{12}$ Nanosheet Anode. *Adv. Energy Mater.* **2017,** *7* (5), 1601825.

(**5.**24) Hirayama, M.; Kim, K.; Toujigamori, T.; Cho, W.; Kanno, R. Epitaxial growth and electrochemical properties of $Li_4Ti_5O_{12}$ thin-film lithium battery anodes. *Dalton Trans.* **2011,** *40* (12), 2882.

(**5.**25) Shi, Y.; Gao, J.; Abruña, H. D.; Liu, H.; Li, H.; Wang, J.; Wu, Y. Rapid synthesis of Li4Ti5O12/graphene composite with superior rate capability by a microwave-assisted hydrothermal method. *Nano Energy* **2014,** *8*, 297.

(**5.**26) Li, N.; Mei, T.; Zhu, Y.; Wang, L.; Liang, J.; Zhang, X.; Qian, Y.; Tang, K. Hydrothermal synthesis of layered $Li_{1.81}H_{0.19}Ti_2O_5.xH_2O$ nanosheets and their transformation to single-crystalline $Li_4Ti_5O_{12}$ nanosheets as the anode materials for Li-ion batteries. *CrystEngComm* **2012,** *14* (20), 6435.

(**5.**27) Chiu, H. C.; Brodusch, N.; Gauvin, R.; Guerfi, A.; Zaghib, K.; Demopoulos, G. P. Aqueous Synthesized Nanostructured $Li_4Ti_5O_{12}$ for High-Performance Lithium Ion Battery Anodes. *J. Electrochem. Soc.* **2013,** *160* (5), A3041.

(**5.**28) Wang, Y.-Q.; Gu, L.; Guo, Y.-G.; Li, H.; He, X.-Q.; Tsukimoto, S.; Ikuhara, Y.; Wan, L.-J. Rutile-TiO_2 Nanocoating for a High-Rate $Li_4Ti_5O_{12}$ Anode of a Lithium-Ion Battery. *J. Am. Chem. Soc.* **2012,** *134* (18), 7874.

(**5.**29) Liu, J.; Li, X.; Yang, J.; Geng, D.; Li, Y.; Wang, D.; Li, R.; Sun, X.; Cai, M.; Verbrugge, M. W. Microwave-assisted hydrothermal synthesis of nanostructured spinel $Li_4Ti_5O_{12}$ as anode materials for lithium ion batteries. *Electrochim. Acta* **2012,** *63* (0), 100.

(**5.**30) Chen, J.; Yang, L.; Fang, S.; Tang, Y. Synthesis of sawtooth-like $Li_4Ti_5O_{12}$ nanosheets as anode materials for Li-ion batteries. *Electrochim. Acta* **2010,** *55* (22), 6596.

(**5.**31) Chen, S.; Xin, Y.; Zhou, Y.; Ma, Y.; Zhou, H.; Qi, L. Self-supported $Li_4Ti_5O_{12}$ nanosheet arrays for lithium ion batteries with excellent rate capability and ultralong cycle life. *Energy. Environ. Sci.* **2014**, DOI:10.1039/c3ee42646g 10.1039/c3ee42646g.

(**5.**32) Chiu, H.-C.; Lu, X.; Elouatik, S.; Zaghib, K.; Demopoulos, G. P. Formation of Lithium Titanate Hydrate Nanosheets: Insight into a Two-Dimension Growth Mechanism by in Situ Raman. *Cryst. Growth. Des.* **2016,** *16* (7), 3898.

(**5.**33) Wang, C.; Wang, S.; He, Y.-B.; Tang, L.; Han, C.; Yang, C.; Wagemaker, M.; Li, B.; Yang, Q.-H.; Kim, J.-K.et al. Combining Fast Li-Ion Battery Cycling with Large Volumetric Energy Density: Grain Boundary Induced High Electronic and Ionic Conductivity in Li4Ti5O12 Spheres of Densely Packed Nanocrystallites. *Chem. Mater.* **2015,** *27* (16), 5647.

(**5.**34) Han, C.; He, Y.-B.; Li, B.; Li, H.; Ma, J.; Du, H.; Qin, X.; Yang, Q.-H.; Kang, F. Highly Crystalline Lithium Titanium Oxide Sheets Coated with Nitrogen-Doped Carbon enable High-Rate Lithium-Ion Batteries. *ChemSusChem* **2014,** *7* (9), 2567.

(**5.**35) Xiao, L.; Chen, G.; Sun, J.; Chen, D.; Xu, H.; Zheng, Y. Facile synthesis of $Li_4Ti_5O_{12}$ nanosheets stacked by ultrthin nanoflakes for high performance lithium ion batteries. *Journal of Materials Chemistry A* **2013**, DOI:10.1039/c3ta12569f 10.1039/c3ta12569f.

(**5.**36) Ravel, B.; Newville, M. ATHENA, ARTEMIS, HEPHAESTUS: data analysis for X-ray absorption spectroscopy using IFEFFIT. *J. Synchrotron Radiat.* **2005,** *12* (Pt 4), 537.

(**5.**37) Gao, T.; Fjellvåg, H.; Norby, P. Defect Chemistry of a Zinc-Doped Lepidocrocite Titanate $Cs_xTi_{2-x/2}Zn_{x/2}O_4$ ($x = 0.7$) and its Protonic Form. *Chem. Mater.* **2009,** *21* (15), 3503.

(**5.**38) Shirpour, M.; Cabana, J.; Doeff, M. Lepidocrocite-type Layered Titanate Structures: New Lithium and Sodium Ion Intercalation Anode Materials. *Chem. Mater.* **2014,** *26* (8), 2502.

(**5.**39) Sasaki, T.; Watanabe, M.; Michiue, Y.; Komatsu, Y.; Izumi, F.; Takenouchi, S. Preparation and Acid-Base Properties of a Protonated Titanate with the Lepidocrocite-Like Layer Structure. *Chem. Mater.* **1995,** *7* (5), 1001.

(**5.**40) Sasaki, T.; Kooli, F.; Iida, M.; Michiue, Y.; Takenouchi, S.; Yajima, Y.; Izumi, F.; Chakoumakos, B. C.; Watanabe, M. A Mixed Alkali Metal Titanate with the Lepidocrocite-like Layered Structure. Preparation, Crystal Structure, Protonic Form, and Acid−Base Intercalation Properties. *Chem. Mater.* **1998,** *10* (12), 4123.

(**5.**41) Grey, I. E.; Li, C.; Madsen, I. C.; Watts, J. A. The stability and structure of $Cs_x[Ti_{2-x/4}\square_{x/4}]O_4$, $0.61 < x < 0.65$. *J. Solid State Chem.* **1987,** *66* (1), 7.

(**5.**42) Kooli, F.; Sasaki, T.; Watanabe, M. Pillaring of a lepidocrocite-like titanate with aluminium oxide and characterization. *Micropor. Mesopor. Mat.* **1999,** *28* (3), 495.

(**5.**43) Ma, R. Z.; Bando, Y.; Sasaki, T. Nanotubes of lepidocrocite titanates. *Chem. Phy. Lett.* **2003,** *380* (5-6), 577.

(**5.**44) Gao, T.; Fjeld, H.; Fjellvag, H.; Norby, T.; Norby, P. In situ studies of structural stability and proton conductivity of titanate nanotubes. *Energy. Environ. Sci.* **2009,** *2* (5), 517.

(**5.**45) Hunt, J. A.; Williams, D. B. Electron Energy-Loss Spectrum-Imaging. *Ultramicroscopy* **1991,** *38* (1), 47.

(**5.**46) Leapman, R. D.; Swyt, C. R. Separation of Overlapping Core Edges in Electron-Energy Loss Spectra by Multiple-Least-Squares Fitting. *Ultramicroscopy* **1988,** *26* (4), 393.

(**5.**47) Gao, T.; Fjellvåg, H.; Norby, P. Raman Scattering Properties of a Protonic Titanate $H_xTi_{2-x/4}\square_{x/4}O_4{\cdot}H_2O$ (□, vacancy; x = 0.7) with Lepidocrocite-Type Layered Structure. *J. Phys. Chem. B* **2008,** *112* (31), 9400.

(**5.**48) Gao, T.; Fjellvag, H.; Norby, P. Crystal structures of titanate nanotubes: a Raman scattering study. *Inorg Chem* **2009,** *48* (4), 1423.

(**5.**49) Gao, T.; Wu, Q. L.; Fjellvag, H.; Norby, P. Topological properties of titanate nanotubes. *J. Phys. Chem. C* **2008,** *112* (23), 8548.

(**5.**50) Ma, R.; Fukuda, K.; Sasaki, T.; Osada, M.; Bando, Y. Structural features of titanate nanotubes/nanobelts revealed by Raman, X-ray absorption fine structure and electron diffraction characterizations. *J. Phys. Chem. B* **2005,** *109* (13), 6210.

(**5.**51) Chem. Commun.Ma, R.; Sasaki, T.; Bando, Y. Alkali metal cation intercalation properties of titanate nanotubes. *Chem. Commun.* **2005**, DOI:10.1039/B415983G 10.1039/B415983G(7), 948.

(**5.**52) Raju, M.; van Duin, A. C. T.; Fichthorn, K. A. Mechanisms of Oriented Attachment of TiO_2 Nanocrystals in Vacuum and Humid Environments: Reactive Molecular Dynamics. *Nano Lett.* **2014,** *14* (4), 1836.

(**5.**53) Bahrig, L.; Hickey, S. G.; Eychmuller, A. Mesocrystalline materials and the involvement of oriented attachment - a review. *CrystEngComm* **2014,** *16* (40), 9408.

(**5.**54) Xue, X.; Penn, R. L.; Leite, E. R.; Huang, F.; Lin, Z. Crystal growth by oriented attachment: kinetic models and control factors. *CrystEngComm* **2014,** *16* (8), 1419.

(**5.**55) Zhan, H.; Yang, X.; Wang, C.; Chen, J.; Wen, Y.; Liang, C.; Greer, H. F.; Wu, M.; Zhou, W. Multiple Nucleation and Crystal Growth of Barium Titanate. *Cryst. Growth. Des.* **2012,** *12* (3), 1247.

(**5.**56) Iddir, H.; Öğüt, S.; Zapol, P.; Browning, N. D. Diffusion mechanisms of native point defects in rutile TiO_2: *ab-initio* total-energy calculations. *Phys. Rev. B: Condens. Matter Mater. Phys.* **2007,** *75* (7), 073203.

(**5.**57) de Groot, F. M. F.; Fuggle, J. C.; Thole, B. T.; Sawatzky, G. A. $L_{2,3}$ x-ray-absorption edges of d^0 compounds: K^+, Ca^{2+}, Sc^{3+}, and Ti^{4+} in O_h (octahedral) symmetry. *Phys. Rev. B: Condens. Matter Mater. Phys.* **1990,** *41* (2), 928.

(**5.**58) Henderson, S. G.; Liu, X.; Fleet, E. M. A Ti L-edge X-ray absorption study of Ti-silicate glasses. *Phys. Chem. Miner.* **2002,** *29* (1), 32.

(**5.**59) Zhou, J. G.; Fang, H. T.; Maley, J. M.; Murphy, M. W.; Peter Ko, J. Y.; Cutler, J. N.; Sammynaiken, R.; Sham, T. K.; Liu, M.; Li, F. Electronic structure of TiO_2 nanotube arrays from X-ray absorption near edge structure studies. *J. Mater. Chem.* **2009,** *19* (37), 6804.

(**5.**1) Gröger, O.; Gasteiger, H. A.; Suchsland, J.-P. Review—Electromobility: Batteries or Fuel Cells? *J. Electrochem. Soc.* **2015,** *162* (14), A2605.

(**5.**2) Ohzuku, T.; Ueda, A.; Yamamoto, N. Zero-Strain Insertion Material of $LiLi_{1/3}Ti_{5/3}O_4$ for Rechargeable Lithium Cells. *J. Electrochem. Soc.* **1995,** *142* (5), 1431.

(**5.**3) Scharner, S.; Weppner, W.; Schmid-Beurmann, P. Evidence of Two-Phase Formation upon Lithium Insertion into the $Li_{1.33}Ti_{1.67}O_4$ Spinel. *J. Electrochem. Soc.* **1999,** *146* (3), 857.

(**5.**4) Pan, H.; Lu, X.; Yu, X.; Hu, Y.-S.; Li, H.; Yang, X.-Q.; Chen, L. Sodium Storage and Transport Properties in Layered $Na_2Ti_3O_7$ for Room-Temperature Sodium-Ion Batteries. *Adv. Energy Mater.* **2013,** *3* (9), 1186.

(**5.**5) Lu, X.; Zhao, L.; He, X.; Xiao, R.; Gu, L.; Hu, Y.-S.; Li, H.; Wang, Z.; Duan, X.; Chen, L.et al. Lithium Storage in $Li_4Ti_5O_{12}$ Spinel: The Full Static Picture from Electron Microscopy. *Adv. Mater.* **2012,** *24* (24), 3233.

(**5.**6) Lu, X.; Gu, L.; Hu, Y.-S.; Chiu, H.-C.; Li, H.; Demopoulos, G. P.; Chen, L. New Insight into the Atomic-Scale Bulk and Surface Structure Evolution of $Li_4Ti_5O_{12}$ Anode. *J. Am. Chem. Soc.* **2015,** *137* (4), 1581.

(**5.**7) Su, D.; Wang, F.; Ma, C.; Jiang, N. Engineering nano-composite Li4Ti5O12 anodes via scanning electron-probe fabrication. *Nano Energy* **2013,** *2* (3), 343.

(**5.**8) Coleman, J. N.; Lotya, M.; O'Neill, A.; Bergin, S. D.; King, P. J.; Khan, U.; Young, K.; Gaucher, A.; De, S.; Smith, R. J.et al. Two-dimensional nanosheets produced by liquid exfoliation of layered materials. *Science* **2011,** *331* (6017), 568.

(**5.**9) Nicolosi, V.; Chhowalla, M.; Kanatzidis, M. G.; Strano, M. S.; Coleman, J. N. Liquid Exfoliation of Layered Materials. *Science* **2013,** *340* (6139), 1224619.

(**5.**10) Novoselov, K. S.; Jiang, D.; Schedin, F.; Booth, T. J.; Khotkevich, V. V.; Morozov, S. V.; Geim, A. K. Two-dimensional atomic crystals. *Proc Natl Acad Sci U S A* **2005,** *102* (30), 10451.

(**5.**11) Wang, C.; Wang, S.; Tang, L.; He, Y.-B.; Gan, L.; Li, J.; Du, H.; Li, B.; Lin, Z.; Kang, F. A robust strategy for crafting monodisperse Li4Ti5O12 nanospheres as superior rate anode for lithium ion batteries. *Nano Energy* **2016,** *21*, 133.

(**5.**12) Ziebarth, B.; Klinsmann, M.; Eckl, T.; Elsässer, C. Lithium diffusion in the spinel phaseLLi$_4$Ti$_5$O$_{12}$ and in the rocksalt phase Li$_7$Ti$_5$O$_{12}$ of lithium titanate from first principles. *Phys. Rev. B: Condens. Matter Mater. Phys.* **2014,** *89* (17), 174301.

(**5.**13) Schmidt, W.; Bottke, P.; Sternad, M.; Gollob, P.; Hennige, V.; Wilkening, M. Small Change-Great Effect: Steep Increase of Li Ion Dynamics in Li$_4$Ti$_5$O$_{12}$ at the Early Stages of Chemical Li Insertion. *Chem. Mater.* **2015,** *27* (5), 1740.

(**5.**14) Wagemaker, M.; van Eck, E. R.; Kentgens, A. P.; Mulder, F. M. Li-ion diffusion in the equilibrium nanomorphology of spinel Li$_{4+x}$Ti$_5$O$_{12}$. *J. Phys. Chem. B* **2009,** *113* (1), 224.

(**5.**15) Pang, W. K.; Peterson, V. K.; Sharma, N.; Shiu, J. J.; Wu, S. H. Lithium Migration in Li$_4$Ti$_5$O$_{12}$ Studied Using in Situ Neutron Powder Diffraction. *Chem. Mater.* **2014,** *26* (7), 2318.

(**5.**16) Wagemaker, M.; Simon, D. R.; Kelder, E. M.; Schoonman, J.; Ringpfeil, C.; Haake, U.; Lutzenkirchen-Hecht, D.; Frahm, R.; Mulder, F. M. A kinetic two-phase and equilibrium solid solution in spinel Li$_{4+x}$Ti$_5$O$_{12}$. *Adv. Mater.* **2006,** *18* (23), 3169.

(**5.**17) Laumann, A.; Boysen, H.; Bremholm, M.; Fehr, K. T.; Hoelzel, M.; Holzapfel, M. Lithium Migration at High Temperatures in Li$_4$Ti$_5$O$_{12}$ Studied by Neutron Diffraction. *Chem. Mater.* **2011,** *23* (11), 2753.

(**5.**18) Borghols, W. J. H.; Wagemaker, M.; Lafont, U.; Kelder, E. M.; Mulder, F. M. Size Effects in the Li$_{4+x}$Ti$_5$O$_{12}$ Spinel. *J. Am. Chem. Soc.* **2009,** *131* (49), 17786.

(**5.**19) Feng, W.; Lijun, W.; Chao, M.; Dong, S.; Yimei, Z.; Jason, G. Excess lithium storage and charge compensation in nanoscale $Li_{4+x}Ti_5O_{12}$. *Nanotechnology* **2013,** *24* (42), 424006.

(**5.**20) Wagemaker, M.; Mulder, F. M. Properties and promises of nanosized insertion materials for Li-ion batteries. *Acc. Chem. Res.* **2013,** *46* (5), 1206.

(**5.**21) Kavan, L.; Procházka, J.; Spitler, T. M.; Kalbáč, M.; Zukalová, M.; Drezen, T.; Grätzel, M. Li Insertion into $Li_4Ti_5O_{12}$ (Spinel) : Charge Capability vs. Particle Size in Thin-Film Electrodes. *J. Electrochem. Soc.* **2003,** *150* (7), A1000.

(**5.**22) Ganapathy, S.; Wagemaker, M. Nanosize Storage Properties in Spinel $Li_4Ti_5O_{12}$ Explained by Anisotropic Surface Lithium Insertion. *Acs Nano* **2012,** *6* (10), 8702.

(**5.**23) Chiu, H.-C.; Lu, X.; Zhou, J.; Gu, L.; Reid, J.; Gauvin, R.; Zaghib, K.; Demopoulos, G. P. Capacity Fade Mechanism of $Li_4Ti_5O_{12}$ Nanosheet Anode. *Adv. Energy Mater.* **2017,** *7* (5), 1601825.

(**5.**24) Hirayama, M.; Kim, K.; Toujigamori, T.; Cho, W.; Kanno, R. Epitaxial growth and electrochemical properties of $Li_4Ti_5O_{12}$ thin-film lithium battery anodes. *Dalton Trans.* **2011,** *40* (12), 2882.

(**5.**25) Shi, Y.; Gao, J.; Abruña, H. D.; Liu, H.; Li, H.; Wang, J.; Wu, Y. Rapid synthesis of Li4Ti5O12/graphene composite with superior rate capability by a microwave-assisted hydrothermal method. *Nano Energy* **2014,** *8*, 297.

(**5.**26) Li, N.; Mei, T.; Zhu, Y.; Wang, L.; Liang, J.; Zhang, X.; Qian, Y.; Tang, K. Hydrothermal synthesis of layered $Li_{1.81}H_{0.19}Ti_2O_5.xH_2O$ nanosheets and their transformation to single-crystalline $Li_4Ti_5O_{12}$ nanosheets as the anode materials for Li-ion batteries. *CrystEngComm* **2012,** *14* (20), 6435.

(**5.**27) Chiu, H. C.; Brodusch, N.; Gauvin, R.; Guerfi, A.; Zaghib, K.; Demopoulos, G. P. Aqueous Synthesized Nanostructured $Li_4Ti_5O_{12}$ for High-Performance Lithium Ion Battery Anodes. *J. Electrochem. Soc.* **2013,** *160* (5), A3041.

(**5.**28) Wang, Y.-Q.; Gu, L.; Guo, Y.-G.; Li, H.; He, X.-Q.; Tsukimoto, S.; Ikuhara, Y.; Wan, L.-J. Rutile-TiO_2 Nanocoating for a High-Rate $Li_4Ti_5O_{12}$ Anode of a Lithium-Ion Battery. *J. Am. Chem. Soc.* **2012,** *134* (18), 7874.

(**5.**29) Liu, J.; Li, X.; Yang, J.; Geng, D.; Li, Y.; Wang, D.; Li, R.; Sun, X.; Cai, M.; Verbrugge, M. W. Microwave-assisted hydrothermal synthesis of nanostructured spinel $Li_4Ti_5O_{12}$ as anode materials for lithium ion batteries. *Electrochim. Acta* **2012,** *63* (0), 100.

(**5.**30) Chen, J.; Yang, L.; Fang, S.; Tang, Y. Synthesis of sawtooth-like $Li_4Ti_5O_{12}$ nanosheets as anode materials for Li-ion batteries. *Electrochim. Acta* **2010,** *55* (22), 6596.

(**5.**31) Chen, S.; Xin, Y.; Zhou, Y.; Ma, Y.; Zhou, H.; Qi, L. Self-supported $Li_4Ti_5O_{12}$ nanosheet arrays for lithium ion batteries with excellent rate capability and ultralong cycle life. *Energy. Environ. Sci.* **2014**, DOI:10.1039/c3ee42646g 10.1039/c3ee42646g.

(**5.**32) Chiu, H.-C.; Lu, X.; Elouatik, S.; Zaghib, K.; Demopoulos, G. P. Formation of Lithium Titanate Hydrate Nanosheets: Insight into a Two-Dimension Growth Mechanism by in Situ Raman. *Cryst. Growth. Des.* **2016,** *16* (7), 3898.

(**5.**33) Wang, C.; Wang, S.; He, Y.-B.; Tang, L.; Han, C.; Yang, C.; Wagemaker, M.; Li, B.; Yang, Q.-H.; Kim, J.-K.et al. Combining Fast Li-Ion Battery Cycling with Large Volumetric Energy Density: Grain Boundary Induced High Electronic and Ionic Conductivity in Li4Ti5O12 Spheres of Densely Packed Nanocrystallites. *Chem. Mater.* **2015,** *27* (16), 5647.

(**5.**34) Han, C.; He, Y.-B.; Li, B.; Li, H.; Ma, J.; Du, H.; Qin, X.; Yang, Q.-H.; Kang, F. Highly Crystalline Lithium Titanium Oxide Sheets Coated with Nitrogen-Doped Carbon enable High-Rate Lithium-Ion Batteries. *ChemSusChem* **2014,** *7* (9), 2567.

(**5.**35) Xiao, L.; Chen, G.; Sun, J.; Chen, D.; Xu, H.; Zheng, Y. Facile synthesis of $Li_4Ti_5O_{12}$ nanosheets stacked by ultrthin nanoflakes for high performance lithium ion batteries. *Journal of Materials Chemistry A* **2013**, DOI:10.1039/c3ta12569f 10.1039/c3ta12569f.

(**5.**36) Ravel, B.; Newville, M. ATHENA, ARTEMIS, HEPHAESTUS: data analysis for X-ray absorption spectroscopy using IFEFFIT. *J. Synchrotron Radiat.* **2005,** *12* (Pt 4), 537.

(**5.**37) Gao, T.; Fjellvåg, H.; Norby, P. Defect Chemistry of a Zinc-Doped Lepidocrocite Titanate $Cs_xTi_{2-x/2}Zn_{x/2}O_4$ (x = 0.7) and its Protonic Form. *Chem. Mater.* **2009,** *21* (15), 3503.

(**5.**38) Shirpour, M.; Cabana, J.; Doeff, M. Lepidocrocite-type Layered Titanate Structures: New Lithium and Sodium Ion Intercalation Anode Materials. *Chem. Mater.* **2014,** *26* (8), 2502.

(**5.**39) Sasaki, T.; Watanabe, M.; Michiue, Y.; Komatsu, Y.; Izumi, F.; Takenouchi, S. Preparation and Acid-Base Properties of a Protonated Titanate with the Lepidocrocite-Like Layer Structure. *Chem. Mater.* **1995,** *7* (5), 1001.

(**5.**40) Sasaki, T.; Kooli, F.; Iida, M.; Michiue, Y.; Takenouchi, S.; Yajima, Y.; Izumi, F.; Chakoumakos, B. C.; Watanabe, M. A Mixed Alkali Metal Titanate with the Lepidocrocite-like Layered Structure. Preparation, Crystal Structure, Protonic Form, and Acid−Base Intercalation Properties. *Chem. Mater.* **1998,** *10* (12), 4123.

(**5.**41) Grey, I. E.; Li, C.; Madsen, I. C.; Watts, J. A. The stability and structure of $Cs_x[Ti_{2-x/4}\square_{x/4}]O_4$, $0.61 < x < 0.65$. *J. Solid State Chem.* **1987,** *66* (1), 7.

(**5.**42) Kooli, F.; Sasaki, T.; Watanabe, M. Pillaring of a lepidocrocite-like titanate with aluminium oxide and characterization. *Micropor. Mesopor. Mat.* **1999,** *28* (3), 495.

(**5.**43) Ma, R. Z.; Bando, Y.; Sasaki, T. Nanotubes of lepidocrocite titanates. *Chem. Phy. Lett.* **2003,** *380* (5-6), 577.

(**5.**44) Gao, T.; Fjeld, H.; Fjellvag, H.; Norby, T.; Norby, P. In situ studies of structural stability and proton conductivity of titanate nanotubes. *Energy. Environ. Sci.* **2009,** *2* (5), 517.

(**5.**45) Hunt, J. A.; Williams, D. B. Electron Energy-Loss Spectrum-Imaging. *Ultramicroscopy* **1991,** *38* (1), 47.

(**5.**46) Leapman, R. D.; Swyt, C. R. Separation of Overlapping Core Edges in Electron-Energy Loss Spectra by Multiple-Least-Squares Fitting. *Ultramicroscopy* **1988,** *26* (4), 393.

(**5.**47) Gao, T.; Fjellvåg, H.; Norby, P. Raman Scattering Properties of a Protonic Titanate $H_xTi_{2-x/4}\square_{x/4}O_4 \cdot H_2O$ ($\square$, vacancy; $x = 0.7$) with Lepidocrocite-Type Layered Structure. *J. Phys. Chem. B* **2008,** *112* (31), 9400.

(**5.**48) Gao, T.; Fjellvag, H.; Norby, P. Crystal structures of titanate nanotubes: a Raman scattering study. *Inorg Chem* **2009,** *48* (4), 1423.

(**5.**49) Gao, T.; Wu, Q. L.; Fjellvag, H.; Norby, P. Topological properties of titanate nanotubes. *J. Phys. Chem. C* **2008,** *112* (23), 8548.

(**5.**50) Ma, R.; Fukuda, K.; Sasaki, T.; Osada, M.; Bando, Y. Structural features of titanate nanotubes/nanobelts revealed by Raman, X-ray absorption fine structure and electron diffraction characterizations. *J. Phys. Chem. B* **2005,** *109* (13), 6210.

(**5.**51) Chem. Commun.Ma, R.; Sasaki, T.; Bando, Y. Alkali metal cation intercalation properties of titanate nanotubes. *Chem. Commun.* **2005**, DOI:10.1039/B415983G 10.1039/B415983G(7), 948.

(**5.**52) Raju, M.; van Duin, A. C. T.; Fichthorn, K. A. Mechanisms of Oriented Attachment of TiO_2 Nanocrystals in Vacuum and Humid Environments: Reactive Molecular Dynamics. *Nano Lett.* **2014,** *14* (4), 1836.

(**5.**53) Bahrig, L.; Hickey, S. G.; Eychmuller, A. Mesocrystalline materials and the involvement of oriented attachment - a review. *CrystEngComm* **2014,** *16* (40), 9408.

(**5.**54) Xue, X.; Penn, R. L.; Leite, E. R.; Huang, F.; Lin, Z. Crystal growth by oriented attachment: kinetic models and control factors. *CrystEngComm* **2014,** *16* (8), 1419.

(**5.**55) Zhan, H.; Yang, X.; Wang, C.; Chen, J.; Wen, Y.; Liang, C.; Greer, H. F.; Wu, M.; Zhou, W. Multiple Nucleation and Crystal Growth of Barium Titanate. *Cryst. Growth. Des.* **2012,** *12* (3), 1247.

(**5.**56) Iddir, H.; Öğüt, S.; Zapol, P.; Browning, N. D. Diffusion mechanisms of native point defects in rutile TiO_2: *ab-initio* total-energy calculations. *Phys. Rev. B: Condens. Matter Mater. Phys.* **2007,** *75* (7), 073203.

(**5.**57) de Groot, F. M. F.; Fuggle, J. C.; Thole, B. T.; Sawatzky, G. A. $L_{2,3}$ x-ray-absorption edges of d^0 compounds: K^+, Ca^{2+}, Sc^{3+}, and Ti^{4+} in O_h (octahedral) symmetry. *Phys. Rev. B: Condens. Matter Mater. Phys.* **1990,** *41* (2), 928.

(**5.**58) Henderson, S. G.; Liu, X.; Fleet, E. M. A Ti L-edge X-ray absorption study of Ti-silicate glasses. *Phys. Chem. Miner.* **2002,** *29* (1), 32.

(**5.**59) Zhou, J. G.; Fang, H. T.; Maley, J. M.; Murphy, M. W.; Peter Ko, J. Y.; Cutler, J. N.; Sammynaiken, R.; Sham, T. K.; Liu, M.; Li, F. Electronic structure of TiO_2 nanotube arrays from X-ray absorption near edge structure studies. *J. Mater. Chem.* **2009,** *19* (37), 6804.

Chapter 6

Capacity Fade Mechanism of $Li_4Ti_5O_{12}$ Nanosheet Anode

In Chapter 5, it was shown that strain induced into the 2-D LTO nanocrystals during their preparation leads to performance deterioration upon cycling. In this work, detailed characterization is undertaken to understand the exact Li storage mechanism of LTO nanosheets. It is shown that excess Li stored in nano-LTO (over the stoichiometric $Li_7Ti_5O_{12}$ of 175 mAh/g), as a result of Li-ion occupation at vacancies that are thermodynamically unfavorable in bulk LTO, modifies the properties near the surface through formation of an electrochemically inactive phase. This new phase growth is responsible for capacity fade. The study is complemented with the development of a kinetic model of the formation of relaxed LTO as the result of irreversible Li-ion intercalation in the near-surface region.

Meanwhile, LTO has been long considered as a SEI-free electrode material because of its high voltage at which intercalation/deintercalation occurs. However, recent research works have revealed that interfacial reactions take place between LTO and electrolyte carbonate components leading to destructive gas generation. Most of the previous efforts focused on the interfacial reaction mechanism, and little on the influence of the interfacial reaction on electrochemical performance. This issue is also addressed in this chapter. More specifically, it is shown that SEI does form as a result of the interfacial reaction, which leads to another type capacity fade beyond the one linked to strain-induced structural relaxation.

The study described in this Chapter was previously published in: **Chiu H-C**, Lu X, Zhou J, Gu L, Reid J, Gauvin R, et al. *Capacity Fade Mechanism of $Li_4Ti_5O_{12}$ Nanosheet Anode. Adv Energy Mater.* 2016:1601825. DOI: 10.1002/aenm.201601825.

6.1.Abstract

Zero-strain and long-term stability of nanoscale lithium titanate (LTO) anode materials make possible the fabrication of exceptionally stable lithium ion batteries. But one issue must be considered that of nanostructure-induced relaxation in 2D LTO nanosheets which profoundly modifies their Li storage properties and structural stability. Excessively intercalated Li ions at both

8*a* and 16*c* sites triggers nucleation of the relaxed LTO structure in the near-surface region, which impedes Li-ion diffusion and causes the increasing polarization of LTO nanosheet electrodes. Nuclei of relaxed LTO then undergo isotropic growth along the 3D Li-ion pathways in LTO to completely convert near-surface regions into relaxed LTO. With increasing population of trapped Li ions, the enhanced conductivity due to Ti^{4+}/Ti^{3+} reduction gradually eliminates the raised polarization. In the meantime, spontaneous electrolyte / LTO reduction to form the solid electrolyte interphase (SEI) starts playing a major role in capacity loss once the transformation of near-surface region into relaxed LTO becomes saturated. Elucidation of these fundamental intercalation-induced surface structure transformations contribute greatly into the design of highly performing 2D nanoscaled LTO and other electrode materials.

6.2.Introduction

A well-known intercalation compound,[6.1-3] spinel lithium titanate $Li_4Ti_5O_{12}$ (LTO) has become one of the most popular anode materials for secondary lithium ion batteries (LIBs), because of its extremely long-term stability and rapid lithium (Li) deintercalation.[6.4] The outstanding stability is accomplished by the "zero-strain" feature,[6.5] with negligible (0.2%) volume change during electrochemical Li intercalation/deintercalation.[6.6] During intercalation, spinel LTO $[Li]^{8a}[Li_{1/3}Ti_{5/3}]^{16d}[O_4]^{32e}$ with lattice parameter 8.3595 Å[6.3] undergoes a first-order phase transformation into rock-salt $[Li_2]^{16c}[Li_{1/3}Ti_{5/3}]^{16d}[O_4]^{32e}$ ($Li_7Ti_5O_{12}$) with lattice parameter 8.3538 Å.[6.7] This occurs by inserting one Li ion into the interstitial 16*c* sites and the simultaneous self-diffusion of originally existing Li ions at 8*a* sites in spinel structure towards the 16*c* sites.[6.8] As a result, the electrochemical response exhibits a very flat voltage plateau at 1.55 V *vs.* Li/Li^+ over a wide range, *i.e.* $Li_{4+x}Ti_5O_{12}$ where $0.09 < x < 2.91$, with theoretical capacity of 175 mAh g^{-1}.[6.8] According to recent studies, spinel/rock-salt co-existence is fulfilled by small domains (< 10 nm) of each phase that are intimately mixed together.[6.8,9] Lu *et al.* made direct observation of two-phase boundaries among nanodomains in the atomic-scale, but these observations only provide a static picture of the spinel/rock-salt co-existence at equilibrium.[6.10] The dynamic model for the spinel/rock-salt interface propagation, which is directly related to the electrode kinetics of LTO, is still ambiguous due to the intrinsically undistinguishable 3D Li-ion channels in the LTO spinel structure.[6.11] In general, Li diffusivity in LTO is considered to be a function of the Li content and coordination environment of mobile Li ions.[6.11-13] Wagemaker *et al.* found Li ions are nearly immobile in both spinel and rock-salt structures, but can readily jump between 8*a* and 16*c* sites in partially lithiated $Li_{4+x}Ti_5O_{12}$,[6.9] because of the strong Coulomb repulsion from the simultaneous occupation at neighboring 8*a* and 16*c* sites across the boundaries of spinel / rock-salt nanodomains.[6.11] Spinel LTO is initially a pure ionic conductor possessing a 3.80 eV band gap with ultraslow Li diffusion, which is the result of a high energy barrier (*ca.* 0.86 eV) as experimentally determined using spin-alignment echo nuclear magnetic resonance (SAE-NMR).[6.12] Ziebarth *et al.* theoretically predicted the high energy barrier (from 0.30 to 0.48 eV) for Li diffusion in spinel LTO, which is arisen from the trapping of mobile Li vacancies at 16*d* sites.[6.14] By contrast the diffusion energy barrier in the rock-salt $Li_7Ti_5O_{12}$ is about 0.20 eV that is lower than in spinel $Li_4Ti_5O_{12}$. This explains the intrinsically superior deintercalation capability of LTO electrode over intercalation.[6.15] This conclusion is also supported by the calculation work of Chen *et al.*[6.16] and Bhattacharya *et al.*.[6.17]

Unlike bulk LTO with highly periodic crystals, nano-LTO experiences significant structural relaxation to compensate for the non-fully coordinated ions near the surface. As a result, their Li storage properties differ significantly from the generally understood bulk LTO properties. For instance, Li diffusivity in nano-LTO decreases with particle size reduction as reported by Kavan *et al.*.[6.18] Pang *et al.* made similar conclusion using *in situ* neutron diffraction characterization that the Li-ion filling rate into empty 16*c* sites of larger-size LTO (500 nm) was almost 1.3 times higher than smaller-size LTO (200 nm).[6.19] This size-dependent Li diffusivity can be explained by lattice distortions.[6.20] Song *et al.* shows that 1% volume contraction of the rock-salt structure would significantly enhance the activation energy (from 0.43 eV to 0.61 eV) and results in Li diffusivity dropping from 4.9×10^{-11} to 5.5×10^{-14} $cm^2\ s^{-1}$.[6.21]

Nanostructure-induced structural relaxation also leads to the curved voltage profile and excess Li intercalation of nano-LTO.[6.22-27] According to calculations conducted by Swapna *et al.*,[6.23] energetically favorable (111) planes allow Li intercalation to exceed 175 mAh g^{-1} by simultaneously occupying tetrahedral 8*a* and octahedral 16*c* sites *via* surface reconstruction / relaxation that alleviates strong Coulomb repulsion among neighboring Li ions. In addition to excessive Li intercalation, nano-LTO exhibits a curved voltage profile as a result of the anisotropic orientation-dependent Li environment in the near-surface region. However, the large surface area of nano-LTO leads to significant battery performance deterioration, which is manifested by high irreversible capacity loss and the notorious gas generation.[6.28-33] The capacity fade stems from the excess near-surface Li storage in nano-LTO as a consequence of 8*a*-16*c* cointercalation because of the likely enlarged overpotential needed for spinel/rock-salt transformation to proceed.[6.24,25] In the meantime, the severe swelling issue in LTO-based LIBs (because` of gas generation at elevated temperature) is attributed to a spontaneous electrolyte/LTO reaction, which can be broken down into: i) hydrolytic decomposition of electrolyte because of trace amounts of water that yields HF;[6.28] ii) intrinsic catalysis by Ti^{4+} species;[6.29] and iii) electrolyte reduction from lithiated LTO.[6.31] Hydrogen, CO, CO_2 and C_2H_4 are the main gaseous products of the electrolyte/LTO interfacial reaction, with the simultaneous formation of solid electrolyte interphase (SEI) consisted of Li_2CO_3 and lithium alkyl carbonate (ROCOOLi) as major components.[6.29-31]

While particle size and surface area effects on LTO's Li storage dynamics are well established, the same is not true when it comes to nanocrystal morphology effects. 2D nanostructures are of particular interest here because of their acknowledged importance in energy storage systems.[6.34] It is indeed the purpose of this study to elucidate the influence of nanosheet morphology on LTO's Li storage properties (*i.e.* the electrode kinetics and capacity reversibility); and to shed light into the intricate capacity fade mechanism during galvanostatic charge/discharge. Different characterization techniques including scanning transmission electron microscopy (STEM), synchrotron powder X-ray diffraction (syn-PXRD) and X-ray absorption near edge (XANES) are employed on pristine and cycled LTO nanosheets for both qualitative and quantitative analyses.

6.3.Experimental Section

Synthesis: The synthesis method has been already reported in our previous work,[6.35,36] which involved the preparation of the intermediate LTH phase followed by its thermal conversion into crystallized LTO. LTH preparation began with a hydrous precipitate obtained by hydrolysis; titanium tetrachloride (20 mL of 2 **M,** 99.0% $TiCl_4$, Sigma-Aldrich, USA) aqueous solution was added drop-wise at a rate of 1 mL·min^{-1} into ice-cold lithium hydroxide (LiOH) aqueous solution (180 mL of 1.33 **M,** 98.0% $LiOH\cdot H_2O$, Sigma-Aldrich, USA) under vigorous stirring. The solution was maintained at about 4°C to avoid premature nucleation of TiO_2 during the precipitation reaction. At a final pH between 11.5 and 12 the solution was stirred continuously for 2 hours. The as-neutralized white precipitate was collected, rinsed with deionized (DI) water and the Li/Ti ratio was adjusted to 1.3 using a LiOH (0.25 **M**) aqueous solution (at a pH of 10.5). The LTH intermediate was produced by heating the prepared colloidal suspension to 85ºC under vigorous stirring for 24 hour. Layered LTH crystalline product was recovered by washing with DI water, oven dried at 80 ºC, and annealed for 6 hrs at 500 ºC (3 ºC/min ramp rate) in ambient atmosphere.

Characterization: Scanning electron microscopy (SEM) was performed with a Hitachi SU–8000 cold-field emission SEM (Hitachi High Technologies, Rexdale, Canada), while transmission electron microscopy (TEM) was performed with a Philips CM200 TEM at 200 kV. Aberration-corrected scanning transmission electron microscope (STEM) characterization was performed using a JEM-ARM Model 200F TEM microscope operated at 200 kV. The attainable spatial resolution of the microscope is 80 pm at an incident semiangle of 25 mrad. Nitrogen absorption / desorption technique provided information about LTO nanosheets' morphological features, using a Micromeritics TriStar 3000 apparatus to determine Brunaer-Emmett-Teller (BET) surface area and Barrett-Joyner-Halenda (BJH) pore size and volume analysis.

Spectroscopic techniques were employed to reveal information about composition and crystal structure. Raman spectroscopy was performed on a Renishaw RM 3000 and InVia spectrophotometer by using 514 nm Ar ion laser. Attenuated total reflectance Fourier transform infrared (ATR-FTIR) spectroscopy was performed, using a Frontier FT-NIR/MIR spectrometer in the wavenumber range from 4000 to 1000 cm^{-1}. UV–Vis absorption spectra were recorded in reflection mode, with samples diluted to 1% concentration with KBr, using a Thermo Scientific Evolution300 UV-visible Spectrometer in the wavelength range 1000 – 190 nm for information about the optical transitions in the band structure. Chemical analysis was performed on an inductively coupled plasma optical emission spectrometer (ICP-OES, Thermo Jarell Ash Trace Scan).

Synchrotron-based material characterization, including power x-ray diffraction (PXRD) and x-ray absorption fine structure (XAFS), was conducted at the Canadian Light Source (CLS). To conduct PXRD, the samples were loaded in 0.5 mm ID Kapton capillaries which were sealed at both ends with a Loctite adhesive. PXRD patterns were collected at the Canadian Macromolecular Crystallography Facility beamline (CMCF-BM or 08B1-1) at CLS. 08B1-1 is a bending magnet beamline with a Si (111) double crystal monochromator. Two-dimensional (2D) data was obtained using a Rayonix MX300HE detector with an active area of 300 mm × 300 mm. The patterns were collected at an energy of 18 keV ($\lambda = 0.68880$ Å) and capillary-detector distance of 250 mm. The XRD patterns were calibrated and integrated using the GSASII software package.[6.37] The sample-detector distance, detector centering and tilt were calibrated using a lanthanum hexaboride (LaB_6) standard reference material from the National Institute for Standards and Technology (NIST SRM 660a LaB_6) and the calibration parameters were applied to all patterns. After calibration, the 2D patterns were integrated to obtain standard 1D powder diffraction patterns. A pattern from an empty Kapton capillary was subtracted from the sample data during integration. The integrated LaB_6 pattern was used to obtain the instrument resolution of the beamline for the Rietveld refinement of the samples.

XAFS was carried out at the Variable Line Spacing Plane Grating Monochromator (VLS PGM) and High Resolution Spherical Grating Monochromator (SGM), respectively, at the CLS. Spectra of the LTO samples, which were mounted on double-sided conducting carbon tape, were recorded in both the surface sensitive total electron yield (TEY) and bulk sensitive fluorescence yield (FY) mode, respectively, using a silicon drift detector (SDD). TEY is a widely used technique to collect the yield of Auger electrons / secondary electrons in the near-surface region because of the short escape depth of electrons; while FY is a useful bulk sensitive method. Background subtraction and normalization of the X-ray absorption near-edge structure (XANES) spectra were conducted using Athena.[6.38]

Electrochemical tests: The composite electrodes were made of the active material, LTO nanosheets (80 wt%), conductive carbon black (10 wt%) and polyvinylidene fluoride (PVDF) binder (10 wt%) homogeneously dispersed in a mixture to 1 ml N-methyl pyrrolidinone (NMP), coated on 15 μm aluminum foil with (1.4 mg). These electrodes were dried at 150 °C in vacuum for 12 hours. Home-made Swagelok cells were assembled with the prepared working electrode and reference/counter electrodes made of Li metal (Sigma-Aldrich) in an argon-filled glove box (M. Braun Co., $[O_2] < 0.5$ ppm, $[H_2O] < 0.5$ ppm). A 25 μm polypropylene (PP)/polyethylene (PE) separator (PP/PE/PP) (Celgard 2325) was used, and 1 M $LiPF_6$ in ethylene carbonate (EC) and dimethyl carbonate (DMC) (1:1, v/v) was used as the electrolyte.

Electrochemical tests, including galvanostatic experiments and cyclic voltammetry (CV), were conducted in the range of 2.5 - 1.0 V vs. Li/Li^+. The galvanostatic experiments were performed using a standard battery cycler (BT2043-10V-100mA-40, Arbin) and the cyclic voltammetry was performed on a BioLogic VSP potentiostat/galvanostat/EIS system at different scan rates. In the meantime, the polarization evolution of LTO nanosheet electrodes was estimated from the change of differential capacity (dQ/dV) with respect to the galvanostatic cycle test at 1C rate (1C = 175 mA g^{-1}). Differential capacity was determined via a simple two-point numerical differentiation from the collected charge/discharge voltage profiles of each cycle. The color temperature in the polarization variation figures represents the intensity of the peaks of the differential capacity curves. This is illustrated in the Appendix D section with the help of Figure D7. The polarization of the LTO electrodes was determined from the change in voltage plateau positions. The peaks positions were obtained from the differential capacitance analysis (dQ/dV) of each cycle, which are selectively provided in Figure D6.

6.4. Results

6.4.1. Structural Relaxation in Pristine LTO Nanosheets

The prepared LTO nanosheets possess $Fd\overline{3}m$ spinel structure with lattice constant 8.356(4) Å, whose morphology consists of the top (010) facets of 50-100 nm, and 5 nm-lateral $(\overline{1}01)$ facets as shown in Figure D1. Detailed atomic-scale images of LTO lattices are given in Figures 6.1a and 1b obtained by using aberration-corrected STEM with annular-bright-field (ABF) and high-angle annular-dark-field (HAADF) techniques, whose contrast is a function of atomic number varying as $Z^{1.7}$ for HADDF and $Z^{1/3}$ for ABF images.[6.39-41] Bright spots with different contrast reveals two types of Ti columns separated by 0.24 nm (Figure 6.1e), which are marked as Ti_A and Ti_B, respectively. As quantitatively presented in the line profile Figure 6.1e, the strong spots Ti_B are almost twice as bright as the Ti_A spots, meaning twice the Ti content. Structural relaxation results in the local deformation of TiO_6 octahedra, which is presented in the form of the distorted quadrilaterals constructed of 4 neighboring Ti_B spot patterns as illustrated in the marked region in Figure 6.1d. There is a wide spectrum of the long diagonal/short diagonal ratio of the distorted quadrilaterals in the range of 1.3-1.55. As a result, the lattice stripes fluctuate prominently along the [111] direction of LTO nanosheets (yellow line in Figure 6.1d).

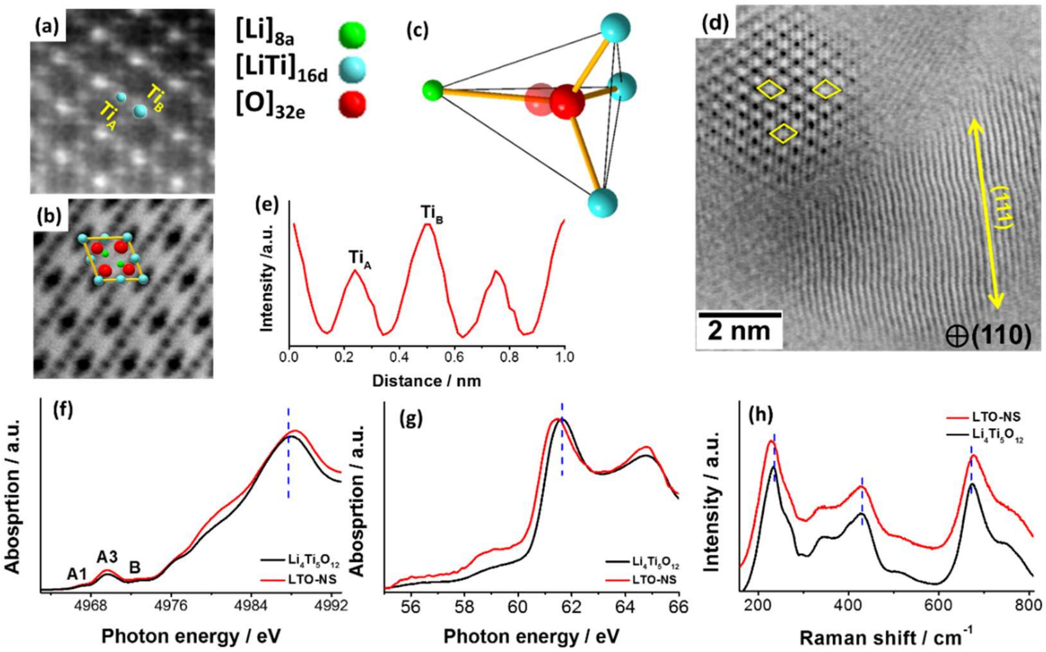

Figure 6.1. Atomic-resolution STEM HADDF (a) and ABF(b) images of spinel lattice along [110] zone axis, and (c) the tetrahedron centered at $[O]_{32e}$ (red) coordinated with $[Li]_{8a}$ (green) and $[LiTi]_{16d}$ (cyan) that has Li/Ti ratio of 1/5. The transparent and solid oxygens represent the positions in LTO nanosheets and ideal crystals, respectively. (d) STEM image of LTO nanosheet with discernable lattice distortion. (e) The corresponding line-scan profile of Ti columns in HADDF image from Figure 6.1 (a). Comparison of normalized (f) Ti K-edge and (g) Li K-edge XANES TEY spectra and (h) Raman spectra of LTO nanosheets (red) and well-crystalline $Li_4Ti_5O_{12}$ spinel sample (black).

The local symmetry of LTO nanosheet crystals changes as a result of the lattice distortion. As indicated by the strong pre-edge features of LTO nanosheets labelled as A1, A3 and B in Ti K-edge XANES TEY spectra (Figure 6.1f), the TiO_6 octahedra of LTO are more distorted in nanosheet crystals than in well-crystalline bulk LTO sample. In perfect O_h symmetry of TiO_6 octahedra, Ti_{1s}-Ti_{3d} electron transition is forbidden; only distorted TiO_6 octahedra allow Ti_{3d}-Ti_{4sp} hybridization, which determines the intensity of pre-edge features. Also the chemical shift of the main peak (*ca.* 4988 eV) of LTO nanosheets toward high energy, is the result of shortened Ti-O bond length that enhances their ionic property. But the chemical shift of LTO nanosheets exhibits an opposite tendency in Li K-edge TEY spectra (Figure 6.1g), thus the peak of core exciton around 61.5 eV shifts toward lower energy. This red shift means that Li-O hybridization becomes more covalent because the Coulombic interactions between the nuclei and excited electrons are screened by the pre-occupying electrons in Li_{2p} orbitals.[6.42] This covalency change implies certain Li-O bond length elongation in the LTO nanosheets. The bond length and bond angle change in LTO nanosheets was further evaluated with the help of Raman spectroscopy (Figure 6.1h). The A_{1g} mode corresponding to the symmetric stretching vibration of Ti-O bonds contributes to the band at 685 cm^{-1}. The blue shift of A_{1g} band of LTO nanosheets (red) with respect to the well crystyalline LTO (black) is the result of Ti-O bond contraction. But the stationary E_g band at 430 cm^{-1}, which is related to the Li-O assymetric stretching in LiO_6 octahedra, indicates the LiO_6 of Li ions located at 16*d* are relatively rigid.[6.43] In the meantime, the F_{2g} mode of Ti-O bending vibration at 231 cm^{-1} in LTO nanosheets exhibits a red shift in comparison to that of the well crystalline LTO. This implies a change in the bond angle of O-Ti-O in the TiO_6 octahedra. Therefore, the corrugated lattice stripes are the consequence of inhomogeneous expansion of TiO_6/LiO_6 octahedra, as shown in Figure 6.1d. When the 4-fold coordination environment of oxygen is considered, the the said relative motion can be represented by the position shift of oxygen ions. In LTO nanosheets, the oxygen ions locate closer to Ti ions (*i.e.*, the solid red ball) due to the structural relaxation, hence the long Li-O bonds and short Ti-O bonds are given with respect to the well-crystalline bulk LTO (transparent ball).

6.4.2. Electrochemistry of LTO Nanosheets

The CV test scanned from 1.0 – 2.5 V at different scan rates from 0.083 to 0.416 mV/s is given in the plot on right-hand side of Figure 6.2a (right-hand side). Additional electrochemical data are given in Figure D3. The average Li diffusivity of intercalation process in LTO spinel, $D_{insert}$is, is 1.71 × 10^{-11} cm^2 s^{-1}. This value is almost one order of magnitude higher than the reported value of approximately 10^{-12} cm^2 s^{-1} for LTO nanoparticles with the same BET specific surface area (~ 80 m^2 g^{-1}, Figure D2).[6.44] In the meantime, prepared LTO nanosheets exhibit slower kinetics of Li-ion diffusion in $Li_7Ti_5O_{12}$, as their diffusivity of deintercalation process D_{extra} was calculated to be 3.99 × 10^{-12} cm^2 s^{-1}. Such asymmetry was more clearly presented in Tafel plot of Figure 6.2b, which shows better overpotential performance during intercalation than during deintercalation when subjected to galvanostatic charge/discharge at rates from C/24 to 20C. The electrode kinetics of the LTO nanosheets were compared to other modified nano-LTO materials such as carbon-encapsulated F-doped LTO,[6.45] Cr-doped LTO,[6.46] nanowire,[6.47] rutile-coated nanosheets and pure nanosheets (NS-ref),[6.48] and nanocrystal,[6.49] by plotting in a Ragone plot in Figure 6.2c.

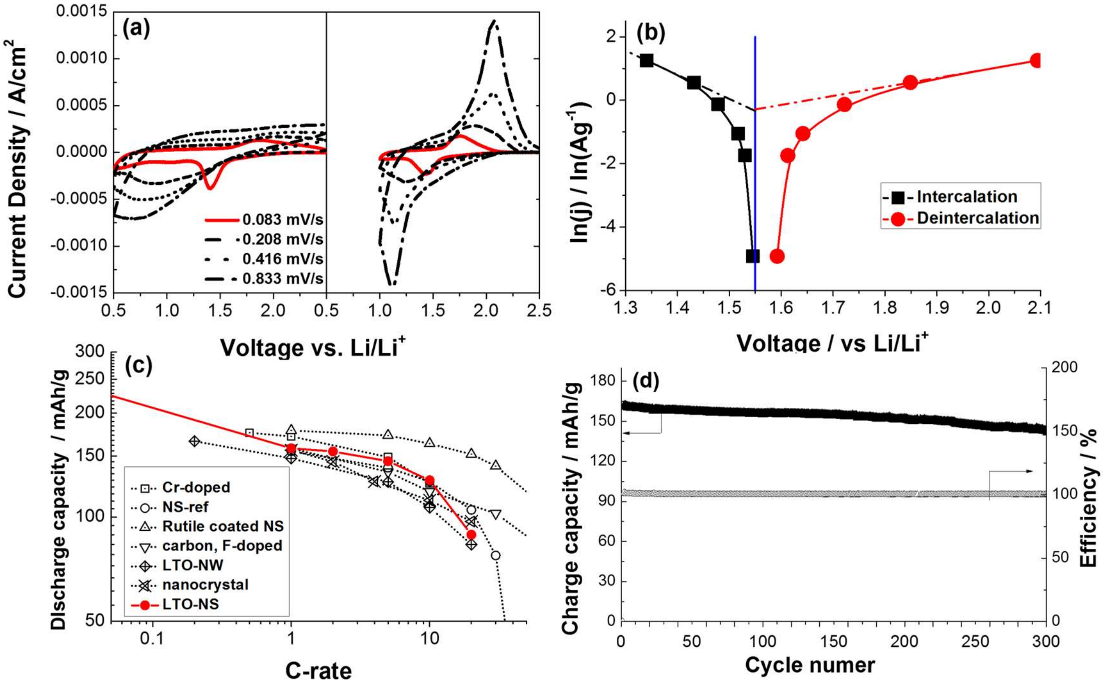

Figure 6.2. (a) Cyclic voltammograms at variable scanning rates from 0.083 to 0.416 mV/s within the voltage range of 0.5-2.5 V (left) and 1.0-2.5V *vs.* Li/Li$^+$, respectively. Electrochemical performance of LTO nanosheets operated from 1.0 to 2.5 V as (b) Tafel plot of applied constant current in the range of C/24 to 20 C against the corresponding voltage plateau positions, in which the vertical line represents the equilibrium potential 1.55 V *vs.* Li/Li$^+$. (c) Comparison of rate capability to other recently published LTO materials using a Ragone plot. (d) Galvanostatic 1C discharge/charge cycling performance.

All nanostructured LTO materials basically exhibit similar performance except for the high energy density of rutile TiO_2 coated-LTO nanosheet electrodes, which was attributed to the nanocoating of rutile TiO_2 that greatly improves the electrode kinetics of nano-LTO.[6.22,48]

According to the measured Li diffusivity, the 5-nm thick LTO nanosheets require merely 10^{-2} s for crossing that distance. This is in the same order as the characteristic time, 0.025 s, of the charge-transfer process of LTO nanosheet electrodes, which was estimated by the electrochemical impedance spectroscopy (EIS) technique-results are given in Figure D3d. The consistency in these two time-constants means that these two processes are equally important to determine Li transport in LTO nanosheet electrodes. It becomes evident that synergistic approaches that simultaneously enhance diffusion (nanostructuring) and electronic conductivity (doping or carbon coating) can lead to performance optimization. In the meantime, LTO nanosheets synthesized in this work exhibit, as shown in Figure 6.2d, competitive cyclic stability where there is still 87.6 % capacity retention (141.8 mAh g^{-1}) after 300 cycles at 1C rate.

6.4.3. Relaxed LTO Structure Formation Induced by Cycling

Microstructure characterization of the pristine LTO nanosheet crystals and the post-mortem sample of cycled LTO is given in Figures 6.3a and 6.3b, respectively. The latter were charged to 2.5 V (formation at C/24) for 80 cycles at 1C rate. In both pristine and cycled LTO, there should be no HADDF signals detected at 16*c* sites as shown in Figure 6.3a and the red profile in Figure 6.3c. Nonetheless, a prominent peak of atomic contrast appears at 0.3 nm in cycled LTO nanosheets (black profile in Figure 6.3c) as a result of Li-Ti exchange at 16*c* sites occuring in the outmost surface as given in Figure 6.3b. Thus, the near surface structure is reconstructed / relaxed via Ti ion migration in LTO nanosheet upon cycling. In the meantime, such structural relaxation is accompanied by polarization changes of LTO nanosheet electrodes. Figure 6.3d gives the polarization evolution during galvanostatic 1 C cycle test after formation at C/24. There is a declining transition of polarization with the charging plateau voltage dropping from 1.67 V at the beginning to 1.60 V at around 10 cycles. But there is another raising transition of polarization appearing upon increase of the formation current from C/24 to 1C. In this case, a gradual increase from an initial charging plateau with value 1.65 V to a plateau voltage of 1.69 V at fourth cycle is observed as shown in Figure 6.3e.

6.4.4. LTO nanosheet/Electrolyte Interfacial Reaction

The voltage profile of C/24 formation cycle is given in Figure 6.4a, where the first discharge capacity is 225.0 mAh g^{-1} of an overlithiated $Li_{7+x}Ti_5O_{12}$. At the end of the formation cycle an irreversible capacity loss of 61.3 mAh g^{-1} as charge capacity is only 163.7 mAh g^{-1}. High irreversible loss of nano-LTO has been widely reported as the result of surface reconstruction/relaxation.[6.22-24] After 80 galvanostatic cycles at 1C rate, the reversible capacity has further decreased to 149.9 mAh g^{-1}. Additional galvanostatic curves and differential charge plots are given in Figure D6 in Appendix D. To probe the origin of the observed capacity fading, post-mortem XANES analyses were employed on LTO nanosheet samples collected at various depths of discharge (DOD) within the formation cycle and on the 1C cycled sample collected after 80 cycles. Each condition is labeled accordingly in Figure 6.4a. The features of the bulk-sensitive FY O K-edge XANES spectra (Figure 6.4b) can be separated into (i) pre-edge peaks of t_{2g}-e_g splitting in the range of 527-535 eV due to O_{2p}-Ti_{3d} hybridization in TiO_6 octahedra, and (ii) high energy features originated from the O_{2p}-Ti_{4sp} hybridization, where the peak around 537 eV is associated with tetrahedral Li ions in 8*a* sites.[6.50] In Figure 6.4b, the pristine LTO nanosheets (black) exhibit analogous features to the reported patterns of LTO spinel.[6.51,52] As Li ion intercalation begins, the spectrum of $Li_7Ti_5O_{12}$ theoretically would exhibit an enhanced feature at 540 eV because tetrahedral Li ions hop into octahedral 16*c* sites.[6.25,51,52] Also the Ti^{4+}/Ti^{3+} reduction decreases the t_{2g}/e_g ratio because the partially filled t_{2g} orbitals suppress the electron transition probability, and hence lower t_{2g} peak intensity. In other words, the population variation of Ti^{4+} and Ti^{3+} ions during galvanostatic charge/discharge can be estimated from the change of t_{2g}/e_g ratio. Figure D4a presents a self-consistently linear relationship of t_{2g}/e_g variation *vs.* Ti^{3+} percentage, and the latter is estimated from the irreversible capacity loss.

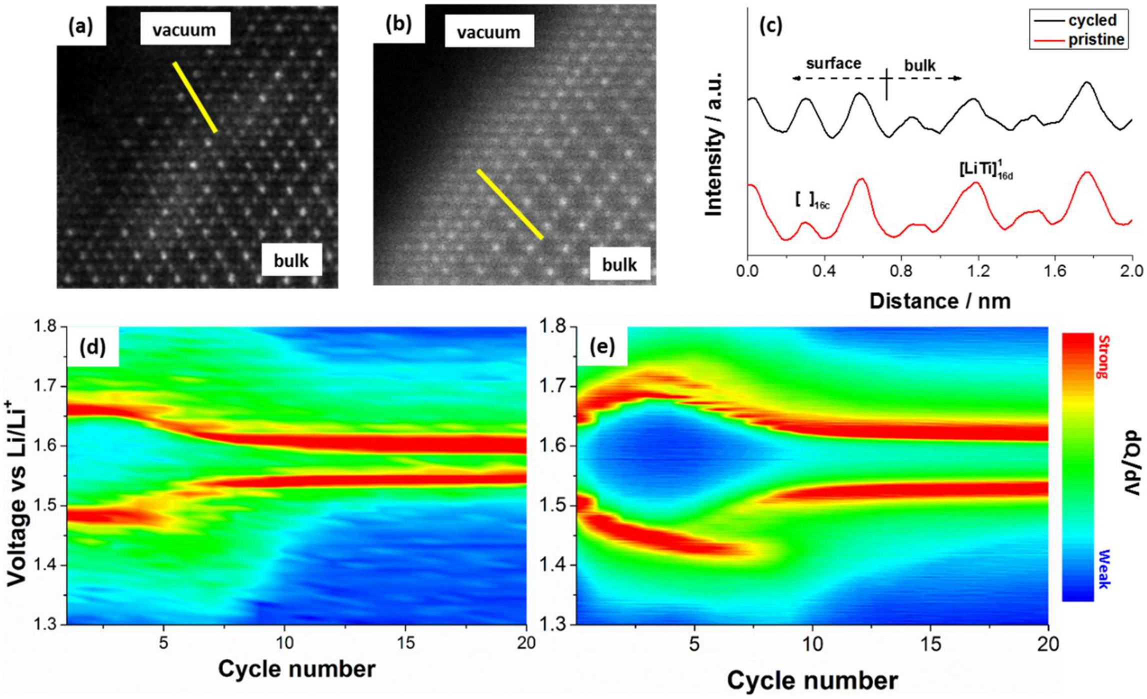

Figure 6.3. The HADDF images of (a) pristine and (b) cycled LTO nanosheet crystals at [110] zone axis; and (c) line intensity profiles obtained from each HADDF image. Polarization variation during 1C galvanostatic

charge/discharge of LTO nanosheets with the applied formation current at (d) 1/24C and (e) 1C rate, where the color temperature corresponds to the peak intensity as indicated by the scale bar.

The pristine LTO nanosheets exhibit the highest t_{2g}/e_g ratio, and then this ratio monotonically declines as intercalation proceeds discharge, downwards to the over-lithiated LTO at 1 V. During the deintercalation process, the irreversible Li ions trapped in LTO prevent the complete restoration of Ti valence back to Ti^{4+}, explaining the lower t_{2g}/e_g ratio of the post-formation (blue) sample by comparison to the pristine LTO. But the t_{2g}/e_g ratio is found to be independent on cycle numbers, giving a steady value for both post-formation and 80-cycled LTO (cyan dash line in Figure D4a). This reversible change of the t_{2g}/e_g ratio implies the LTO nanosheets have excellent durability. However, surface-sensitive TEY Ti L-edge XANES spectra (Figure 6.4c) suggest considerable interfacial reaction occurring at the electrolyte/LTO interface, which consumes Ti^{3+} ions in the near-surface region by oxidizing them back to Ti^{4+} state.

Characteristic features in Figure 6.4c include the t_{2g} bands of Ti^{4+} at 461.3 eV and a split e_g level at 463.3 and 464.1 eV. The t_{2g} bands decrease because of Ti^{4+}/Ti^{3+} reduction, and generated Ti_{2p} holes are screened from the excited electrons making e_g bands of Ti^{3+} shifting toward 462.7 eV.[6.53] The Ti^{3+}/Ti^{4+} ratio can be estimated by spectral deconvolution of overlapped e_g levels as presented in Figure D4b. The ratio is negatively associated with the estimated Ti^{3+} percentage from capacity loss, and there is an initial outlier of pristine LTO (black square) left at origin. This inverse relationship implies the Ti^{3+} consumption due to spontaneous reaction of highly reactive lithiated LTO to reduce the electrolyte.[6.54] The post-formation LTO shows to have more Ti^{3+} than $Li_7Ti_5O_{12}$, despite the fact it was charged to 2.5 V. 80-cycled LTO has an even higher value of Ti^{3+} population, as can be seen in Figure D4b. However, over-lithiated $Li_{7+x}Ti_5O_{12}$ has unexpectedly low Ti^{3+} population accompanied by dramatically raised background before 460 eV as shown in Figure 6.4c. This raising background implies the surface is covered by poorly conductive interphasial (SEI) film.

The surface-sensitive TEY mode of O K-edge XANES was used to identify the composition of the established SEI film. The pristine LTO nanosheets in Figure 6.4d has an SEI-free surface, as supported by the TEM image in Figure D1b. During formation at C/24, one new feature at 533.7 eV appears in the $Li_7Ti_5O_{12}$ pattern (red), with peak grown at 535.5 eV. These features develop with galvanostatic cycling and become dominantly significant after 80 cycles (cyan). According to core-level spectroscopy techniques such as XPS, there are two commonly

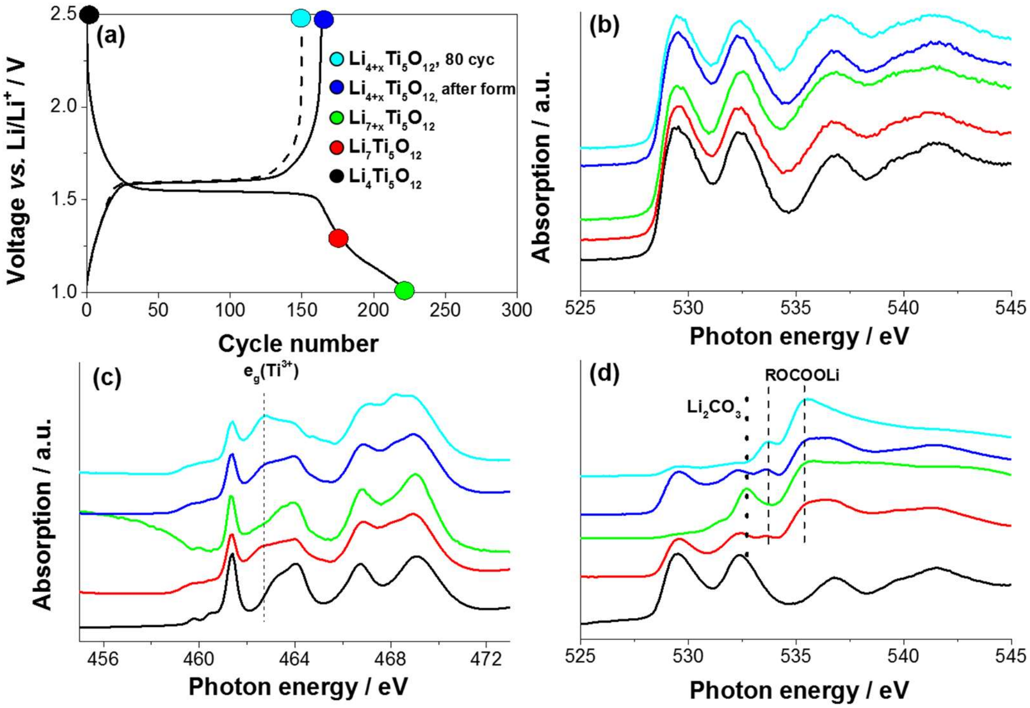

Figure 6.4. (a) Voltage profiles of LTO nanosheets during the formation cycle (solid) and the charge curve at 80 cycles (dash). The marked points represent different states of charge of pristine (black), $Li_7Ti_5O_{12}$ (red), over-lithiated $Li_{7+x}Ti_5O_{12}$ (green), formation-cycled $Li_{4+x}Ti_5O_{12}$ (at C/24) (blue), and $Li_{4+x}Ti_5O_{12}$ after 80 cycles at 1C rate (cyan) operated from 1 to 2.5 V vs. Li/Li$^+$, respectively. The corresponding (b) bulk-sensitive FY mode O K-edge, (c) surface sensitive TEY mode Ti L-edge and (d) O K-edge XANES spectra of the different charge-state LTO samples.

detectable components observed in SEI, including Li_2CO_3 and ROCOOLi. The latter component becomes evident by the functional groups C=O and C-O-C that appear around 1 eV higher in binding energy than Li_2CO_3 in O_{1s} XPS spectra.[6.30] Qiao *et al.* also found significantly enhanced features at around 534 and 537 eV in XANES spectra due to SEI formation on the surface of a Sn electrode when cycling from 0.8 to 2.5 V *vs.* Li/Li$^+$,[6.55] possibly consists of organic compounds such as lithium oxalate, lithium carboxylate, lithium alkoxide, *etc.* Therefore, the assignment of these two developing new features in the range between 534 and 537 eV to ROCOOLi is reasonable.

However, the over-lithiated LTO yields a totally different pattern from other spectra, with one prominent peak at 532.7 eV and a plateau starting at 535 eV, closely matching the published O K-edge spectrum of Li_2CO_3.[6.55-57] Considering both the Ti L-edge and O K-edge spectra for overlithiated $Li_{7+x}Ti_5O_{12}$, Li_2CO_3 appears to be the primary component of the SEI layer in this case as a result of a spontaneous electrolyte/LTO reaction. The difference in the SEI composition is as expected, according to the gas chromatograph (GC) analysis reported by He *et al.* due to different gaseous products released by fully-lithiated LTO and by cycled LTO.[6.29]

6.5.Discussion

The presented results clearly show that the Li storage properties of LTO nanosheets, such as their electrode kinetics and cyclic performance, were deeply influenced by the structural relaxation in the 2D nanostructure occurring during cycling. The role of nanosheet morphology in this dynamic behaviour deserves further explorations.

6.5.1. Abnormal Asymmetry in Electrode Kinetics of LTO nanosheets

Similar to the $LiFePO_4$-$FePO_4$ system,[6.58] the $Li_4Ti_5O_{12}$-$Li_7Ti_5O_{12}$ couple also exhibits asymmetric electrode kinetics with better Li deintercalation capability (*i.e.*, lower overpotential),[6.19,44] because of lower Li-ion diffusion activation energy in rock-salt $Li_7Ti_5O_{12}$ than that in spinel $Li_4Ti_5O_{12}$.[6.11,14] Thus, $D_{insertion}$ is typically 10-100 times lower than $D_{extraction}$ in nano-LTO.[6.44] However, in the relaxed LTO structure in nanosheet crystals, a rather abnormal asymmetry with the deintercalation process (red) exhibiting higher overpotential as it can be seen in the Tafel plot of Figure 6.2b. In the meantime, based on the Li diffusivity calculated, deeper DOD (scanning from 0.5 to 2.5 V of the plot on left-hand side of Figure 6.2a) causes more sluggish, about 10 times slower, Li diffusivity than the one operated in the range of 1 to 2.5 V. Also as was demonstrated in our earlier research,[6.35] LTO nanosheets delivered higher initial intercalation capacity but had more irreversible capacity loss when discharged to deeper DOD on formation cycle. Such deterioration in Li-ion diffusion capability is arising as determined in this work from the structural relaxation occurring in LTO nanosheet crystals, which modifies the electronic structure of LTO structure.

The relaxed LTO structure in nanosheet crystals provides more covalent Li-O bonds, meaning relatively higher charge density at Li sites with respect to the perfect LTO lattices; those excess charges at Li sites are compensated by more ionic Ti-O bonds. As a result, the screening of the strong Coulombic repulsion among the intercalated Li ions at 16*c* sites and those originally

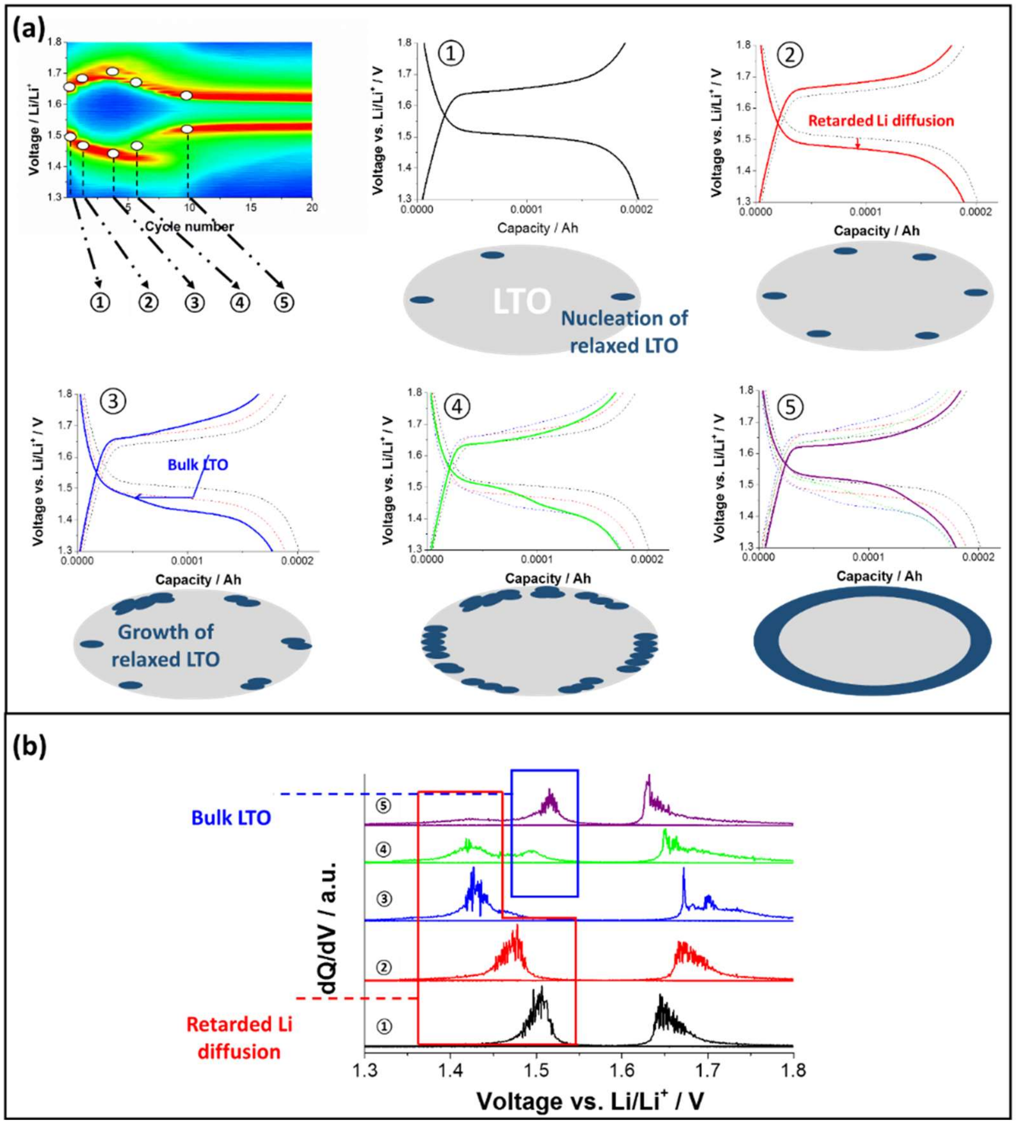

Figure 6.5. (a) Schematic illustration of voltage profile evolution during several galvanostatic charge/discharge cycles linked to the corresponding formation of the relaxed LTO surface zone: (1) Charge/discharge curves of formation cycle; during the formation cycle, the relaxed LTO nucleates because of conintercalation in the near-surface region leading to polarization transition. (2) During the 2nd cycle, the population of relaxed LTO nucleu increases causing Li diffusion retardation that translates to an increase in polarization. (3) A transition occurs as result of formation of semi-continuous zone of relaxed LTO, which facilitates intercalation into bulk region

because improved. (4) As the near-surface continuous zone of relaxed LTO expands, the contribution of bulk region becomes more prominent. (5) The contribution from bulk becomes dominant when the near-surface is completely transformed into relaxed LTO. (b) Corresponding differential capacity plots at the 5 different stages of relaxed LTO surface zone. The timing at which each stage of relaxed LTO formation corresponds is indicated on the polarization variation plot with open circles.

occupying neighboring 8*a* sites would be less effective in relaxed LTO structure of nanosheet crystals. LTO nanosheets therefore should tolerate more excessive Li intercalation that further alters their Li storage properties mentioned.

Even though a higher storage capacity can be expected in LTO nanosheets because of their better tolerance to 8*a*-16*c* cointercalation, many of the intercalated Li ions become irreversibly trapped in the relaxed LTO structure imposing obstruction to Li-ion diffusion. As a consequence, the polarization of LTO nanosheet electrode would rise as reflected, for example, by the reduction peak shifting towards lower voltage when scanning is done in the range of 0.5 – 2.5 V (Figure 6.2a).

6.5.2. Structural Relaxation-Induced Capacity Fade

Based on the findings presented in the **Results** section, two different mechanisms were proposed that contribute to the capacity fade of LTO nanosheet electrodes. One relates to a surface reconstruction/relaxation-induced material degradation occuring during early cycling; and the other to a side reaction at LTO/electrolyte interface.

According to the cycling performance presented in Figure D5, capacity fade of LTO nanosheet electrodes can be readily divided into three distinct stages: (i) a deep drop of 64.8 mAh g^{-1} capacity loss in stage I when moving from the C/24 formation cycle to the first 1C cycle, this drop was limited to only 12.7 mAh g^{-1} when applying 1C as formation current; (ii) an exponential decay during the subsequent 10 cycles at 1C rate following the formation cycle, contributing ~5-10 mAh g^{-1} capacity loss - this is stage II; and (iii) a linearly minor decline of capacity retention responsible for ~4 mAh g^{-1} loss in the end of 80 cycles - stage III. Capacity fade during stages I and II is attributed to the first mechanism of material degradation. It is proposed that the cointercalation of external Li ions induces structural relaxation, which impedes Li diffusion resulting in polarization increase as reflected by the initial rising transition of polarization over the first 4 cycles, clearly seen in Figure 6.3e. By contrast when C/24 was applied as formation current this initial rise in polarization is absent (Figure 6.3d) because evidently one cycle is sufficient to accomplish the structural relaxation at such a low rate.

Following the first increasing polarization transition, there is a declining transition occurring at *ca.* 10 cycles in both Figure 6.3d and 6.3e. This is so because the developing relaxed LTO provides better electrical conductivity. The lithiated LTO has good electrical conductivity due to well-known transition from an insulator as spinel $Li_4Ti_5O_{12}$ (10^{-9} S cm^{-1}) to a semiconductor for the rock-salt $Li_7Ti_5O_{12}$ (8 S cm^{-1}).[6.59] Namely, continuous trapping of Li ions in the near-surface region as shown in the XANES results of Figure 6.4, gradually eliminate the raised polarization in the first transition leading to the second transition of polarization decline. The proposed mechanism can be better understood with the help of Figure 6.5. A series of schematic illustrations of the near-surface nucleation-growth of relaxed LTO is provided, which is linked to different stages of voltage profile evolution during galvanostatic charge/discharge cycling (Figure 6.3e). As shown in Figure 6.5a, in the first several cycles, formation of relaxed LTO in the near-surface region initially impedes Li diffusion and therefore the polarization increases (Figure 6.5a ① &②). As a larger portion of near-surface region is converted into relaxed LTO structure, a continuous network (zone) of relaxed LTO is established. This helps to improve the electrochemical charge-transfer process because the relaxed LTO has higher conductivity because of irreversibly trapped Li ions. As a result, the contribution from the bulk region of LTO gradually increases, as shown in Figure 6.5a ③-⑤. In discharge polarization, there appears to be a rather mismatched transition as moving from ③-⑤. This is attributed to the competition between the contribution from bulk LTO or from relaxed LTO structure in the near-surface region. This is further examined by referring to the Johnson-Mehl-Avrami-Kolmogorov (JMAK) kinetic model that we developed to describe the formation of relaxed LTO (details given in Appendix D).

For both LTO electrodes subjected to C/24 and 1C formation currents, the Avrami model exponents are symmetric for either intercalation or deintercalation processes and have: (i) the value of 1 for the first polarization-raising transition implying continuous nucleation at constant rate dominates the formation of relaxed LTO structure. This is a legitimate assumption because $8a$-$16c$ cointercalation is caused by the applied constant current hence the constant rate of nucleation of relaxed LTO. Furthermore, this nucleation process can be completed if a quasi-equilibrium condition is applied, as it happened in the formation cycle at C/24. (ii) When the population of stable nuclei of relaxed LTO (*i.e.*, reach their critical size) is high enough, the contribution of growth becomes relatively important. The conductivity improvement due to the irreversibly tapped Li ions that increase the Ti^{3+} population causes the successive declining transition of polarization at *ca.* 10 cycles. Therefore, the kinetics of this declining transition is determined by both contineous nucleation and three-dimentioanl growth processes of relaxed LTO. Thus, conintercalation occurs along the 3D pathway in the host matrix of LTO crystals. The Avrami exponent is hence raised in this case to the value of 4 for both intercalation and deintercalation processes. The JMAK model describing the formation of the relaxed LTO was found to be in good agreement with the experimental capacity fade data and polarization variation as shown in Figure D10b, supporting the proposition that Stage II capacity fade is linked to relaxed LTO. The rising and declining parts of the charge polarization curve are gonverned by nucleation and nucleation-growth of relaxed LTO, respectively. This postulation is consistent with the observed dependency on rate as with C/24 current the mismatch is almost eliminated (compare Figure 6.3d to 6.3e). Finally, the end of the exponential decay part (Figure D10a) coincides with the saturation of the declining transition of polarization at *ca.* 10 cycles. This means there would be no more capacity loss arising from relaxed LTO formation as soon as the near-surface region is totally transformed. As a result, the Li-Ti antisite defects in the 10-Å thick near-surface region shown in Figure 6.3b reflect the relaxed LTO structure after the cointercalation-induced transformation.

Unlike stage I and II capacity fade, the stage III capacity loss is attributed to a spontaneous LTO/electrolyte reduction reaction. The organic solvent in $LiPF_6$-based electrolyte, in our case the used DMC and EC, would be spontaneously reduced into organic Li interphase ROCOOLi/Li_2CO_3, respectively, [6.60] at the expense of intercalated Li ions in the near-surface region. Lu *et al.* provided a direct proof of a linear gradient of Ti^{3+} population pointing towards the bulk region of $Li_7Ti_5O_{12}$. Similar tendency is also given in the Ti L-edge XANES (Figure 6.4d), in which Ti^{3+} ions in the near-surface region of LTO nanosheets are consumed by the spontaneous electrolyte/LTO redox reaction. This spontaneous reduction continuously occurs feeding more SEI formation that is directly related to the severe swelling phenomenon of LTO batteries. According to molecular dynamics simulations published by Kim *et al.*, C_2H_4 and CO are the major gaseous components generated during SEI formation.[6.60] Their findings basically coincide with the in-situ observations done by He *et al.* on stored and cycled LTO batteries.[6.29,30] As SEI formation proceeds, the well-grown SEI helps to preserve Ti^{3+} species in the near-surface region by avoiding further spontaneous electrolyte reduction. As a result, strong signals of Ti^{3+} species are present in Ti L-edge XANES. This finding also implies that LTO anodes require a properly matching electrolyte formulation as in the case of graphite anodes to supress Li ion consumption via the formation of the right SEI film.

6.6.Conclusion

New understanding of the structural relaxation occurring in nano-LTO and most importantly in two-dimensional morphology was provided. They extends our capability to manipulate the Li storage properties for optimized advanced nano-LTO electrodes. Unlike the well-developed carbon-coating strategies that improve the electron tunnelling efficiency at the electrolyte/LTO interface, introduction of lattice distortion modifies the electrode kinetics on the basis of Li diffusivity enhancement. This strategy is more straightforward because the electrode kinetics of LTO nanosheets is determined by the Li diffusion in the near-surface region. Furthermore, the knowledge developed about the capacity fade mechanism due to cointercalation-induced structural relaxation in nano-LTO plus the spontaneous electrolyte/LTO redox reaction, is critical to improve the durability of nano-LTO electrode materials. Future optimization strategies may include surface modification to prevent/manipulate $8a$-$16c$ cointercalation on one hand and on the other new electrolyte formulations/additives for LTO batteries to suppress the electrolyte/LTO reaction, and the associated severe swelling issue of LTO electrodes. Besides these battery chemistry advances, employment of the developed JMAK kinetics model to describe LTO electrode degradation should enable potentially on-board diagnosis systems for batteries in electric vehicles.

6.7.Acknowledgements

This work is supported through a Hydro-Québec/Natural Sciences & Engineering Research Council of Canada (NSERC) Collaborative R&D research grant. Synchrotron radiation measurements were performed at the CLS, which is supported by CFI, NSERC, University of Saskatchewan, Province of Saskatchewan, Western Economic Diversification Canada, NRC Canada, and CIHR. Expert assistance by Dr. Lucia Zuin in CLS for data collection and processing of Li K-edge XANES spectra is especially acknowledged.

6.8.References

(**6.**1) Colbow, K. M.; Dahn, J. R.; Haering, R. R. Structure and electrochemistry of the spinel oxides $LiTi_2O4$ and $Li_{4/3}Ti_{5/3}O_4$. *J. Power Sources* **1989,** *26* (3), 397.

(**6.**2) Ferg, E.; Gummow, R. J.; de Kock, A.; Thackeray, M. M. Spinel Anodes for Lithium-Ion Batteries. *J. Electrochem. Soc.* **1994,** *141* (11), L147.

(**6.**3) Deschanvres, A.; Raveau, B.; Sekkal, Z. Mise en evidence et etude cristallographique d'une nouvelle solution solide de type spinelle $Li_{1+x}Ti_{2-x}O_4$ $0 \leqslant x \leqslant 0, 333$. *Mater. Res. Bull.* **1971,** *6* (8), 699.

(**6.**4) Zaghib, K.; Simoneau, M.; Armand, M.; Gauthier, M. Electrochemical study of $Li_4Ti_5O_{12}$ as negative electrode for Li-ion polymer rechargeable batteries. *J. Power Sources* **1999,** *81* (0), 300.

(**6.**5) Wagemaker, M.; Mulder, F. M.; Van der Ven, A. The Role of Surface and Interface Energy on Phase Stability of Nanosized Insertion Compounds. *Adv. Mater.* **2009,** *21* (25-26), 2703.

(**6.**6) Sun, Y.; Zhao, L.; Pan, H.; Lu, X.; Gu, L.; Hu, Y. S.; Li, H.; Armand, M.; Ikuhara, Y.; Chen, L.et al. Direct atomic-scale confirmation of three-phase storage mechanism in $Li_4Ti_5O_{12}$ anodes for room-temperature sodium-ion batteries. *Nat. Commun.* **2013,** *4*, 1870.

(**6.**7) Scharner, S.; Weppner, W.; Schmid-Beurmann, P. Evidence of Two-Phase Formation upon Lithium Insertion into the $Li_{1.33}Ti_{1.67}O_4$ Spinel. *J. Electrochem. Soc.* **1999,** *146* (3), 857.

(**6.**8) Wagemaker, M.; Simon, D. R.; Kelder, E. M.; Schoonman, J.; Ringpfeil, C.; Haake, U.; Lutzenkirchen-Hecht, D.; Frahm, R.; Mulder, F. M. A kinetic two-phase and equilibrium solid solution in spinel $Li_{4+x}Ti_5O_{12}$. *Adv. Mater.* **2006,** *18* (23), 3169.

(**6.**9) Wagemaker, M.; van Eck, E. R.; Kentgens, A. P.; Mulder, F. M. Li-ion diffusion in the equilibrium nanomorphology of spinel $Li_{4+x}Ti_5O_{12}$. *J. Phys. Chem. B* **2009,** *113* (1), 224.

(**6.**10) Lu, X.; Zhao, L.; He, X.; Xiao, R.; Gu, L.; Hu, Y.-S.; Li, H.; Wang, Z.; Duan, X.; Chen, L.et al. Lithium Storage in Li4Ti5O12 Spinel: The Full Static Picture from Electron Microscopy. *Adv. Mater.* **2012,** *24* (24), 3233.

(**6.**11) Schmidt, W.; Bottke, P.; Sternad, M.; Gollob, P.; Hennige, V.; Wilkening, M. Small Change-Great Effect: Steep Increase of Li Ion Dynamics in $Li_4Ti_5O_{12}$ at the Early Stages of Chemical Li Insertion. *Chem. Mater.* **2015,** *27* (5), 1740.

(**6.**12) Wilkening, M.; Amade, R.; Iwaniak, W.; Heitjans, P. Ultraslow Li diffusion in spinel-type structured $Li_4Ti_5O_{12}$-A comparison of results from solid state NMR and impedance spectroscopy. *Phys. Chem. Chem. Phys.* **2007,** *9* (10), 1239.

(**6.**13) Wilkening, M.; Iwaniak, W.; Heine, J.; Epp, V.; Kleinert, A.; Behrens, M.; Nuspl, G.; Bensch, W.; Heitjans, P. Microscopic Li self-diffusion parameters in the lithiated anode material $Li_{4+x}Ti_5O_{12}$ ($0 <x < 3$) measured by ^{7}Li solid state NMR. *Phys. Chem. Chem. Phys.* **2007,** *9* (47), 6199.

(**6.**14) Ziebarth, B.; Klinsmann, M.; Eckl, T.; Elsässer, C. Lithium diffusion in the spinel phaseL$Li_4Ti_5O_{12}$ and in the rocksalt phase $Li_7Ti_5O_{12}$ of lithium titanate from first principles. *Phys. Rev. B: Condens. Matter Mater. Phys.* **2014,** *89* (17), 174301.

(**6.**15) Morgan, D.; Van der Ven, A.; Ceder, G. Li Conductivity in Li_xMPO_4 (M=Mn, Fe, Co, Ni) Olivine Materials. *Electrochem. Solid. St.* **2004,** *7* (2), A30.

(**6.**16) Chen, Y. C.; Ouyang, C. Y.; Song, L. J.; Sun, Z. L. Lithium ion diffusion in $Li_{4+x}Ti_5O_{12}$: From ab initio studies. *Electrochim. Acta* **2011,** *56* (17), 6084.

(**6.**17) Bhattacharya, J.; Van der Ven, A. Phase stability and nondilute Li diffusion in spinel $Li_{1+x}Ti_2O_4$. *Phys. Rev. B: Condens. Matter Mater. Phys.* **2010,** *81* (10), 104304.

(**6.**18) Kavan, L.; Prochazka, J.; Spitler, T. M.; Kalbac, M.; Zukalova, M. T.; Drezen, T.; Gratzel, M. Li insertion into $Li_4Ti_5O_{12}$ p(Spinel) - Charge capability vs. particle size in thin-film electrodes. *J. Electrochem. Soc.* **2003,** *150* (7), A1000.

(**6.**19) Pang, W. K.; Peterson, V. K.; Sharma, N.; Shiu, J. J.; Wu, S. H. Lithium Migration in $Li_4Ti_5O_{12}$ Studied Using in Situ Neutron Powder Diffraction. *Chem. Mater.* **2014,** *26* (7), 2318.

(**6.**20) Kang, K.; Ceder, G. Factors that affect Li mobility in layered lithium transition metal oxides. *Phys. Rev. B: Condens. Matter Mater. Phys.* **2006,** *74* (9), 094105.

(**6.**21) Song, K.; Seo, D. H.; Jo, M. R.; Kim, Y. I.; Kang, K.; Kang, Y. M. Tailored Oxygen Framework of $Li_4Ti_5O_{12}$ Nanorods for High-Power Li Ion Battery. *J. Phys. Chem. Lett.* **2014,** *5* (8), 1368.

(**6.**22) Wagemaker, M.; Mulder, F. M. Properties and promises of nanosized insertion materials for Li-ion batteries. *Acc. Chem. Res.* **2013,** *46* (5), 1206.

(**6.**23) Ganapathy, S.; Wagemaker, M. Nanosize Storage Properties in Spinel $Li_4Ti_5O_{12}$ Explained by Anisotropic Surface Lithium Insertion. *Acs Nano* **2012,** *6* (10), 8702.

(**6.**24) Borghols, W. J. H.; Wagemaker, M.; Lafont, U.; Kelder, E. M.; Mulder, F. M. Size Effects in the $Li_{4+x}Ti_5O_{12}$ Spinel. *J. Am. Chem. Soc.* **2009,** *131* (49), 17786.

(**6.**25) Feng, W.; Lijun, W.; Chao, M.; Dong, S.; Yimei, Z.; Jason, G. Excess lithium storage and charge compensation in nanoscale $Li_{4+x}Ti_5O_{12}$. *Nanotechnology* **2013,** *24* (42), 424006.

(**6.**26) Shu, J. Electrochemical behavior and stability of $Li_4Ti_5O_{12}$ in a broad voltage window. *J Solid State Electr* **2009,** *13* (10), 1535.

(**6.**27) Ge, H.; Li, N.; Li, D.; Dai, C.; Wang, D. Electrochemical characteristics of spinel $Li_4Ti_5O_{12}$ discharged to 0.01&0 V. *Electrochem. Commun.* **2008,** *10* (5), 719.

(**6.**28) Belharouak, I.; Koenig, G. M.; Tan, T.; Yumoto, H.; Ota, N.; Amine, K. Performance Degradation and Gassing of $Li_4Ti_5O_{12}/LiMn_2O_4$ Lithium-Ion Cells. *J. Electrochem. Soc.* **2012,** *159* (8), A1165.

(**6.**29) He, Y.-B.; Li, B.; Liu, M.; Zhang, C.; Lv, W.; Yang, C.; Li, J.; Du, H.; Zhang, B.; Yang, Q.-H.et al. Gassing in $Li_4Ti_5O_{12}$-based batteries and its remedy. *Sci. Rep.* **2012,** *2*.

(**6.**30) He, Y.-B.; Liu, M.; Huang, Z.-D.; Zhang, B.; Yu, Y.; Li, B.; Kang, F.; Kim, J.-K. Effect of solid electrolyte interface (SEI) film on cyclic performance of $Li_4Ti_5O_{12}$ anodes for Li ion batteries. *J. Power Sources* **2013,** *239*, 269.

(**6.**31) Wu, K.; Yang, J.; Liu, Y.; Zhang, Y.; Wang, C.; Xu, J.; Ning, F.; Wang, D. Investigation on gas generation of $Li_4Ti_5O_{12}/LiNi_{1/3}Co_{1/3}Mn_{1/3}O_2$ cells at elevated temperature. *J. Power Sources* **2013,** *237*, 285.

(**6.**32) Bernhard, R.; Meini, S.; Gasteiger, H. A. On-Line Electrochemical Mass Spectrometry Investigations on the Gassing Behavior of $Li_4Ti_5O_{12}$ Electrodes and Its Origins. *J. Electrochem. Soc.* **2014,** *161* (4), A497.

(**6.**33) He, M.; Castel, E.; Laumann, A.; Nuspl, G.; Novák, P.; Berg, E. J. In Situ Gas Analysis of $Li_4Ti_5O_{12}$ Based Electrodes at Elevated Temperatures. *J. Electrochem. Soc.* **2015,** *162* (6), A870.

(**6.**34) Peng, L.; Zhu, Y.; Chen, D.; Ruoff, R. S.; Yu, G. Two-Dimensional Materials for Beyond-Lithium-Ion Batteries. *Adv. Energy Mater.* **2016,** *6* (11), 1600025.

(**6.**35) Chiu, H. C.; Brodusch, N.; Gauvin, R.; Guerfi, A.; Zaghib, K.; Demopoulos, G. P. Aqueous Synthesized Nanostructured $Li_4Ti_5O_{12}$ for High-Performance Lithium Ion Battery Anodes. *J. Electrochem. Soc.* **2013,** *160* (5), A3041.

(**6.**36) Chiu, H.-C.; Lu, X.; Elouatik, S.; Zaghib, K.; Demopoulos, G. P. Formation of Lithium Titanate Hydrate Nanosheets: Insight into a Two-Dimension Growth Mechanism by in Situ Raman. *Cryst. Growth. Des.* **2016,** *16* (7), 3898.

(**6.**37) Toby, B. H.; Von Dreele, R. B. GSAS-II: the genesis of a modern open-source all purpose crystallography software package. *J. Appl. Cryst.* **2013,** *46* (2), 544.

(**6.**38) Ravel, B.; Newville, M. ATHENA, ARTEMIS, HEPHAESTUS: data analysis for X-ray absorption spectroscopy using IFEFFIT. *J. Synchrotron Radiat.* **2005,** *12* (Pt 4), 537.

(**6.**39) Hunt, J. A.; Williams, D. B. Electron Energy-Loss Spectrum-Imaging. *Ultramicroscopy* **1991,** *38* (1), 47.

(**6.**40) Leapman, R. D.; Swyt, C. R. Separation of Overlapping Core Edges in Electron-Energy Loss Spectra by Multiple-Least-Squares Fitting. *Ultramicroscopy* **1988,** *26* (4), 393.

(**6.**41) Lu, X.; Sun, Y.; Jian, Z.; He, X.; Gu, L.; Hu, Y.-S.; Li, H.; Wang, Z.; Chen, W.; Duan, X.et al. New Insight into the Atomic Structure of Electrochemically Delithiated O3-$Li_{1-x}CoO_2$ ($0 \leq x \leq 0.5$) Nanoparticles. *Nano Lett.* **2012,** *12* (12), 6192.

(**6.**42) Tsuji, J.; Nakamatsu, H.; Mukoyama, T.; Kojima, K.; Ikeda, S.; Taniguchi, K. Lithium K-edge XANES spectra for lithium compounds. *X-Ray Spectrom.* **2002,** *31* (4), 319.

(**6.**43) Mukai, K.; Kato, Y.; Nakano, H. Understanding the Zero-Strain Lithium Insertion Scheme of $Li[Li_{1/3}Ti_{5/3}]O_4$: Structural Changes at Atomic Scale Clarified by Raman Spectroscopy. *J. Phys. Chem. C* **2014,** *118* (6), 2992.

(**6.**44) Kavan, L.; Procházka, J.; Spitler, T. M.; Kalbáč, M.; Zukalová, M.; Drezen, T.; Grätzel, M. Li Insertion into $Li_4Ti_5O_{12}$ (Spinel) : Charge Capability vs. Particle Size in Thin-Film Electrodes. *J. Electrochem. Soc.* **2003,** *150* (7), A1000.

(**6.**45) Ma, Y.; Ding, B.; Ji, G.; Lee, J. Y. Carbon-Encapsulated F-Doped $Li_4Ti_5O_{12}$ as a High Rate Anode Material for Li^+ Batteries. *Acs Nano* **2013,** *7* (12), 10870.

(**6.**46) Song, H.; Yun, S. W.; Chun, H. H.; Kim, M. G.; Chung, K. Y.; Kim, H. S.; Cho, B. W.; Kim, Y. T. Anomalous decrease in structural disorder due to charge redistribution in Cr-doped $Li_4Ti_5O_{12}$ negative-electrode materials for high-rate Li-ion batteries. *Energy. Environ. Sci.* **2012,** *5* (12), 9903.

(**6.**47) Shen, L.; Uchaker, E.; Zhang, X.; Cao, G. Hydrogenated $Li_4Ti_5O_{12}$ Nanowire Arrays for High Rate Lithium Ion Batteries. *Adv. Mater.* **2012,** *24* (48), 6502.

(**6.**48) Wang, Y.-Q.; Gu, L.; Guo, Y.-G.; Li, H.; He, X.-Q.; Tsukimoto, S.; Ikuhara, Y.; Wan, L.-J. Rutile-TiO_2 Nanocoating for a High-Rate $Li_4Ti_5O_{12}$ Anode of a Lithium-Ion Battery. *J. Am. Chem. Soc.* **2012,** *134* (18), 7874.

(**6.**49) Laumann, A.; Bremholm, M.; Hald, P.; Holzapfel, M.; Fehr, K. T.; Iversen, B. B. Rapid Green Continuous Flow Supercritical Synthesis of High Performance $Li_4Ti_5O_{12}$ Nanocrystals for Li Ion Battery Applications. *J. Electrochem. Soc.* **2012,** *159* (2), A166.

(**6.**50) Lippens, P.-E.; Womes, M.; Kubiak, P.; Jumas, J.-C.; Olivier-Fourcade, J. Electronic structure of the spinel Li4Ti5O12 studied by ab initio calculations and X-ray absorption spectroscopy. *Solid State Sci* **2004,** *6* (2), 161.

(**6.**51) Kitta, M.; Akita, T.; Tanaka, S.; Kohyama, M. Characterization of two phase distribution in electrochemically-lithiated spinel $Li_4Ti_5O_{12}$ secondary particles by electron energy-loss spectroscopy. *J. Power Sources* **2013,** *237* (0), 26.

(**6.**52) Kitta, M.; Akita, T.; Tanaka, S.; Kohyama, M. Two-phase separation in a lithiated spinel $Li_4Ti_5O_{12}$ crystal as confirmed by electron energy-loss spectroscopy. *J. Power Sources* **2014,** *257*, 120.

(**6.**53) Ouyang, C. Y.; Zhong, Z. Y.; Lei, M. S. Ab initio studies of structural and electronic properties of $Li_4Ti_5O_{12}$ spinel. *Electrochem. Commun.* **2007,** *9* (5), 1107.

(**6.**54) Lu, X.; Gu, L.; Hu, Y.-S.; Chiu, H.-C.; Li, H.; Demopoulos, G. P.; Chen, L. New Insight into the Atomic-Scale Bulk and Surface Structure Evolution of $Li_4Ti_5O_{12}$ Anode. *J. Am. Chem. Soc.* **2015,** *137* (4), 1581.

(**6.**55) Qiao, R. M.; Lucas, I. T.; Karim, A.; Syzdek, J.; Liu, X. S.; Chen, W.; Persson, K.; Kostecki, R.; Yang, W. L. Distinct Solid-Electrolyte-Interphases on Sn (100) and (001) Electrodes Studied by Soft X-Ray Spectroscopy. *Adv. Mater. Interfaces* **2014,** *1* (3), 1300115.

(**6.**56) Kobayashi, H.; Emura, S.; Arachi, Y.; Tatsumi, K. Investigation of inorganic compounds on the surface of cathode materials using Li and O K-edge XANES. *J. Power Sources* **2007,** *174* (2), 774.

(**6.**57) Qiao, R.; Chuang, Y. D.; Yan, S.; Yang, W. Soft x-ray irradiation effects of Li_2O_2, Li_2CO_3 and Li_2O revealed by absorption spectroscopy. *PLoS One* **2012,** *7* (11), e49182.

(**6.**58) Bai, P.; Bazant, M. Z. Charge transfer kinetics at the solid-solid interface in porous electrodes. *Nat. Commun.* **2014,** *5*, 3585.

(**6.**59) Young, D.; Ransil, A.; Amin, R.; Li, Z.; Chiang, Y.-M. Electronic Conductivity in the $Li_{4/3}Ti_{5/3}O_4$-$Li_{7/3}Ti_{5/3}O_4$System and Variation with State-of-Charge as a Li Battery Anode. *Adv. Energy Mater.* **2013,** *3* (9), 1125.

(**6.**60) Kim, S.-P.; Duin, A. C. T. v.; Shenoy, V. B. Effect of electrolytes on the structure and evolution of the solid electrolyte interphase (SEI) in Li-ion batteries: A molecular dynamics study. *J. Power Sources* **2011,** *196* (20), 8590.

Chapter 7

Synopsis

In this final Chapter, first the most important global conclusions are highlighted; conclusions that focus on the nano-LTO synthesis process, the formation mechanism of LTH nanosheet crystals, the LTH-LTO topotactic transformation mechanism, and the capacity fade mechanism during cycling. Second, the *Claims to Originality* associated with this work are given; and finally some suggestions for *Future Work* are outlined.

7.1. Conclusions

A novel environmentally-friendly synthesis process of nano-LTO was developed. The process has the following advantageous characteristics: 100 % inorganic precursors and low-operating temperature (<100 °C) during aqueous synthesis of the LTH intermediate phase fulfill the criteria of sustainability. LTH as intermediate provides a facile way via annealing to promote LTO nanostructurization. Different nanostructures of LTO (nanosheets or nanoparticles) can be obtained by simply manipulating the synthesis/annealing conditions.

Material synthesis histories profoundly influence the electrochemistry of prepared nano-LTO, including the crystallization of intermediate phase LTH and its thermal conversion to LTO. A methodology combining in situ Raman spectroscopy and Johnson-Mehl-Avrami-Kolmogorov (JMAK) nucleation-growth kinetic modeling, which was modified to account for the 2D anisotropic growth of LTH nanocrystals, has been successfully employed to monitor the evolution from amorphous particles to 2D LTH crystals.

The Li-ion storage properties of nano-LTO highly depend on crystal properties such as morphology, surface area and crystallinity, which are impacted by the formation pathway of LTH→LTO thermal conversion process. By synchrotron and other types of characterization, the mechanism of topotactic transformation from lepidocrocite LTH into spinel LTO was elucidated. More importantly, it was shown that residual strain in the thermally synthesized LTO nanosheets renders the structure more “flexible” for structural relaxation to accommodate excess Li storage, leading to performance deterioration. By carefully selecting the annealing protocol the strain-induced relaxation is eliminated hence opening the way for highly stable performance.

Upon further studying the structural relaxation phenomenon observed in nano-LTO during intercalation/deintercalation, i.e. during cycling, some new insights on Li storage in nano-LTO were obtained. These helped explaining the capacity fade problem from which nanostructured LTO anodes suffer. Thus, it was found that excessively stored Li ions due to co-intercalation during intercalation/deintercalation lead to structure relaxation near the surface zone, which interferes with Li-ion diffusion and storage and eventually causes capacity fade. A JMAK kinetic model was developed to describe the formation of relaxed LTO. Once the near-surface zone of relaxed LTO is fully saturated, the capacity fade is then governed by electrolyte/LTO interfacial reaction instead. These findings would be very valuable as the Li-ion battery research community is working to develop methods to stabilize electrode materials and prevent them from further side reactions after assembly.

7.2.Claims of Originality

1) This is the first time that LTH was prepared without hydrothermal treatment.
2) The bottom-up formation mechanism of layered titanates was proposed for the first time.
3) This is the first time that the topotactic transformation from lepidocrocite LTH to spinel LTO was elucidated.
4) For the first time, the correlation between chemical bond characteristics and Li storage properties of nano-LTO were quantitatively associated in terms of lattice deformation.
5) A kinetic model describing LTO deterioration induced by Li-ion co-intercalation was proposed for the first time.
6) It is the first time that a comprehensive mechanism is presented to account for capacity fade experienced by nano-LTO anodes as the result of LTO structure deterioration and LTO/electrolyte interfacial reaction.

7.3.Future Work

Below some ideas for further in-depth studies of some of the phenomena identified in the present work are proposed:

- Conduct crystal engineering studies taking advantage of the ion-exchange features of layered LTH crystals to create superlattices or nanocomposites with tailored Li-O bonding properties for higher Li-ion storage capacities.
- Surface modification via doping or core-shell structuring in the form of metal oxide protective layers could be explored as avenues to suppress cointercalation-induced relaxation.
- Study further the cointercalation-induced relaxation in nano-LTO during cycling via direct *operando* observation.
- Finally, conduct thorough phase determination of the relaxed structure induced by cointercaltion on nano-LTO surface at atomic scale.

Appendix A

Experimental methods

The following three sections provide a description of the synthesis methods and chemicals, materials characterization techniques, and electrochemical tests conducted.

A.1. Synthesis procedures and chemicals. Figure A1 gives the flowchart of proposed nano-LTO synthesis, which consists of an aqueous preparation of the LTH intermediate phase and LTH→LTO thermal conversion.

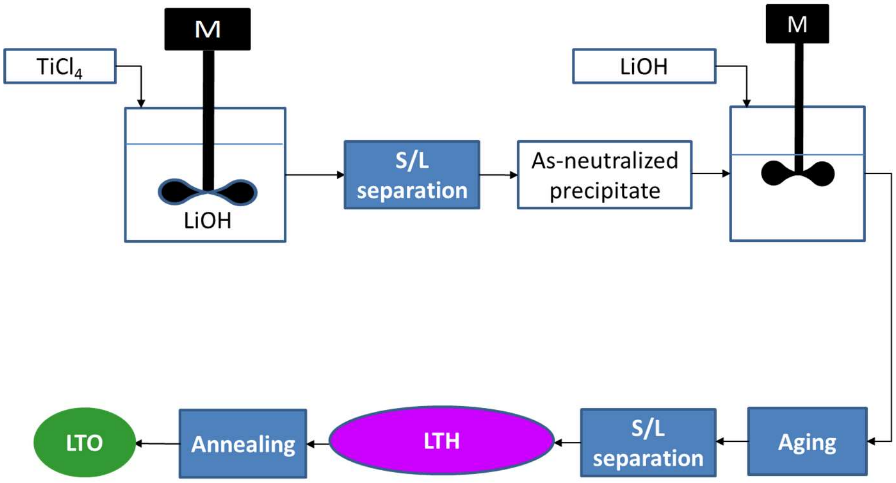

Figure A1. Process flowchart for proposed nano-LTO synthesis

Synthesis of LTH phase. The synthesis method for LTH phase is can be divided into two steps. In the first step of "cold-neutralization", the hydrolytic precipitate was prepared by drop-wise adding 20 mL of 2 M titanium tetrachloride (99.0% $TiCl_4$, Sigma-Aldrich, USA) aqueous solution at 1 mL/min rate, into 180 mL LiOH 1.33 M lithium hydroxide (LiOH) aqueous solution (98.0% $LiOH{\cdot}H_2O$, Sigma-Aldrich, USA) under vigorous mechanical stirring (1000 rpm). The temperature of the mixed solution was controlled at about 2 ºC (<4 ºC) to avoid premature nucleation of titania during the precipitation reaction; the final pH was in the range of 11.5 - 12 at which the solution was continuously stirred for 2 hours. The as-neutralized white precipitates were collected then rinsed with DI water for three times with the assistance of centrifugation at 6,000 rpm for 45 min. After that 0.25 M LiOH aqueous solution was used for an extra washing cycle, involving mixing ~7 mL of wet precipitate with LiOH solution until the total volume reaches 22.5 mL. After washing, the precipitates were collected by centrifuging at 6,000 rpm for 2 min.

To conduct the second step of "aging process", the suspension with Li/Ti=1.3 and pH = 10.5 was prepared by mixing 7 mL of washed (as described above) precipitate with 50 mL 0.25 M LiOH aqueous solution. The prepared suspension was subjected to isothermal aging at 85 ^{o}C for 24 hours under vigorous mechanical stirring at 200 rpm. After aging, centrifugation at 6,000 rpm was applied for solid/liquid phase separation, followed by washing of the recovered precipitate with 50 mL DI water. Layered LTH crystals were obtained after drying the aged precipitate at 80 ^{o}C for 12 hours.

Thermal conversion for nano-LTO preparation. LTH nanocrystals were subjected to annealing in ambient atmosphere (ThermoFisher Scientific Lindberg/Blue M) over the temperature range 400 - 600 ^{o}C for 6 hours at the ramp rate of 3 ^{o}C/min.

A.2. Materials characterization

Scanning Electron Microscopy. Scanning electron microscopy (SEM) was performed with a Hitachi SU–8000 cold-field emission SEM (Hitachi High Technologies, Rexdale, Canada) at an accelerating voltage of 30 kV, and Hitachi S-4700 field-emission at 10kV, respectively.

Transmission Electron Microscopy. Transmission electron microscopy (TEM) was performed with a Philips CM200 TEM at 200 kV to collect images, high-resolution transmission electron microscopic (HR-TEM) ones and the selected area electron diffraction (SAED) patterns.

Scanning Transmission Electron Microscope. A JEM-ARM Model 200F TEM microscope operated at 200 kV to acquire aberration-corrected scanning transmission electron microscope (STEM) images. The attainable spatial resolution of the microscope is 80 pm at an incident semi-angle of 25 mrad of aberration-corrected STEM.

Power X-ray diffraction. Phase composition and crystal structures were determined by powder X-ray diffraction (PXRD) employing a Bruker D8 Discover GADDS XRD^2-microdiffractometer using Bragg–Brentano geometry, at 40 kV, 20 mA for Cu Kα ($\lambda = 1.5418$ Å). The collected PXRD patterns were analyzed using TOPAS (Version 4.2, Bruker AXS, Karlsruhe, Germany).

Brunauer–Emmett–Teller (BET) surface area. The Brunauer–Emmett–Teller (BET) surface area was determined using the Micromeritics TriStar 3000 apparatus under nitrogen controlled atmosphere. Each sample weighed approximately 200 mg and had been degassed for 4 hrs at 80 °C prior to nitrogen physisorption.

Inductive Coupled Plasma-Atomic Emission Spectroscopy (ICP-AES). Chemical composition of prepared crystals was determined by digestion in HNO_3 solution followed inductively coupled plasma - atomic emission spectroscopy (ICP-AES, Thermo Jarell Ash Trace Scan) analysis. Standards of 50, 100, and 300 ppm of titanium prepared by dilution of a 1000 ppm ICP grade standard, and a blank (4 vol. % HNO_3) were used for the calibration.

Raman Spectroscopy. Raman spectroscopy was performed for the short-range order detection of prepared crystals using a Renishaw RM 3000 & InVia spectrophotometer by applying 513.5 nm Ar-ion laser. The samples for quantitative analysis were all mixed with silicon powder (325 mesh, 99%, Sigma-Aldrich) that was used as the inner standard for calibration.

Thermal Analysis. A Thermal Analyzer (TGA/DSC 1, Mettler Toledo) was used to reveal the weight loss and heat flow when heating from room temperature to 800 °C at a heating rate of 15 °C/minute in ambient atmosphere.

Synchrotron X-ray Material Characterization

Synchrotron X-ray related material characterization, including PXRD and X-ray absorption near-edge structure (XANES), were conducted at the Canadian Light Source (CLS) in Saskatoon, SK. To conduct PXRD, the samples were loaded in 0.5 mm ID Kapton capillaries, which were sealed at both ends with a Loctite adhesive. PXRD patterns were collected at the Canadian Macromolecular Crystallography Facility beamline (CMCF-BM or 08B1-1) at CLS. 08B1-1 is a bending magnet beamline with a Si (111) double crystal monochromator. Two-dimensional (2D) data was collected using a Rayonix MX300HE detector with an active area of 300 mm × 300 mm. The patterns were collected at an energy of 18 keV ($\lambda = 0.68880$ Å) and capillary-detector distance of 250 mm. The XRD patterns were calibrated and integrated using the GSASII software package[A1]. The sample-detector distance, detector centering and tilt were calibrated using a lanthanum hexaboride (LaB_6) standard reference material from the National Institute for Standards and Technology (NIST SRM 660a LaB_6) and the calibration parameters were applied to all patterns. After calibration, the 2D patterns were integrated to obtain standard 1D powder diffraction patterns. A pattern from an empty Kapton capillary was subtracted from the sample data during integration. The integrated LaB_6 pattern was used to obtain the instrument resolution of the beamline for the Rietveld refinement of the samples. The latter was conducted by using TOPAS (Version 4.2, Bruker AXS, Karlsruhe, Germany).

XANES was carried out at the Soft X-ray Microcharacterization Beamline (SXRMB) at the CLS. LTO samples were mounted on double-sided conducting carbon tape to collect total electron yield (TEY) and fluorescence yield (FY) signals, respectively. TEY is a widely-used technique to collect the yield of Auger electrons/secondary electrons in the near-surface region because of the short escape depth of electrons; while FY is a useful bulk sensitive method. Background subtraction and normalization spectra were conducted using Athena[A2].

Hard X-ray XAENS were recorded from 4880 to 5720 eV for the Ti K-edge spectra at Variable Line Spacing Plane Grating Monochromator (VLS PGM) using a silicon drift detector (SDD). The spectra in soft X-ray range of Ti L-edge and O K-edge were collected on the spherical grating monochromator (SGM) beamline ($\Delta E/E$:~10^{-4}) in the energy range of 459-480 eV and 525-550 eV, respectively; Li K-edge spectra were obtained on the plane grating monochromator (PGM) beamline ($\Delta E/E$:~10^{-4}) and collected from 55 to 70 eV.

A.3. Electrochemical testing

Electrode Preparation. The composite electrodes were made of the active material, LTO nanosheets (80 wt%), conductive carbon black (10 wt%) and polyvinylidene fluoride (PVDF) binder (10 wt%) homogeneously dispersed in the ratio of 1 gram of mixture to 5 ml N-methyl pyrrolidinone (NMP). The prepared slurry was coated on 15 μm aluminum foil with a coating loading of about 12 mg/cm^2. The prepared electrode sheets were then punched into circles with 10 mm in diameter dried at 110 °C in vacuum for 12 hours.

Battery Assembly. CR2032 coin cells (Figure A2) were assembled with the prepared working electrode and Li metal (Sigma-Aldrich) as reference/counter electrode in an argon-filled glove box (M. Braun Co., [O_2] < 0.5 ppm, [H_2O] < 0.5 ppm). A 25 μm polypropylene (PP)/polyethylene (PE) separator (PP/PE/PP) (Celgard 2325) was used, and 1 M $LiPF_6$ in ethylene carbonate (EC) and dimethyl carbonate (DMC) (1:1, v/v) was used as the electrolyte.

Galvanostatic Charge/Discharge. The galvanostatic experiments were performed using a standard battery cycler (BT2043-10V-100mA-40, Arbin) in the voltage range of 2.5 - 1.0 V vs. Li/Li$^+$. 1C rate was applied for cycle life test (1 C = 175 mA/g); Rate capability was evaluated by applying various rate 0.05, 0.2, 0.5, 1, 2, 5, 10 and 20 C for 5 cycles at each rate. Another 5 cycles at 1C rate were applied in the end to appraise the durability of nano-LTO.

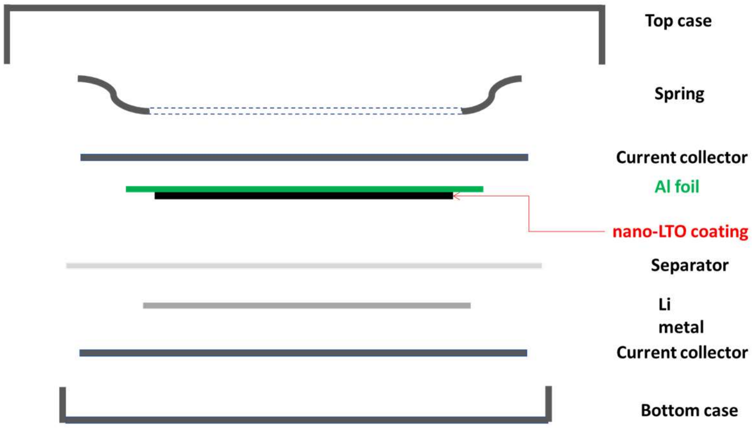

Figure A2. Exploded drawing of CR2032 coin cells

Polarization evolution contour plot. Differential capacitance (dQ/dV) evolution during the 1C galvanostatic cycle test was visualized by a contour plot. Differential capacitance, defined as the relative change in capacity (dQ) over the corresponding voltage range (dV), was determined via a simple two-point numerical differentiation from the collected charge/discharge voltage profiles of 1 C cycles All collected dQ/dV plots were then presented as a contour plot with respect to the cycle numbers. The color temperature in the polarization variation figures represents the intensity of the peaks of the differential capacitance curves, which correspond to the phase equilibrium voltage of the spinel/rock-salt phase transformation.

Cyclic Voltammetry and Electrochemical Impedance Spectroscopy. Biologic VSP Potentiostat/Galvanostat/EIS system was used for cyclic voltammetry (CV) and electrochemical impedance spectroscopy (EIS) on three-electrode cells. Cyclic voltammetry (CV) test was scanned from 1.0 – 2.5 V vs. Li/Li$^+$ at different scan rates from 0.083 to 0.416 mV/s; EIS was performed in the frequency range from 100,000 to 0.01 Hz, with modulation at 5 mV. The cells were kept at open-circuit condition for 6 hour before performing impedance tests to reach equilibrium.

A.4. References

(A1) Toby, B. H.; Von Dreele, R. B. GSAS-II: the genesis of a modern open-source all purpose crystallography software package. *J. Appl. Cryst.* **2013,** *46* (2), 544.

(A2) Ravel, B.; Newville, M. ATHENA, ARTEMIS, HEPHAESTUS: data analysis for X-ray absorption spectroscopy using IFEFFIT. *J. Synchrotron Radiat.* **2005,** *12* (Pt 4), 537.

Appendix B

Supporting Information for Chapter 4:

Formation of Lithium Titanate Hydrate Nanosheets: Insight into a Two-Dimension Growth Mechanism by in Situ Raman

B.1. Derivation of Johnson-Mehl-Avrami-Kolmogorov (JMAK) Model for Anisotropic Growth

The modified JAMK kinetic model for anisotropic growth was derived directly from Kooi's work.[B1,2] Only a special case of 2D growth in 3D space with continuous nucleation at constant rate was considered in our study.

The kinetics of isothermal phase transformation proceeding via nucleation and subsequent growth are generally described by the JMAK theory, which states that the fraction of transformed space x is related to the extended fraction $x_{extended}$ according to:

$$x(t) = 1 - \exp[-x_{extended}(t)] \tag{B1a}$$

where the extended fraction $x_{extended}(t)$ obeys

$$x_{extended}(t) = \int_0^t I(\tau)V(t-\tau)d\tau \tag{B1b}$$

With *I* the nucleation rate per unit of untransformed space; and V the extended space of a single transformed grain at time t; τ is the nucleation time of that transformed grain.

According to the first assumption of constant nucleation rate, the total number of nuclei formed per unit of untransformed space with dimension, d_s, at a given temperature, behaves as a linear equation i.e. $N = N_0 t$, which define the initial nucleation rate N_0 with temperature dependency becomes:

$$N(t,T) = N_0 t \exp\left(\frac{-E_n}{kT}\right) \tag{B2}$$

From which the nucleation rate can be easily calculated as:

$$I(t,T) = \frac{dN(t,T)}{dt} = N_0 \exp\left(\frac{-E_n}{kT}\right) \tag{B3}$$

Then the second assumption of linear growth of grain for the interfacial reaction process is reasonable for the present system as it involves crystallization from an amorphous precursor with highly disordered interface. [B3,4] The growth rate in this case can be formulated as the difference in forward and backward reaction rates:

$$G(T) = G_0 \exp\left(\frac{-E_g}{k_B T}\right)[1 - \exp(\frac{\Delta G}{k_B T})]$$

where E_g is the activation energy for growth (E_g>0) and ΔG is the difference in Gibbs free energy per atom of the phase, after and before the phase transformation. The transformation would be spontaneous if ΔG<0. If the driving force -ΔG is larger compared to thermal excitation (kT~0.03 eV), the backward reaction rate can be neglected:

$$G(T) = G_0 \exp\left(\frac{-E_g}{k_B T}\right)[1 - \exp(\frac{\Delta G}{k_B T})] \rightarrow G(T) = G_0 \exp\left(\frac{-E_g}{k_B T}\right) \tag{B4}$$

Now let us consider that 2D plates with thickness *w* have equal probability to grow in three orthogonal directions in 3D space. The average length the grains are able to grow before their growth is blocked is the characteristic length $\overline{L_\iota}$ which is expressed as:

$$\overline{L_\iota} = \frac{C}{\sqrt[3]{N(\tau^a)}}$$

By replacing the $V(t-\tau)$ in Eq. (B1b) by the width *w*, times the square of characteristic length $\overline{L_\iota}$ as

$$V(t-\tau) = w\overline{(L_\iota)}^2 = \frac{wC^2}{(N\tau^a)^{2/3}} \qquad \text{(B5)}$$

and then inserting it as well as I(t,T) from Eq. (B3) back into Eq. (B1b) we obtain:

$$x_{extended}(t) = \int_{t^*}^{t} aN\tau^{a-1}\frac{wC^2}{(N\tau^a)^{2/3}}\,d\tau \qquad \text{(B6)}$$

in which the t* is defined as the time when growth stops because of blocking from a neigbouring 2D plate:

$$Gt^* = \frac{C}{\sqrt[3]{N(t^*)}} \rightarrow t^* = \sqrt[1+3]{\frac{C^3}{NG^3}}$$

By inserting t* into the integration result of Eq. (B6), the modified transformed fraction for two-dimensional anisotropic growth in 3D space is obtained as:

$$x_{extended}(t) = 3wC^2[N(t-t^*)]^{1/3}$$

where the Avrami exponent is equal to 1/3.

In the limitation case of t>>t*, Eq. (B1a) becomes

$$x(t) = 1 - \exp[-x_{extended}(t)] = 1 - \exp[3wC^2[N(t-t^*)^a]^{1/3}] \qquad \text{(B7a)}$$

Employing Avrami plot analysis in the form of ln[-ln[1-x(t)]] vs. ln(t) we get:

$$\ln(-ln[1-x(t)]) = \ln(x_{extended}(t)) = \ln[3wC^2[N(t-t^*)]^{\frac{1}{3}}]$$

$$\ln(-ln[1 - x(t)]) = \ln\left(3wC^2(N)^{\frac{1}{3}}\right) + \frac{1}{3} ln(t - t^*) \tag{B7b}$$

now replacing N in Eq. (B7) by Eq. (B2), the intercept in Avrami plot becomes

$$\ln\left(3wC^2(N)^{\frac{1}{3}}\right) = \ln(3wC^2) + \frac{1}{3}\ln[N_0 \exp\left(\frac{-E_n}{kT}\right)]$$

$$\rightarrow \ln(3wC^2) + \frac{1}{3}\ln(N_0) + \frac{1}{3}\left(\frac{-E_n}{kT}\right) \tag{B8}$$

In the Arrhenius plot analysis, its slope turns out to be $\frac{1}{3}\left(\frac{-E_n}{kT}\right)$

B.2. Estimation of Residual Strain from Raman Measurements

The quantitative estimation of residual strain is conducted via calculating the peak position difference between reference LTH material and the different LTH crystallization products. Precise Peak position was determined by applying pseudo-Voigt type [B5] fitting on one of the significant Ag bands at 433 cm^{-1}. The referenced LTH material was prepared by 240 ºC hydrothermal treatment [B6-8] and is considered as the “perfect” crystal without residual strain, *i.e.* only relative residual train is obtained by this method. In the end, the residual strain can be calculated according to equation[B9,10]:

$$\frac{\Delta\omega}{\omega_0} = -K\frac{a-a_0}{a_0} = -K\frac{\Delta a}{a_0} \tag{B9}$$

where ω_0 is the Raman shift 433 cm^{-1} of referenced LTH; $\Delta\omega$ is the difference between the reference 433 cm^{-1} and the crystallized LTH sample at specific time; a_0 is the lattice constant of referenced LTH; only *b*-axis with 16.7023(2) Å is employed for simplicity; *a* is the lattice constant of *b*-axis of the corresponding LTH samples; and *K* is a constant containing the Grüneisen parameter[2].

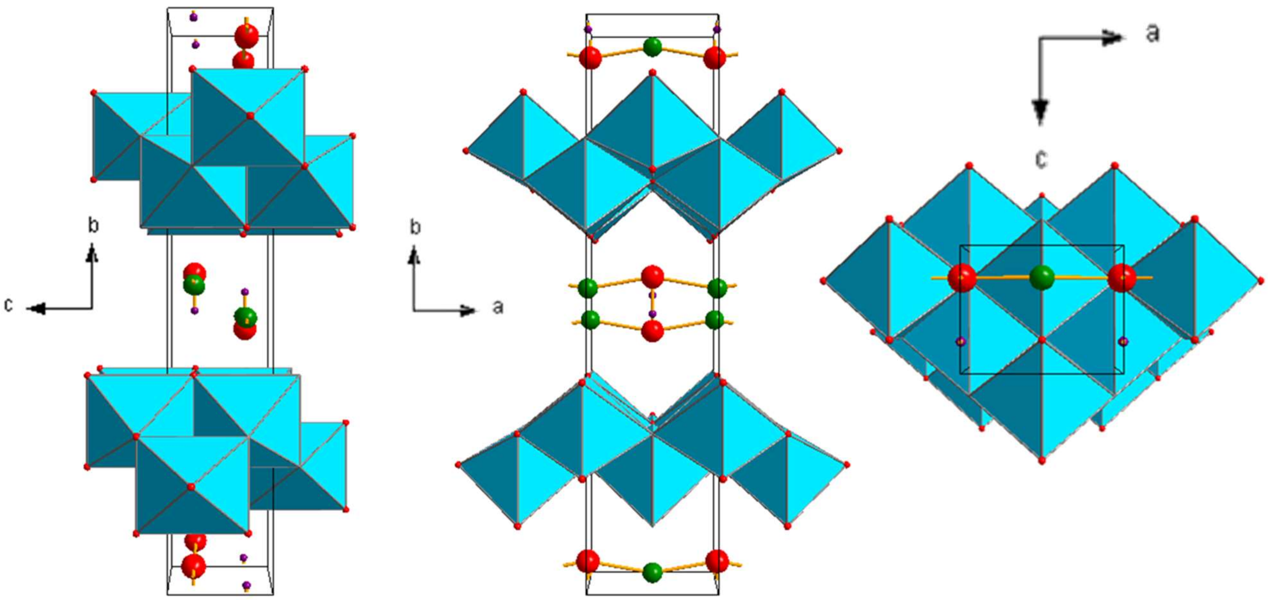

Figure B1. The schematic of the proposed orthorhombic lepidocrocite LTH (space group *Cmcm*) model with lattice parameters: *a*-axis = 3.8020 Å; *b* axis = 16.6729 Å; and *c*-axis = 3.0093 Å. Red balls are oxygen atoms, green represents lithium atoms and the small purple balls are hydrogen.

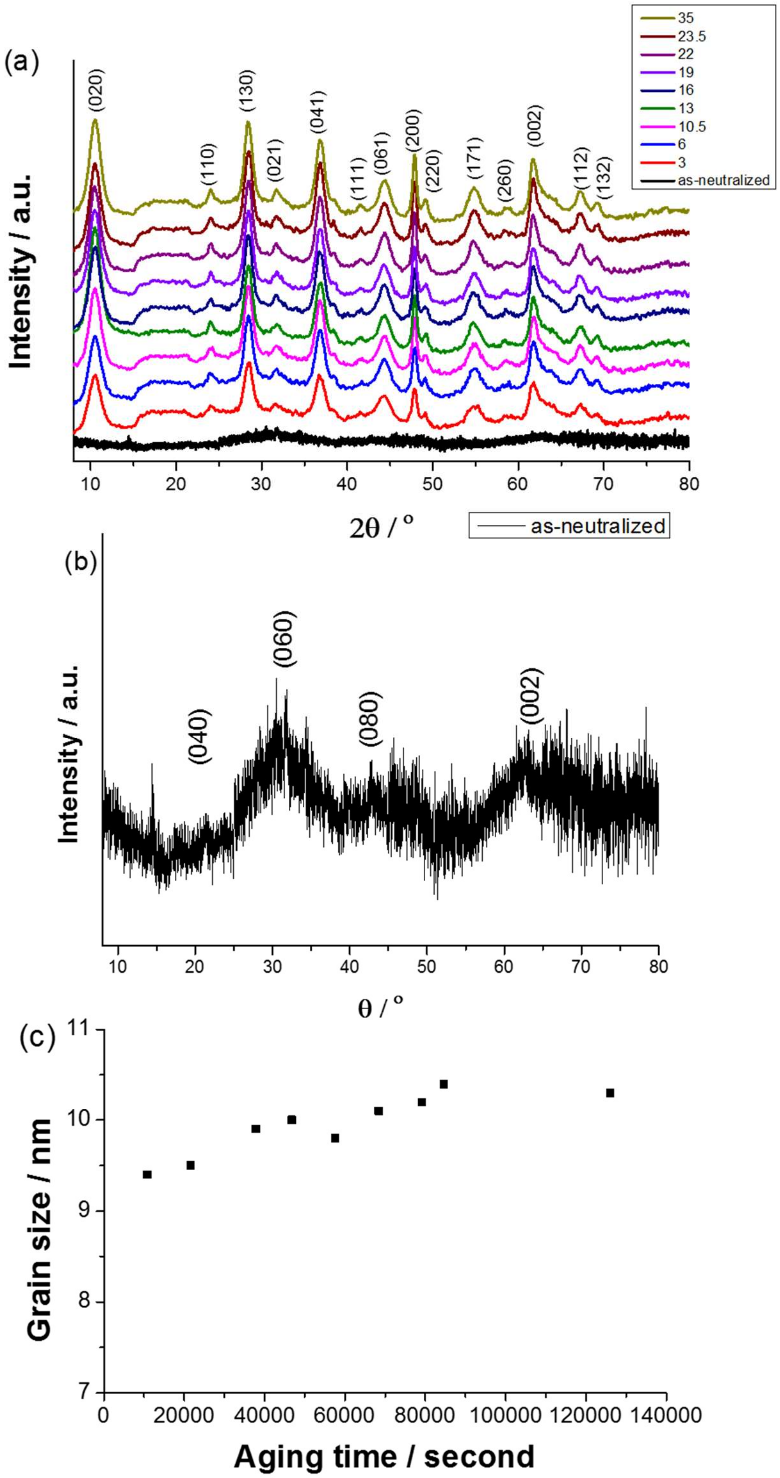

Figure B2. (a) Time evolution of PXRD patterns of isothermally aged samples, (b) the magnified pattern of as-neutralized precipitate, and (c) the grain size calculated by Scherrer equation according to the PXRD patterns in (a).

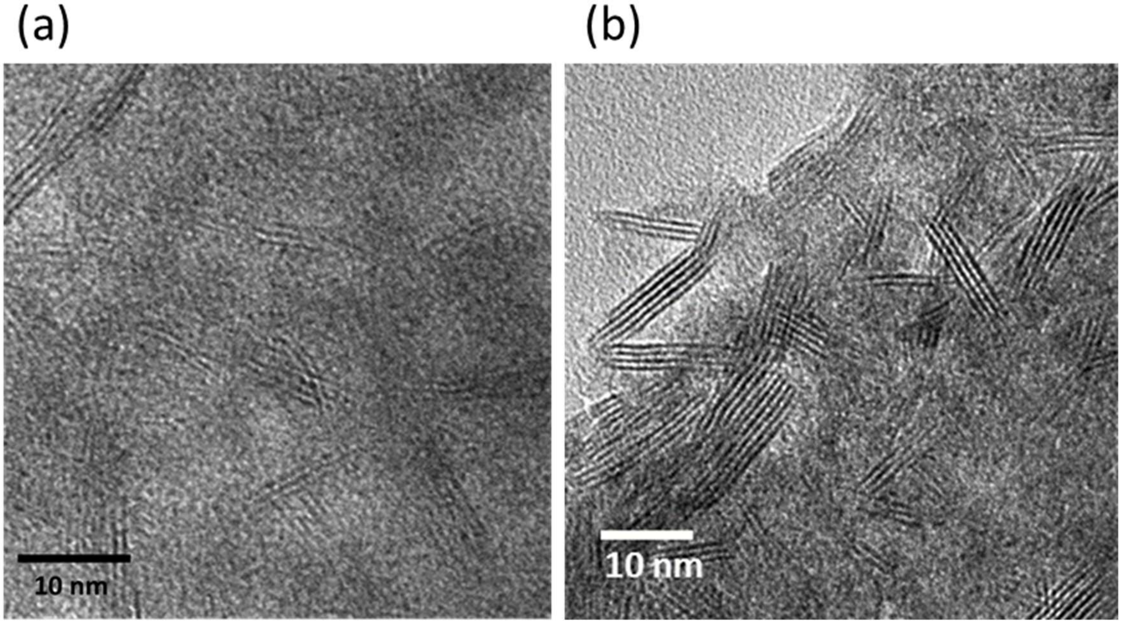

Figure B3. Nanoscale curved features of (a) as-neutralized precursor precipitate and (b) isothermally crystallized LTH at 90 ºC for 3 hours.

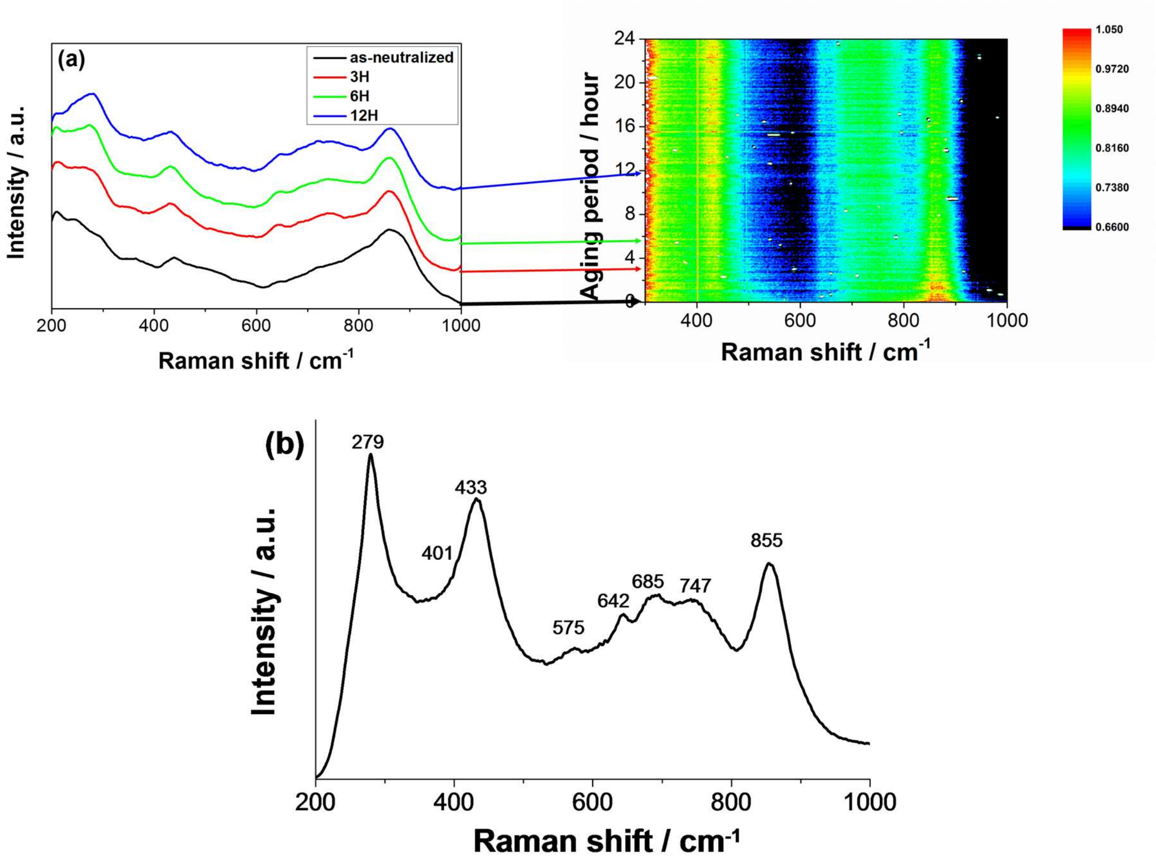

Figure B4. (a) Schematic diagram describing the obtainment of the Raman spectra on the left by cross sectioning of the in situ Raman contour plots on the right; (b)the Raman spectrum of the reference LTH phase prepared by hydrothermal process at 240 ºC for 48 hours.

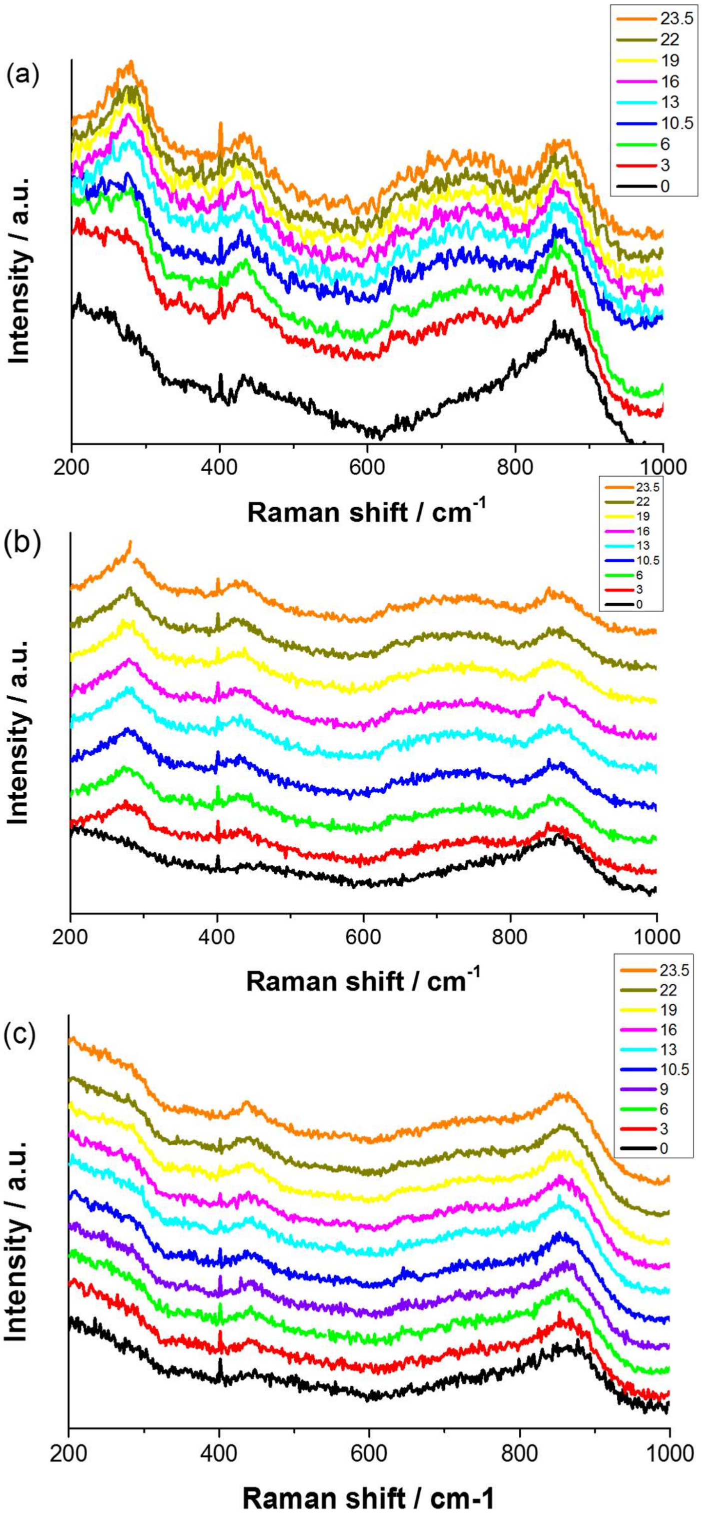

Figure B5. In-situ Raman measurements during isothermal crystallization at (a) 90 (b) 75 and (c) 50 °C.

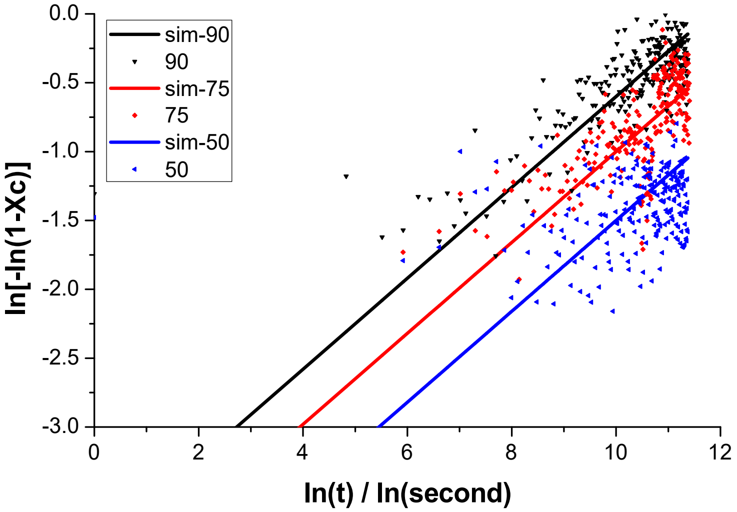

Figure B6. The Avrami plot ($\ln[-ln(1-x)]\ vs\ \ln(t)$) of LTH growth in isothermal condition at (a) 90 ^{o}C (black), (b) 75 ^{o}C (blue) and (c) 50 ^{o}C (red). Please note the Avrami exponent = 1/3.

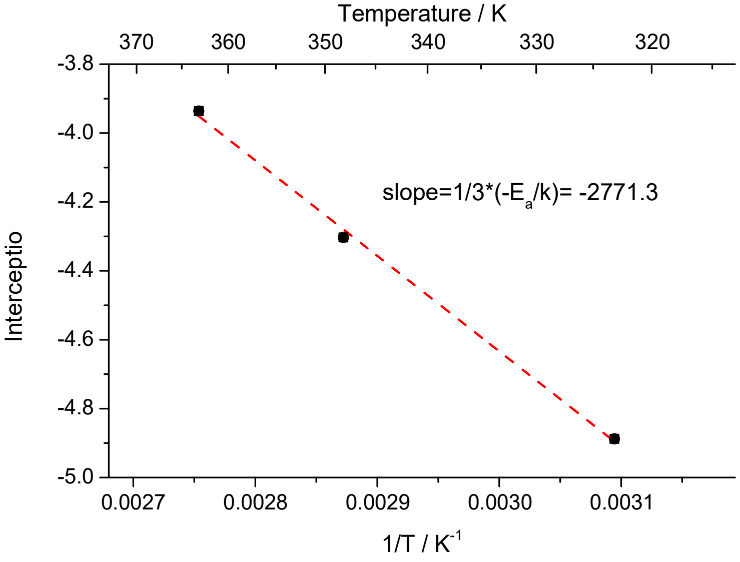

Figure B7. The Arrhenius plot calculated from the intercept on Y-axis of the Avrami plot (Figure B6), in which the slope corresponds to the activation energy E_n in the form of $\frac{1}{3}\left(\frac{-En}{k}\right)$ where k is Boltzmann's constant.

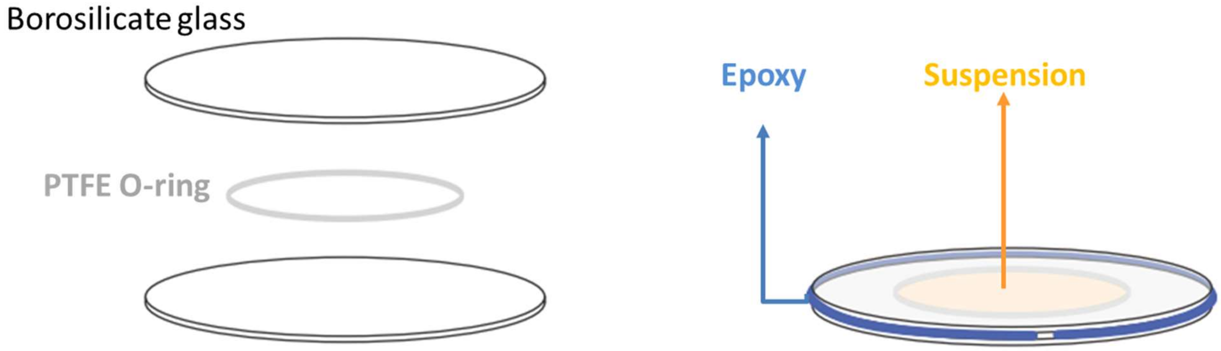

Figure B8. The schematic diagram of the in situ reactor for isothermal crystallization of LTH

References

(B1) Kooi, B. J. Extension of the Johnson-Mehl-Avrami-Kolmogorov theory incorporating anisotropic growth studied by Monte Carlo simulations. *Phys. Rev. B: Condens. Matter Mater. Phys.* **2006,** *73* (5), 054103.

(B2) Kooi, B. J. Monte Carlo simulations of phase transformations caused by nucleation and subsequent anisotropic growth: Extension of the Johnson-Mehl-Avrami-Kolmogorov theory. *Phys. Rev. B: Condens. Matter Mater. Phys.* **2004,** *70* (22), 224108.

(B3) Kingary, W.; Bowen, H.; Uhlmann, D. *Introduction to Ceramics*, 1976.

(B4) Kirkpatrick, R. J. Crystal Growth from the Melt: A Review. *Am. Mineral.* **1975,** *60*, 798.

(B5) Thompson, P.; Cox, D. E.; Hastings, J. B. Rietveld Refinement of Debye-Scherrer Synchrotron X-Ray Data from Al2o3. *J. Appl. Cryst.* **1987,** *20* (2), 79.

(B6) Shirpour, M.; Cabana, J.; Doeff, M. Lepidocrocite-type Layered Titanate Structures: New Lithium and Sodium Ion Intercalation Anode Materials. *Chem. Mater.* **2014,** *26* (8), 2502.

(B7) Sugita, M.; Tsuji, M.; Abe, M. Synthetic Inorganic Ion-Exchange Materials. LVIII. Hydrothermal Synthesis of a New Layered Lithium Titanate and Its Alkali Ion Exchange. *Bull. Chem. Soc. Jpn.* **1990,** *63* (7), 1978.

(B8) Li, N.; Mei, T.; Zhu, Y.; Wang, L.; Liang, J.; Zhang, X.; Qian, Y.; Tang, K. Hydrothermal synthesis of layered $Li_{1.81}H_{0.19}Ti_2O_5.xH_2O$ nanosheets and their transformation to single-crystalline $Li_4Ti_5O_{12}$ nanosheets as the anode materials for Li-ion batteries. *CrystEngComm* **2012,** *14* (20), 6435.

(B9) Arguirov, T.; Mchedlidze, T.; Kittler, M.; Rolver, R.; Berghoff, B.; Forst, M.; Spangenberg, B. Residual stress in Si nanocrystals embedded in a SiO_2 matrix. *Appl. Phys. Lett.* **2006,** *89* (5), 053111.

(B10) Wang, R. P.; Zhou, G. W.; Liu, Y. L.; Pan, S. H.; Zhang, H. Z.; Yu, D. P.; Zhang, Z. Raman spectral study of silicon nanowires: High-order scattering and phonon confinement effects. *Phys. Rev. B: Condens. Matter Mater. Phys.* **2000,** *61* (24), 16827.

Appendix C

Supporting Information for Chapter 5:

Annealing-regulated elimination of residual strain-induced structural relaxation for high-power $Li_4Ti_5O_{12}$ *nanosheet anodes*

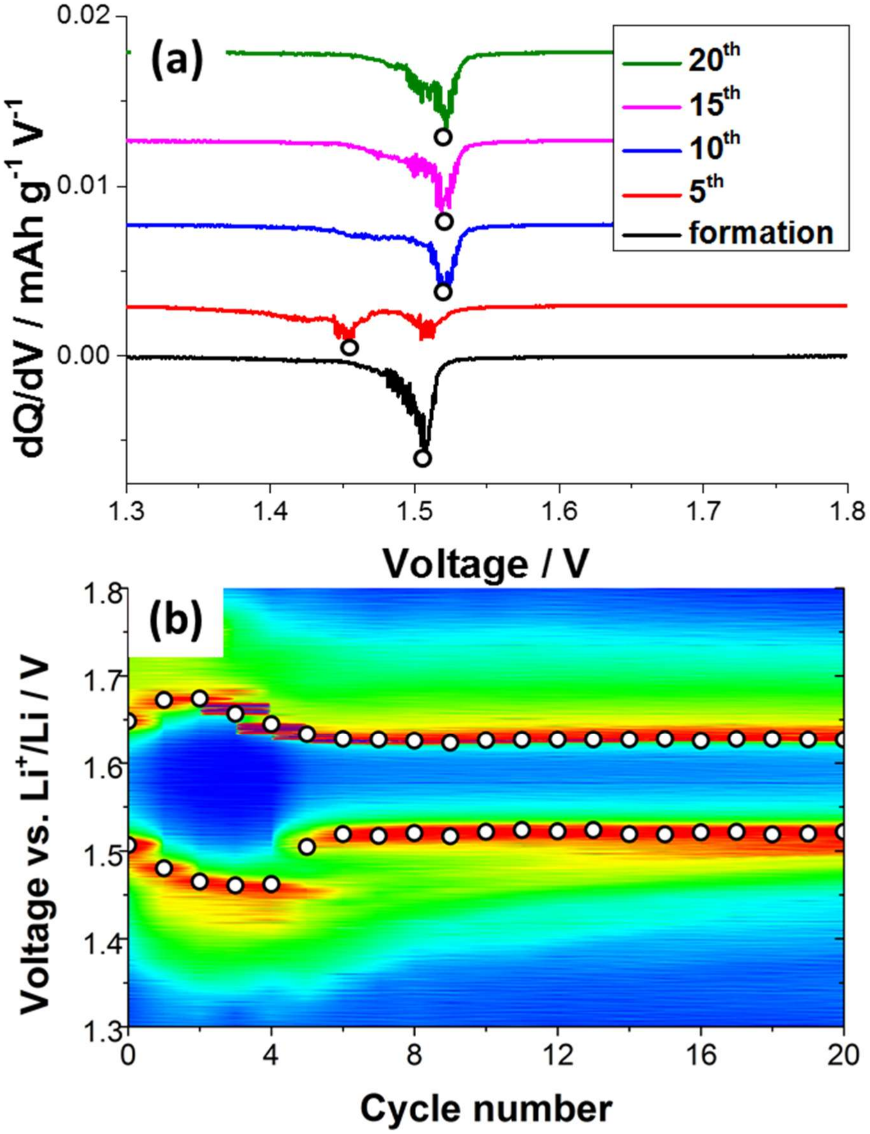

Figure C1. (a) Characteristic dQ/dV plots of 600°C annealed LTO nanocrystals cycled in the range of 1.3-1.8 V vs. Li/Li^{+} at 1C rate, where only discharge peaks were given for simplicity. (b) the corresponding contour plot of polarization evolution converted from the collected dQ/dV plots. The open circles help to locate the strongest peaks in dQ/dV plot onto the contour plot.

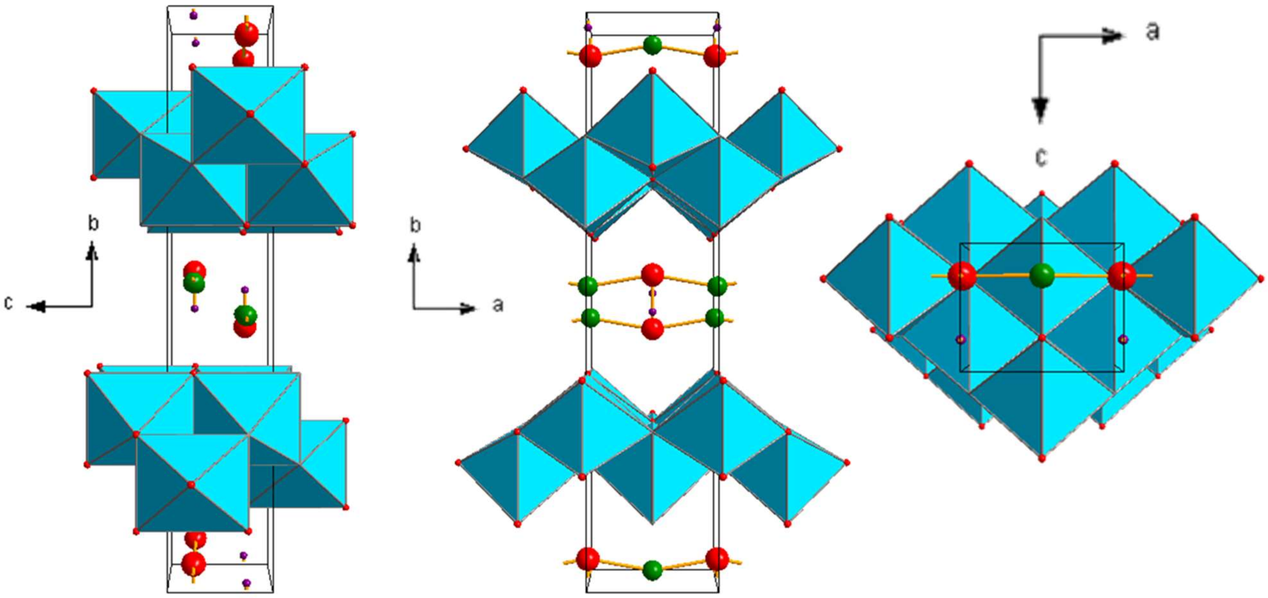

Figure C2. Schematic representation of the proposed orthorhombic lepidocrocite LTH (space group *Cmcm*) model. Red balls are oxygen atoms, green represents lithium atoms and the small purple balls are hydrogen The polyhedral representation was generated using Diamond (V.3.2, Crystal Impact GbR, Bonn, Germany).

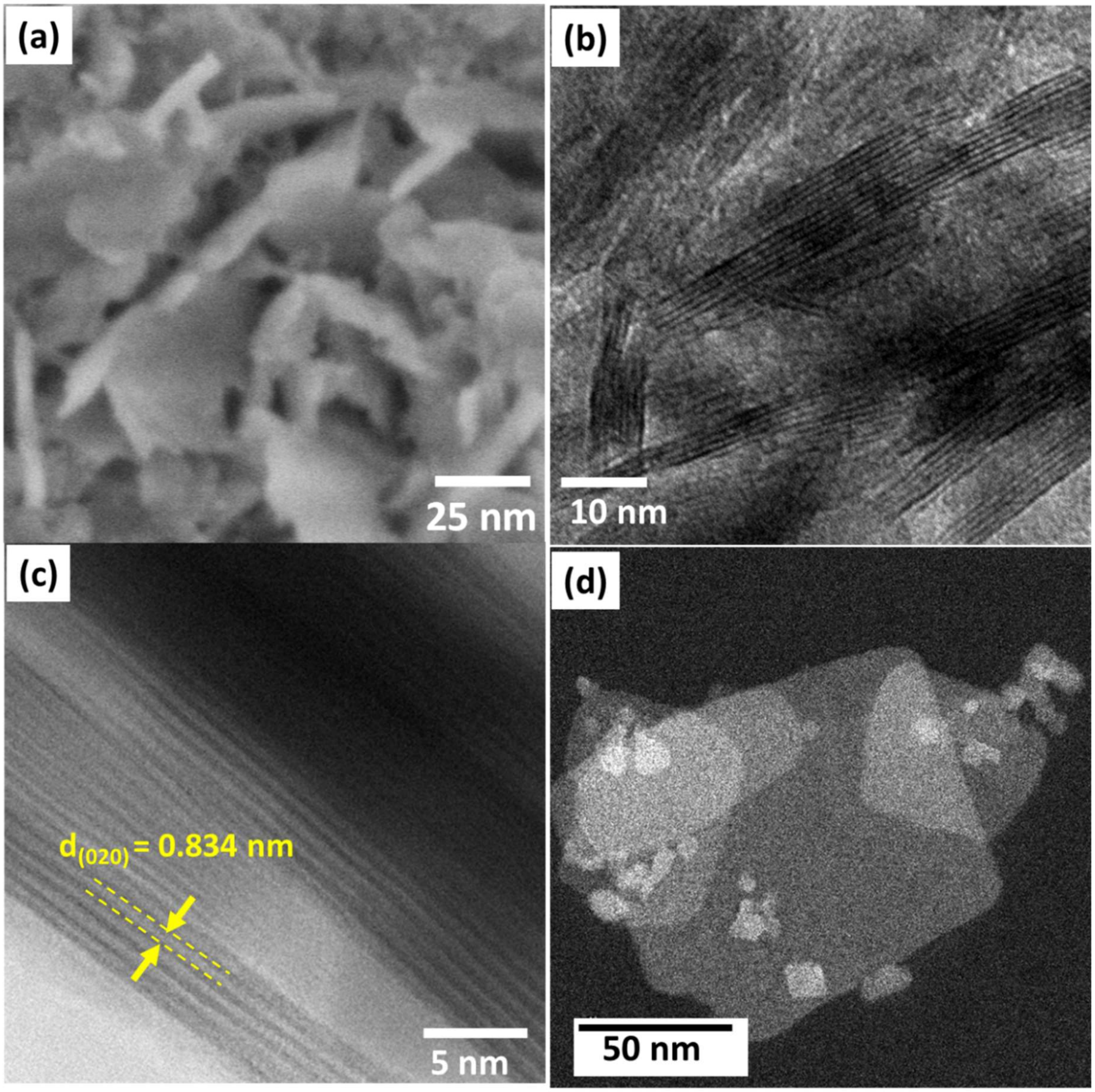

Figure C3. Morphology observation of LTH nanocrystals in different scales.

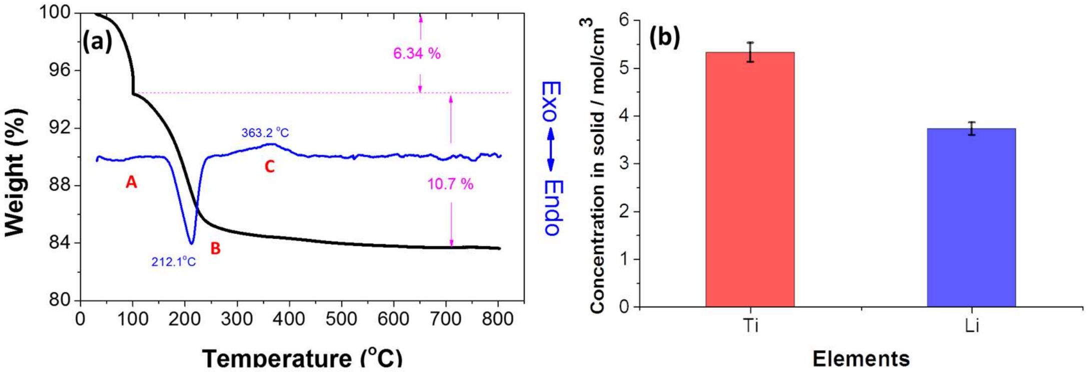

Figure C4. (a) TG-DTA curves of LTH in the temperature range from room temperature to 800 °C in air, where the initial weight loss of 6.3 % is because of the removal of physically adsorbed water; (b) Column chart showing the average concentration of Ti (red) and Li (blue) from ICP analysis, and the error bars indicate the standard deviation.

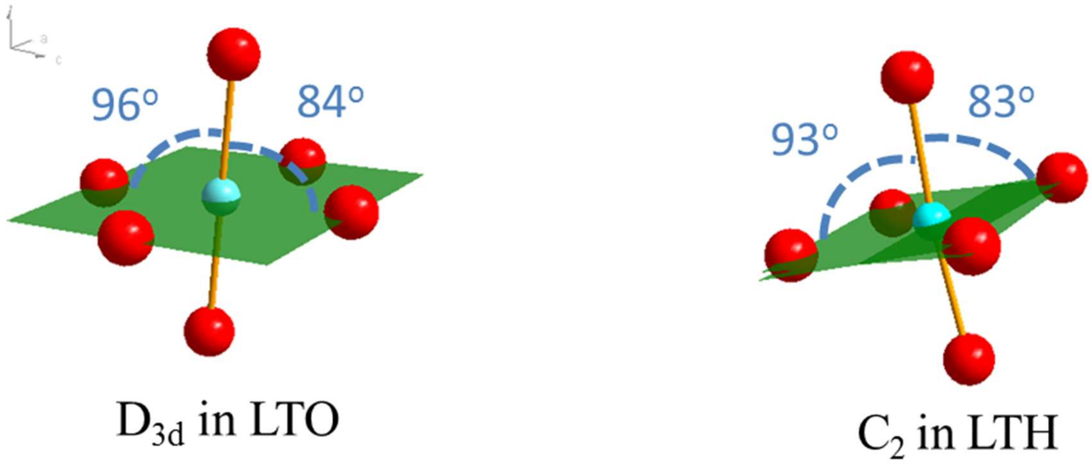

Figure C5. Schematics of TiO_6 octahedra with point group D_{3d} (left) and C_{2v} (right), which correspond to $Fd\bar{3}m$ spinel LTO and *Cmcm* lepidocrocite LTH, respectively.

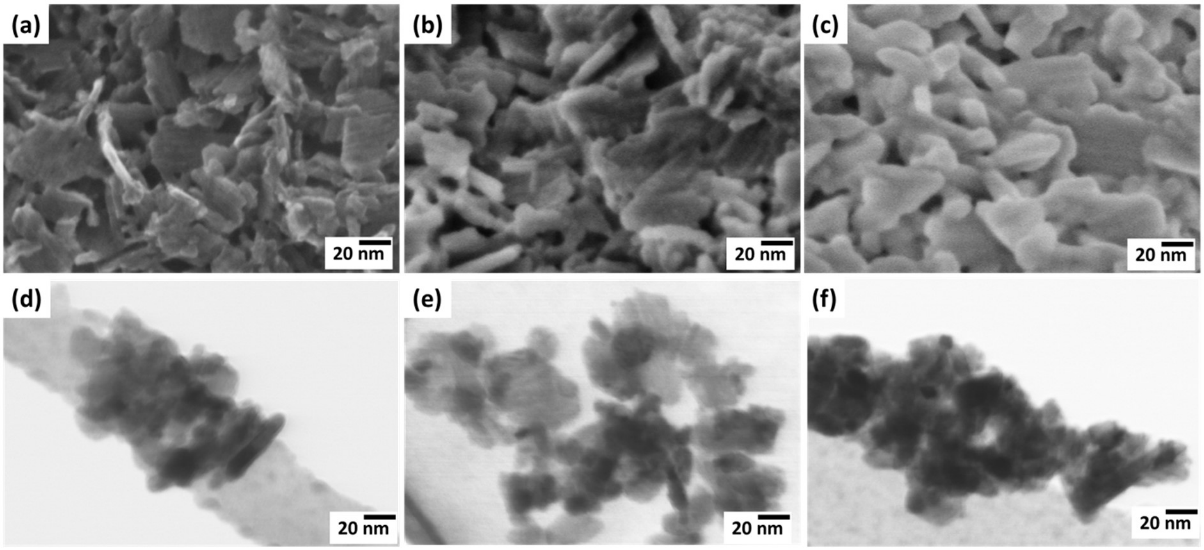

Figure C6. SEM morphology and structure of LTO nanosheet crystals after annealing for 6 hours at (a) 400 (b) 500 and (c) 600 ^{o}C. The corresponding STEM images for each condition are given in the order of (d) 400 (e) 500 (f) 600 ^{o}C, respectively.

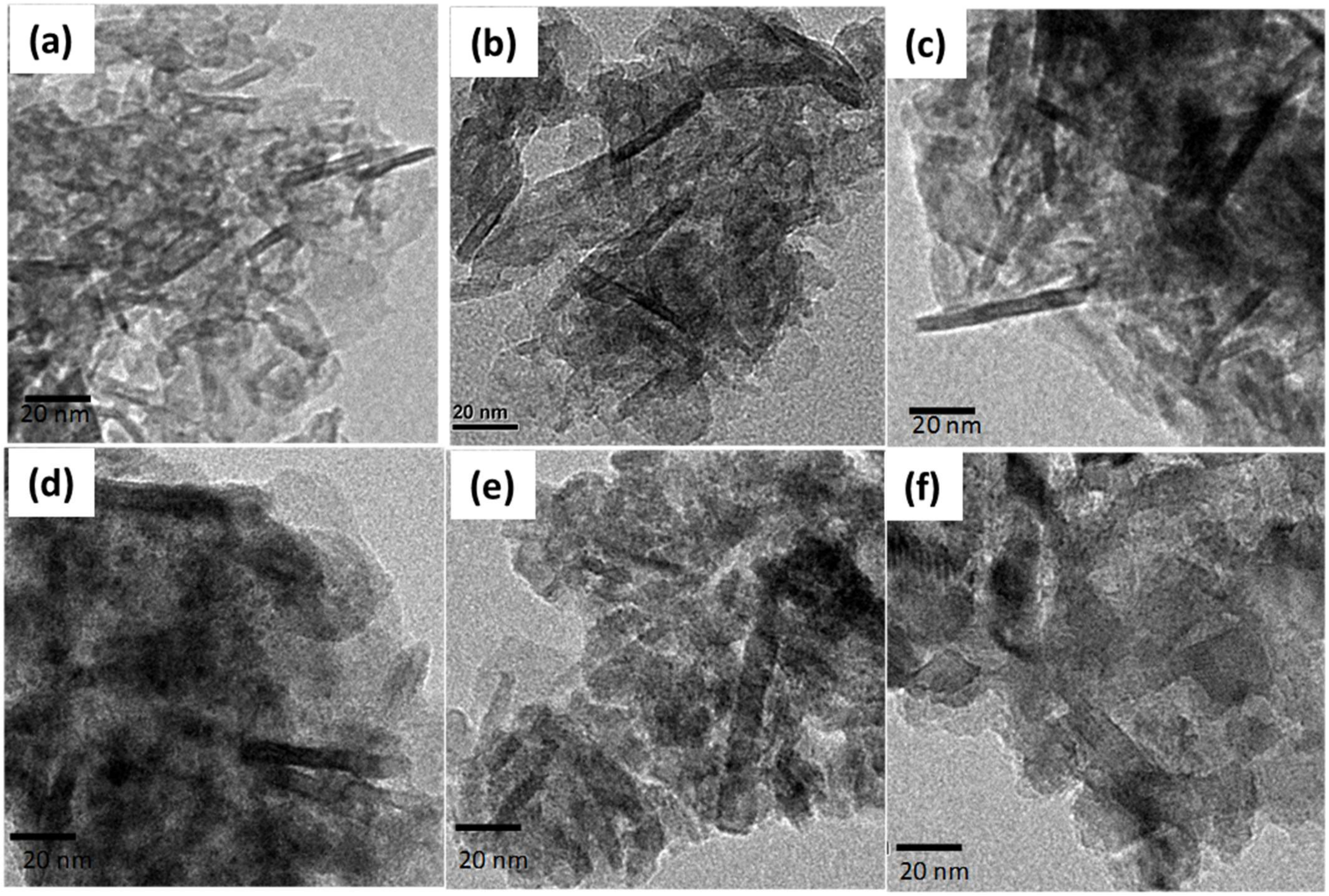

Figure C7. TEM images of LTO nanosheet crystals obtained via annealing for 6 hours at different temperatures: (a) 250 (b) 300 (c) 350 (d) 400 (e) 500 (f) 600 ^{o}C.

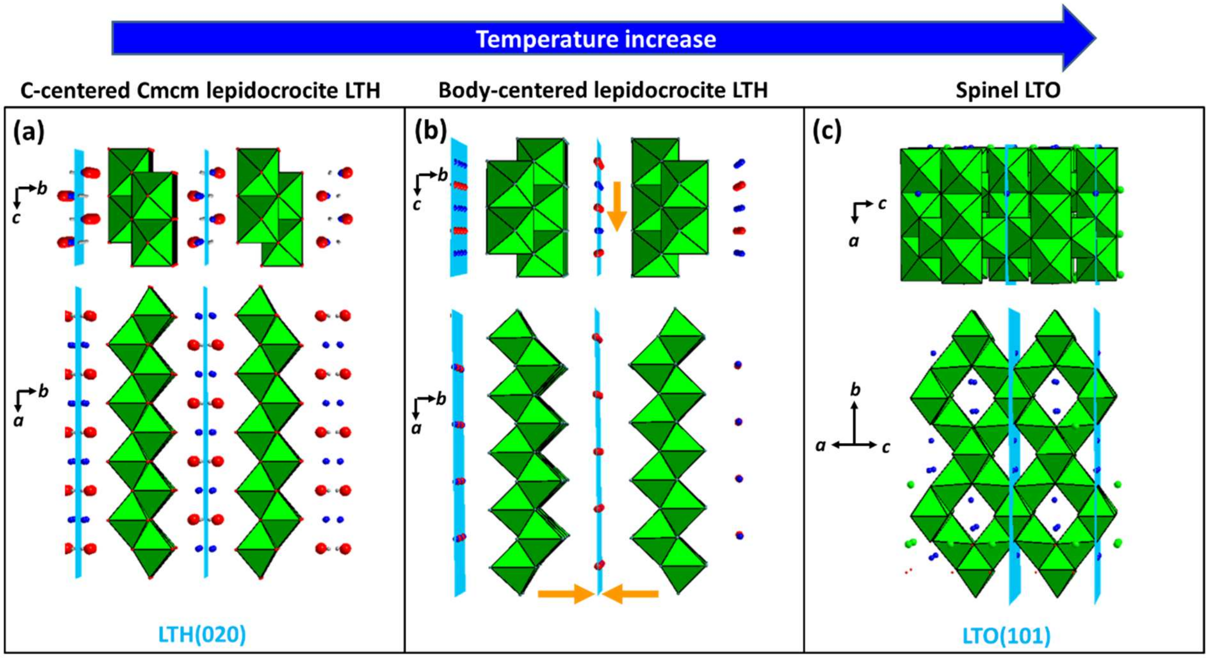

Figure C8. Schematic of LTH→LTO phase transformation. (a) As-prepared LTH phase is of *C*-centered orthorhombic system. (b) After dehydration that removes water from interlayer space, the host layers move closer causing contraction of interlayer distance, d (020), of LTH. A lateral glide along *c*-axis (the orange vertical arrow in the upper part) by *c*/2 during the topotactic transformation results in a symmetry transition from *C*-centered orthorhombic into body-centered orthorhombic. (c) The framework consisted of TiO_6 octahedra also transitions from 2D multilayered structure into a 3D spinel structure by local diffusion of cations. Facets (020) of LTH and (010) of LTO are both indicated to help recognize the relationship between morphology and crystallographic orientation of formed nanocrystals. Red balls are oxygen atoms, blue ones represent lithium atoms and the TiO_6 octahedra are presented in green.

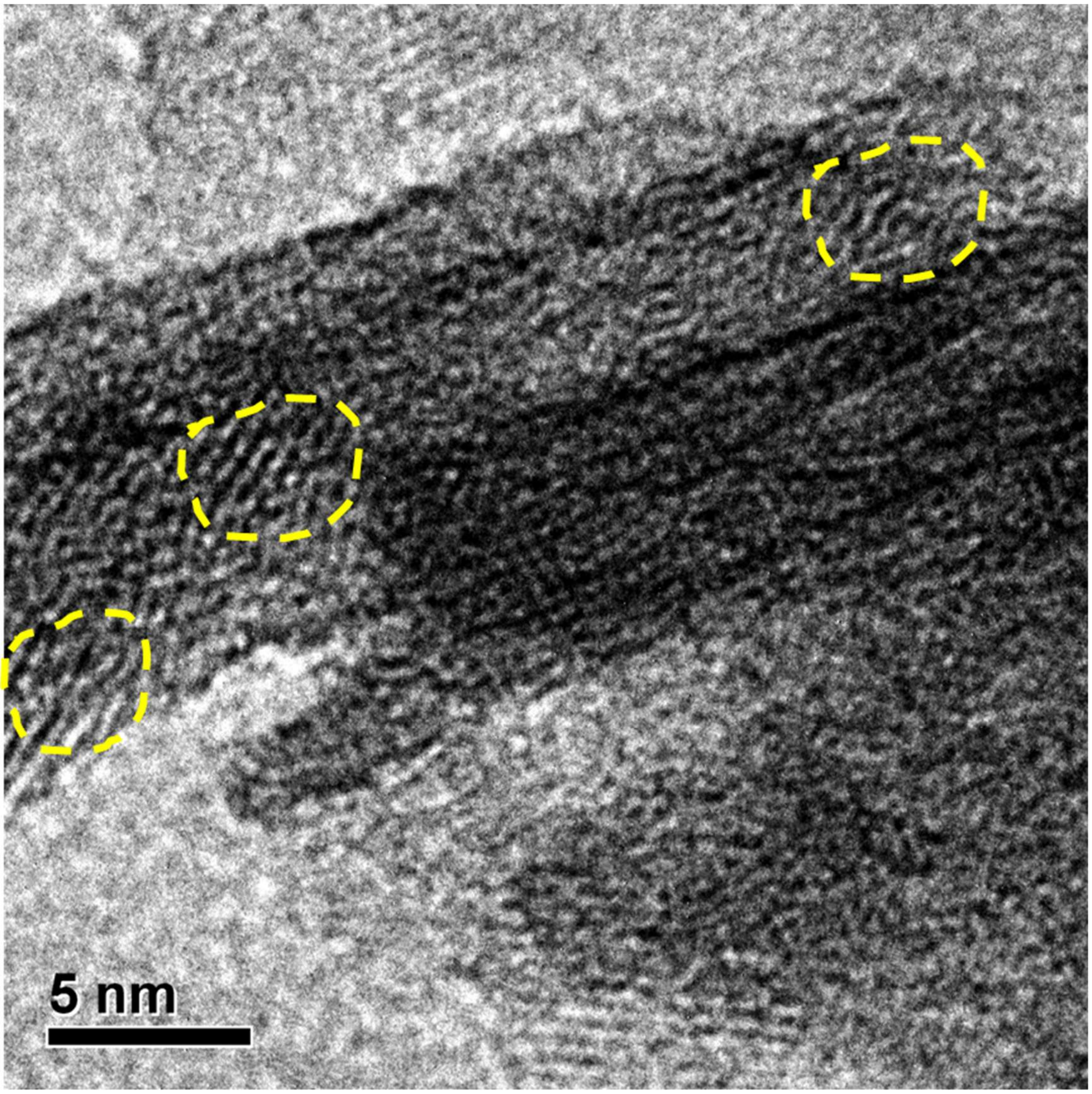

Figure C9. Magnified image of Figure 2d of LTO nanosheets annealed at 300 ^{o}C for 6 hours. Lattice fringes of LTO spinel nuclei can be seen in the circled regions.

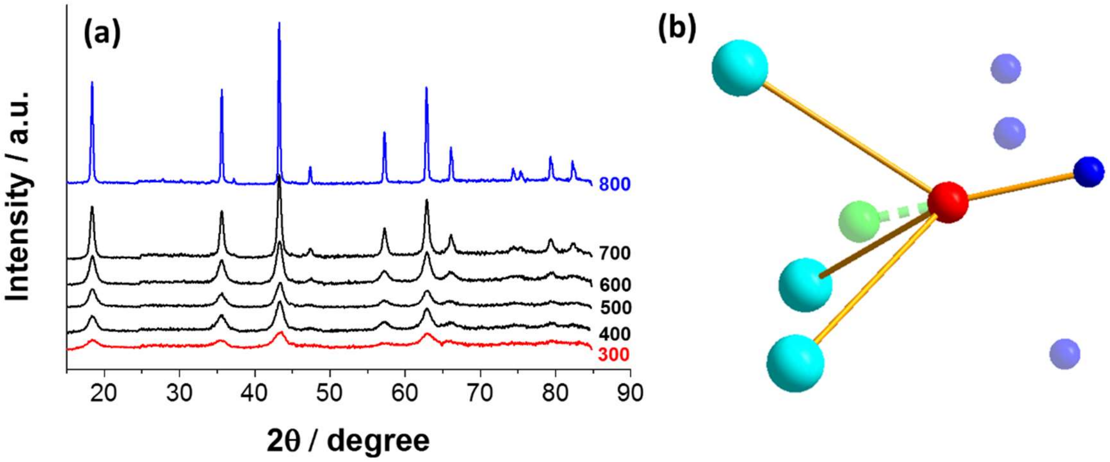

Figure C10. (a) PXRD patterns of LTO nanosheet crystals collected after annealing at different temperature for 6 hours. (b) Depiction of (coordination) structure in distorted and non-distorted annealed LTO crystals, where green ball represents the oxygen position in a less distorted LTO crystal that is annealed at higher temperature, and the red ball represents the oxygen atom in low-temperature annealed LTO (distorted crystal). Cyan and blue balls are Ti and Li atoms, respectively. The faint blue balls signify 16*c* sites in lithiated LTO.

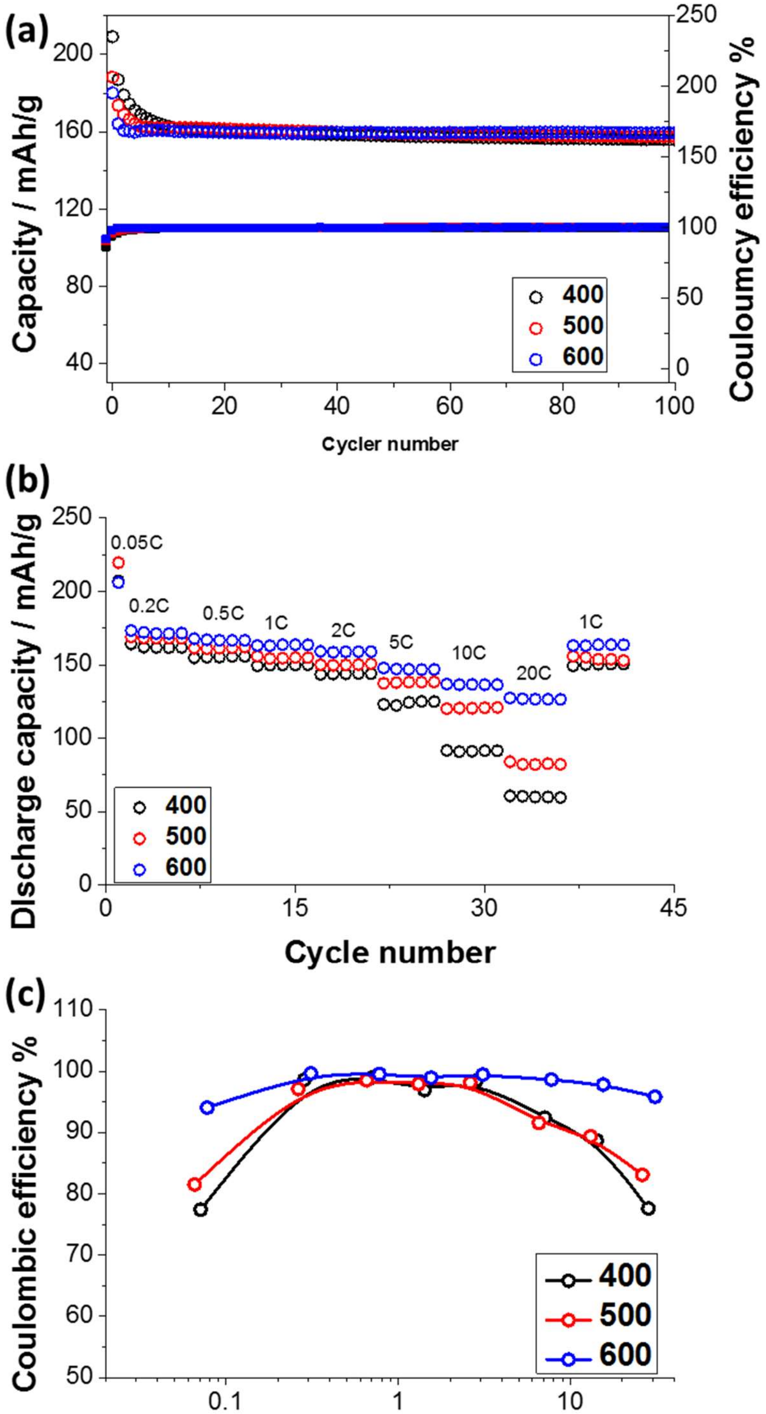

Figure C11. Electrochemical performance of 400, 500 and 600 ^{o}C annealed LTO: (a) Capacity at 1C rate over 100 cycles; (b) discharge capacity at different rates over the C-rate range of 0.05-20C; and (c) the corresponding Coulombic efficiency of the Ragone plot of Figure 5d.

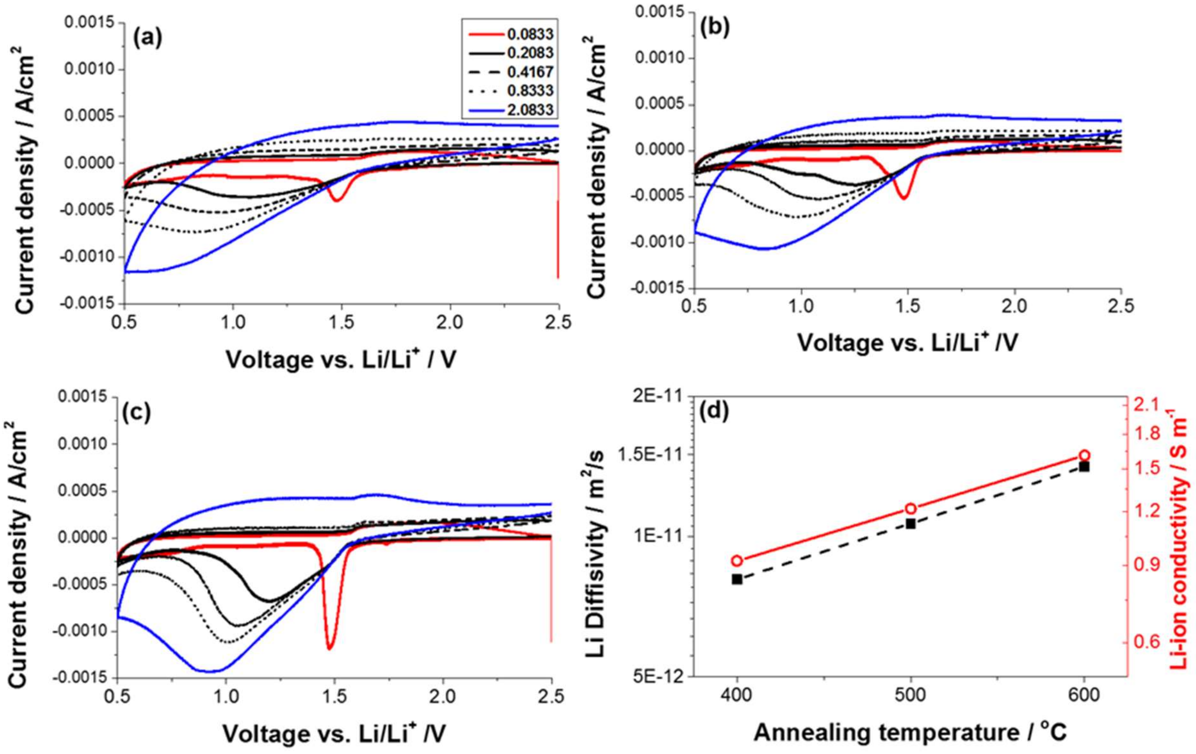

Figure C12. Cyclic voltammograms of LTO nanosheet crystals annealed at (a) 400 (b) 500 and (c) 600 ^{o}C at scan rates in the range from 0.083 to 0.833 mV/s, operating in the voltage range of 0.5 – 2.5 V vs. Li/Li$^+$. (d) Li-ion diffusivity (black square) and conductivity (red circle) of LTO nanosheet crystals plotted with respect to their annealing temperature. The former was estimated using Randles–Sevcik equation [C1,2] and the latter was determined from the diffusivity data using Nernst-Einstein relation as explained below.

C.1. Determination of Li-ion Conductivities

To convert Li-ion diffusivities to Li-ion conductivities (plotted in Figure C12d) we made use of the Nernst-Einstein's relation:

$$\sigma_i = \frac{k_B \cdot T}{n \cdot (Z \cdot e)^2} D_i \tag{C1}$$

where σ_i is Li-ion conductivity; e is the elementary charge; n is the number of carriers (Li ions) in the unit volume; Z is the valence of Li ions; D_i is Li diffusivity; k_B is Boltzmann's constant; T is 298.15 K (25°C) in our case. The number of mobile lithium ions in the unit volume was calculated to be 3.035×10^{-2} mol cm^{-3} on the basis of LTO's 8.357 Å lattice parameter at room temperature. [C3]

Table C1. Unit Cell and Structure of lithium titanate hydrate phase

Space Group: Cmcm (63)

a = 3.8014(9), *b* = 16.7073(1), *c* = 3.0056(8) Å

α = *β* = *γ* = 90°

Unit cell: 190.90 $Å^3$

Atom	X	y	Z	B_{iso} ($Å^2$)	Occupancy	Wyckoff
O1	0	0.7875(1)	0.25	1.3(7)	1	4*c*
O2	0	0.6203(3)	0.25	1.3(7)	1	4*c*
Li1 / Ti	0	0.3084(4)	0.25	1.1(2)	0.203(6) / 0.796(4)	4*c*
Li2 / OH	0.5	0.5250(1)	0.25	3.6(3)	0.444(3) / 0.555(7)	4*c*

Table C2. Fitting parameters of oriented-attachment growth kinetics of LTO nanosheet crystals annealed at various temperatures. The employed kinetic model is the one proposed by Zhan *et al.* [C4] and is given as indicated in the equation below, where d is the average crystal size at time t, d_0 is the initial average crystal size of nuclei, m is the aggregation factor as the indicator of crystal combination, and finally k is the growth rate constant. The activation energy E_a was estimated from Arrhenius equation, where k_B and A are the Boltzmann factor and pre-exponential factor, respectively.

Annealing temperature / ºC	350	425	500
Equation	$d = d_0\left(\frac{1+mkt}{1+kt}\right); lnk = -\frac{E_a}{k_B T} + A$		
d_0 /nm	2.247	2.537	2.583
m	2.671	3.049	3.458
k /min^{-1}	0.0069	0.050	0.628
E_a /kJ·mol^{-1}	119.30		

Table C3. Crystallographic data of prepared LTH and LTO nanocrystals. *a, b, c* are the unit cell dimensions. Additionally, the Rietveld refinement reliability factors of each sample are also listed.

Temperature / ºC	As-prepared LTH	150	200	250	300	350	400	425	500	600	800
a(LTO) / Å	--	--	--	--	8.34592	8.35061	8.36647	8.36417	8.3676	8.37044	8.37104
a(LTH) / Å	3.80057	3.80087	3.79884	3.83839	--	--	--	--	--	--	--
b(LTH) / Å	16.74401	16.71073	16.61658	16.60982	--	--	--	--	--	--	--
c(LTH) / Å	3.00322	3.00704	3.00502	2.95437							
Grain Size / nm	7.9	8.3	8.1	4.6	3.3	4.8	7.5	8.3	9.9	17.6	67.3
BET Specific Surface area / m^2/g							90.6		86.4	70.3	
R_p	4.77	4.57	4.82	8.77	9.01	7.13	4.96	3.04	2.91	2.57	2.23
R_{wp}	4.46	4.23	4.53	7.76	8.12	6.35	4.72	4.03	3.67	3.23	2.01
χ^2	5.05	4.91	5.67	10.55	11.34	8.78	6.01	5.1	3.75	2.81	3.34

C.2. References

(C1) Aoki, K.; Tokuda, K.; Matsuda, H. Theory of Linear Sweep Voltammetry with Finite Diffusion Space. *J. Electroanal. Chem.* **1983,** *146* (2), 417.

(C2) Kavan, L.; Procházka, J.; Spitler, T. M.; Kalbáč, M.; Zukalová, M.; Drezen, T.; Grätzel, M. Li Insertion into $Li_4Ti_5O_{12}$ (Spinel) : Charge Capability vs. Particle Size in Thin-Film Electrodes. *J. Electrochem. Soc.* **2003,** *150* (7), A1000.

(C3) Takai, S.; Kamata, M.; Fujine, S.; Yoneda, K.; Kanda, K.; Esaka, T. Diffusion coefficient measurement of lithium ion in sintered $Li_{1.33}Ti_{1.67}O_4$ by means of neutron radiography. *Solid State Ionics* **1999,** *123* (1–4), 165.

(C4) Zhan, H.; Yang, X.; Wang, C.; Chen, J.; Wen, Y.; Liang, C.; Greer, H. F.; Wu, M.; Zhou, W. Multiple Nucleation and Crystal Growth of Barium Titanate. *Cryst. Growth. Des.* **2012,** *12* (3), 1247.

Appendix D

Supporting Information for Chapter 6:

Capacity Fade Mechanism of $Li_4Ti_5O_{12}$ Nanosheet Anode

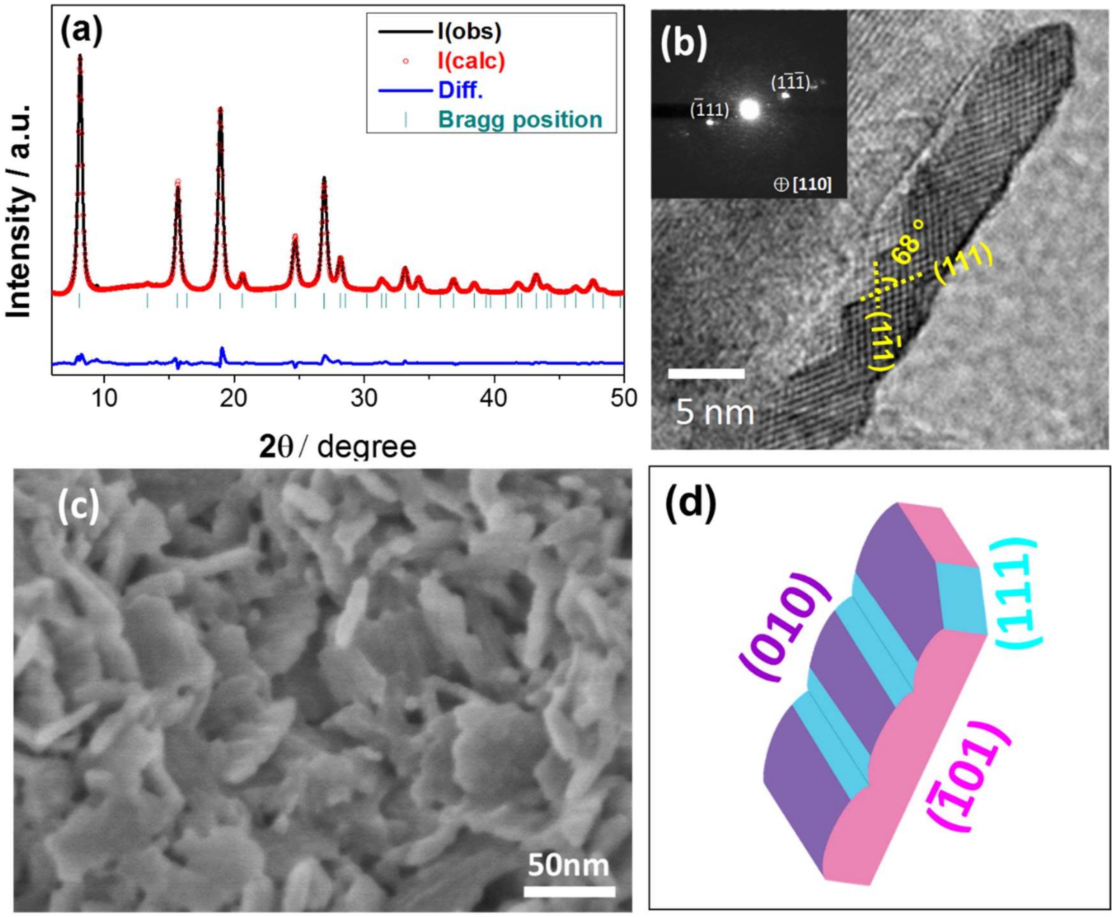

Figure D1. (a) Rietveld refinement results of synchrotron-XRD of LTO nanosheets with reliability factors of: $\chi^2 = 2.43$, $R_{Bragg} = 1.82$ and $R_{wp} = 3.34$; (b) the morphology of the synthesized LTO nanosheet obtained by (b) STEM (c) SEM, and its (d) schematic diagram.

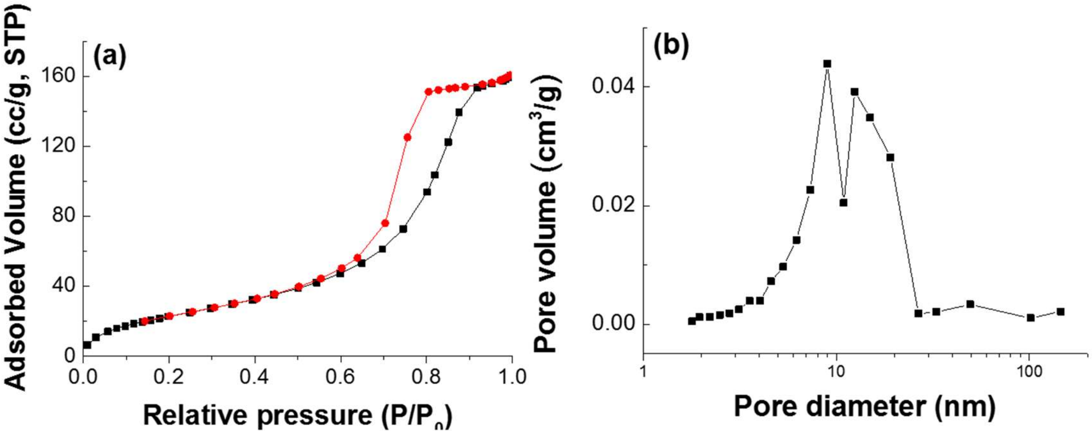

Figure D2. (a) Nitrogen absorption/desorption isotherm and the corresponding (b) Barrett-Joyner-Halenda (BJH) pore size distribution of LTO nanosheets.

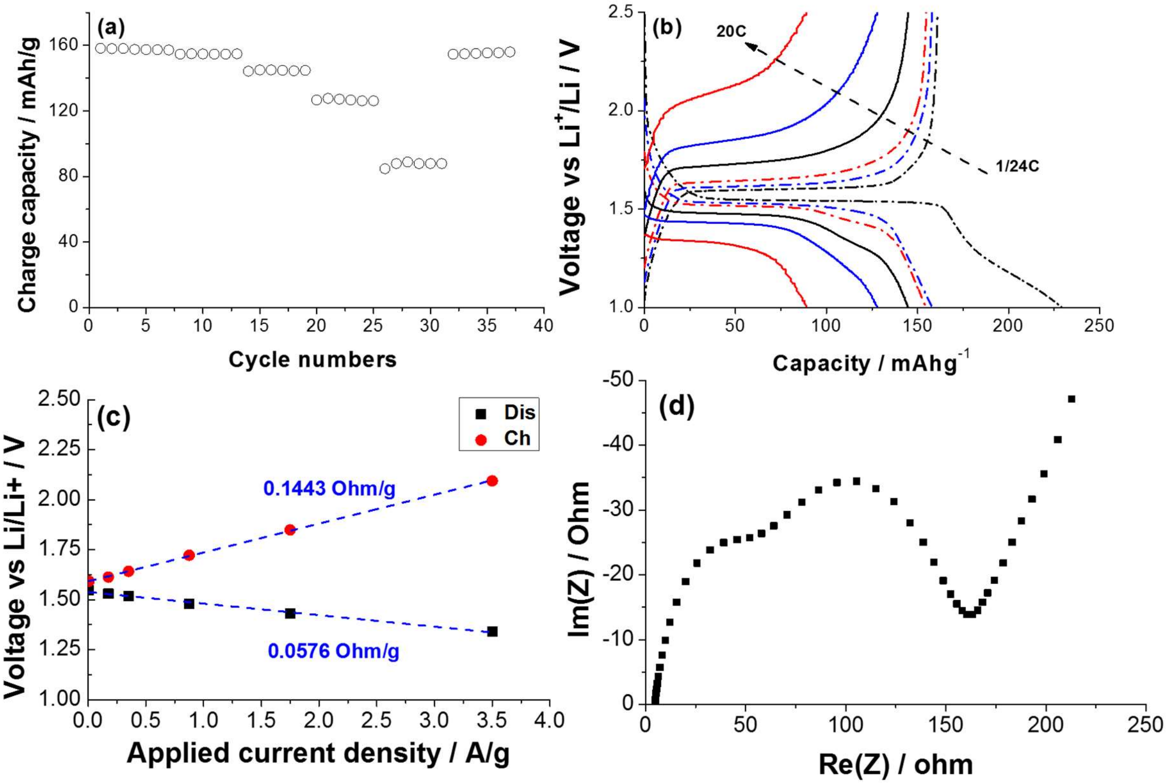

Figure D3. (a) Charge capacity cycling results at various rates from 1/24 C to 20 C of LTO nanosheets with 10% carbon operated from 1.0 to 2.5 V vs. Li/Li$^+$ and (b) the corresponding voltage *vs*. capacity charge/discharge profiles. (c) Electrode polarization evaluation from plateau voltage positions at different charge and discharge rates of LTO nanosheet electrodes. (d) Nyquist plot of LTO/Li half cells (after formation cycle at C/24 rate) discharged to 2.5V vs. Li/Li$^+$.

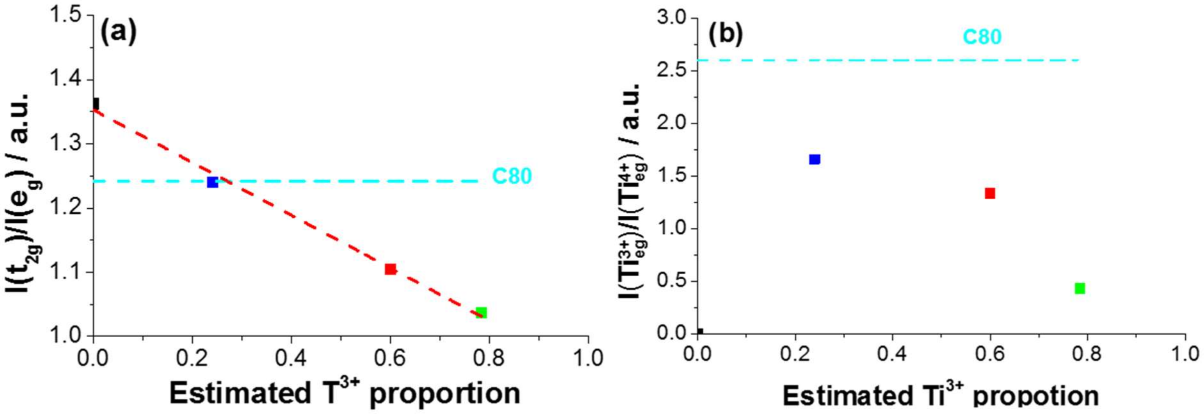

Figure D4. *t_{2g}/e_g* peak ratios of different cycled LTO nanosheets extracted from (a) TEY mode Ti L-edge and (b) FY mode O-kedge XANES spectra.

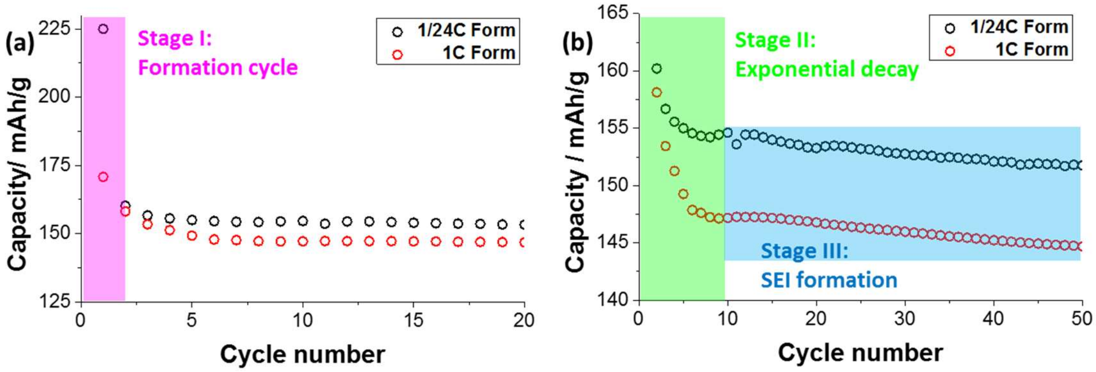

Figure D5. Galvanostatic 1C discharge/charge cycling results of LTO nanosheet electrodes prepared by applying 1/24C (black) and 1C (red) as formation current. The delivered capacity in each formation cycle is included in (a) as the first circles, and (b) shows only the cycling performance at 1C rate after formation at 1/24C or 1C condition. The shaded areas demark the three stages of capacity fade.

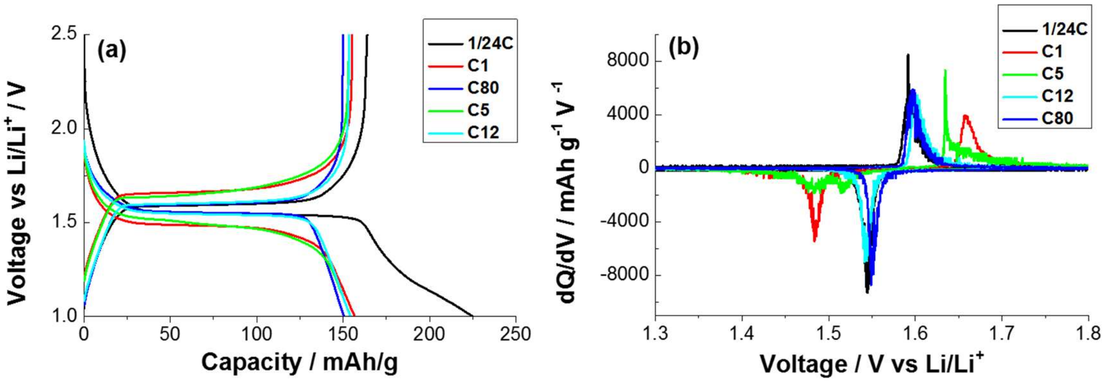

Figure D6. (a) Voltage profiles of LTO electrodes at 1/24C formation cycle and several subsequent 1C cycles; and (b) corresponding differential capacitance, dQ/dV plots.

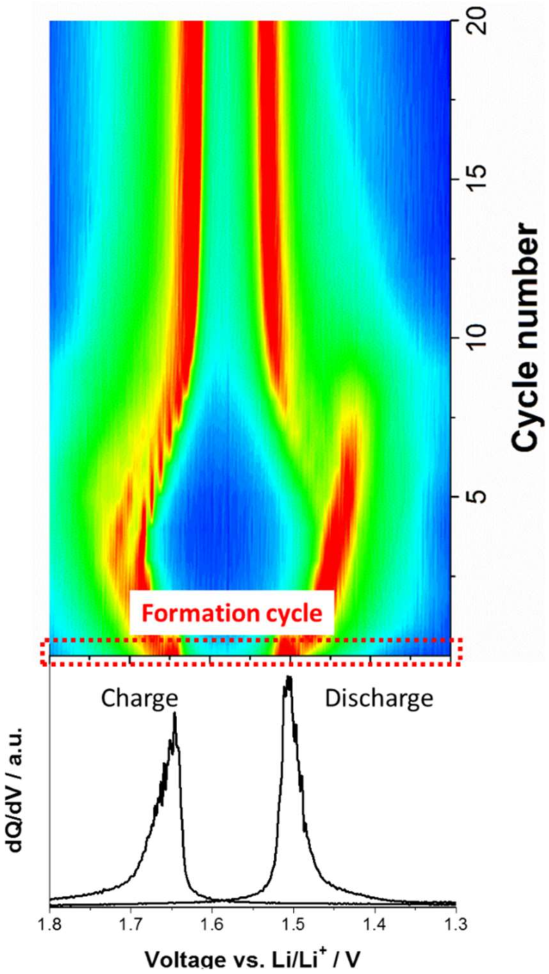

Figure D7. Schematic illustration of how the contour plot of polarization variation relates to the differential capacitance (dQ/dV) plot (black profiles), where the formation cycle is taken as an example. The highest color temperature (red) in the contour plot corresponds to the peaks in dQ/dV plot; and the ascending, descending and valey regions in the dQ/dV plot are presented in lower color temperature in the contour plot.

D.1. Deduction of the overpotential and fraction transformed of irreversibly lithiated LTO

The overpotential of cycled LTO nanosheets is given by the following equation

$$\Delta E = I \cdot R = \mathrm{I} \cdot \frac{1}{\sigma_{eff}} \frac{L}{A} \tag{D1}$$

Due to the unique zero-strain characteristic of $Li_4Ti_5O_{12}$, the overall geometrical parameters A and L are assumed to be constant during cycling.

According to the linear Rule of Mixtures, the effective electrical conductivity of LTO nanosheets after delithiation, i.e., $Li_4Ti_5O_{12}$ phase dominated in the bulk, would be

$$\sigma_{eff} = \sigma_{spinel}(1 - x(t)_{overLi}) + \sigma_{overLi}x(t)_{overLi} \tag{D2}$$

where σ_{spinel}, the electrical conductivity of $Li_4Ti_5O_{12}$ spinel is 10^{-9} S cm^{-1} (this value lies in the insulator range),[D1] σ_{overLi} is the electrically conductive overlithiated phase that is known as a good conductor according to theoretical calculations,[D1] and $x(t)_{overLi}$ is the fraction transformed from spinel into overlithiated phase.

D.2. JMAK kinetics of irreversibly lithiated LTO formation

Meanwhile, the evolution of the fraction transformed with respect to cycle number *h* in 3D space can be expressed by the universal Johnson-Mehl-Avrami-Kolmogorov (JMAK) kinetic model :[D2]

$$x(t) = 1 - \exp[-x_{extended}(h)] \tag{D3}$$

Considering that the contribution of spinel $Li_4Ti_5O_{12}$ is small enough as its conductivity 10^{-9} S cm^{-1} tends to be negligible, Eq. (2) simplifies to:

$$\sigma_{eff} = \sigma_{overLi}\{1 - \exp[-x_{overLi}^{extended}(h)]\} \tag{D4}$$

In this context, the effective electrical conductivity of cycled LTO nanosheets only varies with the transformed volume fraction of overlithiated phase.

The lithiation of LTO is thermodynamically unfavorable unless applying external driving forces such as current, therefore it is reasonable to assume the phase transformation from LTO to overlithiated phase is function of cycle numbers, i.e. the repetitions of intercalation. In this way, the linear growth rate of overlithiated phase, $r(h)=v \cdot h$, where *h* is cycle number and *v* is simply a rate constant, with respect to one cycle of intercalation/deintercalation. In the meantime, because the overlithiated phase mostly grows in the near-surface region, interfacial-controlled reaction was

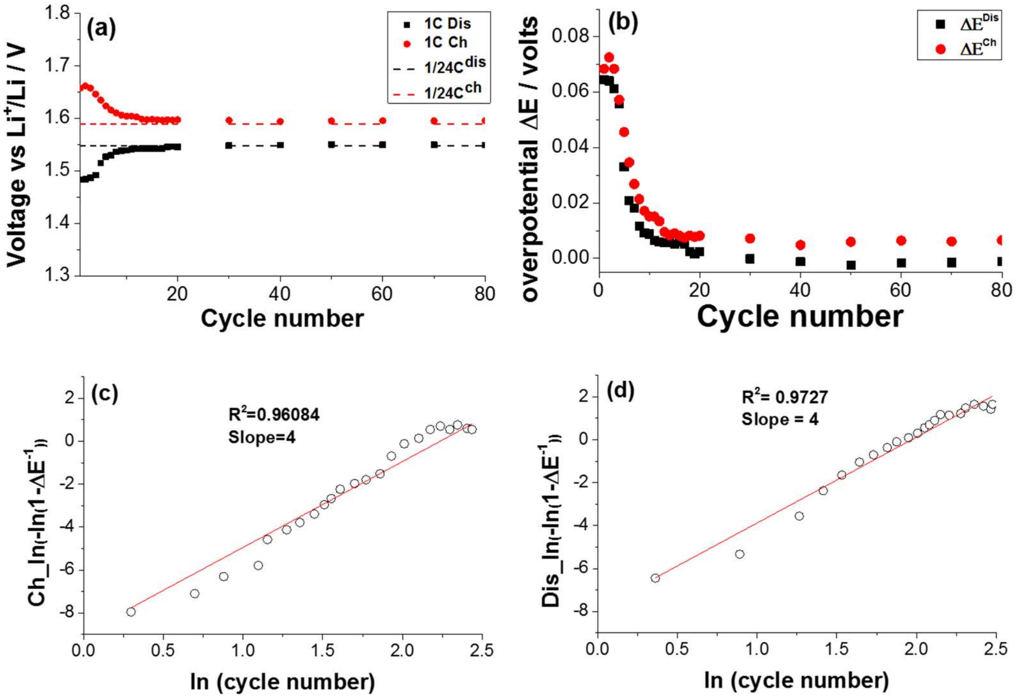

Figure D8. (a) The plateau voltage position variation during 1C cycling test of LTO electrode following 1/24C formation. (b) The overpotential defined as the difference between plateau voltage and the open-circuit voltage (OCV). Avrami exponents of 4 for the formation of relaxed LTO strucutre at constant nucleation rate and 3D isotropically gowth can be extracted from the slope of Avrami plots of (c) charge and (d) discharge process, respectively.

considered. A simple power of cycle number relationship of nucleation as $N=N_0h^a$, where N is the nucleation rate, N_0 is the rate constant and a is the exponent of cycle number h, was employed assuming the formation of overlithiated phase is basically irreversible only depending on the degree of electrochemical intercalation. Furthermore, the dimensionality of overlithiated phase growth is d_g. By combining all factors, the following relation can be obtained:

$$x(h)_{overLi} = 1 - \exp\left[-x_{overLi}^{extended}(h)\right] = 1 - \exp\left[-k \cdot h^{d_g+a}\right] \qquad \text{(D5)}$$

where k is a constant. In the case of continuous nucleation at constant rate (a=1) and three-dimensionally isotropic growth (d_g = 3), the Avrami exponent of cycle number term d_g+a becomes 4.

By combing Eq. (D1), (D4) and (D5), the overpotential ΔE is shown to be inversely proportional to fraction transformed of overlithiated phase:

$$\Delta E^{-1} \propto 1 - \exp\left[-k \cdot h^{d_g+a}\right] \tag{D6}$$

where all symbols have the same definition as above.

It turns out that the Avrami exponent can be extracted from the slope of Avrami plot according to:

$$\ln(-\ln(1 - \Delta E^{-1}) \propto lnk + (d_g + a)lnh \tag{D7}$$

The values of both discharge and charge overpotentials are close to 4, which means the overlithiated phase grew three-dimensionally in the near surface region.

D.3. JMAK Kinetics of Relaxed LTO Formation Induced by 8*a*-16*c* Cointercalation

1) The initial polarization variation as a result of 8*a*-16*c* cointercalation-induced structural relaxation can also be described by the JMAK kinetic model on the basis of the following assumptions: According to a series of NMR experiments done by Wilkening's group,[D3-5] the activation energy of Li diffusion in spinel LTO is 0.62 eV; the corresponding one for partially lithiated $Li_{4+x}Ti_5O_{12}$ (0<x<3) is *circa* 0.36 eV. The Li^+ diffusivity of $Li_{4+x}Ti_5O_{12}$ is therefore 10^5 times higher than that of spinel LTO at room temperature. Also since Li^+ diffusivity in relaxed LTO structure is impeded, it is expected to be even smaller than the order of 10^{-9}.
2) Li^+ diffusion coefficient D, and electrical conductivity σ can be related via mobility and the Einstein relation:

   $$\sigma = ne\tilde{\mu} = ne\frac{D}{k_B T} \tag{D8}$$

   where k_e is Boltzmann's constant, n is the charge number of Li ion, e is the elementary charge of electrons, T is temperature and $\tilde{\mu}$ is the mobility.
3) The conductivity of the mixture of relaxed structure and spinel LTO according to the linear Rule of Mixtures is given by

   $$\sigma_{eff} = \sigma_{spinel}(1 - x(t)_{relaxed}) + \sigma_{relaxed}x(t)_{relaxed} \tag{D9}$$

   The contribution of σ_{spinel} can be ignored as it is extremely small. The effective conductivity σ_{eff} therefore is proportional to Li-ion diffusivity in relaxed LTO, $D_{relaxed}$.
4) By combing Eq. (D1), (D4) and (D5), the overpotential is inversely proportional to fraction transformed of relaxed LTO phases. Following the aforementioned data processing, the Avrami constants of charge/discharge processes can be estimated as shown in Figures D9.

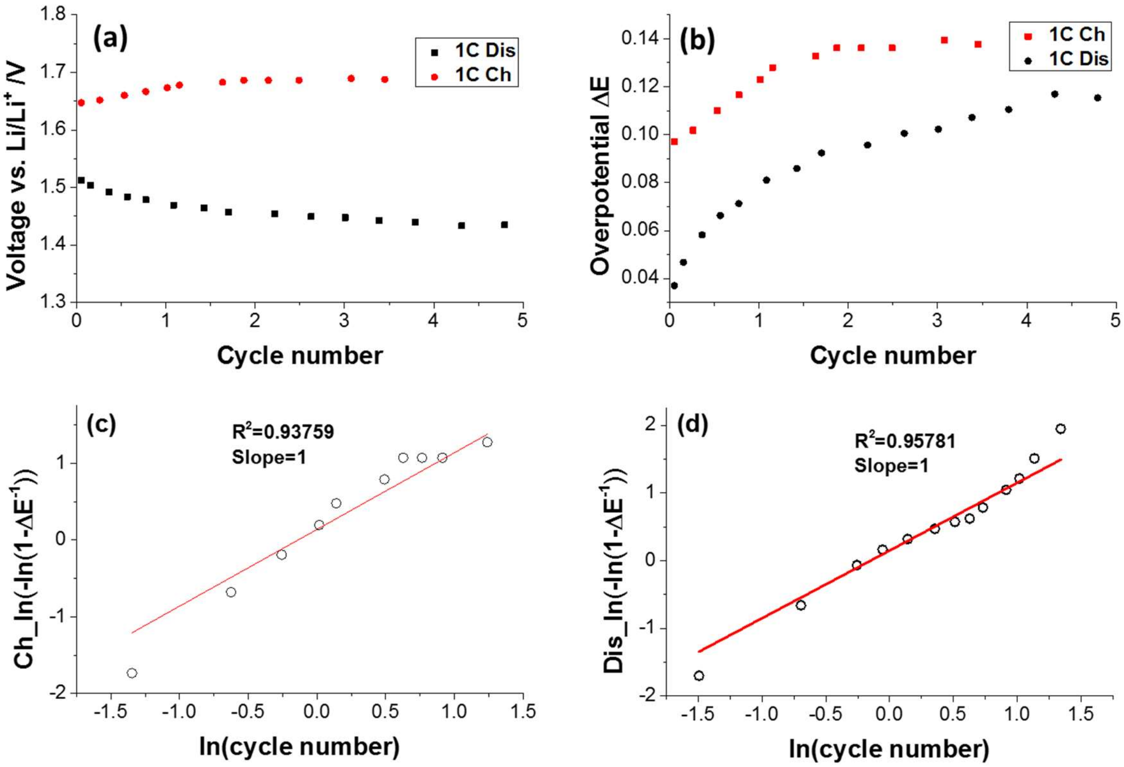

Figure D9. (a) The plateau voltage position variation during 1C cycling test of LTO electrode following 1C foramtion. (b) The overpotential defined as the difference between plateau voltage and the open-circuit voltage (OCV). Avrami exponents of 1 for the formation of relaxed LTO strucutre at constant nucleation rate can be extracted from the slope of Avrami plots of (c) charge and (d) discharge processes, respectively.

D.4. Verification of JMAK kinetic model

Stage I in Figure D10a represents capacity fade during the formation cycle. Stage II represents subsequent exponential decay of capacity due to formation of relaxed LTO. If the applied current for formation cycle is at the same rate as the subsequent galvanostatic charge/discharge, these two stages can be considered as a continuous kinetic process. Thus, formation of relaxed LTO in the near-surface region determines the capacity in Stage I & II. The conintercalation-induced relaxed LTO structure can be described in terms of classical nucleation-growth mechanism (please refer to Figure 5 in Cpater 6). Initially, nucleation of relaxed LTO leads to a random distribution of isolated nuclei that impede Li diffusion in the crystal. Reduced Li diffusivity results in gradual increase of polarization, which is presented as the initial rising transition of polarization increase (marked “Retartded Li diffusion” region” in Figure D10b). As the formation of relaxed LTO continues, a continuous zone is established via both nucleation and growth processes. This helps to improve the conductivity hence facilitating intercalation in the bulk this manifested by the subsequent declining transition of polarization up to ca. 10 cycles (“bulk LTO region“ in Figure D10b).

Comparison of the experimental capacity fade data, polarization variation, and the empirically fitted JMAK kinetic model provides clear connection to the formation of the relaxed LTO phase. In Figure D10b, the empirical JMAK model results are given as the black open squares which very well describe the polarization variation trend (counter plot). That is, the initially increasing transition (the red “retarded Li diffusion” region up to 4 cycles of charging) in the contour plot can be seen to agree well with the JMAK description of the nucleation process of relaxed LTO. Meanwhile, the subsequent declining charge polarization transition (blue “bulk LTO” region in Figure D10b) can be described with the JMAK kinetic model as well by considering the contribution of relaxed LTO growth until the exponential decay of capacity fade gets leveled-off at about 10 cycles. In discharge polarization though there appears to be a rather mismatched transition of the two processes (nucleation and growth respectively of relaxed LTO) resulting in the observed abrupt change in polarization. This is becasue of the competition between the contribution from bulk LTO and relaxed LTO structure in the near-surface region. This postulation is consistent with the observed dependency on rate as with C/24 current the mismatch is almost eliminated.

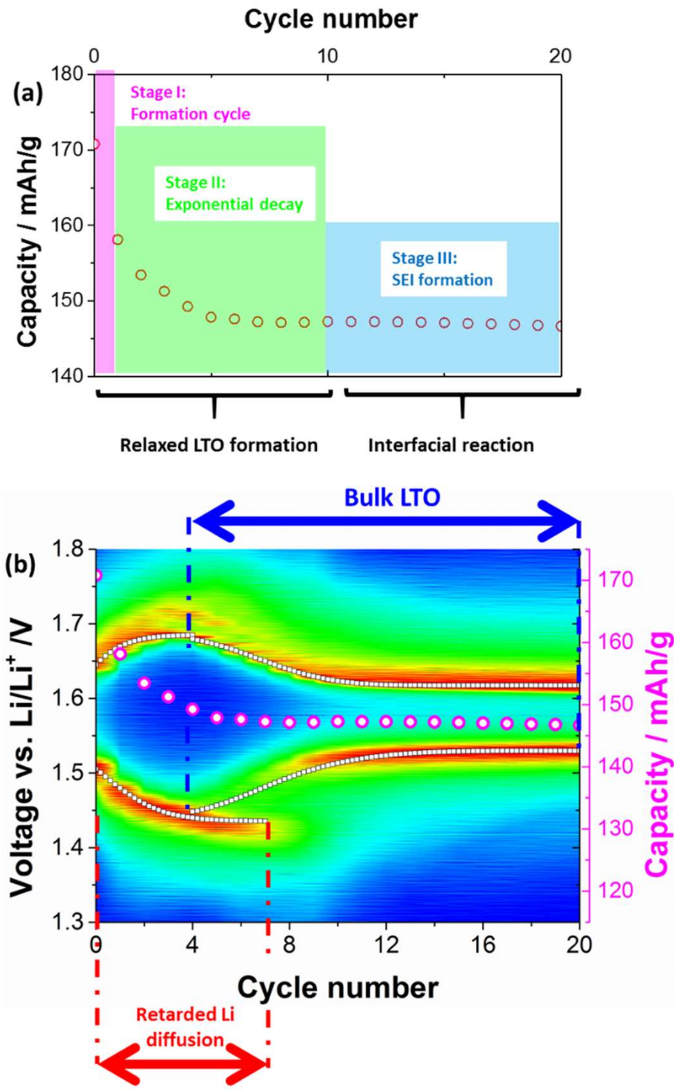

Figure D10. (a) Capacity variation with cycling at 1C galvanostatic charge/discharge, which is divided into: Stage I of formation cycle (magenta), Stage II of exponential decay (green) and Stage III of SEI formation (cyan); (b) the corresponding polarization variation (contour plot) and its empirically fitted results (open squares) of JMAK model. The data before cycle no 5 are fitted with Avrami exponent of 1 to describe the nucleation of relaxed LTO (red region labelled as "Retarded Li diffusion"); and those after 4 cycles are fitted with Avrami exponent of 4 to additionally consider isotropic growth (blue region labelled "bulk LTO"). In discharge polarization (intercalation), the calculation of "Retarded Li diffusion" was extended to 7 cycles in order to show the accuracy of JMAK model. The open magenta circles represent the corresponding capacity retention.

D.5. Effect of Discharge Depth on LTO Cycle Life

Figure D11 compares the performance of galvanostatic charge/discharge 1C cycle life tests operating at 2.5-1.2V (red) and 2.5-1V (blue), respectively to evaluate the effect of depth of discharge on cycle life. As it can be seen the shallow depth of discharge does help to provide a better cycle performance. The formation of $Li_{7+x}Ti_5O_{12}$ is not eliminated (but x becomes smaller), which means that the near-surface relaxed LTO still forms but most likely occupies a thinner zone.

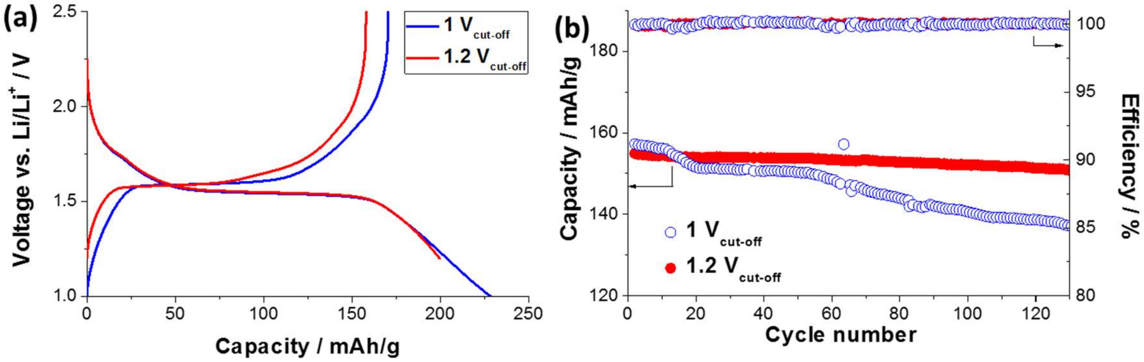

Figure D11. (a) The formation cycle at C/24 cut-off at 1.2 (red) and 1 V vs. Li/Li$^+$ (blue), and (b) the subsequent cycling at 1C.

Table D1. Structural Parameters of LTO nanosheets

Unit Cell and Structure – $Li_4Ti_5O_{12}$ Spinel phase

Space Group : F d $\bar{3}$ m (227)

$a = b = c = 8.3564$ (5) Å

$\alpha = \beta = \gamma = 90°$

Unit cell: 583.36 Å^3

Atom	**X**	**y**	**Z**	**B_{iso} (Å^2)**	**Occupancy**	**Wyckoff**
O1	0.2612(1)	0.2612 (1)	0.2612 (1)	1.40(8)	1	32*e*
Li1	0.125	0.125	0.125	1.1(2)	1	8*a*
Ti2	0.5	0.5	0.5	0.89(3)	0.833(3)	16*d*
Li2	0.5	0.5	0.5	0.89(3)	0.166(7)	16*d*

D.6. References

(D1) Young, D.; Ransil, A.; Amin, R.; Li, Z.; Chiang, Y.-M. Electronic Conductivity in the $Li_{4/3}Ti_{5/3}O_4$-$Li_{7/3}Ti_{5/3}O_4$System and Variation with State-of-Charge as a Li Battery Anode. *Adv. Energy Mater.* **2013,** *3* (9), 1125.

(D2) Fanfoni, M.; Tomellini, M. The Johnson-Mehl- Avrami-Kohnogorov model: A brief review. *Il Nuovo Cimento D* **1998,** *20* (7), 1171.

(D3) Wilkening, M.; Amade, R.; Iwaniak, W.; Heitjans, P. Ultraslow Li diffusion in spinel-type structured $Li_4Ti_5O_{12}$-A comparison of results from solid state NMR and impedance spectroscopy. *Phys. Chem. Chem. Phys.* **2007,** *9* (10), 1239.

(D4) Wilkening, M.; Iwaniak, W.; Heine, J.; Epp, V.; Kleinert, A.; Behrens, M.; Nuspl, G.; Bensch, W.; Heitjans, P. Microscopic Li self-diffusion parameters in the lithiated anode material $Li_{4+x}Ti_5O_{12}$ ($0<x<3$) measured by ^{7}Li solid state NMR. *Phys. Chem. Chem. Phys.* **2007,** *9* (47), 6199.

(D5) Schmidt, W.; Bottke, P.; Sternad, M.; Gollob, P.; Hennige, V.; Wilkening, M. Small Change-Great Effect: Steep Increase of Li Ion Dynamics in $Li_4Ti_5O_{12}$ at the Early Stages of Chemical Li Insertion. *Chem. Mater.* **2015,** *27* (5), 1740.